

Interplay of Microscopic and Emergent Symmetries in a Spin-Orbit Coupled Dirac Semi-Metal

A Thesis

Submitted to the
Tata Institute of Fundamental Research, Mumbai
Subject Board of Physics
for the degree of Doctor of Philosophy

by

Basudeb Mondal

International Centre for Theoretical Sciences

Tata Institute of Fundamental Research

July, 2024

Final Version Submitted in October, 2024

DECLARATION

This thesis is a presentation of my original research work. Wherever contributions of others are involved, every effort is made to indicate this clearly, with due reference to the literature, and acknowledgement of collaborative research and discussions.

The work was done under the guidance of Professor Subhro Bhattacharjee at the International Centre for Theoretical Sciences, Tata Institute of Fundamental Research, Bengaluru.

Basudeb Mondal

Basudeb Mondal

In my capacity as the formal supervisor of record of the candidate's thesis, I certify that the above statements are true to the best of my knowledge.

Subhro Bhattacharjee
Subhro Bhattacharjee

Date: 04/10/2024

Dedicated to my parents

ACKNOWLEDGMENTS

First and foremost, I would like to express my sincere gratitude to my advisor, Prof. *Subhro Bhattacharjee*. His guidance and supervision have been crucial for the completion of my Ph.D. work. I also appreciate his assistance with various non-academic matters at ICTS.

I want to thank all my collaborators. Working with Prof. *Vijay Shenoy* has been an enlightening experience, and I have greatly benefited from his problem-solving approach. Collaborating with Prof. *Tanusri Saha Dasgupta* has also been valuable. I also thank Prof. *Hulikal Krishnamurthy* for discussions on various projects. It was very nice to work with *Manoj*, with whom I had many insightful discussions. Many thanks to the ever-enthusiastic *Ankush* for the countless physics discussions we shared.

I thank Prof. Loganayagam for the many physics discussions during his electromagnetism course. I also thank Prof. Sumilan Banerjee for his valuable advice on various projects.

I am grateful to my batchmates *Junaid, Sarthak, Aditya V, Aditya S, Srashti, Divya, Jitu, Saurav, Saikat, Saumav, and Chandramouli*. Additionally, I would like to thank *Arnab da, Animesh da, Adhip da and Abhaas da* for their support with various physics and non-physics matters. I am thankful for the camaraderie and motivation from *Sugan, Pinak da, and Santhosh*, especially regarding physical activities, which I find essential besides academic work. I also cherish the memorable football sessions with *Joideep da, Santhosh, Ashik, Chandru, Nirnoy, Bhanu, Souvik, Mahaveer, Prashant da, Shibraram da and Subham da*.

I thank *Lalu da, Priyanka di, Pritha di, Bittu da, Monica, Manisha, Akhil, Srikanth, Shashank, Mukesh, Omkar, Tuneer, Anup, Uddepta, Priyadarshi, Tamoghna, Sparsh, Rajarshi, Tushar da, Faruk da and Harsh* for their companionship. Special thanks to *Debarshee da* for introducing me to the world of Indian classical music. I would like to extend my heartfelt thanks to *Kohinoor da, Subhajit da, Soumi di and Sudipta da* for their invaluable support during challenging times, both in physics and beyond.

My journey to this point has been made possible by the unwavering support and immense sacrifices of my parents. Their contributions are beyond words to express. Lastly, I thank all my family members.

List of Figures

1.1	Schematic phase diagram with varying strength of atomic SOC (λ) and on-site Coulomb interaction (U).	5
1.2	Honeycomb lattice with 2-point unit cell. The \mathbf{b}_1 and \mathbf{b}_2 are lattice translation vectors.	9
1.3	Hexagonal Brillouin zone for graphene.	10
1.4	Band structure of the Hamiltonian in Eq. 1.1. The spectrum near one of the Dirac cones is magnified.	10
2.1	Edge-sharing octahedra forming a honeycomb lattice. As elaborated in the main text and in Appendix A.1.1, the honeycomb lattice lies in the [111] plane of the Cartesian coordinate system whose projections are denoted by X, Y , and Z	20
2.2	The filled circles are points of A sub-lattice and the hollow circles are of B sub-lattice. The gray shaded area shows the two points of a single unit cell with \mathbf{b}_1 and \mathbf{b}_2 being unit lattice vectors (see Eq. A.3).	20
2.3	Octahedral structure formed by the anions (shown by red balls) with the TM ion (blue ball) at the center. X, Y, Z are the three crystallographic axes.	23
2.4	Splitting of the d -orbitals under the action of crystal field effect and SOC.	26
2.5	Honeycomb lattice with π -flux and the four-point magnetic unit-cell in the gauge choice (Eq. 2.37): the dashed (continuous) bonds have $\eta(\mathbf{e}_S, \mathbf{e}'_{S'}) = -1(+1)$ (see Eq. 2.36).	28

3.1	(a) Band structure for the Hamiltonian in Eq. 2.35 for the magnetic unit cell consisting of four sites (Fig. 2.5). Each band is four-fold degenerate. For d^1 system, the lowest four bands are occupied with the chemical potential crossing the two Dirac points as shown. (b) Position of the two Dirac points (Eq.3.1) in the chosen gauge (Fig. 2.5 and Eq. 2.37) in the magnetic Brillouin zone (in red). The primitive Brillouin zone of the hexagonal lattice is also drawn in blue.	32
5.1	The mean field hopping model for the Integer Chern insulator. The second neighbour hoppings (in blue) are generated via the spontaneous symmetry breaking and the hopping amplitudes along the directions of the arrows (in local basis) are $i = \sqrt{-1}$. The same hopping pattern also holds for the singlet spin-octupole Hall mass leading to the octupolar Hall effect (Eq. 6.5), except in that case the hopping amplitude is given by $i\Sigma_{45}$	62
5.2	Stripy CDW for $-i \langle \bar{\chi} \zeta_1 \chi \rangle \neq 0$. Here, red circles and blue dots represent opposite charge densities at the honeycomb sites.	63
6.1	Spectrum for $-i\bar{\chi}\Sigma_{45}\chi$ with zig-zag and armchair edges. Both of these plots show gapless states at $1/4th$ filling (shown by black dashed line). To get this spectrum, we consider a honeycomb lattice with cylindrical geometry where the edges of the cylinder have zigzag or armchair-like boundaries. Here k_x is lattice momentum along the periodic direction. We take 32 magnetic unit cells along the length of the cylinder to perform this numerical calculation.	70

6.2	Figure shows the energy spectrum of low-energy fermions along the $k_x = k_y$ line for different combinations of the masses in a triplet. Any linear combination of the masses in a particular triplet can be represented on the surface of a unit sphere shown at the center. The energy spectrum shown in the upper panel of this figure corresponds to the \mathcal{J}_{1u}^e triplets in Eq. 6.12, 7.15 and the \mathcal{J}_{2u}^e triplets in Eq. 6.13, 7.17. The spectrum in (a), (b) and (c) in the upper panel correspond to the spectrum at the points A , C and B on the sphere. Similarly, the spectrum in the bottom panel corresponds to the \mathcal{J}_{1u}^o and \mathcal{J}_{2u}^o triplets in Eq. 7.21, 7.22, 7.29, 7.30. Here again, the spectrum in (d), (e) and (f) correspond to the spectrum at the points A , C , and B on the sphere.	75
7.1	Density pattern for the staggered spin-octupole density waves corresponding to Eqs. 7.7 and 7.8. The red circles and blue dots here represent opposite densities in the spin-octupole operators given by Eqs. 7.9, 7.10.	85
7.2	Zig-zag Density wave pattern corresponding to the masses of Eqs. 7.15, 7.17, 7.21, 7.22, 7.29 and 7.30. The blue dots and the red circles represent opposite densities of spin quadrupole operator Σ_5	87
7.3	Energy spectrum for the fermions along the $k_x = k_y$ line in presence of either of the singlet masses written in Eq. 7.31, 7.32. Each of the gapless bands is two-fold degenerate. So there are four gapless fermion.	94
7.4	Gapless manifold for the triplet Γ -DSMs : Linear combinations of the form given in Eq. 6.16 for the triplet Γ -DSMs is represented on the surface of a unit sphere. The three great circles shown here are obtained by setting one of the Δ_i s to zero in Eq.6.16. For the triplet Γ -DSMs in Eqs. 7.50 and 7.57, on these great circles, the number of gapless modes is eight as opposed to only four at other points on the sphere.	100

8.1 The six masses in Eq. 4.14 are mutually incompatible. A generic linear combination of such masses (similar to Eq. 6.16 extended to the six masses) can be represented on a five-dimensional sphere, \mathcal{S}^5 , as shown in the left-hand figure which has extended gapless critical hyper-lines (in magenta) separating two different phases described by the two triplets \mathcal{J}_{1u}^e and \mathcal{J}_{2u}^e (Eqs. 4.19 and 4.20). The pink line on \mathcal{S}^5 represents a hypersurface on which the fermionic spectrum is gapless (Fig. 6.2(c,f)). This hypersurface projects to the point B on \mathcal{S}^2 as shown by the dotted lines. The images of the two paths from C to D are also shown in \mathcal{S}^5 112

8.2 Phase diagram for $\tilde{u} = \tilde{w}_2 = 0$. The red horizontal line shows the phase boundary between the disordered and the ordered phases. 114

8.3 Phase diagram for $\tilde{u} \neq 0, \tilde{w}_2 \neq 0$. The red line indicates a continuous transition, whereas the dashed blue and dashed green lines represent first-order phase transitions. 115

9.1 (a) Phase diagram in $\tau_m - \tilde{\lambda}$ plane for $r = 0, \tau'_m = 0, \rho = +1$. The two gapped phases are shown with different colors (gray and cyan). The vertical axis is plotted between $\tilde{\lambda} \in [0, 2.0]$. For larger values, no new phases appear and this feature for very large $\tilde{\lambda} (\rightarrow \infty)$ is shown through extrapolation as shown by the break lines on the vertical axis. The band structures, plotted along the Γ , K and the M points of the BZ. at different points on the phase diagram are shown as insets. The blue horizontal lines in the insets *II*, *V* and *VI* show the position of the Fermi level. In the inset *II*, both the bands are six-fold degenerate as explained in the text. The insets *V* and *VI* are for very large value of $\tilde{\lambda}$ and hence the only the four lower energy $j = 3/2$ bands are shown. (b) Band structure in the topological gapped phase (for $\tau_m = 0.9, \tilde{\lambda} = \infty, r = 0, \tau'_m = 0$) in cylindrical geometry. The edge modes at the Fermi-energy are shown by the blue solid line, with Fermi level marked in dashed line. (c) A single hexagon showing the origin of molecular orbitals at point P_2 of the phase diagram in Fig 9.1(a). Different colored dots represent three t_{2g} orbitals. The six sites of the hexagon are labeled with numbers from 1 to 6. The symmetric linear combination of the orbitals connected by the green dotted line form the lowest energy band. Other orbitals are localized on singles bonds of the hexagon are shown by black dotted lines. See text for details. 120

9.2 (a) Phase diagram for $\rho = +1, r = -0.3, \tau'_m = 0$. Two gapped phases shown in gray and cyan shading. The different metallic phases are shown with different colors and labeled as $F1, \dots, F11$. (b) Fermi surfaces corresponding to different metallic phases. The hole-like Fermi surfaces are shown with blue dashed lines and the electron-like FS are shown with solid violet lines. The hexagonal BZ is shown with red solid lines. The $F1'$ Fermi surface corresponds to the O point of the phase diagram shown in panel (a). The un-dotted and dotted region of $F1$ differ by the fact for the Fermi surface corresponding to the dotted region, one of the Fermi pockets around the K points is electron-like and the other is hole-like, while both are electron-like for the un-dotted region. 123

- 9.3 Phase diagram for $r = 0, \tau'_m = -\tau_m, \rho = +1$. Inset *I* shows a prototypical band structure for a point on the OP_9 line where the lowest band touches the next band linearly at the K points, while the inset *II* shows the band structure at the P_3 point. Since $\tilde{\lambda} = \infty$ at P_3 , only four bands ($J = 3/2$ bands) are shown in inset *II*. As in Fig.9.2(a), metallic phases with different Fermi surface topology, are labeled and colored. In addition to $F8, F9$ and $F10$, introduced in Fig.9.2(a), three new phases, labeled as $F2, F3$ and $F12$ appear. The Fermi surface topology for $F2, F3$ and $F12$ phases are shown by the side. 126
- 9.4 Phase diagram for $\rho = +1, r = -0.3, \tau'_m = -\tau_m$ with $0 \leq \tau_m \leq 1$ and $0 \leq \tilde{\lambda} \leq 2.0$. For $\tilde{\lambda} > 2.0$, the $F8$ phase continues to exist. The six different chloride/bromide compounds are placed in this phase diagram, according to the estimated parameter values of the low energy Hamiltonian (cf. Table 9.1), shown in the insets *I, II* and *III*. The phase diagram is demarcated by the red, blue and magenta lines, according to the Z_2 characters of the bands. See text for details. 129
- 9.5 Fermi surfaces for (a) TiCl_3 , (b) TiBr_3 , (c) ZrCl_3 , (d) ZrBr_3 , (e) HfCl_3 , (f) HfBr_3 . The (a) and (b) are $F5$ -type Fermi surface while the rest are $F4$ type. The blue dotted lines show hole-like Fermi surface and the solid indigo colored lines show electron-like Fermi surface. The red line shows the boundary of the hexagonal BZ. 130
- 9.6 $\tau_m - \tilde{\lambda}$ phase diagram with $\rho = -1, r = 0, \tau'_m = 0$. The two gapped phases, shaded as gray and cyan, as well as pink coloured lines in the phase diagram are identical to those in Fig 9.1(a). The band structures on a typical point on the OP_{11} line is shown in inset *II*. The inset *I* shows the band structure on the transition line between the two gapped phases. Note that inset *I* shows only four bands since it is drawn for a large value of $\tilde{\lambda}$ where the four lower energy $J = 3/2$ orbitals are separated from the higher energy $J = 1/2$ orbitals by a large energy separation. As opposed to Fig 9.1(a), this phase diagram hosts two topological metallic phases, marked in lime-green and dark green shades. The Fermi surfaces for the two metallic regions are shown by insets *III* and *IV*. 132

A.1	Brillouin zone and band structure in the global basis. Each of the four bands indicated in a different color are twofold degenerate. At quarter filling, distinct Dirac cones appear at four points (valleys) Γ , M_1 , M_2 , M_3 . The light blue plane indicates the chemical potential at quarter-filling.	163
A.2	Honeycomb lattice with π -flux. (Left) Unit cell consisting of 8 sites adopted for the analysis. Fermions hop to nearest neighbors where red links shown have a hopping amplitude with a negative sign. (Right) Band structure showing four bands, each of which is two-fold degenerate. The light blue plane shows the quarter-filled chemical potential.	166
A.3	Evolution of band structure along the $\tilde{\lambda} = 0$ line of the phase diagram in Fig. 6 of the main text.	176
A.4	Evolution of band structure along the $\tau_m = 0$ line of the phase diagram in Fig. 6 of the main text.	177
A.5	Band structures along the $\tau_m = 1$ line of the phase diagram in Fig. 6 of the main text. All the bands are 2-fold degenerate. For $\tilde{\lambda} = 20$, only four bands are shown leaving out higher energy $J = 1/2$ orbitals.	178
A.6	A single hexagon of a honeycomb lattice showing the three kinds of next nearest neighbour bonds (green bonds). The six sites are labelled with integers from 1 to 6.	180

List of Tables

2.1	This table shows the the action of the microscopic symmetries on lattice sites. Note $\bar{s} = B(A)$ for $s = A(B)$. The transformation of the $j = 3/2$ orbitals (ψ) which appears in presence of strong SOC (discussed later in this chapter near Eq. 2.24) are also shown. The \mathcal{U}_s (\mathcal{S} represents some lattice symmetry) are 4×4 unitary matrices which are given in Appendix A.2 (Eqs A.16 - A.19).	21
4.1	Irreps of the matrices SU(4) flavour space.	45
4.2	Irreps for the matrices in the SU(2) chiral space.	46
4.3	The SU(4) invariant chiral phases. The microscopic symmetry elements mentioned in this and the subsequent tables are defined in Table 2.1. Also, the ζ_i are generators of the chiral SU(2) and Σ_i are generators of flavor SU(4) which are defined in Eq. 3.9 and Appendix A.3 respectively.	53
4.4	The flavor phases	53
4.5	The mixed phases (insulators)	55
4.6	The mixed phases (semimetals)	58
9.1	DFT estimated hopping terms defined for h_z^{AB} matrix (Eq. 9.2) and SOC strength(λ).	118
A.1	The values of $\rho_i(\mathbf{z}_s) = \pm 1$ defined in Eq. A.33 are written in this table. .	143
A.2	List of 1-dimensional irreps of the IR space group	156
A.3	List of 2-dimensional irreps of the IR space group	156
A.4	List of 3-dimensional irreps of the IR space group	156

Contents

1	Introduction	1
1.1	Interplay of symmetry and entanglement in the strongly correlated systems	2
1.2	Energy scales	3
1.3	SOC-U phase diagram	4
1.4	Dirac fermions	6
1.4.1	Dirac theory for graphene	8
1.5	Thesis structure	13
2	Strong SOC and Microscopics Lattice Hamiltonian	17
2.1	Microscopics of SOC	17
2.2	The lattice structure and microscopic symmetries	19
2.2.1	Crystal field splitting	22
2.3	General hopping model for d^1 honeycomb materials	24
2.4	Effect of strong SOC	25
2.5	The tight binding Hamiltonian for indirect hopping	26
3	Free Dirac Theory and it's symmetries	31
3.1	The band structure	31
3.2	Low-energy Dirac theory	34
3.3	Microscopic symmetries in the low energy theory	38
4	Symmetry implementation and three groups of masses	41
4.1	Short range Interactions	41
4.2	Classification of the fermionic bilinears : phases and transitions	43
4.2.1	Group-1 : The chiral masses	46
4.2.2	Group-2 : The flavour masses	47

4.2.3	Group 3 : The mixed masses	50
4.3	Summary of the phases	52
5	Group-1 : Chiral masses	61
5.1	The SU(8) symmetric Integer Chern Insulator	61
5.2	The SU(4) symmetric stripy charge density wave Insulator	63
6	Group-2 : The Flavor masses	67
6.1	Quantum spin-octupole Hall insulators	68
6.1.1	\mathcal{A}_{1g}^e Singlet mass	68
6.1.2	The \mathcal{F}_{1g}^e triplet masses	71
6.1.3	The \mathcal{F}_{1u}^e and \mathcal{F}_{2u}^e triplet masses	72
6.2	Quantum spin-quadrupole Hall insulators	77
6.3	Probing Multipolar Edge Modes	79
7	Group-3 : The Mixed masses	81
7.1	Density wave Insulators	81
7.1.1	Ising ferro spin-quadrupolar insulator	82
7.1.2	Ising ferro spin-octupolar insulator	83
7.1.3	Staggered (“Néel”) spin-octupolar insulator	83
7.1.4	Stripy spin-octupole density wave insulator	85
7.1.5	Zig-zag spin-quadrupole density wave insulator	86
7.1.6	Zig-zag spin-octupole density wave insulator	87
7.2	Density wave semimetals	92
7.2.1	Staggered (“Néel”) spin-octupole density wave semimetal	93
7.2.2	Stripy spin-octupole density wave semimetal	97
7.2.3	Stripy spin-quadrupole density wave semimetal	100
7.2.4	Ferro spin-quadrupole semimetal	102
7.2.5	Ferro spin-octupole semimetal	103
7.3	Experimental Probes for Multipolar Orders	104
8	Phase transitions	107
8.1	Transition from octupolar quantum Hall phase to a $4e$ superconductor	107
8.2	Unnecessary quantum critical points	110

8.3	Weakly 1st order phase transition from the SU(8) DSM to the stripy CDW phase	112
9	Modeling materials	117
9.1	Single electron phase diagram in the $\tau_m - \tilde{\lambda}$ plane	119
9.1.1	$\tau_m - \tilde{\lambda}$ phase diagram with $r = \tau'_m = 0$	121
9.1.2	Effect of $t_{dd\pi}$	124
9.1.3	Effect of $t_{ddm'}$	126
9.1.4	The material phase diagram	127
9.1.5	Nesting and Lifshitz transitions	129
9.2	$\rho = -1$: Implication for Fluorides	131
10	Summary	135
A	Appendix	137
A.1	The microscopic details	138
A.1.1	The lattice	138
A.1.2	Effective angular momentum of the t_{2g} orbitals	138
A.1.3	The $j = 3/2$ orbitals	139
A.2	The Microscopic symmetries	140
A.3	Relation between the $j = 3/2$ matrices and the Σ matrices generating SU(4)	141
A.4	The $\mathcal{G}(\mathbf{z}_S)$ matrices of transformation to manifestly SU(4) invariant local basis	144
A.5	Low-energy Hamiltonian	146
A.5.1	Band structure	146
A.5.2	The low energy Dirac Hamiltonian	146
A.6	Symmetry transformation of the soft modes	149
A.6.1	Action of lattice symmetry transformations on $\phi(\mathbf{z}_S)$ operators	149
A.6.2	Transformation of the $\chi(\mathbf{x})$ operators under lattice symmetries	153
A.7	Irreducible representations of the IR space group	155
A.8	Determination of broken symmetry group	156
A.9	Basis transformation for the density wave semimetals	158
A.9.1	The structure of the density wave semimetal masses	158
A.10	Analysis in the global basis	160

A.11 Spinless fermions on a honeycomb lattice with π -flux at 1/4-th filling . . .	165
A.11.1 Integer Chern insulator	167
A.11.2 Stripy density waves	167
A.12 A model with $j = 1/2$ spins	168
A.12.1 Chiral masses	169
A.12.2 SU(2) Flavor masses	170
A.12.3 Mixed masses	170
A.13 Derivation of the effective action for the CDW order parameter	173
A.14 Evolution of the Band structures in τ_m - $\tilde{\lambda}$ Phase Diagram	175
A.15 Properties of gapped phases	175
Bibliography	182
Publication list	201

Abstract

This thesis investigates the intricate interplay between microscopic and emergent symmetries in a spin-orbit coupled (SOC) Dirac semimetal. Dirac fermions emerge as low-energy degrees of freedom in many condensed matter systems, and the associated phases and phase transitions crucially depend on the emergent symmetries as well as the implementation of microscopic symmetries on these Dirac fermions. In this work, we study this interplay in the context of an $SU(8)$ symmetric Dirac semimetal, which arises from a specific tight-binding model with spin-orbit coupled $j = 3/2$ electrons. This model serves as an effective low-energy description for the d^1 honeycomb materials like $\alpha\text{-ZrCl}_3$ and $\alpha\text{-TiCl}_3$ in the limit of strong spin-orbit coupling. We explicitly find out the implementation of the microscopic symmetries on the low-energy Dirac fermions in this system. This non-trivial embedding of the microscopic symmetries in the low energy is reflected in the nature of phases proximate to the Dirac semimetal. Such phases can arise from finite short-range electron-electron interactions. In particular, we identify 24 such phases – divided into three classes – and their low energy properties are obtained by condensing particle-number conserving fermion bilinears that break very different microscopic symmetries and/or are topologically protected by symmetries. The latter includes interesting generalizations of quantum spin-Hall phases. Remarkably, some of the resultant phases still support a sub-set of gap- less fermions– protected by a sub-group of $SU(8)$ – resulting in interesting density wave semimetals. We also study some of the interesting phase transitions among the phases.

Motivated by the intriguing suggestion of realizing an $SU(8)$ Dirac semimetal, which appears in the limit of strong spin-orbit coupling (SOC) and a restricted regime of the hopping strengths, we provide a systematic study of the interplay between various hopping pathways and atomic SOC for the low-energy electrons in candidate d^1 transition metal halides MX_3 ($M=\text{Ti, Zr, Hf}$; $X=\text{F, Cl, Br}$). We find various compensated metallic phases appearing in the phase diagram when the hopping strength and spin-orbit coupling strength are varied. The resultant compensated metals have varied Fermi surface topologies and are separated by Lifshitz phase transitions. We discuss the implications of the proximate Lifshitz transition, which may be accessed via strain, in the context of the relevant materials.

Chapter 1

Introduction

Strongly correlated systems, characterized by electron-electron interaction strengths comparable to or exceeding the free-electron bandwidth, have garnered significant attention following the Kondo problem's elucidation of the logarithmic temperature dependence of resistivity at low temperatures [1]. This paved the way for extensive investigations into diverse strongly correlated materials, unveiling a rich tapestry of intriguing phases, including heavy fermion superconductivity [2, 3], high temperature superconductors [4], non-Fermi liquid states [5, 6, 7] etc.

Recent studies have revealed that electronic correlations, in conjunction with other energy scales of the system such as the spin-orbit coupling strength, crystal field splitting, etc., can engender phases with non-trivial entanglement pattern and topological characters [8, 9, 10, 11, 12]. These encompass short-range entangled states, such as symmetry-protected topological (SPT) phases [13] like topological insulators, Chern insulators, and topologically ordered phases like the fractional Chern insulators [14, 15] and quantum spin liquids (QSLs) [16, 17]. Among the various energy scales, spin-orbit coupling (SOC) plays a pivotal role in engineering these topological and entangled phases [9, 10, 11].

Developing a profound understanding of the symmetries underpinning these phases is imperative for unraveling their intricate properties. In this context, we first discuss the interplay between symmetry and entanglement in strongly correlated systems in Sec. 1.1 introductory chapter. Subsequently, we discuss various energy scales present in strongly correlated materials and their implications, with a particular emphasis on the role of SOC in realizing topological and entangled phases in Sec. 1.2 and Sec. 1.3.

Notably, a central focus of this thesis revolves around the fascinating concept of Dirac

fermions in condensed matter systems, which lies at the heart of our investigations. These massless relativistic quasiparticle appear as low-energy degrees of freedom in various topological and strongly correlated phases. In Sec. 1.4 we review the very well known case of graphene where the Dirac fermions arise as low-energy degrees of freedom. Finally, in Sec. 1.5, we discuss the structure for the rest of the thesis.

1.1 Interplay of symmetry and entanglement in the strongly correlated systems

The interplay of symmetry and entanglement plays a crucial role in understanding the phases of matter. The conventional phases, *e.g.*, conventional superconductors, density waves, etc., are described by the spontaneous breaking of the microscopic symmetries. This is possible because the underlying many-body state has a trivial entanglement signature and hence can be approximated by product states such that the local order parameter quantifying the symmetry breaking gives a comprehensive picture.

Recent studies have shown that the interplay of entanglement and symmetry can give rise to two new classes of phases which cannot be described just by symmetry breaking [8]. One class of phases has long-range entangled ground states and hence cannot be described by local order parameters (e.g., QSL, FQHE). In these phases, the existence of symmetries can lead to the fractionalization of the quantum numbers of the emergent quasi-particles[16, 18]. Another class of phases is the symmetry protected topological (SPT) phases[19], the prime example of which are the topological insulators[20]. The ground states in SPT phases, although short-range entangled, have non-trivial topological character, and the role of symmetries here is to protect the topological invariants.

In addition to the microscopic symmetries, new symmetries can emerge when we describe the long-wavelength characteristics of a system using low-energy theories, which are known as infrared (IR) symmetries. For example, in graphene, the low-energy theory is described by Dirac fermions in (2+1)-dimensions where Lorentz symmetry emerges[21]. Additionally, the SU(2) spin rotation symmetry gets enhanced to a larger emergent SU(4) symmetry group. Such symmetries can be important in relating long-distance behavior of the correlations of different phases. The existence of such symmetries can even lead to the realization of deconfined quantum phase transitions.

In understanding the structure of the low-energy theory, it becomes important to understand how the low-energy degrees of freedom transform under the action of the microscopic symmetries. Different ways of implementing the symmetries give rise to the realization of newer phases and phase transitions. For example, in QSL, different ways of implementing the microscopic symmetries on the low-energy spinons give rise to different types of QSL phases.

The realization of this rich variety of phases is heavily influenced by the interplay of different energy scales in condensed matter systems. In the following sections, we first discuss briefly the implications of these energy scales and specifically focus on the interplay of spin-orbit coupling (SOC) and electron-electron interactions in Sec. 1.3.

1.2 Energy scales

Condensed matter systems exhibit a rich interplay between various energy scales, and the competition among these scales gives rise to a diverse array of phenomena in these materials. The most prominent energy scales that play a pivotal role include the electron hopping amplitude (t), the Hund's coupling (J_H) associated with the intra-atomic exchange which lowers the energy cost of placing the electrons in different orbitals with parallel spin as opposed to two electrons in the same orbital, the Coulomb repulsion (U) between electrons, the spin-orbit coupling strength (λ), and the crystal field splitting energy (Δ) due to the local ionic environment. The delicate balance and hierarchical ordering of these energy scales ultimately dictate the low-energy degrees of freedom that govern the system's behavior and the emergent phases it can host.

In the weakly correlated regime, where the hopping energy scale (t) dominates over the Coulomb repulsion (U), the electrons are delocalized, and the system can be described within the framework of band theory. This regime can give rise to various band insulators and conventional metallic phases, depending on the band filling and other material-specific details. On the other hand, in the strongly correlated regime, where the Coulomb interactions (U) overwhelm the hopping (t), the electrons tend to localize, and the system is better described by interacting spin degrees of freedom. Materials with transition metal ions are one of the most experimentally relevant platforms for strongly correlated systems. This includes different iridium oxides in the Ruddlesden-Popper sequence

perovskites[22, 23, 24, 25, 26, 27, 28, 29], hexagonal perovskites [30, 31, 32, 33, 34, 35], pyrocholres [36, 37, 38], etc. In these materials, the partially filled d -orbitals have narrow bandwidth which makes the effect of the interactions pronounced [39]. This leads to various Mott insulators and metal-insulator transitions.

Notably, the spin-orbit coupling (λ) and the crystal field splitting (Δ) cooperate with the electron-electron interactions, effectively enhancing their impact. This is because the spin-orbit coupling and crystal fields split the orbital degeneracies, narrowing the effective bandwidths and amplifying the relative strength of the Coulomb interactions. We discuss the effect of SOC in detail in the next section. The Hund’s coupling on the other hand plays two roles. In a multi-orbital atom with half filling, it effectively enhances the effect of interactions by reducing the critical interaction strength required for Mott transition [40, 41, 42, 43, 44], whereas for other fillings, it reduces the effect [45, 46]. Interestingly, there exists a competition between Hund’s coupling, which tends to distribute the electrons across the available orbitals so as to minimize the effect of Coulomb repulsion, and the crystal field effect, which favors occupying the lowest energy orbitals preferentially [46, 47, 48].

Thus, the intricate interplay between the various energy scales and their cooperative or competing effects ultimately give rise to a diverse array of phenomena in condensed matter systems. In the following section, we discuss the effect of the SOC and the Coulomb interaction in detail.

1.3 SOC-U phase diagram

In this thesis, we delve into the intricate interplay of the UV and IR symmetries in a spin-orbit coupled (SOC) system. Recent studies have shown that SOC is a useful microscopic knob for engineering unconventional implementation of the UV symmetries as well as competing microscopic interactions[9]. This makes SOC a crucial ingredient for realizing the long-range entangled and SPT phases in addition to newer symmetry-broken ones. Fig. 1.1 schematically shows the different phases one can obtain in the presence of SOC and onsite Hubbard interaction. The materials with transition metal ions and lanthanides are a rich playground for the interplay of SOC and electron correlations. For example, the 3d transition metal ions have a narrow bandwidth which makes the electron

correlation effects stronger while the SOC is small in these materials. On the other hand, in the 4d and 5d materials, the SOC becomes comparable to the interaction energy scale. Thus, as one moves to different transition metal materials, different parts of the phase diagram (Fig 1.1) become relevant.

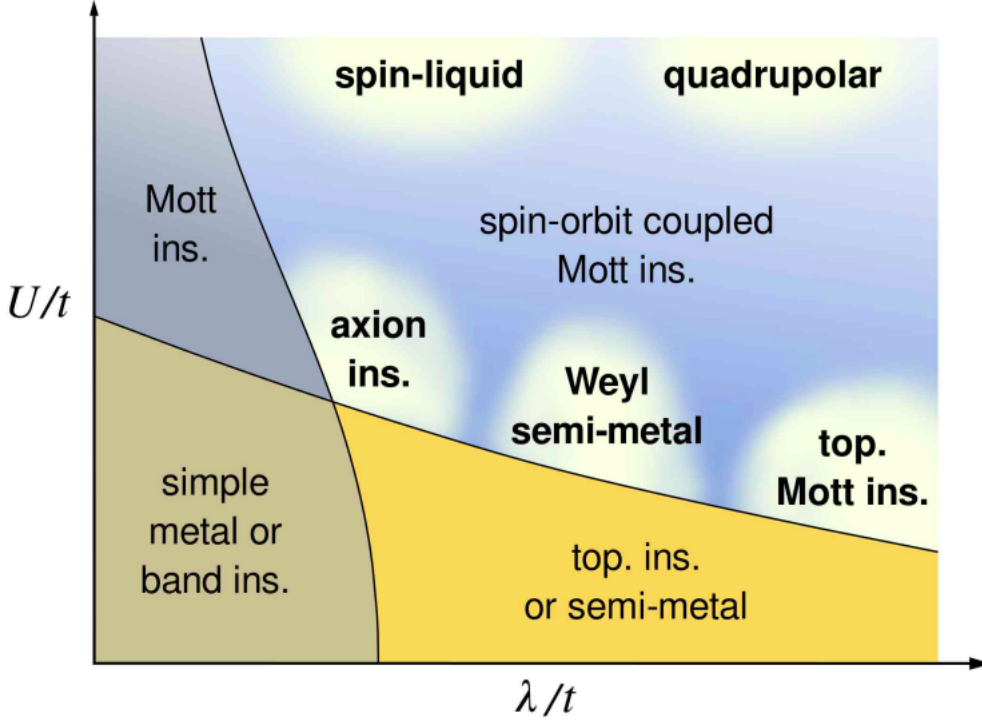


Figure 1.1: Schematic phase diagram with varying strength of atomic SOC (λ) and on-site Coulomb interaction (U). Figure taken from Ref. [9].

In the weakly correlated regime, where electron-electron interactions are relatively weak, the system can be described within the framework of independent and delocalized electrons. In this limit, the spin-orbit coupling (SOC) plays a crucial role by entangling the crystal momentum and spin degrees of freedom. This entanglement can lead to non-trivial topological characters in the ground state, giving rise to various topological insulator phases [20, 49, 50].

In the intermediate correlated regime, interactions open up possibilities for new kinds of topological insulators. In this case, the system can develop magnetic orders but can still be described in terms of weakly interacting quasi-particles and an effective band theory. However, in this regime, spontaneous symmetry breaking can occur, leading to exotic phases such as Weyl semimetals [51, 52, 53], Chern insulators [54, 55], or axionic insulators [56, 57]. For example, in Weyl semimetals, either inversion or time-reversal

symmetry is spontaneously broken, resulting in non-degenerate bands. On the other hand, in axionic insulators, time-reversal symmetry is spontaneously broken, but a new Z_2 topological index emerges, which characterizes the topology of the ground state [58, 59].

In the strongly correlated regime, where the interaction strength is dominant, the system is better described in terms of localized spins. For small values of SOC, the interactions can give rise to various magnetically ordered phases, correlated metallic states, unconventional superconductors [39], etc. However, as the SOC strength increases, it can give rise to anisotropic exchange interactions, which ultimately leads to frustration in the system. A well-known example of this scenario is found in pyrochlore materials with edge-sharing octahedral structures, which can effectively realize the Kitaev model as an effective Hamiltonian. Such systems can host various quantum spin liquid phases. Furthermore, the effective spin degrees of freedom in the strongly correlated regime are spin-orbit entangled. These effective spin degrees of freedom can have higher spin, such as $j = 3/2, 2$, etc [60, 61]. The multipolar couplings in these systems can lead to various interesting phases such as quadrupolar heavy Fermi-liquid, multipolar ordered states [62, 63, 64, 65, 66, 67], etc.

1.4 Dirac fermions

After discussing the various aspects of the strongly correlated systems, we now turn to discuss the Dirac Fermions. Massless Dirac fermions arise in a variety of condensed matter systems [68, 69]. Perhaps the most well-known is the recently studied – both experimentally and theoretically – example of monolayer graphene [70, 71, 72, 73, 74, 75, 76, 77, 78] where such Dirac fermions arise as a low energy limit of electrons hopping on the honeycomb lattice. More generally such Dirac fermions may arise in a variety of other two and three dimensional lattices [68, 79, 80, 81] relevant for several materials including organic semiconductors like α -(BEDT-TTF) $_2$ I $_3$ [81, 82, 83], the $d_{x^2-y^2}$ -wave superconductor in cuprates [84, 85, 86, 87, 88], Dirac and Weyl semimetals [51, 89] and surface of 3D topological insulators [20, 49, 90, 91, 92, 93]. These low-energy Dirac fermions have indelible signatures in a plethora of low-energy experiments of these candidate materials, as is evident in the integer quantum Hall effect [72, 94] as well as other spectroscopic and transport properties [76, 95, 96, 97, 98, 99] of monolayer graphene, surface transport of

3D topological insulators [100] or spectroscopy of d -wave superconductors [84, 85].

Dirac fermions also arise in a somewhat different context as low energy theories of certain quantum spin liquids (QSL). Indeed in U(1) Dirac QSLs, low energy fermionic spinons—minimally coupled to an emergent U(1) gauge field—have free Dirac dispersion with enhanced symmetries at low energies within parton mean-field theories [101]. While in this case of QED₃, the fluctuations of the gauge field ultimately lead to the destruction of the quasi-particles [101, 101, 102, 103, 104, 105, 106, 107, 108], the proximate ordered phases can be obtained by condensing appropriate spinon bilinears that gap out the Dirac spinons. Also, such effective Dirac theories, with or without dynamic gauge fields have also been recently discussed in the context of (2+1) dimensional fermionic particle-vortex dualities emanating out of conjectures of Dirac composite fermions in half-filled Landau level in quantum Hall systems [109].

An equally important question pertains to the nature of the different phases obtained [110] upon gapping out the Dirac fermions via short-ranged four-fermion interactions/other bosonic fields or via external perturbations such as originating from substrate effects in graphene [111]. For the former, a typical effect of such interactions is to condense a fermion-bilinear that dynamically generates mass for the gapless Dirac fermions for a finite strength of the interaction. The nature of the resultant gapped phases ¹ [21, 101, 110, 112, 113] as well as the theory of the associated phase transition from the proximate Dirac semimetal via Gross-Neveu-Yukawa [110, 114, 115, 116, 117] field theories have received considerable attention in a wide array of condensed matter settings and allow for systematic understanding of novel quantum phase transitions including Landau forbidden deconfined quantum criticality [118, 119].

The nature of gapped phases in Dirac systems can be understood by analyzing how mass terms, which open a gap in the initially gapless Dirac fermions, transform under the ultraviolet (UV) symmetries. This approach enables a systematic classification of all possible mass terms based on their symmetry properties. One well-known example of such classification occurs in graphene [21], where different mass terms correspond to conventional symmetry-broken phases such as charge density waves, spin density waves, as well as topological phases like Chern insulators and Z_2 symmetry-protected topological (SPT) phases. We discuss the masses of graphene in detail in Sec. 1.4.1.

¹This phase can have other gapless mode such as Goldstone boson if a continuous symmetry is broken.

This classification methodology extends to other Dirac systems as well. For instance, Ref. [120] presents a classification of mass terms for spinless fermions on a cubic lattice with π -flux through each plaquette. In this context, different mass terms correspond to different density wave phases, bond-order phases, as well as chiral topological insulator and topological superconducting phases.

Dirac theory can also emerge as the low-energy limit of certain spin Hamiltonians [101, 121]. In such cases, different mass terms allow for a systematic identification of all gapped phases. For instance, in a square lattice, the spin Hamiltonian gives rise to an $N_f = 4$ Dirac fermion theory at low energies [101]. Gapping out these Dirac fermions leads to the realization of spin density waves, bond density waves (where spin bilinears order on the lattice bonds), as well as long-range ordered phases such as chiral spin liquid. The classification of mass terms thus provides a comprehensive understanding of the possible gapped phases in these spin systems as well.

A central aspect of the above diverse physics is the implementation of microscopic symmetries on the low-energy Dirac fermions since they ultimately determine the transformation properties of the masses terms. These *ultraviolet* (UV) symmetries typically consist of lattice symmetries, time reversal as well as possible spin-rotation symmetries of the electrons occupying the underlying atomic orbitals. Material-dependent microscopic energetics allow for different implementations of these UV symmetries on the underlying low energy Dirac fermions, opening up avenues to probe the Dirac semimetal [76] as well as stabilize novel proximate phases. Below we discuss the symmetry implementation in the case of graphene and compare it with the spin-orbit coupled Dirac fermions, which is the central aspect of this thesis.

1.4.1 Dirac theory for graphene

In this section, we consider spinful electrons on a honeycomb lattice (Fig. 1.2). The honeycomb lattice is a Bravais lattice with a two-point basis, consisting of the A and B sublattices as shown in the figure. \mathbf{b}_1 and \mathbf{b}_2 shown in Fig. 1.2 are the two lattice translation vectors. The Brillouin zone (BZ) is shown in Fig. 1.3. The nearest-neighbor hopping Hamiltonian for this setting is given by [74, 117]

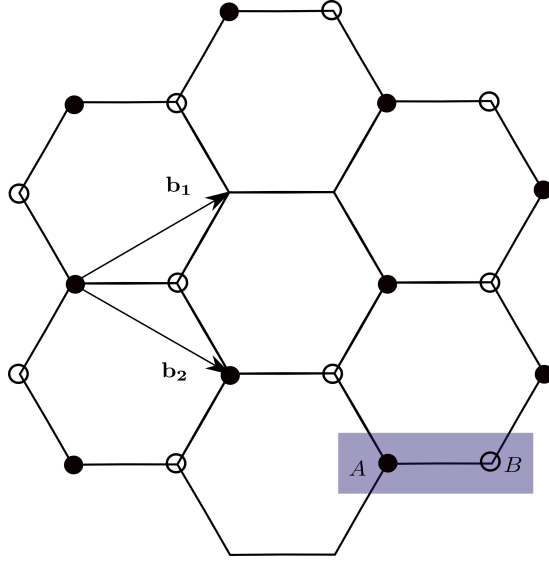


Figure 1.2: Honeycomb lattice with 2-point unit cell. The \mathbf{b}_1 and \mathbf{b}_2 are lattice translation vectors.

$$H_{\text{graphene}} = -t \sum_{\mathbf{R}} \left(c_{\sigma A}^{\dagger}(\mathbf{R}) c_{\sigma B}(\mathbf{R}) + c_{\sigma A}^{\dagger}(\mathbf{R} + \mathbf{b}_1) c_{\sigma B}(\mathbf{R}) + c_{\sigma A}^{\dagger}(\mathbf{R} + \mathbf{b}_2) c_{\sigma B}(\mathbf{R}) + h.c. \right) \quad (1.1)$$

Here $c_{\sigma A(B)}^{\dagger}(\mathbf{R})$ are the electron creation operators at the $A(B)$ sublattice of the unit cell labeled by \mathbf{R} , with spin $\sigma = (\uparrow, \downarrow)$. In terms of the Fourier modes defined as

$$\tilde{c}_{\sigma A(B)}(\mathbf{k}) = \sum_{\mathbf{R}} e^{i\mathbf{k}\cdot\mathbf{R}} c_{\sigma A(B)}(\mathbf{R}), \quad (1.2)$$

the Hamiltonian can be written as

$$H_{\text{graphene}} = -t \sum_{\sigma} \sum_{\mathbf{k}} \left(\tilde{c}_{\sigma A}^{\dagger}(\mathbf{k}), \tilde{c}_{\sigma B}^{\dagger}(\mathbf{k}) \right) \begin{pmatrix} 0 & 1 + e^{-i\mathbf{k}\cdot\mathbf{b}_1} + e^{-i\mathbf{k}\cdot\mathbf{b}_2} \\ 1 + e^{i\mathbf{k}\cdot\mathbf{b}_1} + e^{i\mathbf{k}\cdot\mathbf{b}_2} & 0 \end{pmatrix} \begin{pmatrix} \tilde{c}_{\sigma A}(\mathbf{k}) \\ \tilde{c}_{\sigma B}(\mathbf{k}) \end{pmatrix} \quad (1.3)$$

The dispersion of this Hamiltonian is shown in Fig. 1.4.

This band structure exhibits Dirac cones at half-filling at the K and K' points of the BZ. Expanding this Hamiltonian near the Dirac cones, one gets the low-energy theory for this system as

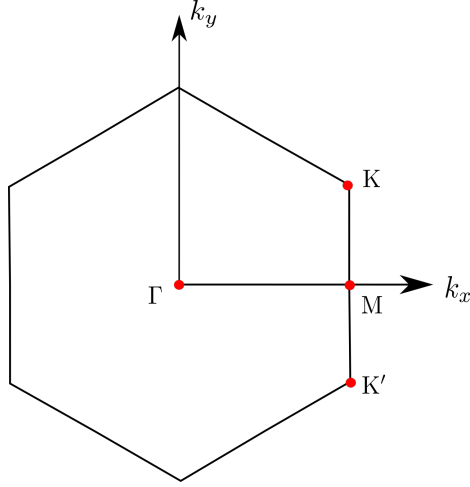


Figure 1.3: Hexagonal Brillouin zone for graphene.

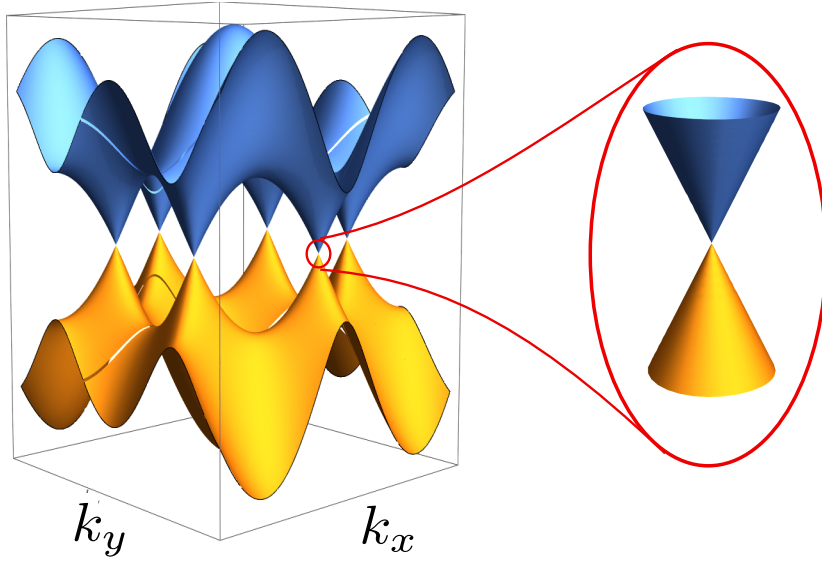


Figure 1.4: Band structure of the Hamiltonian in Eq. 1.1. The spectrum near one of the Dirac cones is magnified.

$$H_{low} = -\frac{3t}{2} \sum_{\sigma} \int d^2x \chi_{\sigma}^{graphene\dagger}(\mathbf{x}) (\alpha_g^{(1)} \partial_x + \alpha_g^{(2)} \partial_y) \chi_{\sigma}^{graphene}(\mathbf{x}). \quad (1.4)$$

Here, \mathbf{x} represents the spatial position vector and $\chi(\mathbf{x})$ is a four-component Dirac spinor given by

$$\chi_{\sigma}^{graphene} = \begin{pmatrix} \chi_{\sigma K}^{graphene} \\ \chi_{\sigma K'}^{graphene} \end{pmatrix}. \quad (1.5)$$

The χ_K and $\chi_{K'}$ are each 2-component Dirac spinors which correspond to the K and the K' valleys respectively and are defined as

$$\chi_{\sigma K}^{graphene}(\mathbf{x}) = \sum_{\mathbf{q} \in \text{HBZ}} e^{i\mathbf{q} \cdot \mathbf{x}} \begin{pmatrix} \tilde{c}_{\sigma A}(\mathbf{K} + \mathbf{q}) \\ \tilde{c}_{\sigma B}(\mathbf{K} + \mathbf{q}) \end{pmatrix}, \quad (1.6)$$

$$\chi_{\sigma K'}^{graphene}(\mathbf{x}) = \sum_{\mathbf{q} \in \text{HBZ}} e^{i\mathbf{q} \cdot \mathbf{x}} \begin{pmatrix} \tilde{c}_{\sigma A}(\mathbf{K}' + \mathbf{q}) \\ \tilde{c}_{\sigma B}(\mathbf{K}' + \mathbf{q}) \end{pmatrix}. \quad (1.7)$$

Here, ‘‘HBZ’’ refers to half Brillouin zone. The $\alpha_g^{(1)}$ and $\alpha_g^{(2)}$ are the Dirac matrices which have the following form:

$$\alpha_g^{(1)} = -\tau_0 \otimes \sigma_2, \quad (1.8)$$

$$\alpha_g^{(2)} = \tau_3 \otimes \sigma_1. \quad (1.9)$$

Here, τ_i and σ_i are the Pauli matrices. The τ_i matrices act in the valley space, while the σ_i matrices act in the sublattice space.

The Hamiltonian can be written in a more compact form using the 8-component spinor

$$\chi^{graphene} = \begin{pmatrix} \chi_{\uparrow}^{graphene} \\ \chi_{\downarrow}^{graphene} \end{pmatrix} \quad (1.10)$$

as

$$H_{low} = -\frac{3t}{2} \int d^2x \chi^{graphene\dagger}(\mathbf{x}) (\mu_0 \otimes \alpha_g^{(1)} \partial_x + \mu_0 \otimes \alpha_g^{(2)} \partial_y) \chi^{graphene}(\mathbf{x}). \quad (1.11)$$

Here, μ_i are the Pauli matrices that act in the spin space of the spinors.

The Hamiltonian described here preserves all the microscopic symmetries, i.e., of the

lattice space group, time reversal, sublattice, SU(2) spin-rotation and particle number conservation. Additionally, new symmetries emerge at lower energies. Notably, the low-energy Hamiltonian exhibits emergent Lorentz symmetry, emergent charge-conjugation, parity, and time reversal symmetries, along with continuous translation symmetries.

Understanding how the low-energy spinor χ transforms under the action of the microscopic symmetries is crucial. Here we discuss the actions of some of the symmetries on the spinors. For example, under the action of the C_6 rotation about the center of a honeycomb plaquette, the K and K' points of the Brillouin zone (BZ) transform into each other, and similarly, the spinors $\chi_{\sigma K}^{graphene}$ and $\chi_{\sigma K'}^{graphene}$ transform into each other. Explicitly, under the action of the C_6 symmetry transformation, the spinor transforms as

$$\chi_{\sigma}^{graphene}(\mathbf{x}) \rightarrow \left(\frac{1}{4} \left(\tau_1 \otimes \sigma_1 + 3i\tau_1 \otimes \sigma_2 + \sqrt{3}(\tau_2 \otimes \sigma_1 - i\tau_2 \otimes \sigma_2) \right) \right) \chi_{\sigma}^{graphene}(C_6^{-1}\mathbf{x}) \quad (1.12)$$

Similarly, under the action of reflection about a line bisecting two horizontal bonds of the lattice shown in Fig .1.2, the spinor transforms as

$$\chi_{\sigma}^{graphene}(\mathbf{x}) \rightarrow \tau_0 \otimes \sigma_1 \chi_{\sigma}^{graphene}(-\mathbf{x}) \quad (1.13)$$

Under time reversal, the transformation is

$$\chi_{\sigma}^{graphene}(\mathbf{x}) \rightarrow i [\mu_2]_{\sigma\sigma'} \mathcal{K} \chi(\mathbf{x})_{\sigma}^{graphene} \quad (1.14)$$

Here, \mathcal{K} represents complex conjugation.

These transformations influence the possible phases obtained by gapping out the Dirac fermions which we now discuss

In the presence of short-range interactions, the Dirac fermions can dynamically acquire a mass, thereby gapping out the spectrum. Here, we focus on the masses that do not break the particle number conservation symmetry. There are 16 possible mass terms [21] of this kind, which can be written as

$$m_{ijk} = \chi^{graphene\dagger} \mu_i \otimes \tau_j \otimes \sigma_k \chi^{graphene}, \quad (1.15)$$

Here, $i = 0, 1, 2, 3$ and (j, k) can be $(1, 1)$, $(2, 1)$, $(0, 3)$, or $(3, 3)$. The transformation properties of these masses can be deduced from the transformation properties of the spinors.

For a particular value of i , the masses m_{i03} and m_{i33} transform as one-dimensional representations of the lattice space group. Specifically

- The m_{i03} masses are invariant under the action of time reversal and odd under the action of reflection. For $i = 0$, it represents a staggered charge density wave. For other values of i , it represents a Néel spin density wave where the i th component of the spin is ordered.
- The masses m_{i33} are odd under the action of reflection. These masses represent different quantum Hall phases. For $i = 0$, the mass is odd under time reversal and corresponds to the Chern insulator phase. For other values of i , the masses are invariant under time reversal and represent quantum spin Hall phases where the i th component of the spin is transported along the edges of the sample.

The masses m_{i11} and m_{i21} transform as a doublet under the action of lattice symmetries for each i . These masses represent Kekulé patterns. This analysis shows that the transformation properties of the low-energy spinors directly dictate the properties of the phases proximate to the Dirac semimetal in graphene.

In the case of the spin-orbit coupled Dirac fermions, which we talk about in detail in this thesis, the Dirac points arise at the three M points and the Γ point of the hexagonal BZ. Thus, under the action of lattice symmetries, the Dirac spinors corresponding to the Γ valley do not mix with the spinors at the M valleys. Thus, the action of the microscopic symmetries on the low-energy spinors is completely different in this case compared to graphene. The central question we then ask in this thesis is— what, then, are the nature of the gapped phases in this spin-orbit coupled two-dimensional Dirac system?

1.5 Thesis structure

In this thesis, we study a system where strong spin-orbit coupling (SOC) leads to an unusually large $SU(8)$ symmetric Dirac theory at low energy. This theory emerges as the low-energy description of a hopping model with $j = 3/2$ electrons on a honeycomb

lattice. These $j = 3/2$ electrons become the appropriate degrees of freedom in the strong SOC limit, possessing a mixed orbital and spin character. Consequently, the $j = 3/2$ orbitals transform differently under lattice symmetries compared to electrons with usual $s = 1/2$ spins. This non-trivial transformation affects the Dirac spinors and the gapped phases that result from opening a gap in the Dirac spectrum.

In this thesis, we focus on the following two aspects of the system described above:

1. The phases obtained by gapping out the $SU(8)$ Dirac fermions in the presence of interactions. Among these phases, there are examples of both conventional symmetry-broken phases and topological insulators (TI). We also discuss some of the associated phase transitions. Due to the non-trivial transformation properties of the Dirac spinors, the phases obtained in this case are different from the phases obtained in the case of graphene.
2. The relevance of the above analysis for some candidate materials where such symmetries are approximately realized.

The aforementioned investigation is conducted for systems containing transition metal ions (TMI) possessing a d^1 electronic configuration and strong SOC, forming a honeycomb lattice within an edge-sharing octahedral motif. Materials such as α - $ZrCl_3$ and α - $TiCl_3$ are examples of such settings. This setting is fairly common and has garnered much recent attention in honeycomb iridates[30, 35], as well as in the potential quantum spin liquid (QSL) candidate α - $RuCl_3$ [122, 123, 124], albeit with a distinct electronic configuration.

The rest of the chapter of the thesis is organized as follows. In Chapter 2, we start with a brief discussion on the effects of spin-orbit coupling (SOC) and crystal field effects on atomic orbitals. In the d^1 materials under consideration, the crystal field effect is more dominant compared to SOC. In these d^1 honeycomb materials, the crystal field effect splits the d -orbitals of each transition metal ion into two-fold degenerate e_g orbitals and three-fold degenerate t_{2g} orbitals, with the t_{2g} orbitals being lower in energy. We discuss the nearest-neighbor hopping Hamiltonian within the t_{2g} orbital sector.

The discussion then turns to the influence of SOC, which further lifts the six-fold degeneracy (including spin) of the t_{2g} orbitals, resulting in the spin-orbit coupled $j = 3/2$ orbitals emerging as the lowest energy states at each site. In the limit of strong SOC, the chapter derives an effective tight-binding Hamiltonian involving only the $j = 3/2$ orbitals

by projecting the t_{2g} Hamiltonian onto the $j = 3/2$ subspace. Notably, the chapter explores an intriguing scenario where direct hopping pathways between the transition metal ions are neglected, considering only a specific indirect hopping pathway. Under this assumption, the projected hopping Hamiltonian exhibits a remarkable global $SU(4)$ symmetry. This symmetry becomes explicitly manifest upon performing a site-dependent unitary transformation, which is also discussed in detail.

In Chapter 3, we delve into the low-energy limit of the $SU(4)$ symmetric Hamiltonian. At the appropriate chemical potential, this Hamiltonian features Dirac cones in the band structure, making the low-energy theory described by a $2 + 1$ dimensional free Dirac Hamiltonian. We explore how the microscopic symmetries act on the low-energy degrees of freedom, which, in this context, are the Dirac spinors. Additionally, we examine the emergent symmetries of the low-energy Hamiltonian. Specifically, we find that this low-energy theory has an emergent internal $SU(8)$ symmetry.

In Chapter 4, we explore the effect of short-range interactions on the free Dirac Hamiltonian. These interactions open a gap in the Dirac spectrum by condensing fermion bilinears. At a mean-field level, the interactions induce mass terms for the free Dirac Hamiltonian. We identify 64 such mass terms and analyze their transformations under the action of microscopic symmetries. Specifically, we classify these masses into the irreducible representations of the space group. This classification reveals all the gapped phases proximate to the Dirac semimetal in the presence of short-range interactions.

Based on their physical properties, we categorize these masses into three groups. The Group-1 masses, referred to as chiral masses, do not break the $SU(4)$ symmetry. These are discussed in Chapter 5 and include a stripy charge density wave and an integer Chern insulator phase. In Chapter 6, we cover the Group-2 masses, which consist of various types of generalized quantum Hall phases, such as octupolar and quadrupolar Hall phases. These phases exhibit symmetry-protected edge modes that carry either quadrupolar or octupolar currents, generalizing the spin quantum Hall phase.

The Group-3 masses represent density wave phases with various kinds of octupolar and quadrupolar ordering. Among the intriguing phases in this group, we find density wave semimetals where some fermionic modes remain gapless. The gapless fermionic modes in these density wave semimetals are protected by symmetries. We discuss these masses in Chapter 7.

In Chapter 8, we explore several fascinating phase transitions between the phases discussed in the earlier chapters. We examine three specific instances. The first is the transition from an octupolar quantum Hall phase to a charge- $4e$ superconducting phase. In this case, the condensation of skyrmions from the octupolar quantum Hall phase leads to the formation of the $4e$ superconductor. Next, we discuss the unnecessary quantum critical points (UQCPs) found in some quantum Hall and density wave phases. The UQCPs, although do not indicate a phase transition, emerge in the parameter space of a specific phase where the system exhibits some extra symmetry. Finally, we cover the transition from the $SU(8)$ Dirac semimetal phase to a chiral stripy charge density wave phase. Here, we demonstrate that the symmetry-allowed terms in the low-energy action result in a weakly first-order phase transition.

In Chapter 9, we discuss some of the candidate materials where the aforementioned theory is approximately realized. For this analysis, we draw inspiration from DFT studies conducted on MX_3 materials ($M=Zr, Ti, Hf$; $X=Cl, Br, F$). By examining the free band structure of these materials under varying strengths of hopping parameters and SOC, we evaluate the phase diagram as a function of hopping strength and SOC. This phase diagram includes several metallic phases with different Fermi surfaces, as well as some of the gapped phases discussed earlier. According to the parameter values estimated by the DFT studies, the mentioned materials fall into the metallic part of the phase diagram. Finally, in Chapter 10, we summarize all the discussions presented in this thesis.

Chapter 2

Strong spin-orbit coupling and the Microscopic Lattice Hamiltonian

In this chapter, we discuss the microscopic lattice Hamiltonian for d^1 transition metal ions in the presence of strong spin-orbit coupling (SOC). We begin by describing the general effect of SOC. Subsequently, we delve into the lattice structure and the effect of crystal field splitting, which lifts the degeneracy of the d -orbitals. Finally, we discuss the most general Hopping Hamiltonian in this context and focus specifically on the case of strong SOC, where $j = 3/2$ electrons emerge.

2.1 Microscopics of SOC

Spin-orbit coupling (SOC) emerges as a relativistic correction to the Schrodinger equation, causing the splitting of degenerate atomic orbitals by coupling the spin and orbital angular momenta of electrons [125]. In this section, we initially explore the impact of SOC on a single-electron system before extending our analysis to multi-electron systems.

For a single electron, the SOC Hamiltonian is expressed as¹

$$H_{soc} = \lambda(r)\mathbf{l} \cdot \mathbf{s} \tag{2.1}$$

where \mathbf{l} and \mathbf{s} represent the orbital and spin angular momentum operators, respectively.

¹The spin-orbit coupling (SOC) Hamiltonian presented in Eq. 2.1, while originating from relativistic effects, is not relativistically invariant. This lack of invariance stems from the omission of higher-order relativistic corrections in its derivation.

The coefficient λ depends on the radial coordinate r and is given by

$$\lambda(r) = \frac{1}{2m_e^2 c^2} \frac{1}{r} \frac{\partial V(r)}{\partial r}. \quad (2.2)$$

Here, $V(r)$ denotes the Coulomb potential induced by the nucleus, m_e is the electron's mass, and c is the speed of light. In the absence of SOC, energy levels are labeled by the radial quantum number n , azimuthal quantum number l , and magnetic quantum number m , which we denote by $|nlm\rangle$. For a particular n and l , the SOC introduces a splitting among the previously degenerate $2(2l+1)$ -fold states (including spin degeneracy). These states are now grouped by the total angular momentum $j = l \pm 1/2$, resulting in an energy difference of $\langle\lambda\rangle(l \pm 1/2)$, where

$$\langle\lambda\rangle = \frac{1}{2m_e^2 c^2} \left\langle nlm \left| \frac{1}{r} \frac{\partial V(r)}{\partial r} \right| nlm \right\rangle. \quad (2.3)$$

The energy ordering between the two groups with $j = l \pm 1/2$ is determined by the sign of $\langle\lambda\rangle$.

In multi-electron atoms or ions, the situation becomes more intricate due to the presence of multiple electrons. The SOC Hamiltonian generalizes to

$$H_{SOC} = \sum_i \lambda_i \mathbf{l}_i \cdot \mathbf{s}_i. \quad (2.4)$$

Here the summation over the index i accounts for the contribution of each individual electron, with λ_i representing the spin-orbit coupling (SOC) strength associated with that particular electron. Since there are many electrons in this case, the inter-electron Coulomb repulsion also comes into the picture. Depending on the relative strength of the SOC and the Coulomb repulsion, the effect of the SOC is treated differently.

Typically, the strength of the SOC Hamiltonian increases with the atomic number, with λ_i scaling roughly as Z^4 (Z being the atomic number of the multi-electron atom/ion) [125]. In the case of lighter elements, where the SOC is weaker than the electron-electron repulsion, the SOC can be treated as a perturbation. The electronic states of the Hamiltonian without the SOC term, which includes the nuclear potential and electron-electron repulsion, are characterized by the total orbital angular momentum $\mathbf{L}(= \sum_i \mathbf{l}_i)$ and the total spin angular momentum $\mathbf{S}(= \sum_i \mathbf{s}_i)$. The SOC then acts as a

perturbation, splitting these levels. It can be shown using the Wigner-Eckart theorem that the effective SOC Hamiltonian in (Eq. 2.4) in this case can be written as:

$$H_{SOC} = \tilde{\lambda} \mathbf{L} \cdot \mathbf{S}, \quad (2.5)$$

where $\tilde{\lambda}$ is the effective SOC strength. In the case when the outermost subshell is partially filled, the summation in Eq. 2.4 can be limited to the electrons in the outermost subshell only. This applies to transition metal ions with d^1 electronic configurations, which are the focus of this thesis. The splitting by the SOC in this scenario, in the presence of additional crystal field splitting, is discussed in Sec. 2.4. When there are multiple electrons in the outermost subshell, the ground state is determined by Hund's rules [125].

For heavier elements, where the spin-orbit coupling (SOC) strength dominates over the electron-electron repulsion, a different approach is employed to determine the ground state of the atom or ion. In this regime, the jj coupling scheme, as described in [125], becomes the appropriate framework. In this framework, the dominant effect of the SOC is first treated by labeling the states of the individual electron by their total angular momentum. The effect of the electron-electron repulsion is then treated perturbatively, which finally determines the total angular momentum of the system.

2.2 The lattice structure and microscopic symmetries

The focus of our work is crystalline systems on a honeycomb lattice formed out of edge-sharing octahedra (Fig. 2.1) where the electronically active transition metal ions, with strong atomic SOC, sit at the centres of such octahedra. Such structures are quite common and occur in a several stacked SOC magnets of recent interest such as the honeycomb Iridates $A_2\text{IrO}_3$ ($A=\text{Na}, \text{Li}$) [30, 31, 33], and ruthenates $\alpha\text{-RuCl}_3$ [35, 122, 123, 124].

In this geometry, the active atoms sit at the center of each octahedron and form the honeycomb lattice. It is useful to consider the honeycomb lattice to lie in a plane perpendicular to the Cartesian [111] direction (details in Appendix A.1.1) such that the three nearest neighbor bonds are parallel to the three Cartesian planes shown in Fig. 2.1.

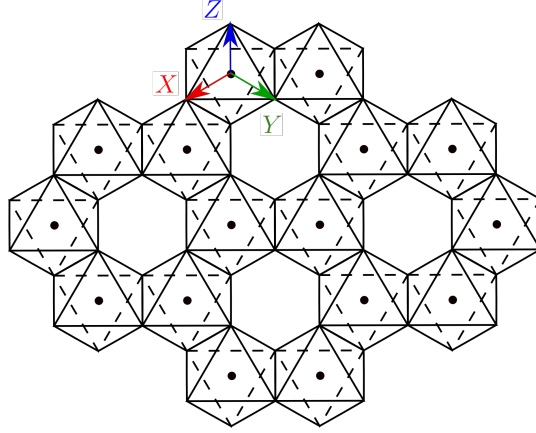


Figure 2.1: Edge-sharing octahedra forming a honeycomb lattice. As elaborated in the main text and in Appendix A.1.1, the honeycomb lattice lies in the $[111]$ plane of the Cartesian coordinate system whose projections are denoted by X, Y , and Z .

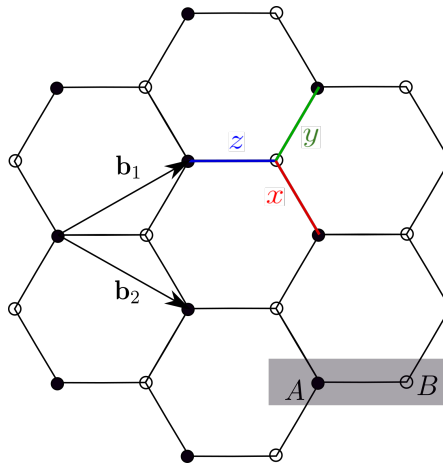


Figure 2.2: The filled circles are points of A sub-lattice and the hollow circles are of B sub-lattice. The gray shaded area shows the two points of a single unit cell with \mathbf{b}_1 and \mathbf{b}_2 being unit lattice vectors (see Eq. A.3).

Correspondingly, we denote these bonds as x , y , and z bonds if they are parallel to the YZ , ZX , and XY planes respectively, following the, by now popular nomenclature in the context of the Kitaev spin model [126] on the honeycomb lattice [127].

The honeycomb net has a triangular Bravais lattice and a two-site unit cell with two sub-lattices, $s = A, B$ as shown in Fig. 2.2. Each point on the honeycomb lattice is labeled by (u_1, u_2, s) where $u_1, u_2 \in \mathbb{Z}$ denote the position of the unit cell via

$$\mathbf{r} = u_1 \mathbf{b}_1 + u_2 \mathbf{b}_2 \quad (2.6)$$

with \mathbf{b}_1 and \mathbf{b}_2 are unit lattice vectors shown in Fig. 2.2.

To understand the lattice symmetries, we take the ideal honeycomb structure of α -

	$\mathbf{r}(u_1, u_2, \delta) \rightarrow \mathbf{r}'(u'_1, u'_2, \delta')$	$\psi(\mathbf{r}) \rightarrow \psi'(\mathbf{r}')$
\mathbf{T}_1	$(u_1, u_2, \delta) \rightarrow (u_1 + 1, u_2, \delta)$	$\psi \rightarrow \mathcal{U}_{\mathbf{T}_1}\psi$
\mathbf{T}_2	$(u_1, u_2, \delta) \rightarrow (u_1, u_2 + 1, \delta)$	$\psi \rightarrow \mathcal{U}_{\mathbf{T}_2}\psi$
\mathbf{C}_3	$(u_1, u_2, \delta) \rightarrow (u_2 - 1, -u_1 - u_2 + \delta_{\delta, A}, \delta)$	$\psi \rightarrow \mathcal{U}_{\mathbf{C}_3}\psi$
\mathbf{S}_6	$(u_1, u_2, \delta) \rightarrow (u_1 + u_2 - \delta_{\delta, A}, -u_1, \bar{\delta})$	$\psi \rightarrow \mathcal{U}_{\mathbf{S}_6}\psi$
\mathbf{C}'_2	$(u_1, u_2, \delta) \rightarrow (u_2 - 1, u_1 + 1, \delta)$	$\psi \rightarrow \mathcal{U}_{\mathbf{C}'_2}\psi$
$\boldsymbol{\sigma}_d$	$(u_1, u_2, \delta) \rightarrow (-u_2, -u_1, \bar{\delta})$	$\psi \rightarrow \mathcal{U}_{\boldsymbol{\sigma}_d}\psi$
\mathbf{I}	$(u_1, u_2, \delta) \rightarrow (-u_1 - 1, -u_2 + 1, \bar{\delta})$	$\psi \rightarrow \mathcal{U}_{\mathbf{I}}\psi$

Table 2.1: This table shows the the action of the microscopic symmetries on lattice sites. Note $\bar{\delta} = B(A)$ for $\delta = A(B)$. The transformation of the $j = 3/2$ orbitals (ψ) which appears in presence of strong SOC (discussed later in this chapter near Eq. 2.24) are also shown. The $\mathcal{U}_{\mathbb{S}}$ (\mathbb{S} represents some lattice symmetry) are 4×4 unitary matrices which are given in Appendix A.2 (Eqs A.16 - A.19).

ZrCl₃ as a prototypical example, as it has all the representative symmetries. The point group of the α -ZrCl₃ lattice is D_{3d} , which has 12 elements. Keeping in mind the geometry of the edge-sharing ligand octahedra surrounding the active ion (Fig. 2.1), the generators of the lattice symmetries of the system are as follows and their action on the lattice coordinates are given in Table 2.1.

- $\mathbf{T}_1, \mathbf{T}_2$: Two-dimensional lattice translations of the honeycomb lattice by \mathbf{b}_1 and \mathbf{b}_2 respectively.
- \mathbf{C}_3 : Rotations by angle $\frac{2\pi}{3}$ about the center of a honeycomb plaquette.
- \mathbf{S}_6 : Rotations about the center of a honeycomb plaquette by angle $\frac{\pi}{3}$ followed by a reflection about the honeycomb plane.
- \mathbf{C}'_2 : Rotations by angle π about the axes lying on the honeycomb plane and passing through two opposite vertices of a honeycomb plaquette. There are three of such axes. One of the \mathbf{C}'_2 axes is parallel to the z -bonds (see Fig. 2.2).
- $\boldsymbol{\sigma}_d$: Reflections about planes which are perpendicular to the honeycomb plane and bisect the angle between two consecutive \mathbf{C}'_2 axes. There are three such planes. One of the planes is the perpendicular bisector of one of the z -bonds in Fig 2.2.
- \mathbf{I} : Inversion about the center of a honeycomb plaquette.

In addition, the system also has time reversal (TR) symmetry \mathbb{T} , with

$$\mathbb{T}^2 = -1. \quad (2.7)$$

In appendix A.2, we provide the details of the transformation of the t_{2g} and the $j = 3/2$ orbitals under the above symmetries.

2.2.1 Crystal field splitting

As mentioned before, the lattice is made out of edge-sharing networks of octahedra. The transition metal (TM) ions at the center of each octahedron are surrounded by six negatively charged ions which sit at the corners of the octahedron (see fig .2.3). This octahedral arrangement breaks the spherical symmetry around each TM ion to the octahedral group O_h . This causes the breaking of the degeneracy of the d -orbitals into $2 \oplus 3$. The two-fold degenerate states with wave function

$$|d_{x^2-y^2}\rangle = \frac{1}{\sqrt{2}} (|2, 2\rangle + |2, -2\rangle) \quad (2.8)$$

$$|d_{3z^2-r^2}\rangle = |2, 0\rangle \quad (2.9)$$

transform in the e_g representation of the O_h group while the three-fold degenerate states given by

$$|d_{yz}\rangle = \frac{i}{\sqrt{2}} (|2, 1\rangle + |2, -1\rangle) \quad (2.10)$$

$$|d_{zx}\rangle = \frac{1}{\sqrt{2}} (|2, -1\rangle - |2, 1\rangle) \quad (2.11)$$

$$|d_{xy}\rangle = \frac{i}{\sqrt{3}} (|2, -1\rangle - |2, -2\rangle) \quad (2.12)$$

transform in the t_{2g} representation. Here, $|2, m\rangle$ are the d -orbital wave functions.

The t_{2g} orbitals possess a lower energy level compared to the e_g orbitals due to their specific orientation, which minimizes the repulsive forces exerted by the negatively charged anions situated at the corners of the octahedron. This can be explicitly demonstrated by considering the Coulomb potential due to the six anions at the corners of the octahedron w.r.t. the TM ion. The electrostatic energy of an electron due to the repulsion from these anions is given by

$$V(\mathbf{r}) = \sum_{i=1}^6 \frac{e^2}{4\pi\epsilon_0 |\mathbf{r} - \mathbf{R}_i|}, \quad (2.13)$$

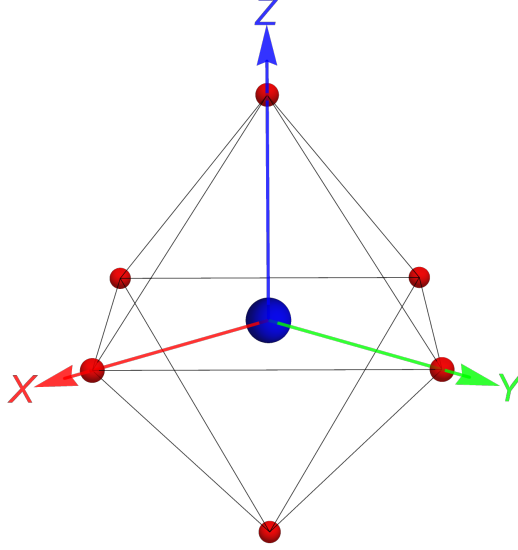


Figure 2.3: Octahedral structure formed by the anions (shown by red balls) with the TM ion (blue ball) at the center. X, Y, Z are the three crystallographic axes.

with \mathbf{R}_i are the positions of the vertices of the octahedron. Expanding near $\mathbf{r} = 0$ (*i.e.*, near the TM ion), we have

$$V(\mathbf{r}) = \frac{e}{4\pi\epsilon_0 a} \left(-\frac{5x^4 + 5y^4 + 5z^4}{4a^4} + \frac{3r^4}{a^4} + \frac{2r^2}{a^2} + 6 \right), \quad (2.14)$$

where a represents the distance between a negative anion and the transition metal ion. The potential $V(\mathbf{r})$ acts as a perturbation on the electrons bound to the transition metal ions, causing the splitting of the d -orbitals into t_{2g} and e_g states. The splitting can be estimated from the expectation values of $V(\mathbf{r})$ with respect to the t_{2g} and e_g orbitals, which are given by:

$$\langle \alpha | V(r) | \beta \rangle = \delta_{\alpha\beta} \left(-\frac{2}{21} a^4 c_1 + c_2 \right) \quad (2.15)$$

$$\langle \tilde{\alpha} | V(r) | \tilde{\beta} \rangle = \delta_{\tilde{\alpha}\tilde{\beta}} \left(\frac{1}{7} a^4 c_1 + c_2 \right) \quad (2.16)$$

where α, β represent the t_{2g} orbitals, and $\tilde{\alpha}, \tilde{\beta}$ represent the e_g states. The quantities c_1 and c_2 are positive real numbers defined as:

$$c_1 = \langle r^4 \rangle \quad (2.17)$$

$$c_2 = \left\langle \left(\frac{2r^2}{a^2} + 6 \right) \right\rangle. \quad (2.18)$$

where the expectation value is evaluated w.r.t. any of the t_{2g} or e_g orbitals. Thus, the t_{2g} orbitals are lower in energy than the e_g states.

2.3 General hopping model for d^1 honeycomb materials

In this section, we discuss the tight-binding Hamiltonian for the d^1 honeycomb materials described in Sec. 2.2 in the presence of SOC. The single electron of the TM ions occupies the six-fold degenerate t_{2g} atomic orbitals (including spin-degeneracy) $|d_{XY}, \sigma\rangle$, $|d_{YZ}, \sigma\rangle$ and $|d_{ZX}, \sigma\rangle$ with $\sigma = \uparrow, \downarrow$ while the high energy e_g orbitals remain empty and are projected out. One can now write down the first NN hopping model for the t_{2g} orbitals as [128]

$$H_{tb} = \sum_{\langle \mathbf{r}, \mathcal{S}; \mathbf{r}', \mathcal{S}' \rangle} \sum_{\alpha, \beta} \sum_{\sigma, \sigma'} \Psi_{\sigma\alpha}^\dagger(\mathbf{r}, \mathcal{S}) \left[\left[h_{\mathbf{r}\mathbf{r}'}^{\mathcal{S}\mathcal{S}'} \right]_{\alpha\beta} \delta_{\sigma\sigma'} \right] \Psi_{\sigma'\beta}(\mathbf{r}', \mathcal{S}') + h.c.. \quad (2.19)$$

Here $\Psi_{\sigma\alpha}(\mathbf{r}, \mathcal{S})$ annihilates electrons at the $(\mathbf{r}, \mathcal{S})$ site of the lattice with spin σ ($=\uparrow, \downarrow$), in the orbital α ($= YZ, ZX, XY$). The $h_{\mathbf{r}\mathbf{r}'}^{\mathcal{S}\mathcal{S}'}$ is a 3×3 Hermitian matrix at the bond connecting the $(\mathbf{r}, \mathcal{S})$ and the $(\mathbf{r}', \mathcal{S}')$ sites of the lattice.

Keeping in mind the different kinds of overlaps of the t_{2g} orbitals, we can write the $h_{\mathbf{r}\mathbf{r}'}^{\mathcal{S}\mathcal{S}'}$ matrix for the z -bond as

$$h_z^{AB} = \begin{pmatrix} t_{dd\pi} & t_{ddm} & t_{ddm'} \\ t_{ddm} & t_{dd\pi} & t_{ddm'} \\ t_{ddm'} & t_{ddm'} & t_{dd\sigma} \end{pmatrix} \\ = t_{dd\sigma} h_\sigma + t_{dd\pi} h_\pi + t_{ddm} h_m + t_{ddm'} h_{m'} \quad (2.20)$$

where $t_{dd\sigma}$, $t_{dd\pi}$ and t_{ddm} , $t_{ddm'}$ are hopping due to direct and indirect overlaps of the t_{2g} orbitals respectively. Also, h_σ , h_π , h_m and $h_{m'}$ are 3×3 matrices given by

$$\begin{aligned}
h_\sigma &= \begin{pmatrix} 0 & 0 & 0 \\ 0 & 0 & 0 \\ 0 & 0 & 1 \end{pmatrix}, & h_\pi &= \begin{pmatrix} 1 & 0 & 0 \\ 0 & 1 & 0 \\ 0 & 0 & 0 \end{pmatrix}, \\
h_m &= \begin{pmatrix} 0 & 1 & 0 \\ 1 & 0 & 0 \\ 0 & 0 & 0 \end{pmatrix}, & h_{m'} &= \begin{pmatrix} 0 & 0 & 1 \\ 0 & 0 & 1 \\ 1 & 1 & 0 \end{pmatrix}.
\end{aligned} \tag{2.21}$$

The form of the hopping of the x and y bonds can be obtained by exploiting the three-fold rotation symmetry of the lattice.

The t_{2g} orbitals effectively behave as a $l = 1$ orbitals under the action of rotations[22, 129]. This is shown in appendix A.1.2 by projecting the $l = 2$ angular momentum generators to the t_{2g} orbitals. With this, the SOC Hamiltonian for the t_{2g} manifold is given by (Appendix A.1.2)

$$H_{\text{SOC}}^{t_{2g}} = -\lambda \mathbf{l} \cdot \mathbf{s} \tag{2.22}$$

where the \mathbf{l} are the three $l = 1$ angular momentum matrices and $\lambda(> 0)$ is the strength of the SOC. Also, the \mathbf{s} are the Pauli matrices denoting the electron spin-1/2 angular momentum. It is noteworthy that the SOC Hamiltonian for the t_{2g} orbitals carries an additional negative sign, which arises as a result of the projection from the $l = 2$ orbitals to the t_{2g} states. With this, the low energy effective tight-binding model can be obtained by adding atomic SOC to Eq. 2.19 and is given by

$$H = \sum_{\langle \mathbf{r}, \mathcal{d}; \mathbf{r}', \mathcal{d}' \rangle} \sum_{\alpha, \beta} \sum_{\sigma \sigma'} \Psi_{\sigma \alpha}^\dagger(\mathbf{r}, \mathcal{d}) \left[\left[h_{\mathbf{r} \mathbf{r}'}^{\mathcal{d} \mathcal{d}'} \right]_{\alpha \beta} \delta_{\sigma \sigma'} - \lambda \mathbf{l}_{\alpha \beta} \cdot \mathbf{s}_{\sigma \sigma'} \delta_{\mathbf{r} \mathbf{r}'} \delta_{\mathcal{d} \mathcal{d}'} \right] \Psi_{\sigma' \beta}(\mathbf{r}', \mathcal{d}') + h.c., \tag{2.23}$$

2.4 Effect of strong SOC

In SOC further breaks the t_{2g} orbitals into $j = 1/2$ and $j = 3/2$ orbitals. In this case the $j = 3/2$ orbitals are of low-energy because of the extra $-ve$ sign appearing in Eq. 2.22 [22]. For the d^1 configuration, the low energy physics in presence of strong SOC is therefore of a 1/4th filled $j = 3/2$ orbitals (Fig. 2.4). We write the single electron creation operators

for the $j = 3/2$ orbitals at the lattice site \mathbf{r} by [129, 130]

$$\psi^\dagger(\mathbf{r}) = \left(\psi_{1/2}^\dagger(\mathbf{r}), \psi_{-1/2}^\dagger(\mathbf{r}), \psi_{3/2}^\dagger(\mathbf{r}), \psi_{-3/2}^\dagger(\mathbf{r}) \right). \quad (2.24)$$

The interplay of hopping and interaction of electrons occupying these four orbitals then determine the low energy electronic properties of the system.

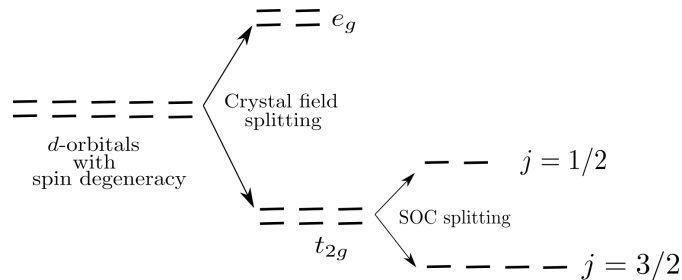


Figure 2.4: Splitting of the d -orbitals under the action of crystal field effect and SOC.

2.5 The tight binding Hamiltonian for indirect hopping

We now focus on the limit where the indirect hopping amplitude t_{ddm} is non-zero and all the other hopping amplitudes are zero, *i.e.*,

$$t_{ddm} \neq 0, \quad t_{dd\sigma} = t_{dd\pi} = t_{ddm'} = 0. \quad (2.25)$$

This particular limit was considered by Yamada et. al.[130] which shows that this limit gives rise to a $SU(4)$ symmetric Hubbard model on the Honeycomb lattice which we discuss now.

The effective Hamiltonian in the parameter regime mentioned above in presence of strong SOC is obtained by projecting the t_{2g} Hamiltonian (Eq. 2.23) to the $j = 3/2$ manifold using Eq. A.8. This minimal hopping Hamiltonian for the $j = 3/2$ orbitals (Eq. 2.24) is given by

$$H = -\frac{t}{\sqrt{3}} \sum_{\langle \mathbf{r}, \mathcal{J}; \mathbf{r}', \mathcal{J}' \rangle} \psi^\dagger(\mathbf{r}, \mathcal{J}) U_{\mathbf{r}\mathbf{r}'}^{\mathcal{J}\mathcal{J}'} \psi(\mathbf{r}', \mathcal{J}') + \text{h.c.} \quad (2.26)$$

where $U_{\mathbf{r}\mathbf{r}'}^{\mathcal{J}\mathcal{J}'}$ are hopping amplitudes of overall strength $t = t_{ddm}$, on nearest neighbor bonds

(hence only between different sublattices) that are given by 4×4 Hermitian matrices which depend on the type (x, y or z , see Fig. 2.2) of the $\langle \mathbf{r}, s; \mathbf{r}', s' \rangle$ bond [130] given by

$$\begin{aligned} U_{\mathbf{r}\mathbf{r}'}^{AB} &\equiv U_x = -\Sigma_1, \text{ if } \langle \mathbf{r}, A; \mathbf{r}', B \rangle = x \\ &\equiv U_y = -\Sigma_2, \text{ if } \langle \mathbf{r}, A; \mathbf{r}', B \rangle = y \\ &\equiv U_z = -\Sigma_3, \text{ if } \langle \mathbf{r}, A; \mathbf{r}', B \rangle = z \end{aligned} \quad (2.27)$$

Here, Σ_i are sixteen 4×4 traceless Hermitian matrices with Σ_0 being the identity matrix and the rest being generators of $SU(4)$. They can be obtained by using $j = 3/2$ matrices as shown in Appendix A.3.

The three U_α (for $\alpha = x, y, z$) matrices square up to identity and mutually anti-commute, i.e.,

$$U_\alpha^2 = \mathbb{I}_4 \equiv \Sigma_0, \quad \{U_\alpha, U_\beta\} = 2\delta_{\alpha\beta}\Sigma_0 \quad \forall \alpha, \beta = x, y, z. \quad (2.28)$$

Before proceeding to diagonalize Eq. 2.26 to obtain the electron band structure, we identify the generic nature of the electron dispersion.

The $SU(4)$ Symmetry and π -flux

As a first step, it is useful to consider the phase picked up by the electron on encircling any closed loop of the lattice. Such loops are formed out of the honeycomb plaquette consisting of six sites. The phase is given by the product of the U_α matrices around a honeycomb plaquette and is generically given by

$$\prod_{\langle \mathbf{r}, s; \mathbf{r}', s' \rangle \in \diamond} U_{\mathbf{r}\mathbf{r}'}^{ss'} = \sum_i W_i \Sigma_i \quad (2.29)$$

where W_i are the respective coefficients that denote a generic direction in the $SU(4)$ space. In the above sum, i runs over the 16 indices of the Σ_i matrices defined in Appendix A.3.

Crucially, however, it was noticed in Ref. [130] that the explicit form of U -matrices (Eq. 2.27) give

$$\prod_{\langle \mathbf{r}, s; \mathbf{r}', s' \rangle \in \diamond} U_{\mathbf{r}\mathbf{r}'}^{ss'} = -\Sigma_0 \quad (2.30)$$

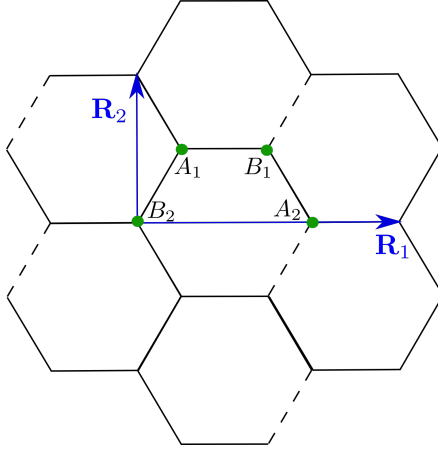


Figure 2.5: Honeycomb lattice with π -flux and the four-point magnetic unit-cell in the gauge choice (Eq. 2.37): the dashed (continuous) bonds have $\eta(\mathbf{z}_s, \mathbf{z}'_{s'}) = -1(+1)$ (see Eq. 2.36).

such that no direction in $SU(4)$ space is favoured and the system has an underlying $SU(4)$ symmetry. This $SU(4)$ symmetry can be made manifest by suitable site-dependent unitary rotations of the ψ fermions (see below, Eq. 2.34) [130].

An equally important feature is the negative sign in Eq. 2.30 which shows that such $SU(4)$ fermions experience a π -flux through every hexagon. Thus the above problem of d^1 fermions is that of $SU(4)$ symmetric fermions hopping on a honeycomb lattice with π -flux per plaquette. The non-trivial effect of π -flux at 1/4-th filling is already apparent by considering the simpler case of spinless fermions on honeycomb lattice with π -flux at quarter-filling. This, as we discuss below, leads to Dirac fermions at low energy whose properties are quite different from those in graphene.

In the rest of this work, we uncover the interplay of $SU(4)$ symmetry and the π -flux that, along with electron-electron interactions, leads to rich low-energy electronic properties of d^1 systems.

$SU(4)$ diagonalization and the local basis

Following Ref. [130], the $SU(4)$ symmetry of the hopping Hamiltonian in Eq. 2.26 can be made manifest by performing site-dependent (local) unitary transformations on the fermions.

To obtain this manifestly $SU(4)$ invariant basis, and also due to the π -flux, it is useful to consider a four site *magnetic unit cell* as shown in Fig. 2.5. The four sites, A_1, A_2, B_1, B_2 , in the magnetic unit cell comprise two sites each of A and B sub-lattices

of the underlying honeycomb net. The lattice translation vectors for this magnetic unit-cell, as shown in Fig. 2.5, are given in terms of the underlying honeycomb lattice primitive vectors as

$$\mathbf{R}_1 = \mathbf{b}_1 + \mathbf{b}_2; \quad \mathbf{R}_2 = \mathbf{b}_1 - \mathbf{b}_2 \quad (2.31)$$

such that the sites with reference to the enlarged unit cell are given by

$$\mathbf{z}_S = n_x \mathbf{R}_1 + n_y \mathbf{R}_2 + \mathbf{d}_S \equiv \mathbf{z} + \mathbf{d}_S. \quad (2.32)$$

with $S \in \{A_1, A_2, B_1, B_2\}$ denotes the four sites in the magnetic unit-cell, \mathbf{d}_S are the position vectors of the S -sublattice site w.r.t. the B_2 site (see Fig. 2.5) of the same magnetic unit cell, \mathbf{z} labelled by integers n_x and n_y .

With this, we can now define new fermion annihilation operators given by

$$\phi(\mathbf{z}_S) = [\phi_1(\mathbf{z}_S), \phi_2(\mathbf{z}_S), \phi_3(\mathbf{z}_S), \phi_4(\mathbf{z}_S)]^T \quad (2.33)$$

as

$$\phi(\mathbf{z}_S) = \mathcal{G}(\mathbf{z}_S)^\dagger \psi(\mathbf{z}_S) \quad (2.34)$$

where $\mathcal{G}(\mathbf{z}_S)$ are 4×4 unitary matrices whose explicit forms are given in Appendix A.4. Any many-body operator can be expressed either in the ϕ basis or ψ . In this article, we use the terms “local basis” and “global basis”, respectively, to refer to these two ways.

The Hamiltonian (Eq. 2.26) written in the local basis is

$$H = -\frac{t}{\sqrt{3}} \sum_{\langle \mathbf{z}_S, \mathbf{z}'_{S'} \rangle} \eta(\mathbf{z}_S, \mathbf{z}'_{S'}) \phi^\dagger(\mathbf{z}_S) \phi(\mathbf{z}'_{S'}) + \text{h.c.} \quad (2.35)$$

which is manifestly SU(4) invariant and $\eta(\mathbf{z}_S, \mathbf{z}'_{S'}) = \pm 1$ implementing the π -flux constraint of Eq. 2.30, via

$$\prod_{\langle \mathbf{z}_S, \mathbf{z}'_{S'} \rangle \in \square} \eta(\mathbf{z}_S, \mathbf{z}'_{S'}) = -1. \quad (2.36)$$

Fig. 2.5 shows a choice for $\eta(\mathbf{z}_S, \mathbf{z}'_{S'})$ which is given by

$$\eta(\mathbf{z}_S, \mathbf{z}'_{S'}) = \begin{cases} -1 & \text{if } S = B_1, S' = A_2 \text{ and } \mathbf{z}' = \mathbf{z} + \mathbf{R}_2 \\ +1 & \text{(otherwise)} \end{cases} \quad (2.37)$$

Obviously, there are many other choices for $\eta(\mathbf{z}_S, \mathbf{z}'_{S'})$ which are related to each other through gauge transformations which correspond to different signs of the $\mathcal{G}(\mathbf{z}_S)$ matrices with respect to the ones introduced in Appendix A.4. An alternate choice for $\eta(\mathbf{z}_S, \mathbf{z}'_{S'})$ and indeed the magnetic unit cell is shown in Fig. A.2. For the rest of our calculation in the main text, we choose $\eta(\mathbf{z}_S, \mathbf{z}'_{S'})$ as given by Eq. 2.37.

Chapter 3

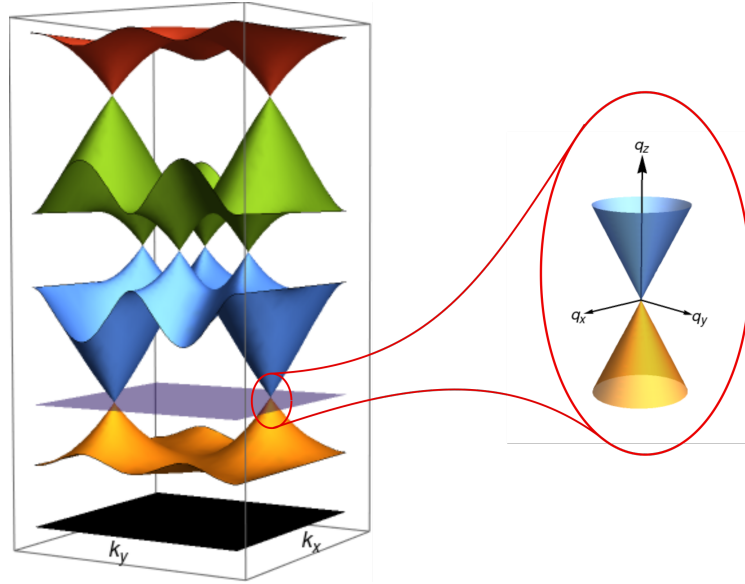
Free Dirac Theory and its symmetries

In this chapter, we derive the low-energy theory for d^1 honeycomb materials at one-quarter filling in the indirect hopping (t_{ddm}) dominant limit in the presence of strong SOC. We start by analyzing the free band structure of the Hamiltonian presented in Eq. 2.35, which displays linear band touching at the Dirac points. Thereafter, we derive the Dirac theory, which serves as the low-energy theory for this system, and discuss the emergent symmetries. Lastly, discuss how the microscopic symmetries act on the low-energy degrees of freedom (*i.e.*, the Dirac spinors).

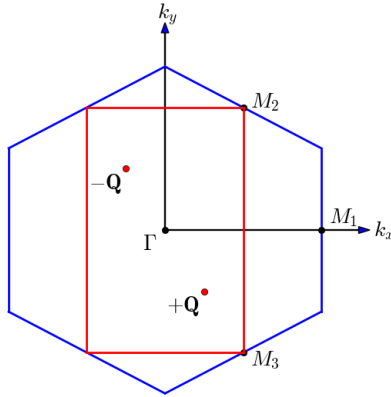
3.1 The band structure

Eq. 2.35 represents four copies of nearest neighbour hopping models on the honeycomb lattice in the presence of π -flux. A single copy of such model at half filling was studied in Ref. [21, 131]. However, we shall find that the underlying SU(4) symmetry in the present case and the 1/4th filling for d^1 materials (see below) along with SOC open up a new regime of possibilities for the resultant system at low energies.

To disentangle the role of the SU(4) and the π -flux, it is useful to consider a single flavour “spinless” version of Eq. 2.35 with $\phi(\mathbf{r}_S)$ being a single component fermion. This is worked out in Appendices A.5 and A.11. The resultant band structure is shown in Fig. 3.1 and consists, for quarter filling, two linearly dispersing band-touching points—Dirac



(a)



(b)

Figure 3.1: (a) Band structure for the Hamiltonian in Eq. 2.35 for the magnetic unit cell consisting of four sites (Fig. 2.5). Each band is four-fold degenerate. For d^1 system, the lowest four bands are occupied with the chemical potential crossing the two Dirac points as shown. (b) Position of the two Dirac points (Eq.3.1) in the chosen gauge (Fig. 2.5 and Eq. 2.37) in the magnetic Brillouin zone (in red). The primitive Brillouin zone of the hexagonal lattice is also drawn in blue.

cones– at

$$\pm\mathbf{Q} = \pm \left[\frac{\pi}{6}, -\frac{\pi}{2\sqrt{3}} \right]. \quad (3.1)$$

We label the two Dirac points (valleys) by the Ising variable $\tau = \pm$. Similar Dirac points also occur at 3/4th filling by particle-hole symmetry of the microscopic problem. Also, note that there are four Dirac points at half filling [131] as is shown in Fig. 3.1. In the rest of the discussion, though, we shall consider exclusively the vicinity of quarter filling and the nature of the low energy Dirac fermions at the two valleys at $\pm\mathbf{Q}$ given by Eq. 3.1.

Turning back to the case of $j = 3/2$ orbitals in d^1 configuration (Eq. 2.35), the band structure is now four-fold degenerate due to the SU(4) symmetry such that the lower four bands are completely filled with the chemical potential again at the two Dirac cones given by Eq. 3.1. As remarked above, the similar Dirac cones are also present for three-quarter filling and hence the rest of our discussion is also applicable to materials with d^3 electronic configuration.¹

At this point, we would like to take a small detour by discussing the above band structure in the *global basis* (Eq. 2.24) which provides interesting complementary insights into the results that follow in the rest of this thesis. This alternate insight arises from the observation that while for a single flavour π -flux problem we are forced to use the magnetic unit cell (Fig. 2.5), for the four flavour version relevant to d^1 or d^3 systems, it is possible to use the two-site primitive honeycomb unit-cell (Fig. 2.2) by diagonalizing the Hamiltonian in Eq. 2.26. However, in this *global basis* neither the SU(4), nor the π -flux is manifest but are mixed together non-trivially. As a result, while all the lattice symmetries (Table 2.1), act in a linear fashion, i. e., they are *non-projective*² despite the fact that each hexagonal plaquette hosts a π -flux as shown in Eq. (2.30). We use the *local basis* for most of our discussion in the rest of the main-texts. Notwithstanding, the *global*

¹In the strong spin-orbit coupling (SOC) regime, the analysis for a system with one electron in the $j = 3/2$ quartet is analogous to that of a system with three electrons. This equivalence arises from the microscopic particle-hole symmetry that relates these two scenarios.

²In the global basis, the local degrees of freedom at each site are the $j = 3/2$ orbitals (ψ). Under the action of the lattice symmetry operations (say, \mathbb{S}), the orbitals at a lattice site \mathbf{r} transform as $\psi(\mathbf{r}) \rightarrow U_{\mathbb{S}}\psi(\mathbb{S}^{-1}\mathbf{r})$ (see Eq. A.15), with $U_{\mathbb{S}}$ being the transformation matrix. Notably, $U_{\mathbb{S}}$ is the same at each site \mathbf{r} . But, for the local basis, the local atomic orbitals (ϕ) are defined by doing a site-dependent unitary transformation (see Eq. 2.34). This makes the transformation of the orbitals in the local basis (i.e., $\phi(\mathbf{r})$), site dependent (see Eq. A.50).

basis is useful to understand certain structures in our calculations which we refer to at relevant places throughout the rest of the thesis. The considerations in the global basis are presented in Appendix A.10. Briefly, Bloch diagonalizing the Hamiltonian in global basis (Eq. 2.26) obtains four bands arising from the four $j = 3/2$ orbitals (Eq. 2.24) and each two-fold degenerate due to inversion symmetry. The first set of bands touches the second set of bands at *four* distinct points with Dirac cone structure, see Fig. A.1. With the quarter filling of the bands the chemical potential is tuned to the Dirac points at the four \mathbf{Q}_g vectors, Γ , M_1 , M_2 , M_3 termed as valleys, in the original honeycomb Brillouin zone. This is to be contrasted with the local basis where one obtains two valleys due to the doubling of the unit cell, and the concomitant folding of the bands. One of the central insights of the global basis is that under lattice symmetries such as \mathbf{S}_6 (Table 2.1), *only* three of the Dirac cones sitting at the three M points (Fig. A.1) mix amongst themselves while the Dirac cone at the BZ center, *i.e.* at Γ -point, remains isolated. This naturally distinguishes the different valleys into two groups– one containing only the Γ point cone and the other containing the other three at the three nonequivalent M points. As we shall see later, the above grouping is a fallout of the fact that the microscopic lattice symmetries get embedded in a larger low energy *IR space group* (see Sec. 4.2) that allows up to three-dimensional representations such that the above grouping is a block diagonalization of a reducible representation, *i.e.*, $\mathbf{4} = \mathbf{1} \oplus \mathbf{3}$. This insight will be important in understanding a subset of *partially gapless masses* discussed in Sec. 7.2.

3.2 Low-energy Dirac theory

Turning back to the local basis (Eq. 2.33 and Fig. 3.1), for 1/4th filling, the low energy theory is obtained by expanding the lattice fermions, $\phi(\mathbf{z}_S)$, in terms of the soft-modes, around the two Dirac points, $\pm\mathbf{Q}$, as

$$\phi_f(\mathbf{z}_S) \sim \mathcal{W}_{S\sigma}^{(+)} \chi_{f\sigma+}(\mathbf{z}) e^{i\mathbf{Q}\cdot\mathbf{z}} + \mathcal{W}_{S\sigma}^{(-)} \chi_{f\sigma-}(\mathbf{z}) e^{-i\mathbf{Q}\cdot\mathbf{z}} \quad (3.2)$$

where $\chi_{f\sigma\tau}(\mathbf{x})$ are the soft modes in the continuum evaluated at $\mathbf{x} = \mathbf{z}$ with $f = 1, \dots, 4$ denote the SU(4) flavour index, $\sigma = 1, 2$ is the particle or hole-like band index and $\tau = \pm$ is the valley index coming from the two Dirac nodes at $\pm\mathbf{Q}$. $\mathcal{W}_{S\sigma}^{(\pm)}$ are two 4×2 matrices (one at each valley, $\tau = \pm$) in the (magnetic) unit-cell (S)-particle-hole (σ) space. The

details are given in Appendix A.5.

In terms of the soft modes, the low energy Hamiltonian takes the canonical Dirac form in two spatial dimensions and is given by

$$H_D = -iv_F \sum_{f=1}^4 \int d^2\mathbf{x} \chi_f^\dagger(\mathbf{x})(\alpha_1\partial_1 + \alpha_2\partial_2)\chi_f(\mathbf{x}) \quad (3.3)$$

where $v_F = \frac{t\ell}{\sqrt{2}}$ is the fermi velocity, ℓ is the length of each side of the hexagon and $\partial_i = \partial/\partial x_i$ ($i = 1, 2$), with

$$\chi_f(\mathbf{x}) = (\chi_{f1+}, \chi_{f2+}, \chi_{f1-}, \chi_{f2-})^T \quad (3.4)$$

a 4-component spinor, one for each SU(4) flavour $f = 1, 2, 3, 4$, which can be further stacked up to form a 16-component spinor, and

$$\alpha_1 = \tau_3\sigma_1, \quad \alpha_2 = \tau_0\sigma_2 \quad (3.5)$$

are the two Dirac Matrices. Here τ_μ and σ_μ ($\mu = 0, 1, 2, 3$) are Pauli matrices that act in the valley space and band/particle-hole space respectively.

The corresponding Euclidean action is given by

$$S_0 = \int d^2\mathbf{x}d\tau \mathcal{L}_0 \quad (3.6)$$

where, \mathcal{L}_0 is given by

$$\mathcal{L}_0 = v_F \sum_{f=1}^{N_f} \bar{\chi}_f(\mathbf{x})(-i\cancel{\partial})\chi_f(\mathbf{x}), \quad (3.7)$$

with $N_F = 4$ and $\bar{\chi}_f = i\chi_f^\dagger\gamma_0$ and

$$\gamma_0 = \tau_3\sigma_3, \quad \gamma_1 = \tau_0\sigma_2 \quad \gamma_2 = -\tau_3\sigma_1 \quad (3.8)$$

such that $\alpha_1 = i\gamma_0\gamma_1$ and $\alpha_2 = i\gamma_0\gamma_2$. Here γ_0, γ_1 and γ_2 generate the Euclidean Clifford Algebra that satisfy $\{\gamma_\mu, \gamma_\nu\} = 2\delta_{\mu\nu}$ with $\mu, \nu = 0, 1, 2$ [132].

The above low-energy free Dirac theory has a much larger symmetry compared to the

microscopic system. Firstly, Eq. 3.6 is invariant under SU(2) transformations on each flavour of χ_f generated by

$$\{\tau_3\sigma_0/2, \tau_1\sigma_2/2, \tau_2\sigma_2/2\} \equiv \{\zeta_1, \zeta_2, \zeta_3\}/2. \quad (3.9)$$

This denotes rotation in the valley and band space similar to Dirac fermions in graphene [112] which we refer to as chiral symmetry [21]. This, along with the manifest invariance under the SU(4) *flavour* symmetry generated by Σ_i (defined in Appendix. A.3), nominally gives rise to an internal symmetry of SU(4) \otimes SU(2). However, the emergent internal symmetry is SU(8) which is generated by 63 traceless Hermitian matrices, \mathcal{P}_b , that are obtained as

$$\mathcal{P}_b = \Sigma_i \zeta_j \quad (3.10)$$

where on the LHS, $b = 1, 2, \dots, 63$ which are made up of the fifteen SU(4) generators, Σ_i , given in Appendix A.3 and three SU(2) generators, ζ_j , defined in Eq. 3.9 along with the identities in the two spaces Σ_0 and ζ_0 respectively.

Under the SU(8) generated by the 16×16 traceless Hermitian matrices, \mathcal{P}_b , the spinors χ transform as

$$\chi \rightarrow \exp(i\xi_b \mathcal{P}_b) \chi \quad (3.11)$$

where $\chi = (\chi_1^T, \chi_2^T, \chi_3^T, \chi_4^T)^T$ is the 16-component spinor with each χ_f ($f = 1, 2, 3, 4$) given by Eq. 3.4. This leads to the conservation of the SU(8) flavour current

$$J_{\mu,b} = -i\bar{\chi}\gamma_\mu\mathcal{P}_b\chi \quad (3.12)$$

i.e. $\partial_\mu J_{\mu,b} = 0 \forall b = 1, \dots, 63$. This is to be contrasted with SU(8) Dirac fermions realised in the π -flux phase on a square lattice [101] for fermionic spinons in a class of quantum spin-liquids, where the resultant implementation of the symmetries on the low energy fermions are very different. Crucially, in the present case, the non-trivial SOC of the underlying orbitals results in the mixing of the spin and the real spaces, under various lattice symmetries and time reversal which leads to important observable consequences which are reflected in the nature of the phases proximate to the semimetal, as we show

below. In addition, in the square lattice spin liquid problem, the spinons couple to an emergent dynamic SU(2) gauge field which is absent in the present case.

In addition to the above internal SU(8), the free Dirac action of Eq. 3.6 has a usual set of emergent space-time symmetries that include :

Emergent Lorentz symmetry generated by the three matrices

$$\gamma_{\mu\nu} = -\frac{i}{4}[\gamma_\mu, \gamma_\nu] \quad (3.13)$$

along with simultaneous rotations of the Euclidean space-time coordinates. Under Lorentz transformation, the spinors transform as $\chi \rightarrow \exp(i\Omega_{\mu\nu}\gamma_{\mu\nu})\chi$. Note that $\gamma_\mu = \epsilon^{\mu\nu\lambda}\gamma_{\nu\lambda}$ where $\mu, \nu, \lambda = 0, 1, 2$.

Continuous spatial translation symmetry under which the soft modes at the two valleys transform as

$$\mathbf{T}_{\mathbf{x}_0}^{\text{cont}} : \begin{cases} \chi_+(\mathbf{x}) \rightarrow \chi'_+(\mathbf{x}) = e^{i\mathbf{Q}\cdot\mathbf{x}_0} \chi_+(\mathbf{x} - \mathbf{x}_0) \\ \chi_-(\mathbf{x}) \rightarrow \chi'_-(\mathbf{x}) = e^{-i\mathbf{Q}\cdot\mathbf{x}_0} \chi_-(\mathbf{x} - \mathbf{x}_0) \end{cases} \quad (3.14)$$

where

$$\chi_\pm(\mathbf{x}) = \frac{1}{2}(1 \pm \zeta_1)\chi(\mathbf{x}) \quad (3.15)$$

are the two spinors associated with the two valleys respectively located at $\pm\mathbf{Q}$. Using Eq. 3.15, we can re-write the free Dirac action (Eq. 3.6) as $S_0 = S_0^+ + S_0^-$ where $S_0^\pm = v_F \int d^2\mathbf{x}d\tau \bar{\chi}_\pm(\mathbf{x})(-i\cancel{\partial})\chi_\pm(\mathbf{x})$ are the actions at the two valleys.

Emergent CPT symmetries : The free Dirac action S_0 is also invariant under emergent charge conjugation(\mathcal{C}), emergent parity(\mathcal{P}) and emergent time reversal(\mathcal{T}') symmetries. These symmetries act on the spinors in the following way:

$$\mathcal{C} : \chi(\mathbf{x}, t) \rightarrow -i\gamma_2\gamma_0\bar{\chi}^T(\mathbf{x}, t), \quad (3.16a)$$

$$\mathcal{P} : \chi(x_1, x_2, t) \rightarrow -i\gamma_1\chi(-x_1, x_2, t), \quad (3.16b)$$

$$\mathcal{T}' : \chi(\mathbf{x}, t) \rightarrow -i\gamma_2K\chi(\mathbf{x}, -t), \quad (3.16c)$$

with K being the complex conjugation operator. Here we denote the emergent time-reversal by \mathcal{T}' to distinguish it from the microscopic time reversal operation defined in Eq. 3.19 (which we denote with \mathbb{T} in Eq. 2.7).

3.3 Microscopic symmetries in the low energy theory

The enhanced IR symmetries provide important insights into the low-energy physics including the properties of the Dirac semimetal and associated quantum phase transitions into proximate symmetry broken phases. The latter is determined by the underlying UV/microscopic symmetries. These UV symmetries are embedded as a subgroup of the emergent (larger) IR symmetry group and are implemented as a combination of the IR symmetry transformations (see, for example, the discussion below Eq. 3.19 for the time-reversal symmetry). This is particularly interesting in the present case where the underlying SOC mixes the lattice and the $j = 3/2$ flavour space such that the embedding of the microscopic symmetries in the IR symmetry group can be rather intricate. It is, therefore, useful to list the symmetry transformation of the low energy Dirac fermions, χ , under various microscopic symmetries discussed above.

The total electronic charge is conserved in the microscopic system. This U(1) electronic charge conservation leads to the conservation of a current

$$J_\mu^{charge} = -i\bar{\chi}\gamma_\mu\chi \quad (3.17)$$

in the low energy Dirac theory, *i.e.*, $\partial_\mu J_\mu^{charge} = 0$.

On the other hand, the transformation of the low energy Dirac fermions, χ , under the discrete lattice symmetries (Table 2.1) as well as microscopic time reversal (Eq. 2.7) have the generic form (see Appendix A.6 for details)

$$\chi(\mathbf{x}) \xrightarrow{\mathbb{S}} \chi'(\mathbf{x}') = \left(\Omega_{\mathbb{S}}^f \otimes \Omega_{\mathbb{S}}^c \right) \chi(\mathbb{S}^{-1}\mathbf{x}) \quad (3.18)$$

where $\mathbb{S}(= \mathbf{T}_1, \mathbf{T}_2, \mathbf{C}_3, \mathbf{S}_6, \mathbf{C}'_2, \boldsymbol{\sigma}_d, \mathbf{I})$ stands for the generators of the lattice symmetries listed in Table 2.1 and $\Omega_{\mathbb{S}}^f, \Omega_{\mathbb{S}}^c$ both are 4×4 unitary matrices that act on the SU(4) flavor space and the chiral space respectively. The explicit form of these matrices is given in Appendix A.6.2. A central aspect of Eq. 3.18 is the fact that because of underlying SOC,

both $\Omega_{\mathbb{S}}^f$ and $\Omega_{\mathbb{S}}^c$ are non-trivial matrices for all the lattice symmetries.

Finally, under the microscopic time-reversal symmetry (Eq. 2.7), we have

$$\mathbb{T} : \chi(\mathbf{x}, t) \rightarrow \chi'(\mathbf{x}, t) = i\gamma^1 \Sigma_{13}\zeta_2 K \chi(\mathbf{x}, -t) \quad (3.19)$$

such that $\mathbb{T}^2 = -\mathbb{I}_{16}$ and thereby accounting for the Kramers' degeneracy for the $j = 3/2$ orbitals. Notably, this transformation is proportional to a simultaneous emergent time reversal, \mathcal{T}' (Eq. 3.16c) combined with a SU(8) rotation by $\Sigma_{13}\zeta_2$ and a Lorentz boost.

Chapter 4

Symmetry implementation and three groups of masses

Having described the free low energy theory for the electrons and its enhanced IR symmetries, we now discuss the effect of interactions on them in this chapter. We consider a generic form of 4-fermion interaction which can lead to the opening of a mass gap in the Dirac spectrum. We explore all possible gap-opening instabilities arising from such interactions and analyze their transformation properties under the action of both the microscopic symmetries and the emergent SU(8) symmetries. Based on this analysis, we identify all possible gapped phases proximate to the SU(8) Dirac semimetal. The summary of these phases are presented in the tables [4.3](#), [4.4](#), [4.5](#), [4.6](#).

4.1 Short range Interactions

We consider a generic form of four-fermion interaction Hamiltonian obtained from an underlying multi-orbital Hubbard-type model for the lattice fermions is given by

$$H_{\text{int}} = \int d^2\mathbf{x}d^2\mathbf{x}' V_{ijkl}(\mathbf{x} - \mathbf{x}') \chi_i(\mathbf{x})^\dagger \chi_j(\mathbf{x}')^\dagger \chi_k(\mathbf{x}) \chi_l(\mathbf{x}') + \dots \quad (4.1)$$

where V_{ijkl} denotes potential (i, j, k, l collectively spans over the different indices) and \dots corresponds to more irrelevant higher fermion interactions. We assume that the interactions are short-ranged in the sense V_{ijkl} is only appreciable for \mathbf{x} and \mathbf{x}' being proximate with a suitable UV regulation. Further, we assume that the form of V is constrained

enough that at low energy it has the full SU(8) symmetry. Long-ranged Coulomb interactions as well as on-site Hubbard repulsion, for example, have such SU(8), symmetry. This immediately means that even in the presence of these short-range interactions, all the flavour currents $J_{\mu,a}$ (Eq. 3.12), in addition to the electronic current J_{μ}^{charge} (Eq. 3.17) remain conserved unless spontaneously broken.

While short-range quartic interactions are perturbatively irrelevant at the free Dirac fixed point [68, 117], on cranking them up they lead to phase transitions possibly gapping out the fermions and associated spontaneous breaking of the symmetries of the free Dirac theory. In the following chapters of this thesis, we provide an understanding of the phases that are obtained by condensing various fermion bilinears which do not carry a net electronic charge, *i.e.* invariant under the U(1) described in Eq. 3.17 and therefore have the form

$$\Delta^a = -i\langle\bar{\chi}\mathcal{M}_a\chi\rangle \neq 0 \quad (4.2)$$

where \mathcal{M}_a are 16×16 *mass matrices* such that $\gamma_0\mathcal{M}_a$ anti-commutes with both the Dirac matrices– α_1 and α_2 – given by Eq. 3.5. . This leaves out another important class of fermion bilinears symbolically of the form $\langle\chi\chi\rangle$ that describes different types of superconductors which will be taken up elsewhere [133].

For such a U(1) invariant massive phase, the mean-field Hamiltonian is given by

$$S_{MF} = S_0 + S_m = -i \int d^2\mathbf{r}d\tau \bar{\chi}(\mathbf{r}) [v_F\cancel{\partial} - \Delta^a\mathcal{M}_a] \chi(\mathbf{r}). \quad (4.3)$$

There are 64 such linearly independent \mathcal{M}_a matrices that can be broadly classified into two classes according to their transformation properties under SU(8). The first class contains a single SU(8) singlet given by

$$-i\langle\bar{\chi}\chi\rangle, \quad (4.4)$$

while the second class corresponds to 63 SU(8) adjoint multiplet

$$-i\langle\bar{\chi}\mathcal{P}_a\chi\rangle, \quad a = 1 \cdots, 63. \quad (4.5)$$

and \mathcal{P}_a being the SU(8) generators (Eq. 3.10).

The microscopic operators that characterise the same broken symmetry – hence can serve as valid order-parameters for appropriate symmetry broken phases– have the same transformation properties as the bilinear and hence are proportional to each other. In principle, the microscopic operators can also get contributions from the conserved currents of the same symmetry, but usually, such currents decay faster than the bilinears, and hence at long distances, the correlation function of the microscopic fields is determined by that of the field theory bilinear (shown in Eq. 4.4 and 4.5) [101].

The correspondence between the microscopic operators and the low-energy fermion bilinears is obtained by comparing their symmetry transformations. In particular, the transformation of the low-energy fermion bilinears under microscopic symmetries can be used to systematically uncover the nature of the phases proximate to the Dirac semimetal. Bilinears that are related by microscopic symmetries together constitute a single phase. This leads to the classification of the fermion masses in terms of broken microscopic symmetries and/or anomalies. In the present case, we find that the 64 masses group together to give rise to 24 phases which we now turn to understand in detail.

4.2 Classification of the fermionic bilinears : phases and transitions

This task of classifying the bilinears according to their microscopic symmetries (and hence identifying the phases) is much more involved compared to the same problem in graphene [21] since the SOC mixes the $j = 3/2$ flavour and the real spaces in a non-trivial way. As a result, the lattice translations, $\mathbf{T}_1, \mathbf{T}_2$ (Table 2.1) do not necessarily commute with the point group symmetries such as $\mathbf{C}_3, \mathbf{S}_6, \mathbf{C}'_2, \boldsymbol{\sigma}_d, \mathbf{I}$ (Table 2.1) and microscopic time reversal, \mathbb{T} , (Eq. 2.7). This is clear by looking at the transformations of the Dirac spinor, χ , under the above lattice symmetries (Eq. 3.18 with the detailed forms given by Eqs. A.70 - A.90). Hence we need to analyse the action of the entire set of transformations generated by the space group and microscopic time reversal on χ to understand the transformation of the fermion bilinears in Eq. 4.2. The resultant symmetry group, we dub as *IR space group*.

IR Space group : To understand the structure of this *IR space group*, we note that the $j = 3/2$ electron states transform under a double group representation of D_{3d} , which has 24 elements. Since the translations do not commute with point group transformations, corresponding to any element (say, \mathbb{S}) of the double group of D_{3d} , there are four elements in the *IR space group* which can be constructed as (say) \mathbb{S} , $\mathbf{T}_1\mathbb{S}$, $\mathbf{S}\mathbf{T}_2$ and $\mathbf{T}_1\mathbf{S}\mathbf{T}_2$ by composing it with translations, \mathbf{T}_1 and \mathbf{T}_2 (Table 2.1). So, the group of microscopic symmetries that act on the spinors has 96 elements in total. These elements can be divided into 20 conjugacy classes and hence there are 20 different irreducible representations of the IR space group. Among these 20, only 10 has +ve character for 2π rotation. Since the fermion bilinears are always invariant under a 2π rotation¹, we consider only these irreps for the classification of the masses.

Among these 10 irreps of the IR space group, four are 1-dimensional ($\mathcal{A}_{1g}, \mathcal{A}_{2g}, \mathcal{A}_{1u}, \mathcal{A}_{2u}$), two are 2-dimensional ($\mathcal{E}_g, \mathcal{E}_u$) and four irreps are 3-dimensional ($\mathcal{J}_{1g}, \mathcal{J}_{2g}, \mathcal{J}_{1u}, \mathcal{J}_{2u}$). Following conventional notation, the subscripts 1(2) and $g(u)$ denote that the irrep is even (odd) under rotation, \mathbf{C}'_2 and inversion, \mathbf{I} , respectively (Table. 2.1). Further, to incorporate microscopic time reversal, \mathbb{T} (Eq. 2.7), we will add a superscript $e(o)$ (e.g., $\mathcal{A}_{1u}^{e(o)}$) to denote the particular irrep is even (odd) under time-reversal. The details of these irreps are given in Appendix A.7.

The central question we now turn to investigate in the rest of this thesis are the nature of the phases obtained by condensing the fermion bilinears $\langle \bar{\chi} \mathcal{P}_a \chi \rangle$. Since this is decided by the microscopic symmetries, we decompose the above bilinears in terms of the irreducible representation of the microscopic symmetries [101]. We find that these 64 bilinears break up into 27 irreps of the space group among which there are six 1-dimensional representations, five 2-dimensional representations and sixteen 3-dimensional representations. This can be obtained as follows.

Starting with Eqs. 3.18 and 3.19, we can derive the action of the microscopic symmetries on the members of the 64 fermion bilinears, which leads to the following structure. Under the action of a lattice symmetry transformation (say \mathbb{S} , corresponding to Table 2.1 and Eq. 3.18), a fermion bilinear of the form $\bar{\chi} \mathcal{P}_a \chi$ (with \mathcal{P}_a given by Eq. 3.10) transforms

¹Explicit calculations of the transformation of the fermion bilinears show that they are invariant under the action of a 2π rotation.

	Irrep	Σ_p	\mathbb{T}
Singlets	\mathcal{A}_{1g}^e	$\Sigma_0 = \mathbf{1}_4$	even
	\mathcal{A}_{2g}^o	Σ_{45}	odd
Doublet	\mathcal{E}_u^e	$\{\Sigma_4, \Sigma_5\}$	even
Triplets	\mathcal{J}_{1g}^e	$\{\Sigma_3, \Sigma_1, -\Sigma_2\}$	even
	\mathcal{J}_{2g}^o	$\{\Sigma_{12}, \Sigma_{23}, \Sigma_{13}\}$	odd
	\mathcal{J}_{1u}^o	$\{\Sigma_{35}, \frac{\sqrt{3}\Sigma_{14}}{2} - \frac{\Sigma_{15}}{2}, \frac{\sqrt{3}\Sigma_{24}}{2} + \frac{\Sigma_{25}}{2}\}$	odd
	\mathcal{J}_{2u}^o	$\{\Sigma_{34}, -\frac{\Sigma_{14}}{2} - \frac{\sqrt{3}\Sigma_{15}}{2}, \frac{\Sigma_{24}}{2} - \frac{\sqrt{3}\Sigma_{25}}{2}\}$	odd

Table 4.1: Irreps of the matrices SU(4) flavour space.

as

$$-i\bar{\chi}\mathcal{P}_a\chi = \chi^\dagger\gamma_0\Sigma_i\zeta_j\chi \xrightarrow{\mathbb{S}} \chi^\dagger(\Omega_S^{f\dagger}\Sigma_i\Omega_S^f) \otimes (\Omega_S^{e\dagger}\gamma_0\zeta_j\Omega_S^e)\chi \quad (4.6)$$

and under the action of microscopic time reversal (Eqs. 2.7 and 3.19), we get

$$\chi^\dagger\gamma_0\Sigma_i\zeta_j\chi \xrightarrow{\mathbb{T}} \chi^\dagger(\Sigma_{13}\Sigma_i^*\Sigma_{13}) \otimes (\tau_1\sigma_0\gamma_0^*\zeta_j^*\tau_1\sigma_0)\chi \quad (4.7)$$

The above structure shows that the action of each symmetry is implemented as a product of the transformations in the flavour and chiral spaces, *i.e.*, for lattice symmetries,

$$\Sigma_i \xrightarrow{\mathbb{S}} \Omega_S^{f\dagger}\Sigma_i\Omega_S^f; \quad \gamma_0\zeta_j \xrightarrow{\mathbb{S}} \Omega_S^{e\dagger}\gamma_0\zeta_j\Omega_S^e \quad (4.8)$$

and for time reversal

$$\Sigma_i \xrightarrow{\mathbb{T}} \Sigma_{13}\Sigma_i^*\Sigma_{13}; \quad \gamma_0\zeta_j \xrightarrow{\mathbb{T}} \tau_1\sigma_0\gamma_0^*\zeta_j^*\tau_1\sigma_0. \quad (4.9)$$

However, due to the SOC, the real space transformations get non-trivially coupled to the flavour space and this resultant inter-locking is reflected in the form of the transformation matrices, particularly in Eq. 4.8 where the Ω_S^f reflects the degree of interlocking between real and flavour spaces. In fact, it is this non-trivial structure that distinguishes the spin-orbit coupled Dirac fermions– the topic of the present work– with multi-flavour (larger N_F) generalisation of graphene where such SOC is usually neglected (except for the spin-Hall effect [134] and related phases where SOC is essential).

Due to the direct product structure of the above transformations, we can analyze the action of the microscopic symmetries on the flavor and the chiral spaces separately

	Irrep	$\gamma_0\zeta_j$	\mathbb{T}
Singlet	\mathcal{A}_{2g}^o	γ_0	odd
Triplet	\mathcal{F}_{1g}^e	$\{\gamma_0\zeta_1, \gamma_0\zeta_2, \gamma_0\zeta_3\}$	even

Table 4.2: Irreps for the matrices in the SU(2) chiral space.

and then use Clebsch-Gordon decomposition, e.g., if the matrix Σ_i transforms in some irreducible representation (say, \mathcal{D}_1) and $\gamma_0\zeta_j$ transforms in some other irrep (say, \mathcal{D}_2), then the bilinear $\bar{\chi}\Sigma_i\zeta_j\chi$ transforms in the product representation $\mathcal{D}_1 \otimes \mathcal{D}_2$. This direct product representation is reducible in general which then is reduced into a direct sum representation.

Table 4.1 shows the Σ_i matrices in the SU(4) flavour space and their irreducible representations under the IR space-group transformations as well as TR. The transformations of the $\gamma_0\zeta_j$ (Eq. 3.9) matrices in the SU(2) chiral space are written in Table 4.2. Details of their symmetry transformations are given in Appendix A.7.

The 64 fermion bilinears are subdivided into three groups depending on the participation of the flavour, Σ_i and the chiral elements, ζ_j , in the fermion bilinear (Eq. 4.2) which, in turn, dictate their transformation properties under the microscopic symmetries. These are – (1) Group-1 : the chiral masses composed of flavour singlets, (2) Group-2 : the flavour masses composed of chiral singlets, and, (3) Group-3 : the mixed masses which are composed of non-trivial combinations of both the flavour and chiral sectors. Here we list the masses in the groups mentioned above and briefly mention their properties in tables 4.3-4.6. The later chapters contain a detailed discussion of their physics.

4.2.1 Group-1 : The chiral masses

There are four masses of the form $-i\langle\bar{\chi}\chi\rangle$ and $-i\langle\bar{\chi}\zeta_i\chi\rangle$ ($i = 1, 2, 3$) that are invariant under the SU(4) flavour symmetry and charge conservation which are broken down by the lattice symmetries and TR as $\mathbf{4} = \mathbf{1} \oplus \mathbf{3}$, *i.e.*,

$$[\mathcal{A}_{1g}^e]^\Sigma \otimes [\mathcal{A}_{2g}^o]^\zeta = \mathcal{A}_{2g}^o \quad (4.10a)$$

$$[\mathcal{A}_{1g}^e]^\Sigma \otimes [\mathcal{F}_{1g}^e]^\zeta = \mathcal{F}_{1g}^e \quad (4.10b)$$

where $[\dots]^\Sigma$ and $[\dots]^\zeta$ denote the two irreducible representations taken from Tables 4.1 and 4.2 respectively.

The singlet represents an Integer Chern insulator (ICI) phase, the triplet corresponds to the three stripy charge density waves (CDW) (Fig. 5.2). Since the flavour index plays no role, we can quantitatively compare the spinless version of the present problem (Appendix A.11) with spinless electrons in graphene [21, 135]. In the case of graphene, the irreducible representation splits up into $\mathbf{4} = \mathbf{1} \oplus \mathbf{1} \oplus \mathbf{2}$ where the two singlets represent the ICI phase [136, 137] and staggered (Néel) CDW, and the doublet corresponds to the two Kekule patterns [21, 135]. This is very different from the present case and this provides a startling example where the microscopic SOC changes the low energy symmetry implementation. We discuss these masses in more detail in Chapter 5.

4.2.2 Group-2 : The flavour masses

There are 15 masses of the form $i\langle\bar{\chi}\Sigma_j\chi\rangle$ where Σ_j are the 15 generators of SU(4) as given by Eq. A.26 in Appendix A.3. Under microscopic symmetries, they break up into six different irreps, *i.e.*, $\mathbf{15} = \mathbf{1} \oplus \mathbf{3} \oplus \mathbf{3} \oplus \mathbf{3} \oplus \mathbf{2} \oplus \mathbf{3}$ given by Eqs. 4.21, 4.22 and 4.23. These correspond to six generalised spin-Hall phases that are summarised in Table 4.4 while the details are given in Chapter 6.

In order to explore the nature of the resultant phases, it is useful to understand in detail the mathematical structure of the implementation of the various microscopic symmetries that break up the 15 flavour masses further into different irreducible representations. Starting with TR, ten of the flavour masses are TR even and are of the form

$$-i\langle\bar{\chi}\Sigma_j\chi\rangle, \quad j = 12, 13, 14, 15, 23, 24, 25, 34, 35 \text{ and } 45. \quad (4.11)$$

These transform into each other under an adjoint representation of an SO(5) sub-group (generated by themselves, Eq. 4.11) of the SU(4) flavour group.

The other five are TR odd and transform under a vector representation of the same SO(5) and are given by

$$-i\langle\bar{\chi}\Sigma_j\chi\rangle \quad \text{with } j = 1, 2, 3, 4 \text{ and } 5 \quad (4.12)$$

Next, the lattice inversion (Table 2.1), **I**, breaks each of the above two sets further.

Out of the 10 adjoint ones (Eq. 4.11), four

$$-i\langle\bar{\chi}\Sigma_j\chi\rangle \quad \text{with } j = 45, 12, 13 \text{ and } 23 \quad (4.13)$$

are even under inversion, \mathbf{I} , while the other six

$$-i\langle\bar{\chi}\Sigma_j\chi\rangle \quad \text{with } j = 14, 15, 24, 25, 34 \text{ and } 35 \quad (4.14)$$

are odd under it. For the 5 vector masses (Eq. 4.12), two

$$-i\langle\bar{\chi}\Sigma_j\chi\rangle \quad \text{with } j = 4 \text{ and } 5 \quad (4.15)$$

are inversion odd, while three

$$-i\langle\bar{\chi}\Sigma_j\chi\rangle \quad \text{with } j = 1, 2 \text{ and } 3 \quad (4.16)$$

are even.

Each of the above four subsets (Eqs. 4.13-4.16) is individually closed under a $U(1) \otimes SU(2)$ sub-group of the $SO(5)$ (eq. 4.11) that is generated respectively by

$$\Sigma_{45} \quad (4.17)$$

and

$$\{\Sigma_{12}, \Sigma_{13}, \Sigma_{23}\}. \quad (4.18)$$

In particular, in the first subset (Eq. 4.13), the first mass is a $U(1) \otimes SU(2)$ singlet while the rest are only $U(1)$ singlets that transform as spin-1 under the $SU(2)$. The three masses in Eq. 4.16 are $U(1)$ singlets and an $SU(2)$ triplet, while the two masses in Eq. 4.15 are $SU(2)$ singlets and transform into each other under the $U(1)$. Finally the six masses in Eq. 4.14, decompose into two $SU(2)$ triplets :

$$\{-i\langle\bar{\chi}\Sigma_{14}\chi\rangle, -i\langle\bar{\chi}\Sigma_{24}\chi\rangle, -i\langle\bar{\chi}\Sigma_{34}\chi\rangle\} \quad (4.19)$$

and

$$\{-i\langle\bar{\chi}\Sigma_{15}\chi\rangle, -i\langle\bar{\chi}\Sigma_{25}\chi\rangle, -i\langle\bar{\chi}\Sigma_{35}\chi\rangle\}. \quad (4.20)$$

The three components of the first triplet mix with their corresponding components of the second triplet under the U(1) generated by Eq. 4.17.

Now, considering the other lattice symmetries the above four subsets (Eqs. 4.13-4.16) break up further into the irreps of the microscopic symmetry group as follows.

The four masses in Eq. 4.13 break up into a singlet and a triplet as

$$[\mathcal{A}_{2g}^o]^\Sigma \otimes [\mathcal{A}_{2g}^o]^\zeta = \mathcal{A}_{1g}^e \quad (4.21a)$$

$$[\mathcal{J}_{2g}^o]^\Sigma \otimes [\mathcal{A}_{2g}^o]^\zeta = \mathcal{J}_{1g}^e \quad (4.21b)$$

whose explicit forms are given in Eqs. 6.1 and 6.8 respectively and correspond to two different kinds of quantum spin-octupole phases discussed in Sec. 6.1.1 and 6.1.2.

The six inversion-odd masses (Eq. 4.14), on the other hand, break up into two triplets

$$[\mathcal{J}_{1u}^o]^\Sigma \otimes [\mathcal{A}_{2g}^o]^\zeta = \mathcal{J}_{2u}^e \quad (4.22a)$$

$$[\mathcal{J}_{2u}^o]^\Sigma \otimes [\mathcal{A}_{2g}^o]^\zeta = \mathcal{J}_{1u}^e. \quad (4.22b)$$

given by a linear combination of the two triplets in Eq. 4.19 and 4.20 as given by Eqs. 6.12 and 6.13 respectively. These too correspond to spin-octupole Hall phases, albeit with interesting fine-tuned gapless points for a special combination of the three components of the triplets as discussed in Sec. 6.1.3.

The doublet and the triplets in Eqs. 4.15 and 4.16 remain intact and result in

$$[\mathcal{E}_u^e]^\Sigma \otimes [\mathcal{A}_{2g}^o]^\zeta = \mathcal{E}_u^o \quad (4.23a)$$

$$[\mathcal{J}_{1g}^e]^\Sigma \otimes [\mathcal{A}_{2g}^o]^\zeta = \mathcal{J}_{2g}^o \quad (4.23b)$$

with explicit forms being given by Eqs. 6.23 and 6.24 respectively. These phases break time-reversal symmetry and describe quantum spin-quadrupole Hall phases as described in Sec. 6.2.

4.2.3 Group 3 : The mixed masses

Finally, the largest set of masses is obtained by taking the direct product of the flavour multiplets and the chiral multiplets. There are 45 such masses of the form $-i\langle\bar{\chi}\Sigma_i\zeta_j\chi\rangle$ where Σ_i are the fifteen generators of flavor SU(4) (see Appendix A.3) and $j = 1, 2, 3$. Therefore these masses transform into each other under transformations of the SU(4) \otimes SU(2) subgroup of SU(8) of the free Dirac theory. Their group decomposition to irreducible representations under the microscopic symmetries is given by

$$[\mathcal{A}_{2g}^o]^\Sigma \otimes [\mathcal{J}_{1g}^e]^\zeta = \mathcal{J}_{2g}^o \quad (4.24a)$$

$$[\mathcal{E}_u^e]^\Sigma \otimes [\mathcal{J}_{1g}^e]^\zeta = \mathcal{J}_{1u}^e \oplus \mathcal{J}_{2u}^e \quad (4.24b)$$

$$[\mathcal{J}_{1g}^e]^\Sigma \otimes [\mathcal{J}_{1g}^e]^\zeta = \mathcal{J}_{1g}^e \oplus \mathcal{J}_{2g}^e \oplus \mathcal{E}_g^e \oplus \mathcal{A}_{1g}^e \quad (4.24c)$$

$$[\mathcal{J}_{2g}^o]^\Sigma \otimes [\mathcal{J}_{1g}^e]^\zeta = \mathcal{J}_{1g}^o \oplus \mathcal{J}_{2g}^o \oplus \mathcal{E}_g^o \oplus \mathcal{A}_{2g}^o \quad (4.24d)$$

$$[\mathcal{J}_{1u}^o]^\Sigma \otimes [\mathcal{J}_{1g}^e]^\zeta = \mathcal{J}_{1u}^o \oplus \mathcal{J}_{2u}^o \oplus \mathcal{E}_u^o \oplus \mathcal{A}_{1u}^o \quad (4.24e)$$

$$[\mathcal{J}_{2u}^o]^\Sigma \otimes [\mathcal{J}_{1g}^e]^\zeta = \mathcal{J}_{1u}^o \oplus \mathcal{J}_{2u}^o \oplus \mathcal{E}_u^o \oplus \mathcal{A}_{2u}^o. \quad (4.24f)$$

The dimension of the representation depends non-trivially on the details of the spin-orbital locking, which, in turn, is reflected in the nature of different density wave phases that these masses lead to. These density wave phases mainly come in two varieties. Out of the total of 45 mixed masses, 18 (marked in black in Eq. 4.24) generically have at least four gapless fermionic modes protected by a subgroup of SU(8), often in conjunction with lattice symmetries. Thus they describe different kinds of *density wave Dirac semimetal* (summarised in Table 4.6). The rest 27 (marked in red in Eq. 4.24) generically consists of density wave-insulators (summarised in Table 4.5). Two of the insulators, both singlets – \mathcal{A}_{1g}^e and \mathcal{A}_{2g}^o , have edge modes whose signature is evident from appropriate Chern-Simons terms.

Before delving into the details of the resultant phases in this category in Chapter 7, we summarise the general structure of these masses and their classification here under various microscopic symmetries leading up to the decomposition in Eq. 4.24. To this end, starting with microscopic TR, \mathbb{T} (Eq. 2.7), the 45 bilinears are divided into two

classes with 15 TR even given by

$$\{-i\langle\bar{\chi}\Sigma_i\zeta_1\chi\rangle, -i\langle\bar{\chi}\Sigma_i\zeta_2\chi\rangle, -i\langle\bar{\chi}\Sigma_i\zeta_3\chi\rangle\} \quad (4.25)$$

where $i = 1, 2, 3, 4, 5$ (same Σ_i content as in Eq. 4.12) and 30 TR odd given by

$$\{-i\langle\bar{\chi}\Sigma_i\zeta_1\chi\rangle, -i\langle\bar{\chi}\Sigma_i\zeta_2\chi\rangle, -i\langle\bar{\chi}\Sigma_i\zeta_3\chi\rangle\} \quad (4.26)$$

with the i indices being given in Eq. 4.11.

Each of these two sets, under lattice inversion, **I** (Table. 2.1), break up into two subsets as odd and even under **I**. Out of the set of 15 in Eq. 4.25 the six odd ones are given by

$$\{-i\langle\bar{\chi}\Sigma_4\zeta_i\chi\rangle, -i\langle\bar{\chi}\Sigma_5\zeta_i\chi\rangle\} \quad (4.27)$$

while nine even ones are given by

$$\{-i\langle\bar{\chi}\Sigma_1\zeta_i\chi\rangle, -i\langle\bar{\chi}\Sigma_2\zeta_i\chi\rangle, -i\langle\bar{\chi}\Sigma_3\zeta_i\chi\rangle\} \quad (4.28)$$

where $i = 1, 2, 3$.

On the other hand, the set of 30 masses in Eq. 4.26 breaks up into two subsets. One of the subsets contains twelve masses that are even under **I** and is given by

$$\{-i\langle\bar{\chi}\Sigma_{45}\zeta_i\chi\rangle, -i\langle\bar{\chi}\Sigma_{12}\zeta_i\chi\rangle, -i\langle\bar{\chi}\Sigma_{23}\zeta_i\chi\rangle, -i\langle\bar{\chi}\Sigma_{13}\zeta_i\chi\rangle\}. \quad (4.29)$$

The other subset containing eighteen **I** odd masses is

$$\begin{aligned} & \{-i\langle\bar{\chi}\Sigma_{14}\zeta_i\chi\rangle, -i\langle\bar{\chi}\Sigma_{15}\zeta_i\chi\rangle, -i\langle\bar{\chi}\Sigma_{24}\zeta_i\chi\rangle, \\ & -i\langle\bar{\chi}\Sigma_{25}\zeta_i\chi\rangle, -i\langle\bar{\chi}\Sigma_{34}\zeta_i\chi\rangle, -i\langle\bar{\chi}\Sigma_{35}\zeta_i\chi\rangle\}. \end{aligned} \quad (4.30)$$

Further application of lattice symmetries (Appendix A.7) break these up into singlets, doublets and triplets as follows. The TR even and inversion odd subset (Eq. 4.27) of six decomposes into two triplets given by Eq. 4.24b which correspond to two different zig-zag spin-quadrupolar density wave insulators given by Eq. 7.14. Similarly, the nine

TR and inversion even masses break up into two triplets, one doublet and one singlet as given by Eq. 4.24c. They represent spin-quadrupole density waves. While the singlet corresponds to an insulator (Eq. 7.1) with quantized spin-octupole filtered edge modes, the rest (Eqs. 7.55, 7.57 and 7.60) are partially gapless semimetals.

The subset of 12 TR odd and inversion even masses (Eq. 4.29) break up into three triplets, one doublet and one singlet under the action of the lattice symmetries (Eqs. 4.24a, 4.24d). The singlet (an anomalous Hall insulator) and one of the triplets represent insulating ferro (uniform) (Eq. 7.4) and stripy (Eq. 7.11) density wave ordering of spin-octupoles respectively. The doublet (Eq. 7.64) corresponds to ferro spin-octupole semimetal and the other two triplets (Eqs. 7.47, 7.50) correspond to different stripy spin-octupole density wave semimetals.

Finally, the 18 TR and inversion odd masses, break up under lattice symmetries into four triplets, two doublets and two singlets given by Eqs. 4.24e and 4.24f. Out of them, the two singlets (Eqs. 7.31 and 7.32) correspond to staggered (“Néel”) spin-octupole density-wave semimetal. The two doublets (Eqs. 7.7 and 7.8) on the other hand, both correspond to Néel spin-octupole density wave insulators. As discussed below Eq. 7.8, they can be rotated into each other via a U(1) transformation generated by Σ_{45} within the flavour space. Given this fact and they break the same symmetries, the two doublets correspond to the same phase and are not distinct from each other. Similar arguments hold for the two sets of triplets, each of which represents zig-zag spin-octupole density wave insulators. The two \mathcal{J}_{1u}^o triplets (Eqs. 7.21 and 7.22) can be continuously connected without change of symmetry and hence represent the same phase. Similarly the two \mathcal{J}_{2u}^o triplets (Eqs. 7.29 and 7.30) give the same phase.

4.3 Summary of the phases

In this section, we briefly mention the phases in the three groups. Table 4.3 and 4.4 discuss the phases in Group-1 (chiral masses) and Group-2 (flavor masses). Tables 4.5 and 4.6 discuss the phases obtained from the mixed masses.

Table 4.3: The SU(4) invariant chiral phases. The microscopic symmetry elements mentioned in this and the subsequent tables are defined in Table 2.1. Also, the ζ_i are generators of the chiral SU(2) and Σ_i are generators of flavor SU(4) which are defined in Eq. 3.9 and Appendix A.3 respectively.

#	The Phase	Irrep	Broken Microscopic symmetries	Fermion Bilinear	Comments
1.	Integer Chern insulator (ICI). (Sec. 5.1)	\mathcal{A}_{2g}^o	$\mathbf{C}'_2, \sigma_d, \text{TR}$	$-i\langle\bar{\chi}\chi\rangle$	Fully gapped. Charge Hall response given by $N_F = 4$ CS theory (Eq. 5.2)
2.	Stripy charge density wave (StCDW). (Sec. 5.2)	\mathcal{F}_{1g}^e	$\mathbf{T}_1, \mathbf{T}_2, \mathbf{C}_3, \mathbf{S}_6, \mathbf{C}'_2, \sigma_d$	$-i\langle\bar{\chi}\zeta_1\chi\rangle,$ $-i\langle\bar{\chi}\zeta_2\chi\rangle,$ $-i\langle\bar{\chi}\zeta_3\chi\rangle$	Fully gapped. Stripy modulation of electronic charge density (Fig. 5.2)

Table 4.4: The flavor phases

#	The Phase	Irrep	Broken Microscopic symmetries	Fermion Bilinear	Comments
3.	Singlet Quantum spin-octupole Hall insulator. (Sec. 6.1.1)	\mathcal{A}_{1g}^e	None	$-i\langle\bar{\chi}\Sigma_{45}\chi\rangle$	Fully Gapped. Spin-octupole Hall response in presence of electric field (Eq. 6.5) via spin-octupole filtered edges protected by $U(1)\times Z_2^{TR}$.
4.	Triplet Quantum spin-octupole Hall insulator.	\mathcal{F}_{1g}^e	$\mathbf{T}_1, \mathbf{T}_2,$ $\mathbf{C}_3, \mathbf{S}_6,$ \mathbf{C}'_2, σ_d	$-i\langle\bar{\chi}\Sigma_{23}\chi\rangle,$ $-i\langle\bar{\chi}\Sigma_{13}\chi\rangle,$ $-i\langle\bar{\chi}\Sigma_{12}\chi\rangle$	Fully gapped. Spin-octupole filtered edge currents. The Skyrmion configurations of the triplet order parameter carry 4

	(Inversion even) (Sec. 6.1.2)				units of electronic charge. Such skyrmion condensation leads to a novel 4e superconductor.
5.	Triplet Quantum spin-octupole Hall insulators. (Inversion odd) (Sec. 6.1.3)	\mathcal{J}_{1u}^e	$\mathbf{T}_1, \mathbf{T}_2,$ $\mathbf{C}_3, \mathbf{S}_6,$ $\mathbf{C}'_2, \sigma_d, \mathbf{I}$	$-i\langle\bar{\chi}\Sigma_{34}\chi\rangle,$ $-i\langle\bar{\chi}\left(-\frac{\Sigma_{14}+\sqrt{3}\Sigma_{15}}{2}\right)\chi\rangle,$ $-i\langle\bar{\chi}\left(\frac{\Sigma_{24}-\sqrt{3}\Sigma_{25}}{2}\right)\chi\rangle.$	Non-compatible masses. Generally fully gapped except for isolated points protected by symmetries. Spin-octupole filtered edge.
6.	Triplet Quantum spin-octupole Hall insulator (Inversion odd) (Sec. 6.1.3)	\mathcal{J}_{2u}^e	$\mathbf{T}_1, \mathbf{T}_2,$ $\mathbf{C}_3, \mathbf{S}_6,$ $\mathbf{C}'_2, \sigma_d, \mathbf{I}$	$-i\langle\bar{\chi}\Sigma_{35}\chi\rangle,$ $-i\langle\bar{\chi}\left(\frac{\sqrt{3}}{2}\Sigma_{24} + \frac{1}{2}\Sigma_{25}\right)\chi\rangle,$ $-i\langle\bar{\chi}\left(\frac{\sqrt{3}}{2}\Sigma_{14} - \frac{1}{2}\Sigma_{15}\right)\chi\rangle.$	Similar to entry No.5 of this table but with different spin-octupole current at the edges protected by different set of symmetries.
7.	Doublet Quantum spin-quadrupole Hall	\mathcal{E}_u^o	$\mathbf{C}'_2, \mathbf{I},$ $\mathbf{C}_3, \mathbf{S}_6,$ σ_d, TR	$-i\langle\bar{\chi}\Sigma_4\chi\rangle, -i\langle\bar{\chi}\Sigma_5\chi\rangle$	Fully gapped. Vortices carry zero modes with charge and

	insulator. (Sec. 6.2)				quadrupole quantum numbers.
8.	Triplet Quantum spin-quadrupole Hall insulator. (Sec. 6.2)	\mathcal{J}_{2g}^o	$\mathbf{T}_1, \mathbf{T}_2,$ $\mathbf{C}_3, \mathbf{S}_6,$ $\mathbf{C}'_2, \sigma_d, \text{TR}$	$-i\langle\bar{\chi}\Sigma_1\chi\rangle,$ $-i\langle\bar{\chi}\Sigma_2\chi\rangle,$ $-i\langle\bar{\chi}\Sigma_3\chi\rangle$	Fully gapped. Quadrupole filtered edge modes protected by U(1) symmetry. TR broken.

Table 4.5: The mixed phases (insulators)

#	The Phase	Irrep	Broken Microscopic symmetries	Fermion Bilinear	Comments
9.	Singlet Spin-quadrupolar ferro Hall insulator. (Sec. 7.1.1)	\mathcal{A}_{1g}^e	None	$-i\langle\bar{\chi}(\Sigma_3\zeta_1 - \Sigma_1\zeta_3 - \Sigma_2\zeta_2)\chi\rangle/\sqrt{3}$	Fully gapped. Octupole (Σ_{45}) filtered edge modes.
10.	Singlet Spin-octupolar	\mathcal{A}_{2g}^o	$\mathbf{C}'_2, \sigma_d, \text{TR}$	$-i\langle\bar{\chi}(\Sigma_{12}\zeta_1 - \Sigma_{23}\zeta_3 + \Sigma_{13}\zeta_2)\chi\rangle/\sqrt{3}$	Fully gapped. Gapless edges carry

	Anomalous ferro Hall Insulator. (Sec. 7.1.2)				quantized charge current via CS term.
11.	Doublet Spin-octupolar Néel insulator. (Sec. 7.1.3)	\mathcal{E}_u^o (2 doublets)	$\mathbf{C}'_2, \sigma_{\mathbf{d}}, \mathbf{I},$ $\mathbf{C}_3, \mathbf{S}_6$ TR	See Eq. 7.7 and Eq. 7.8	Fully gapped. Both doublets correspond to the same phase. Vortices can carry non-trivial quantum number.
12.	Triplet Spin-octupolar stripy density wave (StDW) insulator. (Sec. 7.1.4)	\mathcal{J}_{2g}^o	$\mathbf{T}_1, \mathbf{T}_2,$ $\mathbf{C}_3, \mathbf{S}_6,$ $\mathbf{C}'_2, \sigma_{\mathbf{d}},$ TR	$-i \langle \bar{\chi} \Sigma_{45} \zeta_1 \chi \rangle,$ $-i \langle \bar{\chi} \Sigma_{45} \zeta_2 \chi \rangle,$ $-i \langle \bar{\chi} \Sigma_{45} \zeta_3 \chi \rangle$	Fully gapped.
13.	Triplet Spin-quadrupolar zig-zag density wave (ZDW) insulator. (Sec. 7.1.5)	\mathcal{J}_{1u}^e	$\mathbf{T}_1, \mathbf{T}_2,$ $\mathbf{C}_3, \mathbf{S}_6,$ $\mathbf{C}'_2, \sigma_{\mathbf{d}}, \mathbf{I}$	$-i \langle \bar{\chi} \Sigma_5 \zeta_1 \chi \rangle$ $-i \left\langle \bar{\chi} \left(\frac{-\sqrt{3}\Sigma_4 + \Sigma_5}{2} \right) \zeta_3 \chi \right\rangle,$ $-i \left\langle \bar{\chi} \left(\frac{-\sqrt{3}\Sigma_4 - \Sigma_5}{2} \right) \zeta_2 \chi \right\rangle$	Fully gapped, Masses are non-compatible, Gapless modes for some special linear

					combinations.
14.	Triplet Spin- quadrupolar ZDW insu- lator (Sec. 7.1.5)	\mathcal{J}_{2u}^e	$\mathbf{T}_1, \mathbf{T}_2,$ $\mathbf{C}_3, \mathbf{S}_6,$ $\mathbf{C}'_2, \sigma_d, \mathbf{I}$	$-i \langle \bar{\chi} \Sigma_4 \zeta_1 \chi \rangle,$ $-\frac{i}{2} \langle \bar{\chi} (\sqrt{3} \Sigma_5 + \Sigma_4) \zeta_3 \chi \rangle,$ $-\frac{i}{2} \langle \bar{\chi} (\sqrt{3} \Sigma_5 - \Sigma_4) \zeta_2 \chi \rangle$	Similar to entry No.13 in this table, but different quadrupole operators are ordered.
15.	Triplet Spin- octupolar ZDW insu- lator. (Sec. 7.1.6)	\mathcal{J}_{1u}^o (2 triplets)	$\mathbf{T}_1, \mathbf{T}_2,$ $\mathbf{C}_3, \mathbf{S}_6,$ $\mathbf{C}'_2, \sigma_d, \mathbf{I},$ TR	See Eq. 7.21, 7.22	Both triplets corre- spond to the same phase. Fully gapped, Masses are non- compatible. Gapless modes appear for special linear combinations.
16.	Triplet Spin- octupolar ZDW insu- lator (Sec. 7.1.6)	\mathcal{J}_{2u}^o (2 triplets)	$\mathbf{T}_1, \mathbf{T}_2,$ $\mathbf{C}_3, \mathbf{S}_6,$ $\mathbf{C}'_2, \sigma_d, \mathbf{I},$ TR	See Eq.7.29, 7.30	Similar to entry No. 15 in this table, but different spin-octupole operators are ordered.

Table 4.6: The mixed phases (semimetals)

#	The Phase	Irrep	Broken Microscopic symmetries	Fermion Bilinear	Comments
17.	Singlet Spin-octupolar Néel semimetal. (Reflection odd) (Sec. 7.2.1)	\mathcal{A}_{1u}^o	TR, \mathbf{I} , $\sigma_{\mathbf{d}}$	See Eq. 7.31	Have semimetallic features. Can give rise to integer QH phase which is different from the ICI phase.
18.	Singlet Spin-octupolar Néel semimetal (Reflection even) (Sec. 7.2.1)	\mathcal{A}_{2u}^o	TR, \mathbf{I} , \mathbf{C}'_2	See Eq. 7.32	Similar to entry No.17 in this table, but different spin-octupole operator is ordered.
19.	Triplet Spin-octupolar StDW semimetal (Sec. 7.2.2)	\mathcal{F}_{1g}^o	$\mathbf{T}_1, \mathbf{T}_2,$ $\mathbf{C}_3, \mathbf{S}_6,$ $\mathbf{C}'_2, \sigma_{\mathbf{d}},$ TR	$-i \left\langle \bar{\chi} \left(\frac{-\Sigma_{13}\zeta_3 - \Sigma_{23}\zeta_2}{\sqrt{2}} \right) \chi \right\rangle,$ $-i \left\langle \bar{\chi} \left(\frac{\Sigma_{12}\zeta_2 - \Sigma_{13}\zeta_1}{\sqrt{2}} \right) \chi \right\rangle,$ $-i \left\langle \bar{\chi} \left(\frac{\Sigma_{23}\zeta_1 + \Sigma_{12}\zeta_3}{\sqrt{2}} \right) \chi \right\rangle$	Masses are non-compatible, 8 fermionic modes are gapless, number of gapless modes are same for all linear combinations of

					the masses within a given triplet.
20.	Triplet Spin-octupolar StDW semimetal (Sec. 7.2.2)	\mathcal{J}_{2g}^o	$\mathbf{T}_1, \mathbf{T}_2,$ $\mathbf{C}_3, \mathbf{S}_6,$ $\mathbf{C}'_2, \sigma_d,$ TR	$-i \left\langle \bar{\chi} \left(\frac{\Sigma_{13}\zeta_3 - \Sigma_{23}\zeta_2}{\sqrt{2}} \right) \chi \right\rangle$ $-i \left\langle \bar{\chi} \left(\frac{-\Sigma_{12}\zeta_2 - \Sigma_{13}\zeta_1}{\sqrt{2}} \right) \chi \right\rangle$ $-i \left\langle \bar{\chi} \left(\frac{-\Sigma_{23}\zeta_1 + \Sigma_{12}\zeta_3}{\sqrt{2}} \right) \chi \right\rangle$	Masses are non-compatible, 4 fermionic modes are always gapless, this number changes depending on the linear combinations of the masses.
21.	Triplet Spin-quadrupolar StDW semimetal. (Sec. 7.2.3)	\mathcal{J}_{2g}^e	$\mathbf{T}_1, \mathbf{T}_2,$ $\mathbf{C}_3, \mathbf{S}_6,$ $\mathbf{C}'_2, \sigma_d,$	$-i \left\langle \bar{\chi} \left(\frac{-\Sigma_1\zeta_2 + \Sigma_2\zeta_3}{\sqrt{2}} \right) \chi \right\rangle$ $-i \left\langle \bar{\chi} \left(\frac{\Sigma_3\zeta_2 + \Sigma_2\zeta_1}{\sqrt{2}} \right) \chi \right\rangle$ $-i \left\langle \bar{\chi} \left(\frac{\Sigma_3\zeta_3 + \Sigma_1\zeta_1}{\sqrt{2}} \right) \chi \right\rangle$	Similar to entry No.19 in this table, but different spin-quadrupole operators are ordered.
22.	Triplet Spin-quadrupolar StDW semimetal (Sec. 7.2.3)	\mathcal{J}_{1g}^e	$\mathbf{T}_1, \mathbf{T}_2,$ $\mathbf{C}_3, \mathbf{S}_6,$ \mathbf{C}'_2, σ_d	$-i \left\langle \bar{\chi} \left(\frac{-\Sigma_1\zeta_2 - \Sigma_2\zeta_3}{\sqrt{2}} \right) \chi \right\rangle$ $-i \left\langle \bar{\chi} \left(\frac{-\Sigma_3\zeta_2 + \Sigma_2\zeta_1}{\sqrt{2}} \right) \chi \right\rangle$ $-i \left\langle \bar{\chi} \left(\frac{\Sigma_3\zeta_3 - \Sigma_1\zeta_1}{\sqrt{2}} \right) \chi \right\rangle$	Similar to entry No.20 in this table, but different spin-octupole operators are ordered.
23.	Doublet spin-quadrupolar	\mathcal{E}_g^e	$\mathbf{C}'_2, \sigma_d,$ $\mathbf{C}_3, \mathbf{S}_6$	See Eq. 7.60	Some bands remain gapless. Can give rise to integer QH

	ferro semimetal. (Sec. 7.2.4)				phase different the ICI phase
24.	Doublet Spin- octupolar ferro semimetal. (Sec. 7.2.5)	\mathcal{E}_g^o	$\mathbf{C}'_2, \sigma_d,$ $\mathbf{C}_3, \mathbf{S}_6,$ TR	See Eq. 7.64	Some bands remain gapless

Chapter 5

Group-1 : Chiral masses

In this chapter, we discuss the four chiral masses which are given in Eqs. 4.10a and 4.10b. These are divided into a singlet (\mathcal{A}_{2g}^o) (TR and reflection odd) and a triplet (\mathcal{J}_{1g}^e) (TR and inversion even) under the space-group symmetries while they are all singlets under the flavor SU(4). The details of their transformations under the microscopic symmetries are given in Appendix. A.7. Here we first discuss the details of the singlet mass and then the triplet masses.

5.1 The SU(8) symmetric Integer Chern Insulator

The SU(8) singlet mass,

$$\Delta_{ICI} = -i\langle\bar{\chi}\chi\rangle, \quad (5.1)$$

given by Eq. 4.10a is odd under the action of \mathbb{T} , \mathbf{C}'_2 and $\sigma_{\mathbf{a}}$. This suggests that this mass is the analog of the Chern mass for graphene [136, 137] which shows the integer quantum Hall effect and hence represents the ICI phase. Indeed, minimally coupling the electrons in the massive Dirac action (Eq. 4.3) for the above Chern mass, Δ_{ICI} to a U(1) probe gauge field, A_μ , that couples to the electronic charge and integrating out the gapped fermions, we get a U(1) Chern-Simons term with the (Euclidean) Lagrangian density :

$$\mathcal{L}_{\text{CS}} = i\frac{N_F \text{Sgn}[\Delta_{ICI}]}{4\pi} \epsilon^{\mu\nu\lambda} A_\mu \partial_\nu A_\lambda \quad (5.2)$$

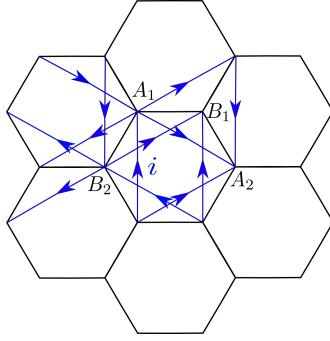


Figure 5.1: The mean field hopping model for the Integer Chern insulator. The second neighbour hoppings (in blue) are generated via the spontaneous symmetry breaking and the hopping amplitudes along the directions of the arrows (in local basis) are $i = \sqrt{-1}$. The same hopping pattern also holds for the singlet spin-octupole Hall mass leading to the octupolar Hall effect (Eq. 6.5), except in that case the hopping amplitude is given by $i\Sigma_{45}$.

where $N_F = 4$ is the number of SU(4) flavors (*i.e.* number of four component Dirac fermion fields). Thus, all the flavors contribute the same amount to the charge Hall conductivity resulting in, $\sigma_{xy} = N_F \frac{e^2}{2\pi}$ [138].

The nature of symmetry breaking can be analysed by considering the low energy projection of the microscopic current operators on the lattice [136, 139]. In particular, starting with the microscopic orbitals in the local basis, $\phi(\mathbf{z}_s)$, given by Eq. 2.34, the hopping operator on the next nearest neighbour (NNN) bonds— say the blue bond in Fig. 5.1 from site B_2 to B_1 — is given by [136]

$$\mathcal{B}_{B_2B_1} = \phi^\dagger(\mathbf{z}_{B_1})\phi(\mathbf{z}_{B_2}) \quad (5.3)$$

The form in the global basis (in terms of the $j = 3/2$ orbitals) can be easily obtained via Eq. 2.34 and using the forms of $\mathcal{G}(\mathbf{z}_s)$ given in Appendix A.4.

In the low energy limit, Eq. 5.3 is equal to

$$\mathcal{B}_{B_2B_1} = \frac{1}{2\sqrt{3}}\bar{\chi}\chi + \dots \quad (5.4)$$

where \dots represent higher order terms. Therefore, for $\Delta_{ICI} \neq 0$, we have an imaginary second neighbour hopping whose sign structure is given by Fig. 5.1. This leads to finite bond current such that the total gauge invariant loop current per hexagon is indeed zero (mod 2π). The loop currents, therefore, form a Z_2 order parameter proportional to the mass, Δ_{ICI} . Such Z_2 order parameters allow domain walls as one-dimensional topological

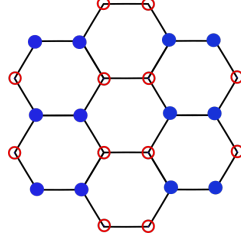


Figure 5.2: Stripy CDW for $-i\langle\bar{\chi}\zeta_1\chi\rangle \neq 0$. Here, red circles and blue dots represent opposite charge densities at the honeycomb sites.

defects in two-dimensional systems across which the sign of the mass changes. As is evident from Eq. 5.2, the edge modes have opposite chirality in the two cases and hence the domain wall is associated with chiral gapless edge modes that are exponentially localised along the domain wall [140].

5.2 The SU(4) symmetric stripy charge density wave Insulator

The three other SU(4) flavour invariant masses given by Eq. 4.10b form a triplet (\mathcal{J}_{1g}^e) which is even under TR symmetry, \mathbb{T} as well as inversion, \mathbf{I} , about the plaquette centre. These are given by

$$\{-i\langle\bar{\chi}\zeta_1\chi\rangle, -i\langle\bar{\chi}\zeta_2\chi\rangle, -i\langle\bar{\chi}\zeta_3\chi\rangle\}. \quad (5.5)$$

They transform into each other under various lattice rotations and reflections as a triplet as shown in Appendix A.7. ζ_i ($i = 1, 2, 3$) of course generates an SU(2) (see Eq. 3.9) which is broken down by the lattice symmetries to a triplet for the space group.

The three bilinears have the same symmetry as that of the three stripy CDW order as shown in Fig. 5.2 for $-i\langle\bar{\chi}\zeta_1\chi\rangle$. The other two can be obtained by \mathbf{C}_3 rotations. Indeed, the analysis of the above three fermion bilinears in the global basis (Eq. 2.24) confirms the symmetry analysis in identifying the above stripy CDW masses. In particular, starting with the electron operators in the global basis *i.e.*, ψ (Eq. 2.24), the projected charge

density operators on different sub-lattices have the following form :

$$:\psi^\dagger(\mathbf{r}_S)\psi(\mathbf{r}_S): = \begin{cases} -i\bar{\chi}\xi_1\chi & \text{For } \mathcal{S} = B_2, A_2 \\ i\bar{\chi}\xi_1\chi & \text{For } \mathcal{S} = A_1, B_1 \end{cases} \quad (5.6)$$

where $:\mathcal{O}:$ denotes normal ordering. Integrating out the gapped fermions in the presence of the mass does not lead to a finite charge Hall response.

The three matrices $\gamma_0\zeta_i$ ($i = 1, 2, 3$) pairwise anti-commute with each other such that the three stripy CDW masses are compatible¹ in the sense that the fermion gap does not close as the three masses are rotated into each other under the chiral SU(2) (see Eq. 3.9) transformations generated by $e^{i\theta\hat{n}\cdot\zeta}$. This would suggest that the order parameter manifold is a unit sphere, \mathcal{S}^2 , similar to collinear magnetic ordering (with one important difference that the present order parameter is even under TR unlike magnetic order). The above SU(2) is, however, broken down by the lattice symmetries, which, in terms of the order parameter, selects out symmetry-allowed points on the sphere, \mathcal{S}^2 . In particular, the leading order anisotropy of the form

$$\mathcal{L}_{aniso} \sim -\omega_1\Delta_1\Delta_2\Delta_3 + \omega_2(\Delta_1^4 + \Delta_2^4 + \Delta_3^4) \quad (5.7)$$

is symmetry allowed (see Table A.4) in the effective action with Δ_i being the amplitude for the three components of the CDW (Eq. 5.5). This reduces the order parameter manifold to discrete points on the sphere. The details of the ordering depend on the signs of the couplings ω_1 and ω_2 . Due to the presence of the third-order invariant, the transition out of the semimetal is expected to be first-order. We discuss the details of this transition in Chapter 8.3.

We conclude the discussion of the chiral masses with two points. First, it is useful to compare the four chiral masses with the case of spinless fermions on the honeycomb lattice with π -flux at one-quarter filling presented in appendix. A.11. The presence of the π -flux breaks up the chiral space as $\mathbf{4} = \mathbf{1} \oplus \mathbf{3}$, as opposed to graphene where the chiral space is decomposed as $\mathbf{4} = \mathbf{1} \oplus \mathbf{1} \oplus \mathbf{2}$. In the present case where the π -flux is a consequence of SOC, the above SU(4) singlet masses can be thought of as four copies

¹Two mass matrices are compatible if they anti-commute with each other. The three matrices $\gamma_0\zeta_i$ anti-commute with each other and hence are mutually compatible

of the spinless case in Appendix [A.11](#). Second, while the three triplet stripy masses are compatible with each other, *i.e.*, the respective mass matrices mutually anticommute, all of them are incompatible with the singlet ICI mass since the corresponding matrices (Table [4.2](#)) pairwise commute. This ensures a phase transition [[21](#)] between the two phases which is accompanied by the change in the nature of broken symmetry as well as the Chern-Simons level (Eq.[5.2](#)) from $N_F = 4$ (in the ICI) to $N_F = 0$ (in the stripy CDW).

Chapter 6

Group-2 : The Flavor masses

In this chapter, we discuss the 15 flavour masses, which are of the form $-i\langle\bar{\chi}\Sigma_i\chi\rangle$. These are divided into six irreducible representations by microscopic symmetries that are given by Eqs. 4.21, 4.22, and 4.23. Each of these 15 masses individually breaks the flavor SU(4) down to $U(1) \otimes SO(4)$. However, linear combinations of them can reduce the symmetry further as we discuss below in the case of each subgroup. A notable feature of these residual sub-groups is that the generators depend on the particular *direction* of the mass matrix and hence are *locally* defined in the space of the order parameters. This is exactly like the case of a collinear ferromagnet/antiferromagnet where the particular generator of the residual U(1) depends on the direction of the ordering of the magnetic moments in the spin-space. We shall study the nature of these for each of the six phases separately, including the action of the lattice symmetries— including the spontaneously broken ones— as well as the nature of the residual symmetry group.

Out of the 15 masses, the ten TR even ones (Eq. 4.11) correspond to four different types of spin-octupole Hall phases, while the five TR odd ones (Eq. 4.12) represent two spin-quadrupole Hall phases. We explain their features in turn.

6.1 Quantum spin-octupole Hall insulators

6.1.1 \mathcal{A}_{1g}^e Singlet mass

For the singlet (Eq. 4.21a), the mass is given by the fermion bilinear

$$\mathcal{A}_{1g}^e : -i\langle\bar{\chi}\Sigma_{45}\chi\rangle \quad (6.1)$$

which fully gaps out all the fermions. This breaks the SU(4) flavour symmetry down to U(1) \otimes SO(4) with the U(1) being generated by Σ_{45} and SO(4) by six other Σ_i 's that commute with Σ_{45} , *i.e.*, $\{\Sigma_1, \Sigma_2, \Sigma_3, \Sigma_{12}, \Sigma_{23}, \Sigma_{13}\}$.

In the microscopic $j = 3/2$ basis (the transformation of the Σ operators from the local to global basis is given in Table A.1), the Σ_{45} operator is given by

$$\Sigma_{45} = -\frac{4}{3\sqrt{3}} \left(J_x J_y J_z + J_y J_z J_x + J_z J_x J_y - \frac{15i}{8} \right) \quad (6.2)$$

where (J_x, J_y, J_z) are the $j = 3/2$ spin operators in the global basis (see Table A.1). Since Σ_{45} is a product of three spin operators, we call it a spin-octupole operator.

Starting with the Euclidean Dirac action in the presence of the mass term (Eq. 4.3), we can diagonalise the spinors χ in terms of the eigenstates of Σ_{45} . The eigenstates consist of two pairs of Kramers doublets. The two members of each doublet have opposite eigenvalues of Σ_{45} , *i.e.* ± 1 . Each of the modes contributes to finite Hall edge current, leading to *spin-octupole* filtered Hall edge modes similar to the quantum spin-Hall effect [134]. The two TR partners carry current in the opposite direction and backscattering within each TR pair is disallowed by TR symmetry – again just like quantum spin Hall effect. However, the scattering between the oppositely moving edge modes belonging to the two different Kramers doublets is not allowed because they necessarily have opposite eigenvalues of Σ_{45} .

A more formal derivation of the resultant symmetry-protected CS action is obtained by coupling probe charge and spin-octupolar gauge fields to Eq. 4.3, *i.e.*, considering

$$S[A_c, A_o] = -i \int d^2\mathbf{r}d\tau \bar{\chi}(\mathbf{r}) [v_F \not{D} - \Delta \Sigma_{45}] \chi(\mathbf{r}) \quad (6.3)$$

where

$$\mathcal{D} = \gamma^\mu (i\partial_\mu - A_{c,\mu} - \Sigma_{45}A_{o,\mu}) \quad (6.4)$$

where \mathbf{A}_c and \mathbf{A}_o are charge and spin-octupole probe gauge fields respectively. Then integrating out the fermions leads to the mutual CS term given by

$$S_{CS}^{mutual} = i\frac{N_F}{2\pi} \text{sgn}(\Delta) \int d^3x \epsilon^{\mu\nu\lambda} A_{c,\mu} \partial_\nu A_{o,\lambda} \quad (6.5)$$

which characterises the *quantum spin-octupolar Hall response*.

The lattice version of this mass can be analyzed in a similar way as done for the ICI mass. For that, we consider microscopic hopping operators on one of the NNN bonds and project that to the low-energy sector. We again take the blue bond in Fig. 5.1 from site B_2 to B_1 and write the following hopping operator

$$\mathcal{B}_{B_2B_1}^{(45)} = \phi^\dagger(\mathbf{z}_{B_1}) \Sigma_{45} \phi(\mathbf{z}_{B_2}). \quad (6.6)$$

In terms, of the low-energy spinors, this has the following form

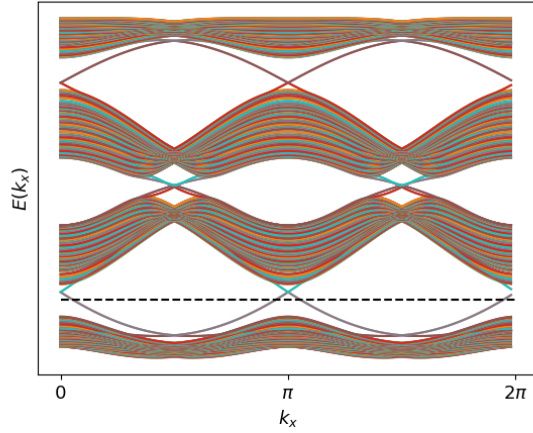
$$\mathcal{B}_{B_2B_1}^{(45)} = \frac{1}{2\sqrt{3}} \bar{\chi} \Sigma_{45} \chi + \dots \quad (6.7)$$

Thus the imaginary part of this hopping operator is proportional to the order parameter in this phase. This shows that there are non-zero bond currents in this phase. The hopping pattern on the other bonds are same as shown in Fig. 5.1 with the hopping amplitudes being $i\Sigma_{45}$ instead of i .

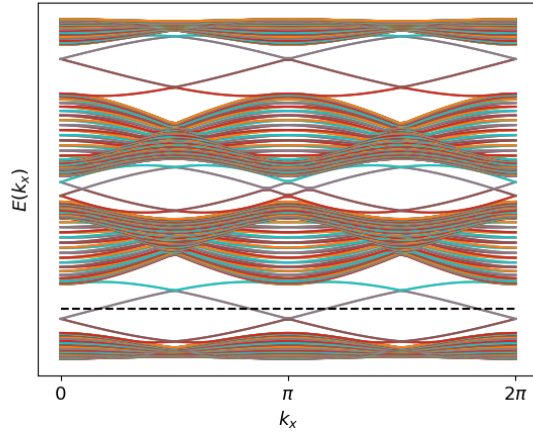
The lattice Hamiltonian can now be used to check for the edge modes by obtaining the spectrum with open boundary conditions. The spectrum on a cylinder for the zig-zag and armchair edges are shown in Fig. 6.1.

Not surprisingly, in Fig. 6.1, such edge modes are also observed for both 3/4th filling as well as 1/2 filling. While the case of 3/4th filling is expected to result from the microscopic particle-hole transformation that maps $1/4 \leftrightarrow 3/4$, the physics of 1/2 filling would be interesting to understand in future.

Similar to the ICI phase, the order parameter for the spin-octupole Hall phase is a Z_2 field and leads to gapless fermionic modes associated with the domain walls of the



(a) Zig-zag edge



(b) Armchair edge

Figure 6.1: Spectrum for $-i\bar{\chi}\Sigma_{45}\chi$ with zig-zag and armchair edges. Both of these plots show gapless states at $1/4th$ filling (shown by black dashed line). To get this spectrum, we consider a honeycomb lattice with cylindrical geometry where the edges of the cylinder have zigzag or armchair-like boundaries. Here k_x is lattice momentum along the periodic direction. We take 32 magnetic unit cells along the length of the cylinder to perform this numerical calculation.

order parameter. Note, however, that such a field is TR even and is symmetric under all lattice transformations. Thus, this mass is naturally allowed by the microscopics. This is analogous to the Kane-Mele mass [134] for graphene, which is symmetry allowed but is energetically suppressed due to the very small value of the SOC in that case.

6.1.2 The \mathcal{J}_{1g}^e triplet masses

The TR even triplet in Eq. 4.21b consists of three masses of the form

$$\mathcal{J}_{1g}^e : \begin{cases} -i \langle \bar{\chi} \Sigma_{12} \chi \rangle \\ -i \langle \bar{\chi} \Sigma_{13} \chi \rangle \\ -i \langle \bar{\chi} \Sigma_{23} \chi \rangle \end{cases} \quad (6.8)$$

which fully gaps out the Dirac fermions. In terms of the $j = 3/2$ operators, the three mass matrices are given by :

$$\Sigma_{\alpha\beta} = \frac{7\epsilon^{\alpha\beta\gamma}}{3} \left(J_\gamma - \frac{4}{7} J_\gamma^3 \right) \quad (6.9)$$

where $\alpha, \beta, \gamma = 1, 2, 3$ with $\alpha \neq \beta$ such that they are a mixture of dipole and spin-octupole operators. Following Eq. 4.3, the generic mass term is given by

$$-i (\Delta_1 \bar{\chi} \Sigma_{23} \chi + \Delta_2 \bar{\chi} \Sigma_{13} \chi + \Delta_3 \bar{\chi} \Sigma_{12} \chi) \quad (6.10)$$

where Δ_i ($i = 1, 2, 3$) are the weights for each of the three components. Hence such masses lie on a 2-sphere with directional cosines given by $\cos \theta_i = \Delta_i / \sqrt{\Delta_1^2 + \Delta_2^2 + \Delta_3^2}$ where the different points can be rotated into each other via the SU(2) symmetry generated by Eq 4.18. With reference to Eq. 6.8, it is now clear that this SU(2) corresponds to the continuous rotation amongst the three spin-octupoles.

At each point on this *mass* sphere, the residual symmetry is $U(1) \otimes SO(4)$. However, the particular generators of this residual symmetry group depend on the location of the point and are related to each other by the same SU(2) transformations (Eq. 4.18). For example, the generators of the residual symmetry at the point [001] are given by

$$\{\Sigma_{12}, \Sigma_3, \Sigma_4, \Sigma_5, \Sigma_{34}, \Sigma_{35}, \Sigma_{45}\} \quad (6.11)$$

where the first generator corresponds to the U(1) (which is left-over of the SU(2) (Eq. 4.18)) and the rest generate the SO(4). The residual groups at other points on the mass sphere are obtained via SU(2) rotations generated by Eq. 4.18.

The phase breaks the spin-octupole SU(2) symmetry (Eq. 4.18) spontaneously and results in quantum spin-octupole Hall effect that is protected by $U(1) \rtimes Z_2^{TR}$ and is similar to the quantum Spin Hall phase obtained via spontaneously broken spin-rotation symmetry discussed in Ref. [141] with interesting differences (see below). The presence of non-trivial spin-octupole filtered edge states is confirmed by calculating the mutual Hall response similar to Eq. 6.3 for the singlet case above which leads to the mutual Chern-Simons action similar to Eq. 6.5.

The presence of the gapless edge-modes can also be checked by going back to the mean-field Lattice Hamiltonian in presence of the lattice version of the mass (not shown). The lattice version of the Hamiltonian corresponding to the continuum bilinear $-i\langle\bar{\chi}\Sigma_{12}\chi\rangle$ is the same as that for the quantum spin-octupolar Hall mass given in Eq. 6.6 with the hopping matrix (i.e., Σ_{45}) replaced by Σ_{12} . An interesting fallout of the present implementation of the symmetry is the fact that the three component spin-octupolar order-parameter allows for Skyrmion configurations. In Chapter 8.1, we show that the condensation of these skyrmions leads to realization of a novel charge-4e superconducting phase.

6.1.3 The \mathcal{J}_{1u}^e and \mathcal{J}_{2u}^e triplet masses

The two inversion odd TR even triplets (Eq. 4.22) are given by

$$\mathcal{J}_{1u}^e : \begin{cases} -i \langle \bar{\chi} \Sigma_{34} \chi \rangle \\ -i \langle \bar{\chi} \frac{\Sigma_{14} + \sqrt{3}\Sigma_{15}}{2} \chi \rangle \\ -i \langle \bar{\chi} \frac{\Sigma_{24} - \sqrt{3}\Sigma_{25}}{2} \chi \rangle \end{cases} \quad (6.12)$$

$$\mathcal{J}_{2u}^e : \begin{cases} -i \langle \bar{\chi} \Sigma_{35} \chi \rangle \\ -i \langle \bar{\chi} \frac{\sqrt{3}\Sigma_{14} - \Sigma_{15}}{2} \chi \rangle \\ -i \langle \bar{\chi} \frac{\sqrt{3}\Sigma_{24} + \Sigma_{25}}{2} \chi \rangle \end{cases} \quad (6.13)$$

In terms of the $j = 3/2$ spin matrices, we have

$$\Sigma_{34} = \frac{2}{3} \left(J_z^3 - \frac{13}{4} J_z \right) \quad (6.14a)$$

$$-\frac{1}{2} \Sigma_{14} - \frac{\sqrt{3}}{2} \Sigma_{15} = \frac{2}{3} \left(J_x^3 - \frac{13}{4} J_x \right) \quad (6.14b)$$

$$-\frac{\sqrt{3}}{2} \Sigma_{25} + \frac{1}{2} \Sigma_{24} = -\frac{2}{3} \left(J_y^3 - \frac{13}{4} J_y \right) \quad (6.14c)$$

for the three \mathcal{F}_{1u}^e masses and

$$\begin{aligned} \Sigma_{35} = \frac{2}{3\sqrt{3}} & \left[(J_x^2 J_z + J_x J_z J_x + J_z J_x^2) \right. \\ & \left. - (J_y^2 J_z + J_y J_z J_y + J_z J_y^2) \right] \end{aligned} \quad (6.15a)$$

$$\begin{aligned} \frac{\sqrt{3}}{2} \Sigma_{24} + \frac{1}{2} \Sigma_{25} = \frac{2}{3\sqrt{3}} & \left[(J_x^2 J_y + J_x J_y J_x + J_y J_x^2) \right. \\ & \left. - (J_z^2 J_y + J_z J_y J_z + J_y J_z^2) \right] \end{aligned} \quad (6.15b)$$

$$\begin{aligned} \frac{\sqrt{3}}{2} \Sigma_{14} - \frac{1}{2} \Sigma_{15} = \frac{2}{3\sqrt{3}} & \left[(J_y^2 J_x + J_y J_x J_y + J_x J_y^2) \right. \\ & \left. - (J_z^2 J_x + J_z J_x J_z + J_x J_z^2) \right]. \end{aligned} \quad (6.15c)$$

for the \mathcal{F}_{2u}^e triplet. Hence, these masses represent two different sets of spin-octupole order. Note that while components of the two triplets can be rotated into each other by a U(1) rotation generated by Σ_{45} , the two triplets represent different phases since they have different transformations under lattice reflection, \mathbf{C}'_2 .

The three masses in each of the triplets are incompatible, *i.e.*, the matrices (m_1, m_2, m_3) in Eq. 6.14 or 6.15 do not mutually pair-wise anticommute. This results in an interesting structure for the residual symmetry in the resultant massive phases. For a generic linear combination of the three masses, similar to Eq. 6.10, but now for the \mathcal{F}_{1u}^e and \mathcal{F}_{2u}^e triplets, *i.e.*,

$$-i (\Delta_1 \bar{\chi} m_1 \chi + \Delta_2 \bar{\chi} m_2 \chi + \Delta_3 \bar{\chi} m_3 \chi), \quad (6.16)$$

where m_1, m_2, m_3 are the three matrices in Eq. 6.14 or 6.15, the flavour SU(4) is broken down to U(1) \otimes U(1) \otimes U(1). However, to get more insights, it is useful to diagonalise the bilinear in Eq. 6.16 for a generic point on the unit sphere described by the directional

cosines $\Delta_i/\sqrt{\Delta_1^2 + \Delta_2^2 + \Delta_3^2}$ (middle panel of Fig. 6.2) to obtain

$$-\bar{\chi}'\mathcal{D}\chi', \quad (6.17)$$

where χ' are the fermions in the diagonalised basis and

$$\mathcal{D} = \begin{pmatrix} a_1\sigma_3 & 0 \\ 0 & a_2\sigma_3 \end{pmatrix} \otimes \zeta_0, \quad (6.18)$$

with a_1, a_2 are two real functions of Δ_i s, σ_3 is the third Pauli matrix, and ζ_0 is the identity matrix that acts in the valley-band space of the spinors, *i.e.* in the chiral SU(2) space (Eq. 3.9).

In this diagonalised basis, it is easy to see that there are three linearly independent matrices (other than the identity matrix) that commute with the \mathcal{D} matrix in Eq. 6.18. These are this matrix, \mathcal{D} , itself and

$$\begin{pmatrix} \sigma_3 & 0 \\ 0 & 0 \end{pmatrix} \otimes \zeta_0, \quad \begin{pmatrix} 0 & 0 \\ 0 & \sigma_3 \end{pmatrix} \otimes \zeta_0. \quad (6.19)$$

The above three matrices generate the residual $U(1) \otimes U(1) \otimes U(1)$ symmetry on generic points on the sphere in the middle panel of Fig. 6.2 like C and D . The first $U(1)$ results in conserved flavour (spin-octupole) currents along the NNN bonds with a flow pattern similar to that shown in Fig. 5.1. For such generic points, the fermions are fully gapped, with each gapped band being 4-fold degenerate (spectrum (b) in the top panel of Fig. 6.2). We can calculate the edge response, which is given by a mutual CS action similar to Eq. 6.5. These spin-octupole filtered edge modes are again protected by the $U(1) \rtimes Z_2^{TR}$ as in the case of \mathcal{F}_{1g}^e mass discussed above.

Interestingly, on putting two of the Δ_i s to zero, such as the point A in Fig. 6.2 (middle panel), while the above conclusions survive, the gapped bands have an enhanced 8-fold degeneracy (as shown in (a) of the top panel of Fig. 6.2) due to enhanced residual flavour symmetry of $U(1) \otimes SO(4)$. From the perspective of Eq. 6.18, the numbers a_1 and a_2 become equal at these points such that we can further basis transform $\mathcal{D} \rightarrow (\sigma_3 \otimes \sigma_0) \otimes \zeta_0$. Now there are six generators in addition to \mathcal{D} that commute with the mass which are

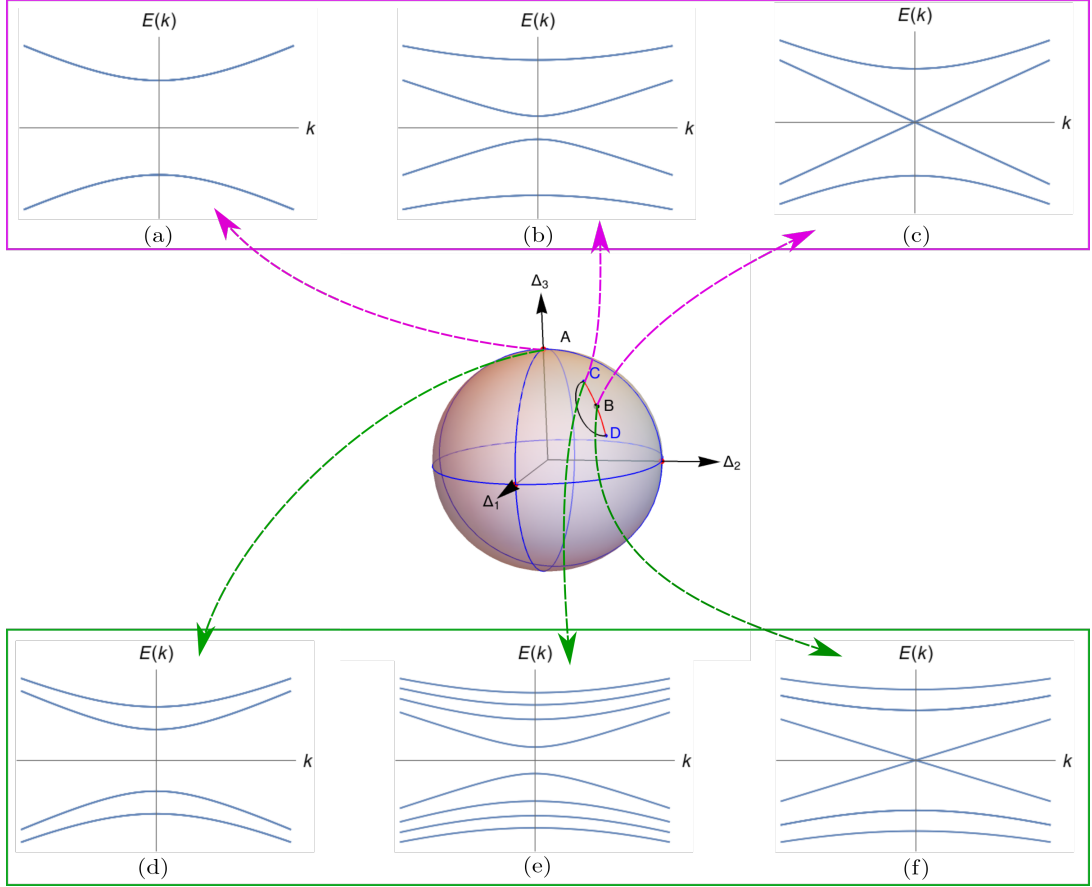


Figure 6.2: Figure shows the energy spectrum of low-energy fermions along the $k_x = k_y$ line for different combinations of the masses in a triplet. Any linear combination of the masses in a particular triplet can be represented on the surface of a unit sphere shown at the center. The energy spectrum shown in the upper panel of this figure corresponds to the \mathcal{J}_{1u}^e triplets in Eq. 6.12, 7.15 and the \mathcal{J}_{2u}^e triplets in Eq. 6.13, 7.17. The spectrum in (a), (b) and (c) in the upper panel correspond to the spectrum at the points A, C and B on the sphere. Similarly, the spectrum in the bottom panel corresponds to the \mathcal{J}_{1u}^o and \mathcal{J}_{2u}^o triplets in Eq. 7.21, 7.22, 7.29, 7.30. Here again, the spectrum in (d), (e) and (f) correspond to the spectrum at the points A, C, and B on the sphere.

given by

$$\begin{pmatrix} \sigma_i & 0 \\ 0 & \sigma_i \end{pmatrix} \otimes \zeta_0, \quad \begin{pmatrix} \sigma_i & 0 \\ 0 & -\sigma_i \end{pmatrix} \otimes \zeta_0. \quad (6.20)$$

with $i = 1, 2, 3$. This generates $SU(2) \otimes SU(2) \equiv SO(4)$ in addition to the $U(1)$ generated by \mathcal{D} itself.

A much more interesting situation arises when one moves from point C (or D) to point B (in the middle panel of Fig. 6.2) which is characterised by

$$|\Delta_1| = |\Delta_2| = |\Delta_3|, \quad (6.21)$$

and is one of the eight isolated special points.

At these points, a_2 in Eq. 6.18 becomes zero. We have assumed $a_1 > a_2$ without any loss of generality. As a result, four flavours of fermions belonging to the a_2 block become gapless while four others belonging to the a_1 block remain gapped. This leads to a partially gapped state. The resultant spectrum is shown in (c) of the top panel in Fig. 6.2. It is clear that at these special points when $a_2 = 0$, in addition to \mathcal{D} and the two matrices given by Eq. 6.19, two additional matrices

$$\begin{pmatrix} 0 & 0 \\ 0 & \sigma_1 \end{pmatrix} \otimes \zeta_0, \quad \begin{pmatrix} 0 & 0 \\ 0 & \sigma_2 \end{pmatrix} \otimes \zeta_0 \quad (6.22)$$

also commute with the mass matrix at this special point. The above two matrices, along with the last one of Eq. 6.19, generate a $SU(2)$ such that at these isolated points the symmetry is given by $U(1) \otimes U(1) \otimes SU(2)$ and it is this last $SU(2)$ which protects a subset of gapless Dirac fermions. On moving away from these special points infinitesimally, the $SU(2)$ is broken down to $U(1)$ as $a_2 \neq 0$ and this gaps out the remaining fermions (spectrum (b) in the top panel of Fig. 6.2). Such isolated gapless points in the parameter space serve as examples of *unnecessary quantum critical points* which we discuss in detail in Chapter 8.2.

6.2 Quantum spin-quadrupole Hall insulators

Turning to the five TR odd masses that form the \mathcal{E}_u^o doublet (Eq. 4.15) and \mathcal{J}_{2g}^o triplet (Eq. 4.16), the respective masses are given by

$$\mathcal{E}_u^o : \begin{cases} -i\langle\bar{\chi}\Sigma_4\chi\rangle \\ -i\langle\bar{\chi}\Sigma_5\chi\rangle \end{cases} \quad (6.23)$$

and

$$\mathcal{J}_{2g}^o : \begin{cases} -i\langle\bar{\chi}\Sigma_1\chi\rangle \\ -i\langle\bar{\chi}\Sigma_2\chi\rangle \\ -i\langle\bar{\chi}\Sigma_3\chi\rangle \end{cases} \quad (6.24)$$

While the doublet (Table A.3) is odd under inversion symmetry and does not break lattice translation, the triplet (Table A.4) is even under inversion, but breaks lattice translation. Transformation under other lattice symmetries is given in respective tables. Further in terms of the IR symmetries, each of the two classes breaks SO(5) down to U(1) \otimes SU(2) as mentioned above (Eq. 4.17 and 4.18) – the doublet (triplet) is a U(1) (SU(2)) singlet.

The two classes of masses fully gap out the fermionic spectrum and break the SU(4) flavour symmetry. Notably, in terms of the spin operators we have

$$\Sigma_4 = \frac{1}{\sqrt{3}}(J_x^2 - J_y^2) \quad \text{and} \quad \Sigma_5 = J_z^2 - \frac{5}{4}. \quad (6.25)$$

for the doublet and

$$\begin{aligned} \Sigma_1 &= (J_y J_z + J_z J_y)/\sqrt{3}, \\ \Sigma_2 &= (J_z J_x + J_x J_z)/\sqrt{3}, \\ \Sigma_3 &= (J_y J_x + J_x J_y)/\sqrt{3}, \end{aligned} \quad (6.26)$$

for the triplet, all of which correspond to spin-quadrupoles. In fact, as we show below, the two correspond to different spin-quadrupole Hall phase protected by U(1) symmetry. Such a phase is an interesting generalisation of the QSH phase, as the quadrupole Hall

phase is TR odd, unlike the QSH phase. This can be traced to the fact that unlike the spin-dipole and the spin-octupole currents, the spin-quadrupole currents are odd under TR.

The resultant non-zero Hall response can be obtained by performing a calculation similar to Sec. 6.1.1. Sitting deep inside the gapped phase with $\langle -i\bar{\chi}\Sigma_4\chi \rangle \neq 0$ (say), we can introduce a spin-quadrupole probe gauge field \mathbf{A}_q in addition to a probe charge field, \mathbf{A}_c , and integrating out the fermions results in a mutual CS action

$$S_{CS}^{mutual} = i\frac{N_F}{2\pi} \text{sgn}(\Delta) \int d^3x \epsilon^{\mu\nu\lambda} A_{c,\mu} \partial_\nu A_{q,\lambda}. \quad (6.27)$$

Such that there is a spin-quadrupolar edge current (corresponding to Σ_4). As in the case of the previously discussed spin-octupolar Hall phases, the presence of edge modes in the case of this mass can be confirmed by taking a mean-field lattice Hamiltonian and performing a band structure calculation on a finite-sized lattice. Similar results can be obtained for the triplet.

Focusing on the \mathcal{E}_u^o doublet, we note that it breaks the SU(4) flavour symmetry to U(1) \otimes SO(4). E.g., for $-i\langle \bar{\chi}\Sigma_4\chi \rangle \neq 0$, the U(1) is generated by Σ_4 and the SO(4) is by $\{\Sigma_{12}, \Sigma_{13}, \Sigma_{15}, \Sigma_{23}, \Sigma_{25}, \Sigma_{35}\}$. Since the two-component order parameter (Eq. 6.23) lives on a circle, it supports point defects– vortices characterized by the winding number. More precisely, consider the mass term

$$-i(\Delta_1\bar{\chi}\Sigma_4\chi + \Delta_2\bar{\chi}\Sigma_5\chi), \quad (6.28)$$

such that under the U(1) transformation generated by Σ_{45} for an angle θ ,

$$\Delta = \Delta_1 + i\Delta_2 \rightarrow \Delta e^{i\theta}. \quad (6.29)$$

At the core of such a vortex, the TRS is restored, and hence, for a *fat* vortex with a sizeable core one expects quadrupole-filtered zero modes around the vortex core. Further following each such unit vortex is expected to trap $N_F/2$ quanta of electronic charge [21, 142]. The transition mediated by the proliferation and condensation of such vortices are then expected to be novel [21, 143] and requires further understanding.

6.3 Probing Multipolar Edge Modes

A key challenge lies in the experimental detection of these phases where the edge modes carry spin-octupolar or quadrupolar moments. Among the spin-octupolar quantum Hall phases discussed, one subset (e.g., the $\mathcal{A}1g^e$ singlet) hosts edge modes that conduct a purely octupolar current (Eq. 6.2). Another subset exhibits edge modes that carry a combination of spin and octupolar currents (e.g., the $\mathcal{J}1u^e$ phase). The latter category of phases might be detectable using techniques analogous to those used for the conventional spin Hall effect, particularly the inverse spin Hall effect (ISHE) [144, 145]. ISHE involves transforming a spin current into a measurable electrical voltage signal. However, detecting the quadrupolar Hall phases poses a more formidable challenge, as there are no known experimental methods to probe or measure currents carrying quadrupolar moments.

Chapter 7

Group-3 : The Mixed masses

We now turn to the structure of the mixed masses, which are obtained by nontrivial contributions from both the flavour and chiral sectors. The complex structure of the mass matrices and the intricate locking of the spin and real space symmetry transformations result in the rich properties of the resultant phases, which we now discuss in detail. There are 45 masses divided into 19 irreducible representations summarised in Eq. 4.24 and they give rise to 16 different phases. These are generic density wave phases, which can be divided into two sub-sets depending on whether the fermions are generically fully gapped (insulators) or partially gapped (semimetals). Two of the insulators have edge modes whose signature is evident from appropriate Chern-Simons terms. In most of the insulators and semimetals, the components of some of the multiplets are incompatible, and hence they lead to gapless sub-manifold as the components of the masses are tuned (similar to the spin-octupole flavour triplet discussed in Sec. 6.1.3).

7.1 Density wave Insulators

There are 27 such mass terms divided into two singlets ($\mathcal{A}_{1g}^e, \mathcal{A}_{2g}^o$), two doublets ($2\mathcal{E}_u^o$) and seven triplets ($\mathcal{J}_{2g}^o, \mathcal{J}_{1u}^e, \mathcal{J}_{2u}^e, 2\mathcal{J}_{1u}^o, 2\mathcal{J}_{2u}^o$). While the singlets and three triplets ($\mathcal{J}_{2g}^o, \mathcal{J}_{1u}^e, \mathcal{J}_{2u}^e$) give rise to *five* distinct phases, the two doublets and the other two triplets with a multiplicity of two, *i.e.*, ($2\mathcal{J}_{1u}^o, 2\mathcal{J}_{2u}^o$) only give rise to *three* distinct phases since members of the same representation can be mixed without breaking any further symmetries. Thus they give rise to a total of *eight* distinct flavour density wave insulating phases – two of which have edge modes.

7.1.1 Ising ferro spin-quadrupolar insulator

The TR even mass for the \mathcal{A}_{1g}^e lattice singlet in Eq. 4.24c is given by

$$\Delta = -i \langle \bar{\chi} (\Sigma_3 \zeta_1 - \Sigma_1 \zeta_3 - \Sigma_2 \zeta_2) \chi \rangle / \sqrt{3} \quad (7.1)$$

While it is a lattice singlet, it breaks the flavour SU(4) down to U(1) (generated by Σ_{45}) and the chiral SU(2) down to Z_2 .

This mass corresponds to a uniform *ferro* ordering in the spin-quadrupole density (in the global basis)

$$\Sigma_1 + \Sigma_2 + \Sigma_3 = \frac{1}{\sqrt{3}} (\{J_x, J_y\} + \{J_y, J_z\} + \{J_z, J_x\}), \quad (7.2)$$

as can be explicitly checked starting with the underlying lattice fermion bilinear similar to the case of CDW (Eq. 5.6). In addition, this singlet supports non-zero quantized spin-octupolar Hall response somewhat similar to that of the \mathcal{A}_{1g}^e mass in Eq. 6.1. To understand this, we write an action similar to that in Eq. 6.3 and integrate out the fermions. This produces a mutual CS action of the form

$$S_{CS}^{mutual} = i \frac{N_F}{2} \frac{1}{2\pi} \text{sgn}(\Delta) \int d^3x \epsilon^{\mu\nu\lambda} A_{c,\mu} \partial_\nu A_{o,\lambda}. \quad (7.3)$$

Here $N_F = 4$ is the number of fermions flavors and $A_{c,\mu}$, $A_{o,\mu}$ are respectively electromagnetic and spin-octupole probe gauge fields as used in Eq. 6.4. Thus, this mass too produces quantum spin-octupolar Hall response, but the CS level is half compared to that for the mass in Eq. 6.1. The resultant counter-propagating edge modes (not shown) can be obtained for appropriate lattice models. These edge modes are protected by the microscopic time-reversal symmetry (\mathbb{T}). Hence this corresponds to a gapped Ising ferro spin-quadrupolar phase with counter-propagating spin-octupole filtered edge modes.

7.1.2 Ising ferro spin-octupolar insulator

Similarly, the TR odd mass for the \mathcal{A}_{2g}^o lattice singlet in Eq. 4.24d given by

$$\tilde{\Delta} = -i \langle \bar{\chi} (\Sigma_{12}\zeta_1 - \Sigma_{23}\zeta_3 + \Sigma_{13}\zeta_2) \chi \rangle / \sqrt{3} \quad (7.4)$$

corresponds to uniform ordering for the spin-octupole density in

$$\Sigma_{12} - \Sigma_{13} + \Sigma_{23} = \frac{7}{3} (J_x + J_y + J_z) - \frac{4}{3} (J_x^3 + J_y^3 + J_z^3) \quad (7.5)$$

However, unlike the above ferro spin-quadrupolar order, this breaks the flavour SU(4) down to SU(2) (generated by $\{\Sigma_4, \Sigma_5, \Sigma_{45}\}$) and is also odd under \mathbf{C}'_2 . The chiral SU(2), on the other hand, is broken down to Z_2 , similar to the ferro spin-quadrupolar case.

The above singlet leads to non-zero quantum Hall response in the presence of an external electromagnetic field. This can again be understood by writing an action of the form as in Eq. 4.3 in the presence of an electromagnetic gauge field $A_{c,\mu}$ and integrating out the fermions. This produces an effective action given by

$$S_{CS} = i \frac{N_F}{2} \frac{1}{4\pi} \text{sgn}(\tilde{\Delta}) \int d^3x \epsilon^{\mu\nu\lambda} A_{c,\mu} \partial_\nu A_{c,\lambda}. \quad (7.6)$$

The CS level of this action is half compared to that for the ICI mass (Eq. 5.2) and hence represents a generalisation of an anomalous Hall insulator.

7.1.3 Staggered (“Néel”) spin-octupolar insulator

The four mixed masses that make up the two \mathcal{E}_u^o doublets in Eqs. 4.24e and 4.24f are respectively comprised of

$$\begin{aligned} & -i \left\langle \bar{\chi} \frac{4\Sigma_{35}\zeta_1 - (\Sigma_{15} - \sqrt{3}\Sigma_{14})\zeta_3 - (\sqrt{3}\Sigma_{24} + \Sigma_{25})\zeta_2}{2\sqrt{6}} \chi \right\rangle, \\ & -i \left\langle \bar{\chi} \frac{(\Sigma_{15} - \sqrt{3}\Sigma_{14})\zeta_3 - (\Sigma_{25} + \sqrt{3}\Sigma_{24})\zeta_2}{2\sqrt{2}} \chi \right\rangle \end{aligned} \quad (7.7)$$

and

$$\begin{aligned}
& -i \left\langle \bar{\chi} \frac{4\Sigma_{34}\zeta_1 - (\Sigma_{14} + \sqrt{3}\Sigma_{15})\zeta_3 + (\sqrt{3}\Sigma_{25} - \Sigma_{24})\zeta_2}{2\sqrt{6}} \chi \right\rangle, \\
& -i \left\langle \bar{\chi} \frac{-(\Sigma_{14} + \sqrt{3}\Sigma_{15})\zeta_3 + (\Sigma_{24} - \sqrt{3}\Sigma_{25})\zeta_2}{2\sqrt{2}} \chi \right\rangle.
\end{aligned} \tag{7.8}$$

The above four masses in the two doublets can be rotated into each other using a U(1) symmetry generated by Σ_{45} . In particular, if $m_1(m'_1)$ and $m_2(m'_2)$ are the components of Eq. 7.7 (7.8), then the linear combinations $m_1^\pm = m_1 \pm im'_1$ and $m_2^\pm = m_2 \pm im'_2$ transform as one-dimensional representations of the above U(1). Hence they describe the same phase.

These masses describe a fully gapped two-sublattice staggered ordering (as shown in Fig. 7.1) in the following spin-octupole operator respectively (whose representation in terms of spin operators are readily obtained using Appendix A.3)

$$\begin{aligned}
& 2\Sigma_{35} + \frac{\Sigma_{15} - \sqrt{3}\Sigma_{14}}{2} + \frac{\sqrt{3}\Sigma_{24} + \Sigma_{25}}{2}, \\
& \frac{\sqrt{3}\Sigma_{14} - \Sigma_{15}}{2} + \frac{\sqrt{3}\Sigma_{24} + \Sigma_{25}}{2}.
\end{aligned} \tag{7.9}$$

and

$$\begin{aligned}
& 2\Sigma_{34} + \frac{\Sigma_{14} + \sqrt{3}\Sigma_{15}}{2} + \frac{\Sigma_{24} - \sqrt{3}\Sigma_{25}}{2}, \\
& \frac{\Sigma_{14} + \sqrt{3}\Sigma_{15}}{2} - \frac{\Sigma_{24} - \sqrt{3}\Sigma_{25}}{2}.
\end{aligned} \tag{7.10}$$

This can be checked starting with the appropriate lattice bilinears similar to Eq. 7.13.

A remarkable difference of the above sub-lattice staggered spin-octupolar orderings compared to *Néel* state in SU(2) spin-rotation invariant graphene is that the latter are given one-dimensional representations, \mathcal{A}_{1u}^o , [21] under lattice transformations, while transform as a O(3) vector under spin rotations. In the present case, due to SOC, we have doublets that transform non-trivially under both SU(4) and lattice symmetries. In fact, this allows for non-trivial quantum numbers for the vortices of the resultant doublet masses which forms an interesting avenue to explore in the future.

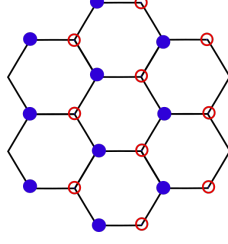


Figure 7.1: Density pattern for the staggered spin-octupole density waves corresponding to Eqs. 7.7 and 7.8. The red circles and blue dots here represent opposite densities in the spin-octupole operators given by Eqs. 7.9, 7.10.

7.1.4 Stripy spin-octupole density wave insulator

The three masses that form the \mathcal{F}_{2g}^o triplet (in Eq. 4.24a) are given by

$$-i\langle\bar{\chi}\Sigma_{45}\zeta_i\chi\rangle \neq 0 \quad (7.11)$$

with $i = 1, 2, 3$. Each mass in this triplet breaks down the flavor $SU(4)$ to $U(1) \otimes SU(2)$ and the chiral $SU(2)$ to $U(1)$.

The transformation properties of the triplet components (see Table A.4) under lattice symmetries are completely determined by ζ_i as Σ_{45} is a lattice singlet (see Table 4.1 and 4.2). Thus they are very similar to the triplet mass in group-1 (Eq. 5.5). However, unlike the CDW, here the density modulation occurs in the spin-octupole moment, *i.e.*,

$$\Sigma_{45} = -\frac{4}{3\sqrt{3}} \left(J_x J_y J_z + J_y J_z J_x + J_z J_x J_y - \frac{15i}{8} \right). \quad (7.12)$$

Hence, they are nothing but stripy spin-octupole density wave, as shown in Fig. 5.2, with the modulation being in the spin-octupole density. This can be seen explicitly by looking at the low energy projection of the microscopic on-site spin-octupole density operator. Similar to the CDW case (Eq. 5.6), here we have

$$:\psi^\dagger(\mathbf{r}_S)\Sigma_{45}\psi(\mathbf{r}_S): = \begin{cases} -i\bar{\chi}\Sigma_{45}\zeta_1\chi & \text{For } \mathcal{S} = A_2, B_2 \\ i\bar{\chi}\Sigma_{45}\zeta_1\chi & \text{For } \mathcal{S} = A_1, B_1 \end{cases} \quad (7.13)$$

The two other members of the triplet describe stripy order along the other two directions rotated by $\pm 2\pi/3$ with respect to Fig. 5.2.

7.1.5 Zig-zag spin-quadrupole density wave insulator

Eq. 4.24b consists of six masses of the form

$$\{-i \langle \bar{\chi} \Sigma_4 \zeta_i \chi \rangle, -i \langle \bar{\chi} \Sigma_5 \zeta_i \chi \rangle\}, \quad (7.14)$$

for $i = 1, 2, 3$. Under the action of the lattice symmetries, these six masses form two triplets with representations \mathcal{J}_{1u}^e and \mathcal{J}_{2u}^e , which leads to two different types of spin-quadrupole density wave phases (Eq. 6.25), which we discuss below.

\mathcal{J}_{1u}^e masses : The \mathcal{J}_{1u}^e masses are given by

$$\begin{aligned} & -i \langle \bar{\chi} \Sigma_5 \zeta_1 \chi \rangle, \\ & -\frac{i}{2} \langle \bar{\chi} (-\sqrt{3} \Sigma_4 + \Sigma_5) \zeta_3 \chi \rangle, \\ & -\frac{i}{2} \langle \bar{\chi} (-\sqrt{3} \Sigma_4 - \Sigma_5) \zeta_2 \chi \rangle. \end{aligned} \quad (7.15)$$

The relation between the first mass and the underlying $j = 3/2$ orbitals is given by

$$: \psi^\dagger(\mathbf{z}_S) \Sigma_5 \psi(\mathbf{z}_S) : = \begin{cases} -i \bar{\chi} \Sigma_5 \zeta_1 \chi & \text{For } \mathcal{S} = A_1, B_2 \\ i \bar{\chi} \Sigma_5 \zeta_1 \chi & \text{For } \mathcal{S} = B_1, A_2. \end{cases} \quad (7.16)$$

Notice the difference in the sign for the different sub-lattices compared to Eq. 5.6 and 7.13. Unlike in these earlier cases, Eq. 7.16 represents *zig-zag* pattern of spin-quadrupolar density wave as shown in Fig. 7.2 which corresponds to spin-quadrupole order in Σ_5 . The other two masses are also zig-zag density waves of the $\frac{1}{2} (\sqrt{3} \Sigma_4 - \Sigma_5)$, $\frac{1}{2} (\sqrt{3} \Sigma_4 + \Sigma_5)$ operators whose patterns are rotated by $\pm 2\pi/3$ with respect to Fig. 7.2.

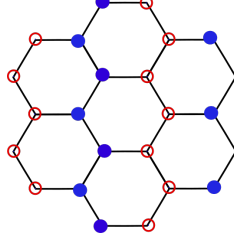


Figure 7.2: Zig-zag Density wave pattern corresponding to the masses of Eqs. 7.15, 7.17, 7.21, 7.22, 7.29 and 7.30. The blue dots and the red circles represent opposite densities of spin quadrupole operator Σ_5 .

\mathcal{J}_{2u}^e masses : The masses in the \mathcal{J}_{2u}^e triplet are given by

$$\begin{aligned}
& -i \langle \bar{\chi} \Sigma_4 \zeta_1 \chi \rangle, \\
& -\frac{i}{2} \langle \bar{\chi} (\Sigma_4 + \sqrt{3} \Sigma_5) \zeta_3 \chi \rangle, \\
& -\frac{i}{2} \langle \bar{\chi} (\sqrt{3} \Sigma_5 - \Sigma_4) \zeta_2 \chi \rangle
\end{aligned} \tag{7.17}$$

Similar to \mathcal{J}_{1u}^e triplet, these are also zig-zag density waves but of different spin-quadrupole operators, namely

$$\Sigma_4, \frac{1}{2} \left(\sqrt{3} \Sigma_5 + \Sigma_4 \right), \frac{1}{2} \left(\sqrt{3} \Sigma_5 - \Sigma_4 \right), \tag{7.18}$$

respectively.

The members of both the above triplets are incompatible, and hence generically one expects gapless points when tuning among different components of the masses similar to the \mathcal{J}_{1u}^e and \mathcal{J}_{2u}^e masses in Eq. 6.12 and Eq. 6.13. In fact, similar to that case, we can consider labeling the linear combination of the six masses in Eq. 7.14 as points on a 5-dimensional sphere, \mathcal{S}^5 . The points on this \mathcal{S}^5 are closed under the action of the $U(1) \otimes SU(2)$ subgroup generated by $\{\Sigma_{45}, \zeta_1, \zeta_2, \zeta_3\}$. Then arguments similar to those discussed for the \mathcal{J}_{1u}^e and \mathcal{J}_{2u}^e masses (in Sec. 6.1.3) hold in the present case. Also, these phases also exhibit unnecessary quantum critical points, as discussed in Chapter. 8.2.

7.1.6 Zig-zag spin-octupole density wave insulator

The four triplets (two \mathcal{J}_{1u}^o and two \mathcal{J}_{2u}^o) in Eq. 4.24e and 4.24f correspond to two different types of spin-octupolar density wave patterns (of the type given by Fig. 7.2). This can be shown by an analysis similar to that in Eq. 7.16. Note that the two triplets in each

of the representations break the same symmetries, and hence they are not counted as distinct phases.

Notably, each triplet is made up of non-compatible members. Thus, while the generic linear combination of the masses (Eq. 6.16) gap out all the fermions, there are special linear combinations, similar to the zig-zag spin-quadrupole density waves (Eq. 7.14) where fermions become gapless giving rise to unnecessary multi-critical points.

The \mathcal{F}_{1u}^o triplets: Two such triplets given by Eqs. 4.24e and Eq. 4.24f correspond to zig-zag ordering in

$$\begin{aligned} & \frac{\sqrt{3}\Sigma_{14} - \Sigma_{15}}{2} - \frac{\sqrt{3}\Sigma_{24} + \Sigma_{25}}{2}, \\ \Sigma_{35} - \frac{\sqrt{3}\Sigma_{24} + \Sigma_{25}}{2}, \\ \Sigma_{35} + \frac{\sqrt{3}\Sigma_{14} - \Sigma_{15}}{2}, \end{aligned} \tag{7.19}$$

and

$$\begin{aligned} & \frac{\sqrt{3}\Sigma_{15} + \Sigma_{14}}{2} + \frac{\sqrt{3}\Sigma_{25} - \Sigma_{24}}{2}, \\ \Sigma_{34} + \frac{\Sigma_{24} - \sqrt{3}\Sigma_{25}}{2}, \\ \Sigma_{34} - \frac{\sqrt{3}\Sigma_{15} + \Sigma_{14}}{2} \end{aligned} \tag{7.20}$$

respectively. The zig-zag patterns for the first mass of both the triplets are similar to the one shown in Fig. 7.2 while that for the other two are obtained by rotating this pattern by $\pm 2\pi/3$.

The fermion bilinear corresponding to the two triplets is given by

$$\begin{aligned} & -i \left\langle \bar{\chi} \left(\left(\Sigma_{15} - \sqrt{3}\Sigma_{14} \right) \zeta_2 + \left(\sqrt{3}\Sigma_{24} + \Sigma_{25} \right) \zeta_3 \right) \chi \right\rangle / 2\sqrt{2}, \\ & -i \left\langle \bar{\chi} \left(- \left(\sqrt{3}\Sigma_{24} + \Sigma_{25} \right) \zeta_1 - 2\Sigma_{35}\zeta_2 \right) \chi \right\rangle / 2\sqrt{2}, \\ & -i \left\langle \bar{\chi} \left(\left(\Sigma_{15} - \sqrt{3}\Sigma_{14} \right) \zeta_1 + 2\Sigma_{35}\zeta_3 \right) \chi \right\rangle / 2\sqrt{2} \end{aligned} \tag{7.21}$$

for and

$$\begin{aligned}
& -i \left\langle \bar{\chi} \left((-\Sigma_{24} + \sqrt{3}\Sigma_{25})\zeta_3 + (\Sigma_{14} + \sqrt{3}\Sigma_{15})\zeta_2 \right) \chi \right\rangle / 2\sqrt{2}, \\
& -i \left\langle \bar{\chi} \left((-\Sigma_{24} + \sqrt{3}\Sigma_{25})\zeta_1 + 2\Sigma_{34}\zeta_2 \right) \chi \right\rangle / 2\sqrt{2}, \\
& -i \left\langle \bar{\chi} \left(-(\Sigma_{14} + \sqrt{3}\Sigma_{15})\zeta_1 + 2\Sigma_{34}\zeta_3 \right) \chi \right\rangle / 2\sqrt{2}.
\end{aligned} \tag{7.22}$$

For a generic linear combination of the three masses (similar to Eq. 6.16) for each of the two triplets, the degeneracy and the magnitude of the fermionic gap change for different points on the sphere, S^2 (middle panel of Fig. 6.2), as members of each triplet are incompatible. The fermionic spectrum corresponding to the three points A, B , and C on the sphere in Fig. 6.2 are shown in the bottom panel of the same figure. This clearly shows the change in the degeneracy of each of the fermionic bands as well as the change in the fermionic gap. For a general point on S^2 (e.g., points C,D on the sphere in Fig. 6.2), the fermionic spectrum has eight bands, each of which is 2-fold degenerate. However, for the points on the great circles obtained by setting one of the Δ_i s to zero (blue circles on the sphere in Fig 6.2 which includes the point A), the spectrum has four bands and each of these is 4-fold degenerate. Finally, for the special eight isolated points given by Eq. 6.21 (such as point B on the sphere in Fig. 6.2), the fermion gap closes partially giving rise to *four* gapless fermionic modes while the rest of the bands remain gapped and two-fold degenerate.

The above pattern is best understood by performing a basis transformation (similar in spirit to Eq. 6.17) which allows useful insights into the breaking of the SU(8) symmetry by the above masses. We explicitly discuss this for the first triplet given by Eq. 7.21. This basis transformation is defined by

$$\chi'' = U'' \chi, \tag{7.23}$$

where

$$U'' = \Sigma_0 \otimes \begin{pmatrix} \sigma_0 & \\ & i\sigma_2 \end{pmatrix}. \tag{7.24}$$

The form of the Dirac Matrices in this new basis is $\gamma_0'' = \Sigma_0 \tau_0 \sigma_3$, $\gamma_1'' = \Sigma_0 \tau_0 \sigma_2$, $\gamma_2'' =$

$-\Sigma_0\tau_0\sigma_1$ such that the SU(8) generators (\mathcal{P} in Eq. 3.10), that commute with the Dirac matrices, in the transformed basis, must have the form :

$$\mathcal{P}'' = \Sigma_a\tau_\beta\sigma_0. \quad (7.25)$$

The six masses in Eqs. 7.21 and 7.22, in this new basis have the following form

$$-i\bar{\chi}'' \gamma_0''(\mathcal{R} \otimes \sigma_3) \chi'', \quad (7.26)$$

where \mathcal{R} are 8×8 Hermitian matrices.

The residual subgroup of the SU(8) in presence of these masses can be obtained from the set of 8×8 linearly independent matrices that commute with \mathcal{R} . As shown in Appendix A.8, this yields the following :

- At generic points such as C, D on the sphere in Fig. 6.2, the SU(8) symmetry breaks down to $U(1) \otimes [U(1) \otimes U(1) \otimes U(1)]^2$ and there are no zero modes (Fig. 6.2(e)).
- For the points on the blue great circles (e.g., point A), the SU(8) symmetry breaks down to $U(1) \otimes [U(1) \otimes SO(4)] \otimes [U(1) \otimes SO(4)]$ and there are no zero modes but because of the larger residual symmetry, the gapped modes have a higher degeneracy (Fig. 6.2(d)).
- Finally, at the special points where all the Δ_i have equal magnitude (e.g., point B in Fig. 6.2), the SU(8) symmetry is broken to $U(1) \otimes U(1) \otimes U(1) \otimes U(2) \otimes SO(4)$. Thus, the isolated gapless points have higher symmetry compared to it's nearby points. This high symmetry preserves a zero block in the \mathcal{R} matrix (Eq. A.95) and this protects the four gapless fermion modes (Fig. 6.2(f)).

The \mathcal{J}_{2u}^o triplets: We now discuss the two \mathcal{J}_{2u}^o triplets. The geometric order and the SU(8) symmetry breaking of these masses are similar to the two \mathcal{J}_{1u}^o triplets leading

respectively to zig-zag ordering of

$$\begin{aligned}
& \frac{\sqrt{3}\Sigma_{14} - \Sigma_{15}}{2} + \frac{\sqrt{3}\Sigma_{24} + \Sigma_{25}}{2}, \\
& \Sigma_{35} + \frac{\sqrt{3}\Sigma_{24} + \Sigma_{25}}{2}, \\
& \Sigma_{35} - \frac{\sqrt{3}\Sigma_{14} - \Sigma_{15}}{2},
\end{aligned} \tag{7.27}$$

and

$$\begin{aligned}
& \frac{\Sigma_{14} + \sqrt{3}\Sigma_{15}}{2} + \frac{\Sigma_{24} - \sqrt{3}\Sigma_{25}}{2}, \\
& \Sigma_{34} + \frac{\sqrt{3}\Sigma_{25} - \Sigma_{24}}{2}, \\
& \Sigma_{34} - \frac{\sqrt{3}\Sigma_{15} + \Sigma_{14}}{2},
\end{aligned} \tag{7.28}$$

spin-octupole operators.

The corresponding masses are given by

$$\left\{ \left\langle -i\bar{\chi} \frac{-(\Sigma_{25} + \sqrt{3}\Sigma_{24})\zeta_3 + (\Sigma_{15} - \sqrt{3}\Sigma_{14})\zeta_2}{2\sqrt{2}} \chi \right\rangle, \right. \\
\left\langle -i\bar{\chi} \frac{-(\Sigma_{25} + \sqrt{3}\Sigma_{24})\zeta_1 + 2\Sigma_{35}\zeta_2}{2\sqrt{2}} \chi \right\rangle, \\
\left. \left\langle -i\bar{\chi} \frac{(\sqrt{3}\Sigma_{14} - \Sigma_{15})\zeta_1 + 2\Sigma_{35}\zeta_3}{2\sqrt{2}} \chi \right\rangle \right\} \neq 0, \tag{7.29}$$

for the \mathcal{J}_{2u}^o triplet in Eq. 4.24e and

$$\left\{ \left\langle -i\bar{\chi} \frac{(\Sigma_{24} - \sqrt{3}\Sigma_{25})\zeta_3 + (\Sigma_{14} + \sqrt{3}\Sigma_{15})\zeta_2}{2\sqrt{2}} \chi \right\rangle, \right. \\
\left\langle -i\bar{\chi} \frac{(-\Sigma_{24} + \sqrt{3}\Sigma_{25})\zeta_1 - 2\Sigma_{34}\zeta_2}{2\sqrt{2}} \chi \right\rangle, \\
\left. \left\langle -i\bar{\chi} \frac{(\Sigma_{14} + \sqrt{3}\Sigma_{15})\zeta_1 + 2\Sigma_{34}\zeta_3}{2\sqrt{2}} \chi \right\rangle \right\} \neq 0. \tag{7.30}$$

for the \mathcal{J}_{2u}^o triplet is given by Eq. 4.24f.

Similar to the \mathcal{J}_{1u}^o triplets discussed above, the SU(8) symmetry breaking for these two triplets depend on the position on the sphere described by the Δ_i s in Eq. 6.16. In fact, the SU(8) symmetry breaking for these two triplets is the same as that of the \mathcal{J}_{1u}^o masses discussed before. The \mathcal{J}_{1u}^o and the \mathcal{J}_{2u}^o masses presented in this section also exhibit unnecessary quantum critical points which we discuss in Chapter. 8.2.

7.2 Density wave semimetals

There are 18 density wave semimetals divided into four triplets ($\mathcal{J}_{1g}^e, \mathcal{J}_{1g}^o, \mathcal{J}_{2g}^e, \mathcal{J}_{2g}^o$), two doublets ($\mathcal{E}_g^e, \mathcal{E}_g^o$) and two singlets ($\mathcal{A}_{1u}^o, \mathcal{A}_{2u}^o$). The analogs of these semimetals are absent in graphene [21]. These 18 density wave semimetals can be divided up into two categories depending on the number of gapless fermionic modes which, for the first set is at least *four* and the second set is always *eight*. Insights into these two sets are best obtained by using the global basis (Eq. 2.24) as discussed in Appendix A.10. As noted in Chapter 3, in the global basis, there are four doubly degenerate Dirac nodes at Γ , M_1 , M_2 , M_3 points in the Brillouin zone as shown in Fig. A.1. To reiterate the crucial aspect, the IR space group does not mix the Dirac spinor at Γ point with the other three at the M points, in other words, the former behaves as a “singlet” and the latter behaves as a “triplet” as mentioned before. As far as the irreducible masses go, this feature throws up the two categories mentioned above : (1) Irreducible masses that vanish on for the spinor at the Γ -point and leave the Dirac cone at Γ ungapped – these are dubbed Γ -Dirac Semimetals (Γ -DSM) guaranteeing *at least four* gapless Dirac modes which do not depend on the mass parameters, and, (2) the masses that couple the Dirac spinors at each $M_i (i = 1, \dots, 3)$ to that at the Γ -point but the Dirac spinors at the M-points do not directly couple to each other and this guarantees the existence of *eight* zero modes– phases thus realized are dubbed M-Dirac Semimetals (M-DSM). Six masses that makeup two triplets ($\mathcal{J}_{2g}^e, \mathcal{J}_{1g}^o$) correspond to M-DSM that give rise to the stripy spin-quadrupole and spin-octupole density waves. The rest of the 12 masses are of Γ -DSM type. These consist of two singlets, two doublets and two triplets. The two singlets ($\mathcal{A}_{1u}^o, \mathcal{A}_{2u}^o$) give rise to staggered spin-octupole density waves, the two doublets ($\mathcal{E}_g^e, \mathcal{E}_g^o$) make up, respectively, ferro spin-quadrupole and spin-octupole density waves. The two triplets ($\mathcal{J}_{2g}^o, \mathcal{J}_{1g}^e$) form

stripy spin-octupole and spin-quadrupole density waves respectively. Finally, the number of gapless Dirac nodes for the Γ -DSM can be greater than four for a specific linear combination of masses as discussed below. In Appendix A.9.1, we note an interesting structure of the above 18 masses with respect to their transformation under SU(8).

7.2.1 Staggered (“Néel”) spin-octupole density wave semimetal

The two TR odd masses that form the $\mathcal{A}_{1_u}^o$ and $\mathcal{A}_{2_u}^o$ singlet masses in Eqs. 4.24e and 4.24f respectively are given by

$$-i \left\langle \bar{\chi} \left(\frac{\Sigma_{35}\zeta_1}{\sqrt{3}} - \frac{(\sqrt{3}\Sigma_{14} - \Sigma_{15})\zeta_3}{2\sqrt{3}} + \frac{(\sqrt{3}\Sigma_{24} + \Sigma_{25})\zeta_2}{2\sqrt{3}} \right) \chi \right\rangle \quad (7.31)$$

and

$$-i \left\langle \bar{\chi} \left(\frac{\Sigma_{34}\zeta_1}{\sqrt{3}} + \frac{(\Sigma_{14} + \sqrt{3}\Sigma_{15})\zeta_3}{2\sqrt{3}} + \frac{(\Sigma_{24} - \sqrt{3}\Sigma_{25})\zeta_2}{2\sqrt{3}} \right) \chi \right\rangle. \quad (7.32)$$

These represent spin-octupole ordering in

$$\begin{aligned} \Sigma_{35} + \frac{\sqrt{3}\Sigma_{14} - \Sigma_{15}}{2} - \frac{\sqrt{3}\Sigma_{24} - \Sigma_{25}}{2} = \\ \frac{2}{3\sqrt{3}} [(J_z J_x J_x + c.p) + (J_y J_z J_z + c.p) + (J_x J_y J_y + c.p) \\ - (J_z J_y J_y + c.p) - (J_y J_x J_x + c.p) - (J_x J_z J_z + c.p)] \end{aligned} \quad (7.33)$$

and

$$\Sigma_{34} - \frac{\Sigma_{14} + \sqrt{3}\Sigma_{15}}{2} - \frac{\Sigma_{24} - \sqrt{3}\Sigma_{25}}{2} = \frac{2}{3}(J_x^3 + J_y^3 + J_z^3) - \frac{13}{6}(J_x + J_y + J_z) \quad (7.34)$$

respectively where “ $c.p$ ” in Eq. 7.33 refers to all possible cyclic permutations of the operators. The main difference between the two spin-octupolar orders is the fact that the former is odd under reflection, $\sigma_{\mathbf{d}}$ (see Table A.2) while the latter is even under it. Both, however, are odd under inversion.

In either case, the fermionic dispersion is given by Fig. 7.3 with twelve of the fermionic modes are gapped while the other four are gapless which can be understood from Eq. 7.41 discussed below. Hence they represent two-sublattice staggered spin-octupolar density

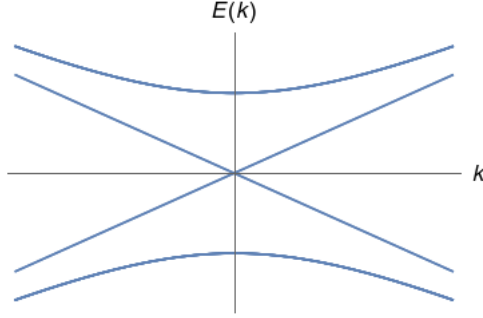


Figure 7.3: Energy spectrum for the fermions along the $k_x = k_y$ line in presence of either of the singlet masses written in Eq. 7.31, 7.32. Each of the gapless bands is two-fold degenerate. So there are four gapless fermion.

wave semimetals of Γ -DSM type, where the symmetry breaking pattern is given by Fig. 7.1.

The gapless fermionic modes are protected by $\mathbb{T}\mathbf{I} \times \text{SU}(2)_{\text{IR}}$, where $\mathbb{T}(\mathbf{I})$ is the microscopic time reversal (inversion) as given by Table 2.1 and $\text{SU}(2)_{\text{IR}}$ is a subgroup of the emergent $\text{SU}(8)$, which is best understood via a basis transformation for the spinors as

$$\tilde{\chi} = U\chi, \quad (7.35)$$

where U is a 16×16 unitary matrix given by Eq. A.96 of Appendix A.9. This transformation relates the low energy Dirac fermions in the local basis (Eq. 2.33) with those in the global basis (Eq. 2.24 and Appendix A.10).

The free Dirac Hamiltonian (Eq. 3.3) in this new basis is given by

$$H_D = v_F \int d^2x \tilde{\chi}^\dagger \left(i\mu_0 \tilde{\Sigma}_{23} \partial_x - i\mu_0 \tilde{\Sigma}_{24} \partial_y \right) \tilde{\chi}. \quad (7.36)$$

where we have introduced two new set of 4×4 matrices, μ_i and $\tilde{\Sigma}_i$ which mixes the flavour and chiral spaces non-trivially. While the form of the $\tilde{\Sigma}_i$ matrices is the same as the Σ_i matrices defined in Appendix A.3, unlike the latter, they do not exclusively act on the flavour space. The μ_i (for $i = 1, \dots, 15$) matrices, on the other hand, are $\text{SU}(4)$ Gell-Mann matrices which are defined in Ref. [146] with $\mu_0 = \mathbb{I}_4$. The combination of $\mu_i \tilde{\Sigma}_j$ then gives a *new* set of 256 linearly independent 16×16 matrices. Such a combined basis is essential to capture the essence of the mixed masses that we are dealing with, which, in turn, stems from the underlying SOC. Equivalently, the free Dirac Lagrangian

in this new basis has the same form as Eq. 3.7 with

$$\tilde{\gamma}_0 = -\mu_0 \tilde{\Sigma}_{34}, \quad \tilde{\gamma}_1 = -\mu_0 \tilde{\Sigma}_{24}, \quad \tilde{\gamma}_2 = \mu_0 \tilde{\Sigma}_{23}. \quad (7.37)$$

being the new Dirac matrices.

In this new basis, the mass terms can be written as $-i\langle \tilde{\chi} \tilde{m} \tilde{\chi} \rangle$, where \tilde{m} is a 16×16 Hermitian matrix. More explicitly, the \mathcal{A}_{1u}^o (Eq. 7.31) and \mathcal{A}_{2u}^o (Eq. 7.32) masses in this new basis are given by

$$-i \left\langle \tilde{\chi} \left(\frac{\mu_8 - \sqrt{2}\mu_{15}}{\sqrt{3}} \tilde{\Sigma}_5 - \frac{\mu_0 + \sqrt{6}\mu_{15} - 2\mu_3}{2\sqrt{3}} \tilde{\Sigma}_{15} \right) \tilde{\chi} \right\rangle, \quad (7.38)$$

and

$$-i \left\langle \tilde{\chi} \left(-\frac{(\sqrt{2}\mu_{15} - \sqrt{3}\mu_3 + 2\mu_8)}{3} \tilde{\Sigma}_5 + \frac{(-\sqrt{3}\mu_0 + \sqrt{2}\mu_{15} + 2\mu_8)}{2\sqrt{3}} \tilde{\Sigma}_{15} \right) \tilde{\chi} \right\rangle. \quad (7.39)$$

The advantage of the new *mixed* basis is the fact that when we decompose the 16-component spinor, $\tilde{\chi}$, into a stack of four 4-component ones as

$$\tilde{\chi} = (\tilde{\chi}_1^T, \tilde{\chi}_2^T, \tilde{\chi}_3^T, \tilde{\chi}_4^T)^T, \quad (7.40)$$

both the mass matrices in Eqs. 7.38 and 7.39 take the generic form

$$\tilde{m} = \left(\begin{array}{c|c} 0_{4 \times 4} & 0_{4 \times 12} \\ \hline 0_{12 \times 4} & \#_{12 \times 12} \end{array} \right), \quad (7.41)$$

where, $0_{m \times n}$ are $m \times n$ null matrices and $\#_{12 \times 12}$ is some 12×12 dimensional Hermitian matrix.

It is then clear that the mass matrix \tilde{m} has a decoupled four-dimensional zero block belonging to $\tilde{\chi}_1$ which gives rise to the gapless modes. In fact, the Dirac action for the

$\tilde{\chi}_1$ sector is given by

$$S_{\tilde{\chi}_1} = v_F \int d\tau d^2x \bar{\tilde{\chi}}_1 \left(i\tilde{\Sigma}_{34}\partial_t + i\tilde{\Sigma}_{24}\partial_x - i\tilde{\Sigma}_{23}\partial_y \right) \tilde{\chi}_1, \quad (7.42)$$

which is similar to that of spinless graphene [21] and hence there is an *emergent chiral* $SU(2)$ which we call $SU(2)_{\text{IR}}$. This $SU(2)_{\text{IR}}$ is generated by

$$\{\tilde{\Sigma}_1, \tilde{\Sigma}_5, \tilde{\Sigma}_{15}\}/2. \quad (7.43)$$

which is actually a projection of the $SU(2)$ generated by $\{\Sigma_4/2, \Sigma_5/2, \Sigma_{45}/2\}$ into the $\tilde{\chi}_1$ sector. This $SU(2)_{\text{IR}}$ along with \mathbb{T} and \mathbf{I} keeps the $\tilde{\chi}_1$ sector gapless.

It is interesting to consider the four fermion bilinear masses that can open up a gap in this sector. They are given by

$$-i\bar{\tilde{\chi}}_1\tilde{\chi}_1, \quad -i\bar{\tilde{\chi}}_1\tilde{\Sigma}_{15}\tilde{\chi}_1, \quad -i\bar{\tilde{\chi}}_1\tilde{\Sigma}_5\tilde{\chi}_1, \quad -i\bar{\tilde{\chi}}_1\tilde{\Sigma}_1\tilde{\chi}_1. \quad (7.44)$$

The first one is actually a $SU(2)_{\text{IR}}$ scalar, but, is odd under \mathbb{TI} and is actually a projection of a group-1, chiral mass, namely the ICI bilinear, $-i\bar{\chi}\chi$ (Eq. 5.1) to the $\tilde{\chi}_1$ subspace and hence itself transforms under a \mathcal{A}_{2g}^o singlet under the microscopic symmetries. Hence this mass breaks the \mathbb{TI} symmetry (or alternatively \mathbf{C}'_2 symmetry for the \mathcal{A}_{1u}^0 singlet) in the $\tilde{\chi}_1$ sector. The resultant massive bands for the $\tilde{\chi}_1$ fermions have a non-zero Chern number while the already gapped $\tilde{\chi}_2, \tilde{\chi}_3$ and $\tilde{\chi}_4$ remain topologically trivial. This is unlike the ICI phase, where all the bands have a non-zero Chern number as is required in that case due to the fact that the ICI mass, (unlike in the present case) is a $SU(4)$ singlet. Indeed, $-i\langle\bar{\tilde{\chi}}_1\tilde{\chi}_1\rangle \neq 0$ leads to a $N_F = 1$ CS term of the form in Eq. 5.2 leading to a single gapless edge mode carrying electronic charge instead of four as in the case of ICI and hence represents a different phase more akin to an anomalous Hall phase.

The last three masses in Eq. 7.44 are \mathbb{TI} singlets but transform as a triplet under $SU(2)_{\text{IR}}$ and break it down to $U(1)$ subgroup. These masses are best thought of as projections of the group-2 and group-3 masses into the $\tilde{\chi}_1$ sector that are invariant under

\mathbb{TI} that are simultaneously odd or even under both \mathbb{T} and \mathbb{I} . In particular, both the \mathcal{A}_{1g}^e masses in Eq. 6.1 and Eq. 7.1 project to the fourth mass term in Eq. 7.44. Also, each of the three \mathcal{E}_u^o doublets in Eq. 6.23, 7.7, 7.8 project to the second and the third masses of Eq. 7.44. It is important to note that while it may appear that the resultant phases may have edge modes since they are obtained as a projection of a mass, which in unprojected form lead to symmetry-protected topological phase, this is not the case, because the respective symmetries are broken by Eq. 7.31 or 7.32.

7.2.2 Stripy spin-octupole density wave semimetal

There are two stripy spin-octupole phases, both TR odd triplets with distinct lattice symmetries, which differ in the nature of the spin-octupolar densities. These are given by \mathcal{J}_{1g}^o and \mathcal{J}_{2g}^o irreps in Eq. 4.24d which are respectively even and odd under \mathbf{C}'_2 . They correspond to stripy pattern (similar to Fig. 5.2) in the spin-octupole densities of

$$\frac{1}{\sqrt{2}}(\Sigma_{13} + \Sigma_{23}), \frac{1}{\sqrt{2}}(\Sigma_{12} + \Sigma_{13}) \quad \text{and} \quad \frac{1}{\sqrt{2}}(\Sigma_{12} - \Sigma_{23}) \quad (7.45)$$

for the \mathcal{J}_{1g}^o and

$$\frac{1}{\sqrt{2}}(\Sigma_{13} - \Sigma_{23}), \frac{1}{\sqrt{2}}(\Sigma_{12} - \Sigma_{13}) \quad \text{and} \quad \frac{1}{\sqrt{2}}(\Sigma_{12} + \Sigma_{23}) \quad (7.46)$$

for \mathcal{J}_{2g}^o .

For all the masses of these two triplets, a certain number of fermionic modes are always gapless. However, due to the difference in the symmetry representation, the number, structure and stability of the remnant gapless fermions are different. While a generic linear combination like Eq. 6.16 for the \mathcal{J}_{1g}^o mass *always* lead to eight gapless fermions, the number of gapless modes for \mathcal{J}_{2g}^o triplet varies. In this latter case, generically there are four gapless modes. However, for special linear combinations, this number increases to eight. Thus, the \mathcal{J}_{1g}^o and the \mathcal{J}_{2g}^o masses represent M-DSM and Γ -DSM types of semimetals respectively. Since the structure of the remnant gapless fermions affects the fate of the low energy theory and the nature of possible phase transitions, we discuss it in some more detail for the two cases separately.

In both cases, however, the structure and the symmetry protection of the fermions that remain gapless are best understood in the basis of $\tilde{\chi}$ spinors introduced in Eq. 7.35.

The \mathcal{F}_{1g}^o triplet : The three masses that form this triplet are

$$\begin{aligned}
& -i \langle \bar{\chi} (-\Sigma_{13}\zeta_3 - \Sigma_{23}\zeta_2) \chi \rangle / \sqrt{2}, \\
& -i \langle \bar{\chi} (\Sigma_{12}\zeta_2 - \Sigma_{13}\zeta_1) \chi \rangle / \sqrt{2}, \\
& -i \langle \bar{\chi} (\Sigma_{23}\zeta_1 + \Sigma_{12}\zeta_3) \chi \rangle / \sqrt{2}.
\end{aligned} \tag{7.47}$$

which, in the $\tilde{\chi}$ basis (Eq. 7.35), become

$$i\sqrt{2} \langle \tilde{\chi} \mu_2 \tilde{\Sigma}_5 \tilde{\chi} \rangle, -i\sqrt{2} \langle \tilde{\chi} \mu_5 \tilde{\Sigma}_0 \tilde{\chi} \rangle, -i\sqrt{2} \langle \tilde{\chi} \mu_9 \tilde{\Sigma}_5 \tilde{\chi} \rangle. \tag{7.48}$$

such that the mass matrices have the generic form

$$\tilde{m} = \left(\begin{array}{c|c} 0_{4 \times 4} & \#_{4 \times 12} \\ \hline \#_{4 \times 12}^\dagger & 0_{12 \times 12} \end{array} \right) \tag{7.49}$$

This generic structure should be contrasted with Eq. 7.41 which gave rise to four gapless modes from the $\tilde{\chi}_1$ sector. In the present case, Eq. 7.49 however gives rise to eight gapless modes. This is because any matrix of the form given in Eq. 7.49 always has eight zero eigenvalues. These gapless modes are protected by $\mathbf{C}'_2 \times \text{SO}(4)$ symmetry, where the $\text{SO}(4)$ is a subgroup of the $\text{SU}(8)$ which acts non-trivially only on the gapless fermions.

One can now consider gapping out these fermions. This can be done by doing a similar analysis as done for the masses in Eq. 7.31 and 7.32. As an example, for the first mass in this triplet, the $\tilde{\chi}_3$ and $\tilde{\chi}_4$ fermions are gapless. One can show that there are 16 independent fermion bi-linears that can gap out the $\tilde{\chi}_3$ and $\tilde{\chi}_4$ fermions in this case and the fate of the resultant phases can be analysed.

The \mathcal{J}_{2g}^o Triplet : The three masses in this triplet are

$$\begin{aligned}
& \langle -i\bar{\chi} (\Sigma_{13}\zeta_3 - \Sigma_{23}\zeta_2) \chi \rangle / \sqrt{2}, \\
& \langle -i\bar{\chi} (-\Sigma_{13}\zeta_1 - \Sigma_{12}\zeta_2) \chi \rangle / \sqrt{2}, \\
& \langle -i\bar{\chi} (-\Sigma_{23}\zeta_1 + \Sigma_{12}\zeta_3) \chi \rangle / \sqrt{2}.
\end{aligned} \tag{7.50}$$

which, in term of the $\tilde{\chi}$ spinors (Eq. 7.35), are given by

$$-i\sqrt{2} \langle \tilde{\chi} \mu_{14} \tilde{\Sigma}_5 \tilde{\chi} \rangle, i\sqrt{2} \langle \tilde{\chi} \mu_{12} \tilde{\Sigma}_0 \tilde{\chi} \rangle, -i\sqrt{2} \langle \tilde{\chi} \mu_6 \tilde{\Sigma}_5 \tilde{\chi} \rangle. \tag{7.51}$$

such that a generic linear combination of the form in Eq. 6.16, but in $\tilde{\chi}$ basis, is given by $-i\tilde{\chi} \tilde{m} \tilde{\chi}$ where the mass matrix has the generic form given by Eq. 7.41. Hence the $\tilde{\chi}_1$ sector gives rise to four gapless fermion modes similar to the Néel spin-octupole density wave semimetal (see the discussion following Eq. 7.41). The rest of the discussion proceeds similarly to that of Néel spin-octupole density wave semimetal. However, here the \mathbf{C}'_2 is already broken and the ICI mass term is generically allowed by symmetry.

In the present case, however, the $\#_{12 \times 12}$ block has a further rich structure that is immediately evident from writing the mass matrix, \tilde{m} , explicitly

$$\tilde{m} = \begin{pmatrix} 0 & 0 & 0 & 0 \\ 0 & 0 & -\Delta_3 \tilde{\Sigma}_{15} & -i\Delta_2 \\ 0 & -\Delta_3 \tilde{\Sigma}_{15} & 0 & -i\Delta_1 \tilde{\Sigma}_5 \\ 0 & i\Delta_2 & i\Delta_1 \tilde{\Sigma}_5 & 0 \end{pmatrix} \tag{7.52}$$

It is clear that if one or two of the Δ_i in Eq. 7.52 are zero, then \tilde{m} has extra four zero eigenvalues and hence total eight fermionic modes are gapless in this case. This is shown in Fig. 7.4, where we represent the linear combination of the masses on the sphere as before. For the three great circles (in Fig. 7.4) that lie in the three coordinate planes, there are eight gapless modes present. For any other point, the number of gapless modes is four.

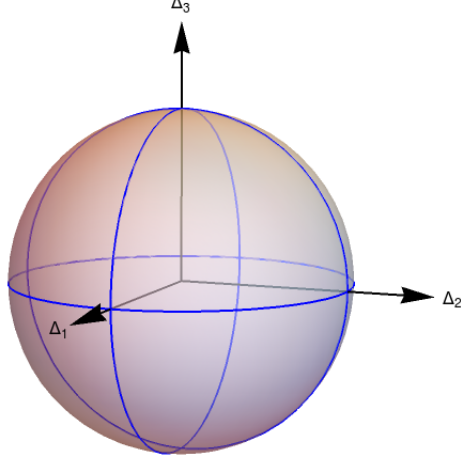


Figure 7.4: Gapless manifold for the triplet Γ -DSMs : Linear combinations of the form given in Eq. 6.16 for the triplet Γ -DSMs is represented on the surface of a unit sphere. The three great circles shown here are obtained by setting one of the Δ_i s to zero in Eq.6.16. For the triplet Γ -DSMs in Eqs. 7.50 and 7.57, on these great circles, the number of gapless modes is eight as opposed to only four at other points on the sphere.

7.2.3 Stripy spin-quadrupole density wave semimetal

There are two distinct stripy spin-quadrupolar density wave semimetal phases both of which are TR even but have distinct lattice symmetries. These are the two triplets given by \mathcal{J}_{1g}^e and \mathcal{J}_{2g}^e irreps in Eq. 4.24c. While the first triplet is even under \mathbf{C}'_2 and corresponds to the stripy pattern (similar to Fig. 5.2) in the spin-quadrupoles

$$\frac{1}{\sqrt{2}}(\Sigma_1 - \Sigma_2), \frac{1}{\sqrt{2}}(\Sigma_2 - \Sigma_3) \text{ and } \frac{1}{\sqrt{2}}(\Sigma_1 - \Sigma_3), \quad (7.53)$$

the second is inversion even and gives rise to stripy pattern in a different set of spin-quadrupoles given by

$$\frac{1}{\sqrt{2}}(\Sigma_1 + \Sigma_2), \frac{1}{\sqrt{2}}(\Sigma_2 + \Sigma_3) \text{ and } \frac{1}{\sqrt{2}}(\Sigma_1 + \Sigma_3). \quad (7.54)$$

Each of these masses breaks the flavour $SU(4)$ to $SU(2)$. E.g., the residual $SU(2)$ for the first mass in both the triplets is generated by $\{\Sigma_{34}, \Sigma_{35}, \Sigma_{45}\}$.

In spite of the opposite behavior under time reversal, \mathbb{T} , the structure of these masses is very similar to the two triplets in Eq. 7.47, 7.50 discussed above that represent stripy

spin-octupolar density wave semimetals. The analysis of the remnant gapless modes proceeds in the same way except for the fact that now the \mathcal{J}_{2g}^e triplet always has eight gapless fermionic modes and is a M-DSM type semimetal while the \mathcal{J}_{1g}^e triplet is a Γ -DSM type semimetal which generically has four gapless modes except at special combination of the mass as shown in Fig. 7.4. Here we briefly summarise this structure for completeness.

The \mathcal{J}_{2g}^e triplet : The three components of the \mathcal{J}_{2g}^e triplet are given by

$$\begin{aligned}
& -i \langle \bar{\chi} (-\Sigma_1 \zeta_2 + \Sigma_2 \zeta_3) \chi \rangle / \sqrt{2}, \\
& -i \langle \bar{\chi} (\Sigma_3 \zeta_2 + \Sigma_2 \zeta_1) \chi \rangle / \sqrt{2}, \\
& -i \langle \bar{\chi} (\Sigma_3 \zeta_3 + \Sigma_1 \zeta_1) \chi \rangle / \sqrt{2}.
\end{aligned} \tag{7.55}$$

which in the $\tilde{\chi}$ basis (Eq. 7.35) is given by

$$-i\sqrt{2} \langle \tilde{\bar{\chi}} \mu_1 \tilde{\Sigma}_{15} \tilde{\chi} \rangle, i\sqrt{2} \langle \tilde{\bar{\chi}} \mu_5 \tilde{\Sigma}_1 \tilde{\chi} \rangle, -i\sqrt{2} \langle \tilde{\bar{\chi}} \mu_{10} \tilde{\Sigma}_{15} \tilde{\chi} \rangle. \tag{7.56}$$

These masses have the same form as in Eq. 7.49 and hence these give rise to eight gapless fermions. The gaplessness of these modes is similarly protected via lattice symmetries and various subgroups of SU(8).

The \mathcal{J}_{1g}^e triplet : The three masses of the \mathcal{J}_{1g}^e triplet are given by

$$\begin{aligned}
& \langle -i\bar{\chi} (-\Sigma_1 \zeta_2 - \Sigma_2 \zeta_3) \chi \rangle / \sqrt{2}, \\
& \langle -i\bar{\chi} (-\Sigma_3 \zeta_2 + \Sigma_2 \zeta_1) \chi \rangle / \sqrt{2}, \\
& \langle -i\bar{\chi} (\Sigma_3 \zeta_3 - \Sigma_1 \zeta_1) \chi \rangle / \sqrt{2}.
\end{aligned} \tag{7.57}$$

In $\tilde{\chi}$ basis, these masses have the form

$$i\sqrt{2} \langle \tilde{\bar{\chi}} \mu_{13} \tilde{\Sigma}_{15} \tilde{\chi} \rangle, i\sqrt{2} \langle \tilde{\bar{\chi}} \mu_{11} \tilde{\Sigma}_1 \tilde{\chi} \rangle, i\sqrt{2} \langle \tilde{\bar{\chi}} \mu_7 \tilde{\Sigma}_{15} \tilde{\chi} \rangle. \tag{7.58}$$

Any linear combination (Eq. 6.16) of these masses can be written as $-i\tilde{\bar{\chi}}\tilde{m}\tilde{\chi}$ where again

\tilde{m} has the structure given by Eq. 7.41, albeit with different entries, *i.e.*,

$$\tilde{m} = \begin{pmatrix} 0 & 0 & 0 & 0 \\ 0 & 0 & -i\Delta_3\tilde{\Sigma}_{15} & \Delta_2\tilde{\Sigma}_1 \\ 0 & i\Delta_3\tilde{\Sigma}_{15} & 0 & \Delta_1\tilde{\Sigma}_{15} \\ 0 & \Delta_2\tilde{\Sigma}_1 & \Delta_1\tilde{\Sigma}_{15} & 0 \end{pmatrix}. \quad (7.59)$$

Therefore, it gives rise to four gapless Dirac fermions except for the three great circles where there are four additional gapless modes due to additional zeros in the $\#_{12 \times 12}$ sector similar to Eq. 7.52.

7.2.4 Ferro spin-quadrupole semimetal

The \mathcal{E}_g^e doublet in Eq. 4.24c corresponds to uniform (ferro) ordering of the spin-quadrupole densities in $(\Sigma_1 - \Sigma_2)/\sqrt{2}$ and $(2\Sigma_3 - \Sigma_1 - \Sigma_2)/\sqrt{6}$. The corresponding two masses are given by :

$$\begin{aligned} & \langle -i\bar{\chi}(-\Sigma_1\zeta_3 + \Sigma_2\zeta_2\chi) \rangle / \sqrt{2}, \\ & \langle -i\bar{\chi}(\Sigma_1\zeta_3 + \Sigma_2\zeta_2 + \Sigma_3\zeta_1)\chi \rangle / \sqrt{6}. \end{aligned} \quad (7.60)$$

These two masses do not fully gap out the fermions and hence represent ferro spin-quadrupolar density wave semimetals. Moreover, depending on the linear combination of these two masses, the number of gapless modes change due to the change in the residual symmetry— similar to the case described above by Eq. 7.52, but now on a circle, *i.e.* S^1 . This is a fallout of the fact that the two masses are non-compatible. Consider a generic linear combination of the two masses of the form akin to Eq. 6.16, but now on a circle, *i.e.*, $-i\bar{\chi}m(\vartheta)\chi$, where

$$m(\vartheta) = \cos \vartheta m_1 + \sin \vartheta m_2, \quad (7.61)$$

and $\{m_1, m_2\}$ represent the two mass matrices in Eq. 7.60 and $\vartheta \in (0, 2\pi]$. For a generic value of ϑ , there are four gapless modes in the spectrum and thus, this doublet is a Γ -DSM type semimetal. The flavour $SU(4)$ is broken down to $U(1)$ at these points. However, for special isolated values of $\vartheta = \frac{n\pi}{3}$ (with $n = 0, 1, \dots, 5$), there are eight gapless modes

since the flavour SU(4) is only broken down to SU(2). Thus, the residual symmetry is larger for the case where there are extra gapless modes.

The appearance of the gapless modes for these masses are better understood in the $\tilde{\chi}$ basis introduced in Eq. 7.35. In this basis, the masses in Eq. 7.60 are given by

$$\begin{aligned} & \langle -i\tilde{\chi} \left(-\sqrt{3}\mu_0 + \mu_{15} + \sqrt{2}\mu_8 \right) \tilde{\Sigma}_1 \tilde{\chi} \rangle / \sqrt{3}, \\ & \langle -i\tilde{\chi} (\mu_0 + \sqrt{3}\mu_{15} - \sqrt{2}\mu_3) \tilde{\Sigma}_1 \tilde{\chi} \rangle / \sqrt{3}. \end{aligned} \quad (7.62)$$

such that the generic mass matrix in Eq. 7.61 is $-i\tilde{\chi}\tilde{m}(\vartheta)\tilde{\chi}$ where

$$\tilde{m}(\vartheta) = \sqrt{2} \begin{pmatrix} 0 & 0 & 0 & 0 \\ 0 & \frac{2\sin\vartheta}{\sqrt{3}} & 0 & 0 \\ 0 & 0 & \frac{\sin\vartheta}{\sqrt{3}} - \cos\vartheta & 0 \\ 0 & 0 & 0 & -\cos\vartheta - \frac{\sin\vartheta}{\sqrt{3}} \end{pmatrix} \otimes \tilde{\Sigma}_1. \quad (7.63)$$

Thus, the $\tilde{\chi}_1$ spinors defined in Eq. 7.40 are always gapless, accounting for the four gapless fermions for generic ϑ . Also, for the special values of ϑ specified before, either the $\tilde{\chi}_2, \tilde{\chi}_3$ or the $\tilde{\chi}_4$ spinors also become gapless.

The gaplessness of the $\tilde{\chi}_1$ modes for generic values of ϑ is protected by TR symmetry and the SU(2)_{IR} subgroup of the SU(8). For the special values of ϑ where there are extra gapless modes, the residual symmetry also becomes large compared to that for other values of ϑ . This is evident because, as mentioned before, the flavour SU(4) breaks down to U(1) at generic values of ϑ . But for the special values noted above, it only breaks down to SU(2).

7.2.5 Ferro spin-octupole semimetal

The \mathcal{E}_g^o doublet in Eq. 4.24d represent uniform (ferro) ordering in the spin-octupoles given by $(\Sigma_{13} + \Sigma_{23})/\sqrt{6}$ and $(2\Sigma_{12} + \Sigma_{13} - \Sigma_{23})/3\sqrt{2}$ respectively. These masses are

given by :

$$\begin{aligned} & \langle -i\bar{\chi}(\Sigma_{13}\zeta_2 + \Sigma_{23}\zeta_3)\chi \rangle / \sqrt{2}, \\ & \langle -i\bar{\chi}(2\Sigma_{12}\zeta_1 - \Sigma_{13}\zeta_2 + \Sigma_{23}\zeta_3)\chi \rangle / \sqrt{6}. \end{aligned} \quad (7.64)$$

Any linear combination of these masses of the form in Eq. 7.61 breaks down the flavour SU(4) to SU(2) generated by $\{\Sigma_4, \Sigma_5, \Sigma_{45}\}$.

Similar to the ferro spin-quadrupole doublet in Eq. 7.60, there are at least four gapless modes present for the masses in this doublet. Thus, this doublet is also a Γ -DSM type semimetal. The number of these gapless modes again depends on their linear combination because of the non-compatibility of these masses and are best analysed in the $\tilde{\chi}$ basis (Eq. 7.35). In this basis, the two masses in Eq. 7.64 are given by

$$\begin{aligned} & \langle -i\tilde{\chi} \left(2\mu_{15} - \sqrt{2}\mu_8 \right) \tilde{\Sigma}_0 \tilde{\chi} \rangle / \sqrt{3}, \\ & \langle -i\tilde{\chi} \left(-2\mu_{15} + \sqrt{6}\mu_3 - 2\sqrt{2}\mu_8 \right) \tilde{\Sigma}_0 \tilde{\chi} \rangle / 3. \end{aligned} \quad (7.65)$$

such that the mass matrices have the generic form given by Eq. 7.41. Hence the $\tilde{\chi}_1$ modes are always gapless. In addition, considering linear combinations as in Eq. 7.61, for some special values of ϑ given by $\vartheta = (2n + 1)\frac{\pi}{6}$ with $n = 0, 1, \dots, 5$, there are extra gapless modes whose existence can be understood via an analysis similar to the ferro spin-quadrupolar doublet in Eq. 7.60 discussed before. However, unlike this previous case, this doublet breaks TR symmetry. So, for generic values of ϑ , the $\tilde{\chi}_1$ spinors can be gapped out by turning on the ICI mass which does not break any further symmetries. Hence the leftover gapless modes are less robust and can easily give way to a $N_F = 1$ ICI phase.

7.3 Experimental Probes for Multipolar Orders

The detection of multipolar orders in materials is an active research frontier, with most studies leveraging the coupling between these multipolar moments and the system's phonons [66, 67, 147]. Direct probing via neutron scattering techniques, which are commonly used for detecting magnetic order, faces challenges due to the weak scattering cross-section of multipolar orders.

Recent proposals have suggested that the coupling between the Goldstone modes associated with quadrupolar order and the lattice phonons can lead to a renormalization of the sound velocity in the material [147]. Crucially, the temperature dependence of this sound velocity renormalization exhibits a distinct behavior compared to other phases, providing a characteristic signature for the detection of quadrupolar density waves, such as those discussed in this chapter.

Furthermore, Raman scattering experiments have been employed to detect octupolar moments by exploiting their effect on the magnetostriction coefficient [66], which can also be utilized to probe the octupolar density waves discussed in this chapter.

Chapter 8

Phase transitions

Having described all the possible phases proximate to the SU(8) Dirac semi-metal, we now discuss some of the interesting phase transitions in this chapter. In Sec. 8.1, we discuss the transition from a octupolar quantum Hall phase to a novel $4e$ -superconducting phase. Then we discuss about unnecessary quantum critical points in Sec. 8.2. Finally, we discuss the transition from the SU(8) DSM to the stripy CDW phase in Sec. 8.3.

8.1 Transition from octupolar quantum Hall phase to a $4e$ superconductor

In this section, we discuss a novel mechanism for realizing superconductivity by condensing topological defects that carry non-zero electric charge. Similar mechanism can be realized in both single-layer and bilayer graphene systems [141, 148]. In the case of single-layer graphene, the skyrmions of the quantum spin-Hall phase carry $2e$ electronic charge, and condensation of these produces a s -wave superconductor. In this section, we discuss a similar mechanism where the skyrmions of the \mathcal{F}_{1g}^e phase (Chapter 6.1.2) carry $4e$ electric charge and condensation of these produce a charge- $4e$ superconductor.

The three masses in the \mathcal{F}_{1g}^e triplet are given by (Eq. 6.8)

$$-i \langle \bar{\chi} \Sigma_{12} \chi \rangle, \quad -i \langle \bar{\chi} \Sigma_{23} \chi \rangle, \quad -i \langle \bar{\chi} \Sigma_{13} \chi \rangle. \quad (8.1)$$

All these masses fully gap out the fermions. Also, since these masses are compatible with

each other, the spectrum remains gapped for a general linear combination

$$-i\Delta \langle \bar{\chi} (n_1 \Sigma_{12} + n_2 \Sigma_{23} + n_3 \Sigma_{13}) \chi \rangle, \quad (8.2)$$

of the masses. Here, Δ is a positive real number and $\vec{n} = \{n_1, n_2, n_3\}$ are is a unit vector such that

$$n_1^2 + n_2^2 + n_3^2 = 1. \quad (8.3)$$

One can now produce a skyrmion configuration with this order parameter by keeping Δ fixed, but varying \vec{n} slowly over space such that the skyrmion number \mathcal{W} given by:

$$\mathcal{W} = \int d^2x \frac{1}{8\pi} \epsilon_{\mu\nu\lambda} \vec{n} \cdot \partial_\nu \vec{n} \times \partial_\lambda \vec{n},$$

is non-zero. These skyrmions are topological defects of the \vec{n} field. The physical significance of a non-zero \mathcal{W} lies in the fact that the vector field $\vec{n}(\mathbf{x})$ wraps around the unit sphere \mathcal{W} times as one traces the spatial coordinates \mathbf{x} . This topological winding is quantified by the skyrmion number \mathcal{W} , which serves as a topological invariant characterizing the field configuration.

In the presence of such a skyrmion configuration, the low-energy action is given by:

$$S = \int d^2x d\tau (v_F \bar{\chi} (-i\partial + e\mathbf{A}) \chi + i\Delta \bar{\chi} (n_1 \Sigma_{12} + n_2 \Sigma_{23} + n_3 \Sigma_{13}) \chi)$$

Here, A_μ is the vector potential for the external electromagnetic field, and e is the charge of an electron. Integrating out the fermions, we get the effective action in the presence of the spatially varying \vec{n} as [149]

$$S_{eff} = \int d^3x \left(iA_\mu J_\mu^{top} + \frac{\Delta}{8\pi v_F} (\partial_\mu \vec{n})^2 \right) + i\pi N_f \Theta[\vec{n}]. \quad (8.4)$$

Here, J_μ^{top} is the topological current density given by

$$J_\mu^{top} = \frac{eN_f}{8\pi} \epsilon_{\mu\nu\lambda} \vec{n} \cdot \partial_\nu \vec{n} \times \partial_\lambda \vec{n}. \quad (8.5)$$

where $N_f (= 4)$ is the number of fermion flavors. The last term in the action is called the

θ -term and is given by

$$\Theta[\vec{n}] = \frac{\epsilon_{\mu\nu\lambda}}{24\pi^2} \int d^3x \operatorname{tr} [(U^{-1}\partial_\mu U) (U^{-1}\partial_\nu U) (U^{-1}\partial_\lambda U)] \quad (8.6)$$

where $U(x)$ is a unitary matrix such that

$$U^{-1}\Sigma_{12}U = n_1\Sigma_{12} + n_2\Sigma_{23} + n_3\Sigma_{13}. \quad (8.7)$$

The details about the derivation of the θ -term is given in Ref [150].

In the presence of a skyrmion configuration, the total electric charge of the system is given by

$$\begin{aligned} Q &= \int d^2x J_0^{top} \\ &= eN_f \int d^2x \frac{1}{8\pi} \epsilon_{\mu\nu\lambda} \vec{n} \cdot \partial_\nu \vec{n} \times \partial_\lambda \vec{n} \\ &= eN_f \mathcal{W}. \end{aligned} \quad (8.8)$$

Thus, the total charge of a skyrmion configuration depends on the skyrmion number \mathcal{W} . Therefore, a skyrmion with $\mathcal{W} = 1$ carries a $4e$ electronic charge (since $N_f = 4$ in our case). On the other hand, the statistics of the skyrmions is determined by the θ -term. It is shown in Ref. [149] that the geometric phase obtained by the ground state wave function upon interchanging two skyrmions is πN_f . Thus, in this case, the skyrmions acquire 4π phase implying that they obey bosonic statistics. Hence, condensation of such Skyrmions within a framework discussed in Ref. [141] would lead to a novel $4e$ superconductor with single electron excitations being gapped and the magnetic flux is quantized in units of $hc/4e$ [151]. This is tantamount to the *fractionalization* [152] of the elementary BCS $hc/2e$ -vortex. The above mechanism to obtain a $4e$ superconductor is rather novel and differs from the usual mechanism of BCS superconductivity, where such a $4e$ superconductor is obtained by forming a 4-electron bound state and condensing them. The novel superconductor here seems to be a natural consequence of the SOC-mediated symmetry implementation in quarter-filled $j = 3/2$ honeycomb lattices that allow binding of $4e$ charges to the topological texture of the spin-octupole order parameter.

8.2 Unnecessary quantum critical points

In this section, we delve into phases belonging to the Group-2 and Group-3 categories that exhibit unnecessary quantum critical points (UQCPs). UQCPs denote continuous phase transitions occurring within the same phase, a concept first proposed by Bi and Senthil in Ref. [153]. Conventionally, quantum phase transitions occur between distinct phases when a relevant coupling parameter reaches a critical value. However, Bi and Senthil demonstrated that such transitions can also occur within the same phase. These UQCPs manifest as high symmetry points in the parameter space, enabling any two points within the same phase to be connected while circumventing the high symmetry point. Additional instances of UQCPs are discussed in Refs. [154, 155].

Among the phases discussed in previous chapters, some feature a discrete set of special points in the order parameter space where the fermionic gap closes, while remaining gapped at adjacent points. This occurs due to the non-compatibility of mass matrices within these triplets and leads to the unnecessary quantum critical points. In this section, we offer insights into these special points, elucidating how they arise from the projection of a critical hyper-surface from a higher-dimensional parameter space onto the triplet parameter space. To illustrate this, we take the \mathcal{F}_{1u}^e and \mathcal{F}_{2u}^e triplets (Chapter 6.1.3) as an example. As discussed before, a generic linear combination of the masses in a particular triplet,

$$-i(\Delta_1 \langle \bar{\chi} m_1 \chi \rangle + \Delta_2 \langle \bar{\chi} m_2 \chi \rangle + \Delta_3 \langle \bar{\chi} m_3 \chi \rangle) \quad (8.9)$$

can be represented on the surface of a 2-sphere (as shown in Fig. 8.1). With this, there are eight points on the \mathcal{S}^2 with

$$|\Delta_1| = |\Delta_2| = |\Delta_3|, \quad (8.10)$$

where the fermionic spectrum becomes gapless (*e.g.*, point B in Fig. 8.1).

The existence of such isolated gapless points is surprising and different from the usual incompatible masses such as the chiral masses [21]. In the case of chiral masses (Chapter 5), in moving from the CDW masses to the ICI mass, one encounters an *unavoidable* line of bulk gap closing corresponding to a phase transition, across which the level of

Chern-Simons term change. However, in the case of the \mathcal{J}_{1u}^e and \mathcal{J}_{2u}^e triplets under discussion, one can conceive two different classes of lines on the sphere joining the same two gapped end-points (C and D) as shown on the sphere in the middle panel of Fig. 8.1, one not passing through the special point (the black path) and the other passing through the special point, B (the red path).

For the second path, one would naively conclude that the system goes through a *phase transition* via a critical point with higher symmetry. The situation can be understood by going back to the six inversion odd masses in Eq. 4.14 and reminding ourselves that the six masses in \mathcal{J}_{1u}^e and \mathcal{J}_{2u}^e are mutually incompatible and together form a reducible representation (Eqs. 4.19 and 4.20) of a $U(1) \otimes SU(2)$ subgroup of $SO(5)$. A generic linear combination of the six masses in this case can be represented as points on the surface of a 5-dimensional sphere, \mathcal{S}^5 , by extending Eq. 6.16 to all the six masses. On this \mathcal{S}^5 due to the incompatibility, there are extended lower dimensional regions of parameter space where the fermions are partially gapless that separates the fully gapped regions as schematically depicted in Fig. 8.1. Projection of the gapless regions from \mathcal{S}^5 to \mathcal{S}^2 for the above two triplets results in the isolated *special* points. This is most easily seen by sitting at one of the special partially gapless points on the \mathcal{S}^2 for a particular triplet (say \mathcal{J}_{1u}^e) and performing the $U(1) \otimes SU(2)$ transformation generated by Eq. 4.17 and 4.18 as discussed above. The resultant mass necessarily involves the other triplet, \mathcal{J}_{2u}^e and hence does not lie on the \mathcal{S}^2 anymore but on the gapless manifold of \mathcal{S}^5 . This is schematically shown in Fig. 8.1. Thus the special point B is the projected image of the gapless manifold on \mathcal{S}^5 to \mathcal{S}^2 and the two classes of paths between C and D mentioned above have a natural interpretation on \mathcal{S}^5 where the black (red) path avoiding (touching) the special isolated point corresponds to paths on \mathcal{S}^5 that lie within a single gapped phase but avoid (touch) the gapless manifold. Very importantly, the special point is mandated to exist under the microscopic symmetries such that a system tuned to pass through the special point B undergoes an *unnecessary phase transition* [153]. In this sense, the special points can be thought of as examples of *symmetry enforced unnecessary multi-critical points*. The multicritical points in the case of the \mathcal{J}_{1u}^e and \mathcal{J}_{2u}^e phases (Chapter 7.1.5) can also be understood in a similar way as a projection of a critical hypersurface on \mathcal{S}^5 to \mathcal{S}^2 .

Such special points are also present in the \mathcal{J}_{1u}^o and \mathcal{J}_{2u}^o phases (Chapter 7.1.6) which represent zig-zag spin-quadrupolar density waves. Here, however, we have to consider

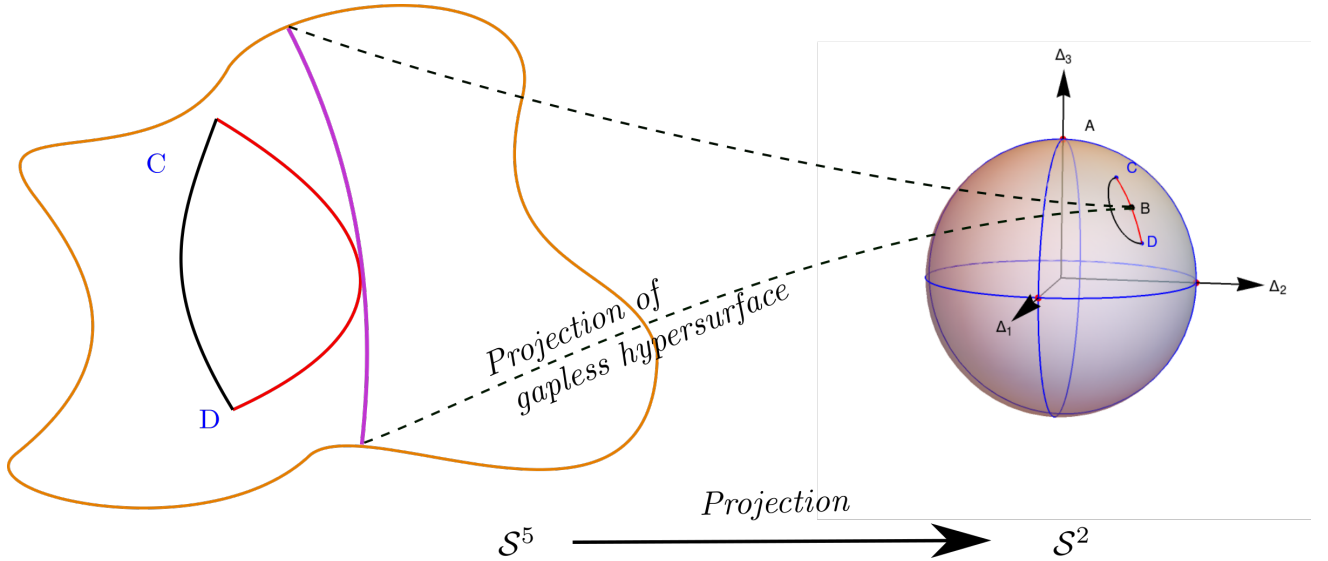


Figure 8.1: The six masses in Eq. 4.14 are mutually incompatible. A generic linear combination of such masses (similar to Eq. 6.16 extended to the six masses) can be represented on a five-dimensional sphere, \mathcal{S}^5 , as shown in the left-hand figure which has extended gapless critical hyper-lines (in magenta) separating two different phases described by the two triplets \mathcal{T}_{1u}^e and \mathcal{T}_{2u}^e (Eqs. 4.19 and 4.20). The pink line on \mathcal{S}^5 represents a hypersurface on which the fermionic spectrum is gapless (Fig. 6.2(c,f)). This hypersurface projects to the point B on \mathcal{S}^2 as shown by the dotted lines. The images of the two paths from C to D are also shown in \mathcal{S}^5 .

a 17-dimensional sphere, \mathcal{S}^{17} arising from considering an 18-dimensional incompatible vector mass comprised of the masses given by Eqs. 4.24e and 4.24f. This is made up of the four zig-zag triplets along with two \mathcal{E}_u^o doublets, the \mathcal{A}_{1u}^o and \mathcal{A}_{2u}^o singlets. Then, on projecting back to the \mathcal{S}^2 spheres spanned by each zig-zag triplet, the isolated points are obtained as a projection of the gapless parts on \mathcal{S}^{17} .

8.3 Weakly 1st order phase transition from the SU(8) DSM to the stripy CDW phase

In this section, we discuss the phase transition from the SU(8) Dirac semi-metal to the stripy CDW phase. For this, we first consider the Landau-Ginzburg action allowed by the microscopic symmetries

$$\mathcal{S} = \int d^3x (\mathcal{L}_f + \mathcal{L}_b + \mathcal{L}_{bf}) \quad (8.11)$$

where \mathcal{L}_f is the Lagrangian for the fermions given by Eq. 3.7. \mathcal{L}_b is the Lagrangian for the CDW order parameter field $\vec{\Delta}$ and is given by

$$\mathcal{L}_b = N_f \left[\frac{1}{2} |\partial_\mu \vec{\Delta}|^2 + \frac{r}{2} |\vec{\Delta}|^2 - u \Delta_1 \Delta_2 \Delta_3 + \frac{w_1}{4} |\vec{\Delta}|^4 + w_2 (\Delta_1^2 \Delta_2^2 + \Delta_2^2 \Delta_3^2 + \Delta_3^2 \Delta_1^2) \right] \quad (8.12)$$

and the coupling of the fermions to the CDW order parameter is

$$\mathcal{L}_{bf} = ig \vec{\Delta} \cdot \bar{\chi} \vec{\zeta} \chi \quad (8.13)$$

Here, r, u, w_1, w_2, g are phenomenological coupling constants. We have kept the N_f (number of fermion flavors) factor in front of the action for later convenience. Ultimately, we want to get the phase diagram in the $N_f \rightarrow \infty$ limit. Since the part of the bosonic action that comes from integrating out the fermions is already of the order of N_f , we also put the extra factor of N_f in front of the bosonic action.

It is important to note the microscopic symmetries allow for the third order term ($-u \Delta_1 \Delta_2 \Delta_3$) in the bosonic action. This term ultimately leads to an interesting phase diagram as we discuss in this section using mean-field approximation. For this purpose, we generalize the theory from $N_f = 4$ flavors of fermions to $N_f = N$ flavors of fermions with N being an arbitrary positive integer. The effective action after integrating out the fermions (from the action in Eq. 8.11) in the $N \rightarrow \infty$ approximation and also with mean field approximation (see Appendix A.13 for details) is given by

$$\begin{aligned} S_{eff} &= NV \left[\frac{r}{2} |\vec{\Delta}|^2 + \frac{w_1}{4} |\vec{\Delta}|^4 - u \Delta_1 \Delta_2 \Delta_3 + w_2 (\Delta_1^2 \Delta_2^2 + \dots) - \frac{g^2}{\pi^2} |\Delta|^2 \Lambda + \frac{g^3}{3\pi} |\Delta|^3 \right] \\ &= N \Lambda^3 V \left[\frac{\tilde{r}}{2} |\vec{\Delta}|^2 + \frac{\tilde{w}_1}{4} |\vec{\Delta}|^4 - u \tilde{\Delta}_1 \tilde{\Delta}_2 \tilde{\Delta}_3 + \tilde{w}_2 (\tilde{\Delta}_1^2 \tilde{\Delta}_2^2 + \dots) - \frac{\tilde{g}^2}{\pi^2} |\tilde{\Delta}|^2 + \frac{\tilde{g}^3}{3\pi} |\tilde{\Delta}|^3 \right] \end{aligned} \quad (8.14)$$

Here, Λ is the ultraviolet momentum cutoff and V is the total volume of the space-

time. Also, $\tilde{r}, \tilde{g}, \tilde{w}_1, \tilde{w}_2, \tilde{u}, \tilde{\Delta}_1$ etc. are dimensionless variables with

$$\begin{aligned}
\vec{\Delta} &= \vec{\tilde{\Delta}}\Lambda^{1/2} \\
g &= \tilde{g}\Lambda^{1/2} \\
r &= \tilde{r}\Lambda^2 \\
w_1 &= \tilde{w}_1\Lambda \\
w_2 &= \tilde{w}_2\Lambda \\
u &= \tilde{u}\Lambda^{3/2}.
\end{aligned} \tag{8.15}$$

Now to get the phase diagram of this theory, we minimize S_{eff} w.r.t., $\vec{\tilde{\Delta}}$. Below we present the results for various parameter regimes.

Phase diagram for $\tilde{u} = \tilde{w}_2 = 0$

We first discuss the phase diagram for $\tilde{u} = \tilde{w}_2 = 0$. In this limit, the effective action has a SO(3) symmetry which corresponds to the orthogonal rotation among the three components of the CDW order parameter. The effective action in this case is given by

$$S_{eff} = N\Lambda^3V \left[\frac{1}{2} \left(\tilde{r} - \frac{2\tilde{g}^2}{\pi^2} \right) |\vec{\tilde{\Delta}}|^2 + \frac{\tilde{w}_1}{4} |\vec{\tilde{\Delta}}|^4 + \frac{\tilde{g}^3}{3\pi} |\vec{\tilde{\Delta}}|^3 \right] \tag{8.16}$$

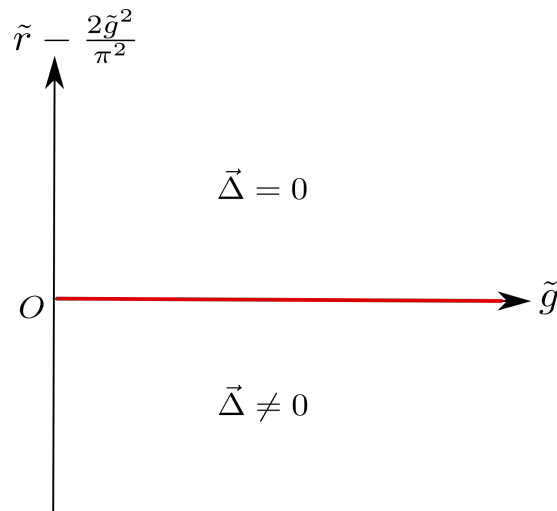


Figure 8.2: Phase diagram for $\tilde{u} = \tilde{w}_2 = 0$. The red horizontal line shows the phase boundary between the disordered and the ordered phases.

For $\tilde{r} - \frac{2\tilde{g}^2}{\pi^2} > 0$, the minima of the action is for $\vec{\tilde{\Delta}} = 0$. For $\tilde{r} - \frac{2\tilde{g}^2}{\pi^2} < 0$, the minima

occurs at

$$|\vec{\Delta}| = \frac{1}{2\tilde{w}_1} \left[-\frac{\tilde{g}^3}{\pi} + \sqrt{\left(\frac{\tilde{g}^3}{\pi}\right)^2 - 4\tilde{w}_1 \left(\tilde{r} - 2\frac{\tilde{g}^2}{\pi^2}\right)} \right] \quad (8.17)$$

The transition from the disordered to the ordered phase happens continuously. This is pictorially shown in the phase diagram in Fig. 8.2.

Phase diagram for $\tilde{u}, \tilde{w}_2 \neq 0$

We now consider the effects of including the third-order term in the effective action. Without loss of generality, we take the parameter \tilde{u} to be positive, as the solutions for negative \tilde{u} are simply related by an inversion of the order parameter vector $\vec{\Delta} \rightarrow -\vec{\Delta}$. The full effective action in this case is given by:

$$S_{eff} = N\Lambda^3V \left[\frac{1}{2} \left(\tilde{r} - \frac{2\tilde{g}^2}{\pi^2} \right) |\vec{\Delta}|^2 + \frac{\tilde{w}_1}{4} |\vec{\Delta}|^4 - u\tilde{\Delta}_1\tilde{\Delta}_2\tilde{\Delta}_3 + \tilde{w}_2 (\Delta_1^2\Delta_2^2 + \dots) + \frac{\tilde{g}^3}{3\pi} |\vec{\Delta}|^3 \right]. \quad (8.18)$$

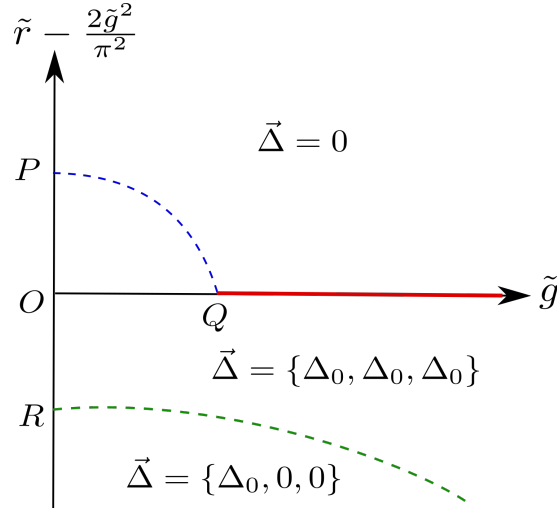


Figure 8.3: Phase diagram for $\tilde{u} \neq 0, \tilde{w}_2 \neq 0$. The red line indicates a continuous transition, whereas the dashed blue and dashed green lines represent first-order phase transitions.

The mean-field phase diagram including this cubic term is shown in Fig. 1. There are two distinct regimes in the mean-field phase diagram obtained in this case (Fig 8.3). For $\frac{\tilde{g}^3}{\pi} < \frac{\tilde{u}}{\sqrt{3}}$, there is a first order phase transition from $\vec{\Delta} = 0$ to $\vec{\Delta} = \{\Delta_0, \Delta_0, \Delta_0\}$ where $\Delta_0 > 0$. This is shown by the blue dotted line in Fig. 8.3. Along this first-order line

given by

$$\tilde{r} - 2\frac{\tilde{g}^2}{\pi^2} = \frac{2}{9\tilde{w}_1 + 12\tilde{w}_2} \left(-\frac{\tilde{g}^3}{\pi} + \frac{\tilde{u}}{\sqrt{3}} \right)^2 \quad (8.19)$$

the magnitude of the discontinuous jump in $\tilde{\Delta}_0$ is given by:

$$\delta\Delta_0 = \frac{2}{3\tilde{w}_1 + 4\tilde{w}_2} \left(-\frac{\tilde{g}^3}{\pi} + \frac{\tilde{u}}{\sqrt{3}} \right) \quad (8.20)$$

At the special point Q where $\frac{\tilde{g}^3}{\pi} = \frac{\tilde{u}}{\sqrt{3}}$, the first-order line terminates. Beyond Q , for $\frac{\tilde{g}^3}{\pi} > \frac{\tilde{u}}{\sqrt{3}}$, the transition becomes a continuous one. Thus, the third order term makes the transition first order for small values of the Yukawa coupling \tilde{g} . But, for larger values of \tilde{g} , the first-order transition becomes weaker which eventually becomes a continuous transition.

Another first order transition happens from $\vec{\Delta} = \{\Delta_0, \Delta_0, \Delta_0\}$ to $\vec{\Delta} = \{\Delta_0, 0, 0\}$ along the green dotted line shown in the Fig .8.3. Notably, the position of this green first-order line is governed by the relative strengths of the parameters \tilde{u} and \tilde{w}_2 . For a fixed value of \tilde{u} , as \tilde{w}_2 approaches zero, the green first-order line progressively shifts downward in the phase diagram. In the limit of $\tilde{w}_2 = 0$, this first-order line completely disappears from the phase diagram. Conversely, for a fixed value of \tilde{w}_2 , as the parameter \tilde{u} approaches zero, the points P and R move closer to the point O along the vertical axis, while the point Q moves closer to O along the horizontal axis. Ultimately, when \tilde{u} becomes exactly zero, the points P, Q , and R all converge at the point O . In this limiting case of $\tilde{u} = 0$, the phase diagram recovers the structure observed in Fig. 8.2, where the \tilde{u} term was absent from the effective action. This highlights the crucial role played by the \tilde{u} parameter in shaping the phase diagram and governing the existence of the weakly first-order phase transition.

Chapter 9

Modeling materials

In the previous chapters, we have discussed the the fate of the low-energy theory of the Hamiltonian (Eq. 2.23)

$$H = \sum_{\langle \mathbf{r}, \delta; \mathbf{r}', \delta' \rangle} \sum_{\alpha, \beta} \sum_{\sigma \sigma'} \Psi_{\sigma \alpha}^\dagger(\mathbf{r}, \delta) \left[\left[h_{\mathbf{r} \mathbf{r}'}^{\delta \delta'} \right]_{\alpha \beta} \delta_{\sigma \sigma'} - \lambda \mathbf{l}_{\alpha \beta} \cdot \mathbf{s}_{\sigma \sigma'} \delta_{\mathbf{r} \mathbf{r}'} \delta_{\delta \delta'} \right] \Psi_{\sigma' \beta}(\mathbf{r}', \delta') + h.c., \quad (9.1)$$

with the hopping matrix $h_{\mathbf{r} \mathbf{r}'}^{\delta \delta'}$ on the z -bond (see Fig. 2.2) being

$$\begin{aligned} h_z^{AB} &= \begin{pmatrix} t_{dd\pi} & t_{ddm} & t_{ddm'} \\ t_{ddm} & t_{dd\pi} & t_{ddm'} \\ t_{ddm'} & t_{ddm'} & t_{dd\sigma} \end{pmatrix} \\ &= t_{dd\sigma} h_\sigma + t_{dd\pi} h_\pi + t_{ddm} h_m + t_{ddm'} h_{m'}, \end{aligned} \quad (9.2)$$

in presence of strong SOC and taking the indirect hopping amplitude t_{ddm} to be the dominant. In this chapter, we provide a controlled understanding of the effect of the other hopping pathways as well as finite SOC.

The DFT estimates¹ [128] for the hopping amplitudes $t_{dd\sigma}, t_{ddm}$, etc., (see Eq. 2.20) for different materials are given in Table 9.1. The generic hierarchy of the relative strengths of the hopping parameters are found to be as follows

$$|t_{dd\sigma}| > |t_{dd\pi}| \gg |t_{ddm}| \geq |t_{ddm'}|. \quad (9.3)$$

¹The DFT studies were performed by M. Gupta and T. S. Dasgupta [128] and the details of it forms a part of the PhD thesis of M. Gupta (unpublished).

	TiX ₃			ZrX ₃			HfX ₃		
	F	Cl	Br	F	Cl	Br	F	Cl	Br
$t_{dd\sigma}$	-0.167	-0.220	-0.164	-0.546	-0.558	-0.476	-0.708	-0.666	-0.569
$t_{dd\pi}$	0.077	0.062	0.046	0.210	0.150	0.126	0.274	0.190	0.157
t_{adm}	0.058	0.078	0.079	-0.061	0.030	0.038	-0.126	0.015	0.031
t_{adm}'	-0.022	-0.030	-0.027	-0.023	-0.020	-0.020	-0.039	-0.022	-0.020
$t_{ad\pi}/t_{dd\sigma}$	-0.463	-0.281	-0.277	-0.385	-0.269	-0.264	-0.387	-0.285	-0.277
$t_{adm}/t_{dd\sigma}$	-0.351	-0.357	-0.481	0.112	-0.053	-0.081	0.178	-0.022	-0.054
$t_{adm}'/t_{dd\sigma}$	0.134	0.136	0.163	0.043	0.037	0.042	0.055	0.033	0.035
λ	0.015	0.028	0.040	0.030	0.043	0.043	0.060	0.152	0.152
$\lambda/t_{dd\sigma}$	-0.089	-0.127	-0.244	-0.055	-0.076	-0.090	-0.085	-0.228	-0.267
$\Delta=E_{eg}-E_{A1g}$	-0.030	0.050	0.039	-0.178	0.057	0.077	-0.212	0.065	0.088
$\Delta/t_{dd\sigma}$	0.180	-0.227	-0.236	0.325	-0.103	-0.161	0.300	-0.097	-0.154

Table 9.1: DFT estimated hopping terms defined for h_z^{AB} matrix (Eq. 9.2) and SOC strength(λ). The last two rows show energy splitting in t_{2g} level due to trigonal distortion. Apart from ratios, all the numbers quoted are in unit of eV. The DFT studies were performed by M. Gupta and T. S. Dasgupta [128] and the details of it forms a part of the PhD thesis of M. Gupta (unpublished). This table is taken from Ref. [128].

For understanding of generic structure of the non-interacting phase diagram in context of the different compounds and possibly others, it is useful to scale out an overall energy-scale, $\mathcal{E} = |t_{dd\sigma}| + |t_{ddm}|$, and study the rescaled Hamiltonian in terms of dimensionless coupling constants. To this end, it is useful to re-write Eq. 9.1 as

$$H = \mathcal{E} \sum_{\langle \mathbf{r}, \mathcal{J}; \mathbf{r}', \mathcal{J}' \rangle} \sum_{\alpha, \beta} \sum_{\sigma \sigma'} \Psi_{\sigma\alpha}^\dagger(\mathbf{r}, \mathcal{J}) \left[\left[H_{\mathbf{r}\mathbf{r}'}^{\mathcal{J}\mathcal{J}'} \right]_{\alpha\beta} \delta_{\sigma\sigma'} - \tilde{\lambda} \mathbf{l}_{\alpha\beta} \cdot \mathbf{s}_{\sigma\sigma'} \delta_{\mathbf{r}\mathbf{r}'} \delta_{\mathcal{J}\mathcal{J}'} \right] \Psi_{\sigma'\beta}(\mathbf{r}', \mathcal{J}') + h.c., \quad (9.4)$$

such that $H_{\mathbf{r}\mathbf{r}'}^{\mathcal{J}\mathcal{J}'}$ can be obtained by re-scaling $h_{\mathbf{r}\mathbf{r}'}^{\mathcal{J}\mathcal{J}'}$ and in particular its form on the z bond is obtained by re-scaling Eq. 9.2 as

$$H_z^{AB} = -(1 - \tau_m)h_\sigma + \rho\tau_m h_m + r(1 - \tau_m)h_\pi + \tau'_m h_{m'} \quad (9.5)$$

with

$$\begin{aligned} t_{dd\sigma} &= -\mathcal{E}(1 - \tau_m); & t_{dd\pi} &= r t_{dd\sigma}; & t_{ddm} &= \rho\mathcal{E}\tau_m; \\ t_{ddm'} &= \mathcal{E}\tau'_m; & \lambda &= \mathcal{E}\tilde{\lambda}. \end{aligned} \quad (9.6)$$

and the parameter, $\rho = \pm 1$ additionally indicates that the indirect hopping amplitude t_{ddm} can be of either sign.

In particular ZrF_3 and HfF_3 have $\rho = -1$ (see Table 9.1), making the situation markedly different from that of chlorides/bromides. This distinct difference of the fluorides arises from the following characteristic features of F – (1) much smaller ionic radius (147 pm), and (2) much higher electronegativity (3.98); compared to chlorine and bromine with ionic radii (electronegativities) of 175 pm (3.16) and 185 pm (2.96) respectively. None of the fluoride compounds have been so far synthesized and hence for the rest of this thesis, we discuss the $\rho = +1$ case in detail and discuss the case for fluorides towards briefly the end in Sec. 9.2.

9.1 Single electron phase diagram in the $\tau_m - \tilde{\lambda}$ plane

The Hamiltonian in Eq. 9.4 leads to a rich set of possibilities even at the non-interacting level which crucially decides the fate of electron-electron interactions and the low energy

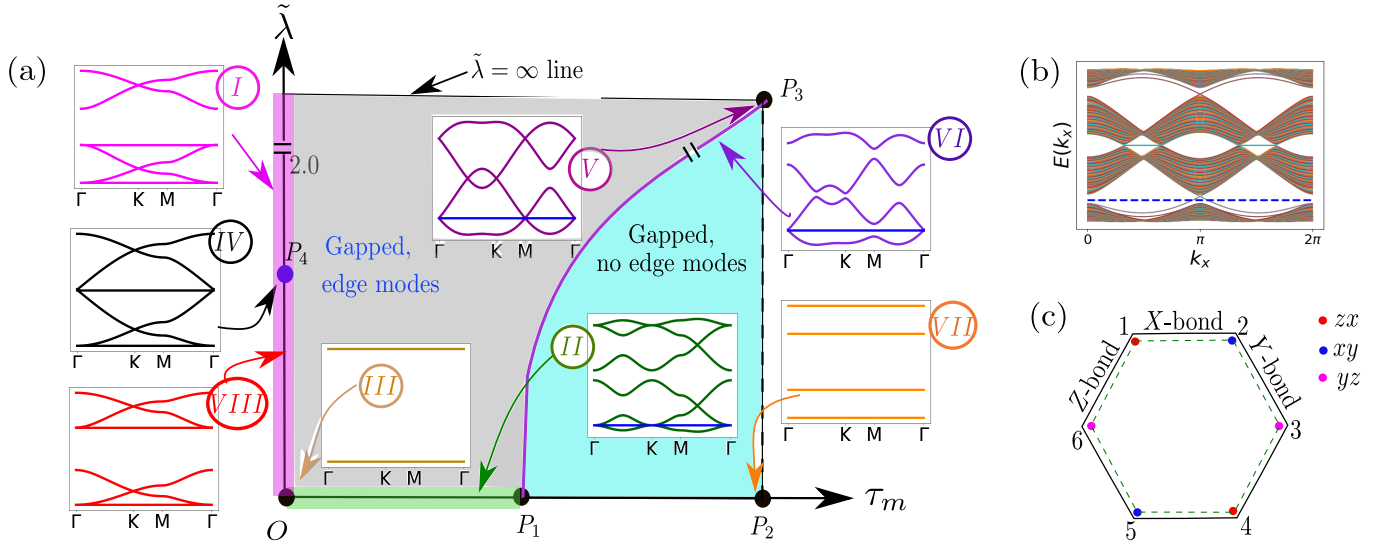


Figure 9.1: (a) Phase diagram in $\tau_m - \tilde{\lambda}$ plane for $r = 0, \tau'_m = 0, \rho = +1$. The two gapped phases are shown with different colors (gray and cyan). The vertical axis is plotted between $\tilde{\lambda} \in [0, 2.0]$. For larger values, no new phases appear and this feature for very large $\tilde{\lambda} (\rightarrow \infty)$ is shown through extrapolation as shown by the break lines on the vertical axis. The band structures, plotted along the Γ, K and the M points of the BZ. at different points on the phase diagram are shown as insets. The blue horizontal lines in the insets *II, V* and *VI* show the position of the Fermi level. In the inset *II*, both the bands are six-fold degenerate as explained in the text. The insets *V* and *VI* are for very large value of $\tilde{\lambda}$ and hence the only the four lower energy $j = 3/2$ bands are shown. (b) Band structure in the topological gapped phase (for $\tau_m = 0.9, \tilde{\lambda} = \infty, r = 0, \tau'_m = 0$) in cylindrical geometry. The edge modes at the Fermi-energy are shown by the blue solid line, with Fermi level marked in dashed line. (c) A single hexagon showing the origin of molecular orbitals at point P_2 of the phase diagram in Fig 9.1(a). Different colored dots represent three t_{2g} orbitals. The six sites of the hexagon are labeled with numbers from 1 to 6. The symmetric linear combination of the orbitals connected by the green dotted line form the lowest energy band. Other orbitals are localized on singles bonds of the hexagon are shown by black dotted lines. See text for details.

phases. While in actual materials all the parameters are present, we unfold the story in steps, by following the hierarchy of different energy scales, and introducing them one by one. This provides understanding at the model level, the influence of each distinct hopping terms in the resulting phases.

The first principle calculations [128] show that the major deviation from the indirect hopping model discussed in Ref. [156, 157] is the direct hopping given by $t_{dd\sigma}$. The simplest model, therefore consists of $t_{dd\sigma}, t_{ddm}$ and λ , setting the other subleading terms, $t_{dd\pi}$ and $t_{ddm'}$ zero. This gives rise to a phase diagram in the $\tau_m - \tilde{\lambda}$ plane, such that the $\tau_m = 0(1)$ corresponds to the purely direct (indirect) hopping limits at different values of SOC with $r = \tau'_m = 0$. Having discussed this phase-diagram of the minimal possible

model, capturing the interplay of direct and indirect hopping, we next sequentially turn on $t_{dd\pi}$ and $t_{ddm'}$, and examine the $\tau_m - \tilde{\lambda}$ phase diagram by first setting $r=-0.3$, and then setting $\tau'_m = -\tau_m$. We note that the importance of direct metal-metal interaction, over the conventional description of ligand-mediated interaction in description of phenomenology of transition metal compounds, has been acknowledged in recent time, in context of cobaltates [158].

9.1.1 $\tau_m - \tilde{\lambda}$ phase diagram with $r = \tau'_m = 0$

The phase diagram in the $\tau_m - \tilde{\lambda}$ plane is shown in Fig. 9.1(a). The top right corner, $P_3(\equiv (\tau_m = 1, \tilde{\lambda} = \infty))$ corresponds to infinite SOC in the purely indirect hopping limit. This, for d^1 gives rise to SU(8) Dirac semi-metal (DSM) as discussed in Ref. [156]. At P_3 , the six t_{2g} orbitals (including spin degeneracy) split up into four $j = 3/2$ and two $j = 1/2$ orbitals as already discussed in Chapter 2.4. The $j = 3/2$ and the $j = 1/2$ states are separated by infinite energy gap ($\propto \tilde{\lambda}$) with the $j = 3/2$ orbitals being of lower energy. Hence at this point we obtain the 1/4th filled $j = 3/2$ orbitals whose band structure is shown in inset (V) of Fig. 9.1(a). As already discussed in Chapter 3, the lowest band linearly touches the upper band at the Γ and the M points of the BZ giving rise to four 4-component Dirac fermions sitting at four valleys – the three M points of the BZ and one at the Γ point that constitutes the SU(8) DSM [156]. Remarkably, almost the entire phase diagram, except the pink and green shaded parts along the $\tau_m = 0$ and $\tilde{\lambda} = 0$ axis, can be understood from this SU(8) limit as we now discuss.

On moving away from the SU(8) point, all the Dirac fermions get gapped out, generically giving rise to band insulators. However the nature of these two band insulators obtained in the two extreme limits of changing τ_m or $\tilde{\lambda}$ away from P_3 , are different. One of them – that obtained by varying only τ_m – is a free fermion symmetry protected topological phase (SPT) [13], as is evident from the gapless edge modes plotted in Fig. 9.1(b). These edge modes are protected by time reversal symmetry. Indeed, out of the 24 distinct ways of gapping out the SU(8) Dirac fermions discussed in Ref. [156], there are precisely two different time reversal invariant lattice (\mathcal{A}_{1g}^e) singlet masses where we have used the notations of Ref. [156] for ready reference. The above two band insulators correspond to these two singlets as detailed in Appendix A.15. The two insulating phases are separated by a phase transition denoted by the magenta curve connecting the points P_3 and

$P_1 \equiv (\tau_m = 0.67, \tilde{\lambda} = 0)$. On this line, only the Dirac fermions at the Γ point become gapless while those at the three M -points remain gapped across the transition as shown in the band-structure (VI) in Fig. 9.1(a). The resultant theory has an enhanced SU(2) symmetry as detailed in Appendix A.15.

In Fig. 9.1(a), diametrically opposite to P_3 is the point $O \equiv (\tau_m = 0, \tilde{\lambda} = 0)$ which describes the purely direct hopping model via $t_{dd\sigma}$ without SOC. Here, the hopping Hamiltonian (Eq. 9.4) reduces to a particularly simple form, given by

$$H = -\varepsilon \sum_{\sigma=\uparrow\downarrow} \left(\sum_{\langle \mathbf{r}, \delta; \mathbf{r}', \delta' \rangle \in z\text{-bonds}} \Psi_{\sigma, XY}^\dagger(\mathbf{r}, \delta) \Psi_{\sigma, XY}(\mathbf{r}', \delta') + \sum_{\langle \mathbf{r}, \delta; \mathbf{r}', \delta' \rangle \in x\text{-bonds}} \Psi_{\sigma, YZ}^\dagger(\mathbf{r}, \delta) \Psi_{\sigma, YZ}(\mathbf{r}', \delta') + \sum_{\langle \mathbf{r}, \delta; \mathbf{r}', \delta' \rangle \in y\text{-bonds}} \Psi_{\sigma, ZX}^\dagger(\mathbf{r}, \delta) \Psi_{\sigma, ZX}(\mathbf{r}', \delta') \right) + h.c. \quad (9.7)$$

such that on the $z/x/y$ -bonds (See Fig. 2.1) respectively only the $XY/YZ/ZX$ -orbitals hop. Since each set of bonds forms a disconnected network of dimers that rotate into itself under C_3 , we get bonding and anti-bonding orbitals of the respective types on each of the three bonds resulting in two sets of 6-fold (including spin $\sigma = \uparrow, \downarrow$) degenerate flat band as shown in inset (III) of Fig. 9.1(a). This kind of separation of the energy bands into two groups of three bands is also seen in the DFT band structures for ZrCl_3 [128] where the direct overlap $t_{dd\sigma}$ dominates (as given in Table 9.1).

The fact that the entire OP_1 segment on the $\tilde{\lambda} = 0$ line is gapless is expected on very general grounds and is in fact dictated by the general structure of the phase diagram starting from the SU(8) symmetric point, P_3 . This can be rationalized based on that fact on this line there is an enhanced SU(2) spin rotation symmetry such that this line cannot be a part of the free fermion SPT lying above it for finite $\tilde{\lambda}$ — as predicted by the SU(8) theory. The trivial insulating phase (shown in cyan in Fig. 9.1(a)) of course can be connected to the spin-rotation symmetric segment P_1P_2 continuously. Finally at the point $P_2 \equiv (\tau_m = 1, \tilde{\lambda} = 0)$, the bands become flat again with a degeneracy of 2-4-4-2 (inset (VII) of Fig. 9.1(a)). At this point (P_2), the lowest band is made up of spin-degenerate *molecular orbitals* of the type shown in Fig. 9.1(c) at each hexagon. On deviating from this point, these orbitals acquire dispersion. Hence the entire gapped trivial insulator (shown in cyan in Fig. 9.1(a)) can be understood in terms of these effective eigenmodes.

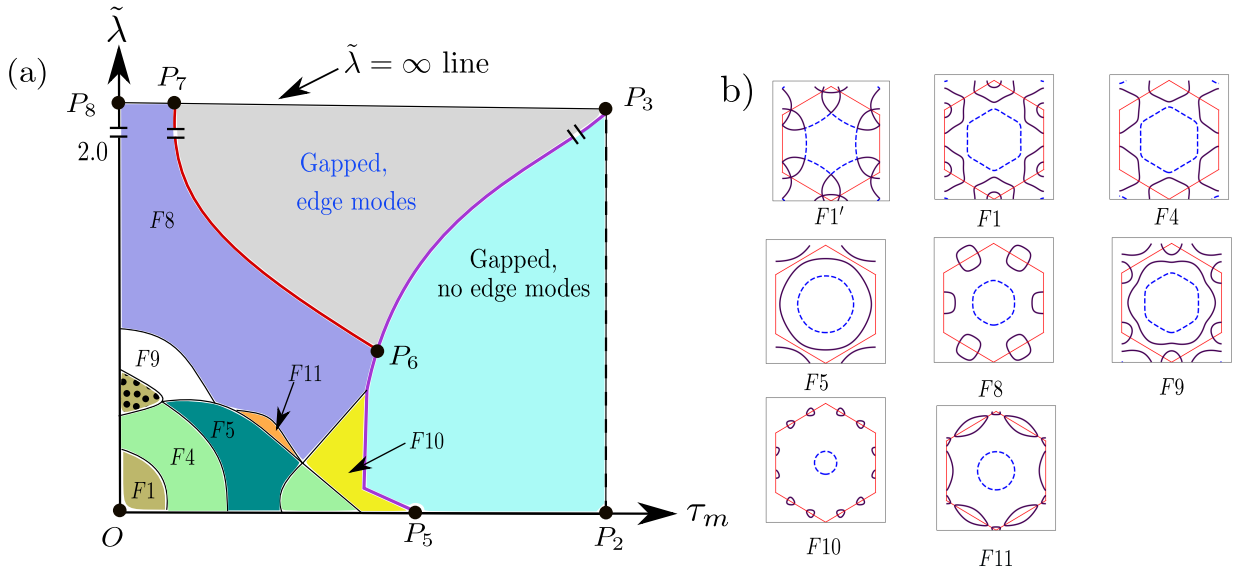


Figure 9.2: (a) Phase diagram for $\rho = +1$, $r = -0.3$, $\tau'_m = 0$. Two gapped phases shown in gray and cyan shading. The different metallic phases are shown with different colors and labeled as $F1, \dots, F11$. (b) Fermi surfaces corresponding to different metallic phases. The hole-like Fermi surfaces are shown with blue dashed lines and the electron-like FS are shown with solid violet lines. The hexagonal BZ is shown with red solid lines. The $F1'$ Fermi surface corresponds to the O point of the phase diagram shown in panel (a). The un-dotted and dotted region of $F1$ differ by the fact for the Fermi surface corresponding to the dotted region, one of the Fermi pockets around the K points is electron-like and the other is hole-like, while both are electron-like for the un-dotted region.

On increasing the SOC ($\tilde{\lambda}$) along the $\tau_m = 0$ line in Fig. 9.1(a), the six-fold symmetry is independently lifted in the bonding and anti-bonding sectors without intermixing for small $\tilde{\lambda}$ as shown in inset (VIII) of the figure. The band structure (inset (VIII)) is very similar to that of monolayer Kagome band structure [159] – for both the bonding and anti-bonding sectors – with the lower dispersing band touching the flat band quadratically at the Γ -point of the BZ. As one increases the SOC, the band-width of each of the two sectors increases while retaining their overall shape such that at the point $P_4 \equiv (\tau_m = 0, \tilde{\lambda} = 1.35)$ the bands touch at the Γ point leading to a spin-1 Dirac dispersion [160] at the touching of the two sectors (inset (IV) of Fig. 9.1(a)). On increasing SOC further, remarkably the second flat band – previously associated with the anti-bonding sector – detaches from it and becomes a part of the bonding sector leading to a division of four lower bands and two higher bands (inset (I) of Fig. 9.1(a)) – as expected from the $j = 1/2$ and $j = 3/2$ splitting of the atomic orbitals at large SOC. For d^1 materials, however, the above change of band structure is not important as only the lowest flat band is filled such that the chemical potential lie at the lowest quadratic band touching points leading to a very unstable (to interactions) quadratic band-touching semimetal with one of the flat bands having divergent effective mass.

The above structure of the phase diagram gives a good starting point to connect to the DFT band structure by incorporating the sub-leading interactions as we now turn to discuss. Two such important sub-leading parameters are $t_{dd\pi}$ and $t_{ddm'}$ representing the sub-leading direct and indirect hopping respectively (see Eqs. 2.20 and 9.6 as well as Table. 9.1). We study their effects as a build up to the material phase diagram.

9.1.2 Effect of $t_{dd\pi}$

The first sub-leading hopping that is relevant across all the compounds is the direct hopping via the π -overlap denoted by $t_{dd\pi}$ and incorporated via the parameter $r = t_{dd\pi}/t_{dd\sigma}$ in our effective tight-binding Hamiltonian (Eq. 9.4) as shown in Eq. 9.6. However, instead of scanning the entire phase diagram as a function of r , we shall confine ourselves to $r = -0.3$ – a value which is roughly consistent for the different materials. The resultant phase diagram is shown in Fig. 9.2.

The P_2P_3 line of Fig. 9.2(a) is exactly equivalent to that of Fig. 9.1(a) and hence the description of the entire trivial gapped band insulator in cyan region remains same

apart from the quantitative renormalization of the band structure away from the $\tau_m = 1$ line. Similarly, the physics of the $\tilde{\lambda} = \infty$ for $\tau_m < 1$ holds until the point P_7 giving rise to the Z_2 free fermion SPT (gray region) with gapless edge modes, exactly in the case of $t_{dd\pi} = 0$ in Fig. 9.1(a). The intermediate line, P_3P_6 , hence is associated with a Dirac band-touching at the Γ -point of the BZ giving rise to a SU(2) DSM. However, the effect of $t_{dd\pi} = r|t_{dd\sigma}| \propto (1 - \tau_m)$ drastically rearranges the band structure for lower τ_m , as we discuss now.

The $t_{dd\pi}$ lifts the threefold degeneracy of the flat bands at the point $O = (\tau_m = 0, \tilde{\lambda} = 0)$ leading to dispersive bands that cross the chemical potential giving rise to a compensated band metal such that the net Luttinger volume is zero. The relevant Fermi surface is named $F1'$ and is shown in Fig. 9.2(b). However, this is highly unstable due to the touching of the hole and particle Fermi pockets and on increasing both τ_m and $\tilde{\lambda}$, the resultant Fermi surface undergoes topological changes giving rise to a plethora of compensated band metals denoted by $F1 - F11$ in Fig. 9.2(a). The intervening Lifshitz transitions [161, 162] include cases where both separate sheets of Fermi surfaces merge, e.g. $F4$ to $F5$ via van-Hove singular necks, as well as, instances where individual sheets of Fermi surfaces disappear, e.g. $F1$ to $F4$. This generic appearance of the compensated band metals with diverse Fermi-surface topology is particularly relevant to the materials under consideration as we discuss in the next section in detail along with the relevant Lifshitz transitions.

We would like to end this discussion about the effect of $t_{dd\pi}$ by commenting on the metals $F1 - F11$ (Fig. 9.2(a)) that occupy the region that was erstwhile (Fig. 9.1(a)) a part of the topological insulator. Interestingly for $F8$, the electron bands evolve continuously from the free fermion SPT and hence it inherits a non-trivial Z_2 invariant for the bands crossing the chemical potential. In fact, except on the $\tilde{\lambda} = 0$ line, we find that for all the metals in the phase diagram under consideration, one of the bands crossing the chemical potential has non-trivial Z_2 index, calculated following the method discussed in Ref. [163]. The method is applicable for systems with inversion symmetry, as is in the present case.

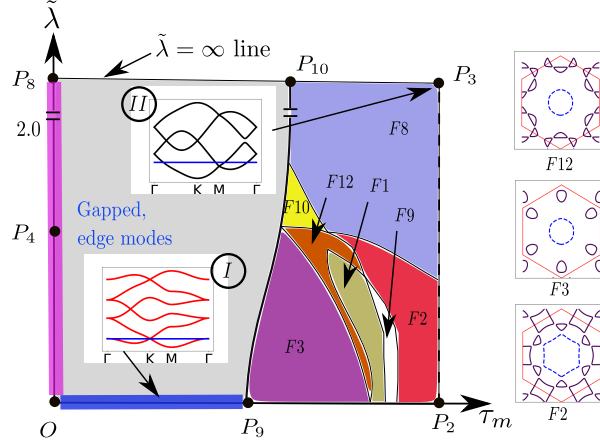


Figure 9.3: Phase diagram for $r = 0, \tau'_m = -\tau_m, \rho = +1$. Inset *I* shows a prototypical band structure for a point on the OP_9 line where the lowest band touches the next band linearly at the K points, while the inset *II* shows the band structure at the P_3 point. Since $\tilde{\lambda} = \infty$ at P_3 , only four bands ($J = 3/2$ bands) are shown in inset *II*. As in Fig.9.2(a), metallic phases with different Fermi surface topology, are labeled and colored. In addition to $F8, F9$ and $F10$, introduced in Fig.9.2(a), three new phases, labeled as $F2, F3$ and $F12$ appear. The Fermi surface topology for $F2, F3$ and $F12$ phases are shown by the side.

9.1.3 Effect of $t_{ddm'}$

We now turn to the effect of the indirect hopping mediated by $t_{ddm'}$ on the minimal model with phase diagram in Fig. 9.1(a). Again we choose a representative value of $t_{ddm'} = -t_{ddm}$ in the regime relevant to the materials – to indicate its effect. Unlike $t_{dd\pi}$, this indirect hopping now drastically reorganizes the $\tau_m \approx 1$ region of the phase diagram – apparent by contrasting Fig. 9.1(a) with Figs. 9.2(a) and 9.3.

In particular, the line $\tau_m = 0$ remains unaltered with respect to the minimal model (Fig. 9.1). Also, the free fermion SPT (in gray in Fig. 9.3) is stable to finite $t_{ddm'}$, albeit it does not extend all the way to the point P_3 . In fact, the $SU(8)$ Dirac point (P_3) now develops into a compensated band metal as the Dirac cones, at the erstwhile P_3 point, moves away from the chemical potential in opposite direction – the Dirac node at the Γ point moves above it and those at the M points move below it – giving rise to Fermi pockets around these points. The band structure at the P_3 point is shown in inset *II* of the phase diagram in Fig. 9.3. The resultant Fermi surface around this point is of $F8$ type given in Fig. 9.2(b).

As we move away from the P_3 point along the $\tilde{\lambda} = \infty$ line by decreasing τ_m (thus increasing $t_{dd\sigma}$), the $F8$ Fermi surface continues to exist, although a finite gap at the

M and the Γ opens up (away from the chemical potential) between the lowest and the second lowest band. This gap opening due to the effect of $t_{dd\sigma}$ gives a non-trivial Z_2 number to the lowest band and hence the $F8$ metal in the phase diagram in Fig. 9.3 is a topological metal. On moving further away from the P_3 point along the $\tilde{\lambda} = \infty$ line, the size of the Fermi pockets of the $F8$ metal continuously shrink and eventually vanish at the P_{10} point after which the system enters into a gapped phase. Since this transition from the $F8$ metal to the gapped phase does not happen through a band touching, the Z_2 invariant of the lower band remains unchanged across this transition and hence the gapped phase is also topological insulator– the same free fermion SPT as in Fig. 9.1.

Turning to low SOC, the P_2 point no longer has flat bands but now gains a dispersion due to τ'_m leading to a compensated metal of Fermi surface type $F2$ as shown in Fig. 9.3. On moving from the point away from the P_2 point along the $\tau_m = 1$ line, the $F2$ Fermi surface transforms into a $F8$ type Fermi surface, which is then connected to the P_3 point. This $F8 - F2$ transition does not involve any band touching, but just a change of the chemical potential and hence the $F2$ region of the phase diagram is also a topological metal. On reducing the values of τ_m from the point P_2 , the system encounters various other metallic phases which have different Fermi surfaces ($F9, F1, F12, F3$ etc.). We find that for all these phases, the bands crossing the Fermi energy always have a nontrivial Z_2 index. Thus, all the metals in this phase diagram are also topological metals.

Finally, on the line OP_8 , $\tau_m = \tau'_m = 0$ and hence the description of this line is the same as in the phase diagram in Fig. 9.1. On the other hand, along the OP_9 line (for which $\tilde{\lambda} = 0$), the lowest band touches the upper band linearly at the K points. The effect of finite $\tilde{\lambda}$ opens up gap at the K points and the system enters into the topological gapped (gray shaded region).

9.1.4 The material phase diagram

Having discussed the minimal tight-binding model and the effect of the sub-leading hopping terms resulting in a rich single-particle phase diagram, we now turn to the regime that may be most suited to the material parameters, except for the fluorides. To this end we choose the representative hyperplane given by $\rho = +1, r = 0.3, \tau'_m = -\tau_m$ and vary $\tau_m \in (0, 1)$ and $\tilde{\lambda} \in (0, \infty)$.

The phase diagram in this parameter regime is shown in Fig. 9.4. Due to the comple-

mentary effects of the secondary direct and indirect hopping $-t_{dd\pi}$ and $t_{ddm'}$ respectively – the resultant phase diagram is in a way superposition of Figs. 9.3 and 9.2(a) such that all the phases appearing in this case are gapless, perfectly compensated and have Fermi surfaces with at least one partially filled band having non-trivial Z_2 invariant.

Based on which particular band(s) carry non-trivial Z_2 , the phase diagram can be demarcated by red, magenta and blue lines (see Fig. 9.4). The Z_2 index for the lowest band is non-zero for the region of the phase diagram which is in the right hand side of the red solid line. On the other hand, the second lowest band has nontrivial Z_2 index for the regions of the phase diagram which are either left to the red solid line or right to the magenta solid line. On the red line, the lowest and the second lowest bands touch at the M point and the Z_2 character of the two bands switch. On the magenta line, the second lowest band touches the third lowest band and thus encounters another change in Z_2 character. The third lowest band, which crosses the Fermi energy only at the $F1$ region which is near the origin O , has non-trivial Z_2 index for the region which is left to the blue solid line in the phase diagram. On this blue line, the third lowest band touches the fourth lowest band and encounters a change in Z_2 character.

The positioning of the materials ZrX_3 , TiX_3 and the HfX_3 ($X = Cl, Br$) in the phase diagram, based on the estimated parameters given in Table 9.1 is shown in zoomed plots given in Fig. 9.4. Due to weaker SOC compared to the strength of leading hopping interactions, the studied compounds are all placed towards the bottom of the phase diagram. Given the fact, that $t_{dd\sigma}$ (t_{ddm}) is significantly larger (smaller) in Zr/Hf compounds compared to Ti compounds, as expected, Zr and Hf compounds are placed left to Ti compounds. Given the similarity in electronic structure of Zr and Hf compounds (see Fig. 3), it is not surprising that they belong to the same $F4$ class, with Hf compounds lying higher in position compared to Zr, due to stronger SOC. On the other hand, Ti compounds belong to distinctly different $F5$ class. Systematically, bromine compounds lie higher and right to chlorine compounds, due to stronger SOC and weaker direct hopping strength, respectively.

The detailed Fermi surface(FS)s of the compensated, topological metallic phases of the six compounds are shown in Fig. 9.5. The $F4$ type FS of ZrX_3 and HfX_3 compounds is characterized by three disjoint Fermi pockets– two electron-like pocket around the two K points and one hole-like pocket around the Γ point. On the other hand, the TiX_3

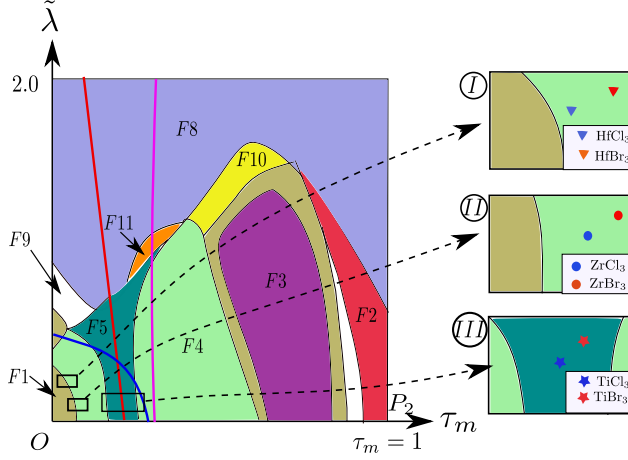


Figure 9.4: Phase diagram for $\rho = +1$, $r = -0.3$, $\tau'_m = -\tau_m$ with $0 \leq \tau_m \leq 1$ and $0 \leq \tilde{\lambda} \leq 2.0$. For $\tilde{\lambda} > 2.0$, the $F8$ phase continues to exist. The six different chloride/bromide compounds are placed in this phase diagram, according to the estimated parameter values of the low energy Hamiltonian (cf. Table 9.1), shown in the insets *I*, *II* and *III*. The phase diagram is demarcated by the red, blue and magenta lines, according to the Z_2 characters of the bands. See text for details.

compounds having $F5$ -type FS, have two Fermi pockets, one electron-like and one hole-like around the Γ point.

9.1.5 Nesting and Lifshitz transitions

A characteristic feature of some of the FSs in Fig. 9.5 are the flattish *almost nested* sections – involving both intra and inter-pockets. This makes them particularly susceptible to nesting instabilities in presence of electron-electron interactions at appropriate wave-vectors. Our preliminary results indeed indicate enhanced susceptibilities in the charge-density-wave channel due to such nesting. The detailed characterization of such instabilities though require more accurate study particularly due to the intricate structure of the FS's involved.

Another feature of the phase diagram is the presence of plethora of Lifshitz phase transitions [161, 162] between the variety of compensated metals (Fig. 9.4). These phase transitions involving a change in the Fermi surface topology can be classified into two broad categories [161, 164] – (1) *pocket vanishing* type associated with disappearance of new segments of Fermi surface *e.g.*, between $F1$ and $F4$ where the Fermi pockets centered around the BZ corners appear– possibly relevant for $Zr(Hf)Cl_3$ and $Zr(Hf)Br_3$, and, (2) *neck collapsing* type associated with merging of two segments of Fermi surfaces *e.g.*, the transition between $F4$ and $F5$ where two particle-like Fermi pockets develop a

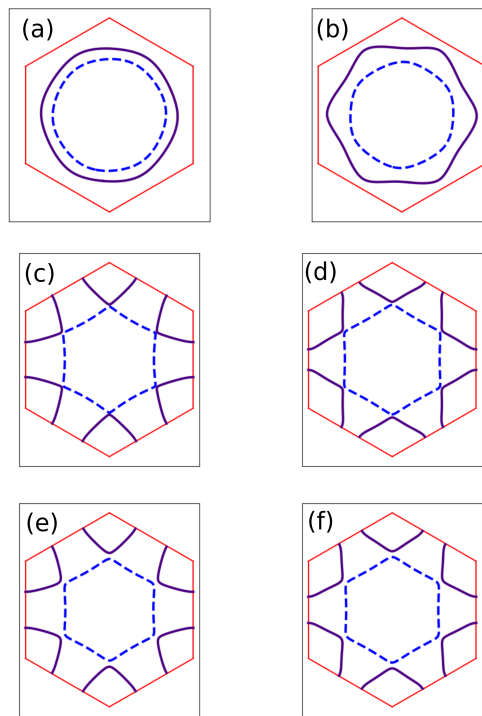


Figure 9.5: Fermi surfaces for (a) TiCl_3 , (b) TiBr_3 , (c) ZrCl_3 , (d) ZrBr_3 , (e) HfCl_3 , (f) HfBr_3 . The (a) and (b) are $F5$ -type Fermi surface while the rest are $F4$ type. The blue dotted lines show hole-like Fermi surface and the solid indigo colored lines show electron-like Fermi surface. The red line shows the boundary of the hexagonal BZ.

neck that meets at the M points possibly relevant for TiCl_3 and TiBr_3 . These transitions, accessed, in the present case, by tuning the band parameters at a particular filling, occur due to the change of the band-structure at the chemical potential. While the former leads to a step function in the single-particle density of states, $\rho(\epsilon - \epsilon_F) \sim \theta(\epsilon - \epsilon_F)$, the latter has a logarithmic singularity, *i.e.*, $\rho(\epsilon - \epsilon_F) \sim -\ln|\epsilon - \epsilon_F|$ and hence has a van Hove singularity arising from the vanishing Fermi velocity for the electrons on the Fermi surface. This singular behavior can be reflected in thermodynamic measurements such as magnetic susceptibility [164] as well as scaling of bipartite entanglement entropy [165]. Interestingly, the tuning of the band parameters can be achieved through bi-axial straining which should be achievable considering the layered structure of the materials similar to SrRuO_4 [166]. Considering about 2% compressive strain on ZrCl_3 , the direct $dd\sigma$ hopping is found to enhance by about 20% while the indirect hopping is found to be heavily suppressed, thereby conducive to triggering a $F4 \rightarrow F1$ transition. This may be even easier for Hf compounds, which are even closer to the $F4$ - $F1$ boundary. DFT calculated FS for 1% strained Hf compound, indeed shows a $F1$ type [128]. Straining on Ti compounds shows similar effect, although the percentage change is found to be much smaller. Therefore, such straining may be of interest in investigating the physics of the Lifshitz transition.

9.2 $\rho = -1$: Implication for Fluorides

Having discussed the situation with the chlorides and the bromides, we now turn to fluorides, which as indicated above (cf Table 9.1) show markedly different electronic structure. Furthermore, unlike chlorides and bromides, the tight-binding parameters for fluorides show diverse behavior even among the 3d, 4d and 5d transition metals, the parameters for Ti being rather different from that of Zr/Hf. This hinders providing a universal framework to describe the three fluoride compounds, captured through a common phase diagram, as was possible for chlorides and bromides. We thus concentrate on the most striking difference between Zr/Hf chlorides and bromides, and Zr/Hf fluorides, namely the change in sign of the indirect hopping, t_{ddm} , captured by the parameter ρ in Eq. 9.6. This affects some of the basic conclusions stemming from the structure of the minimal phase diagram, presented in Fig. 9.1. In the following, we thus confine ourselves

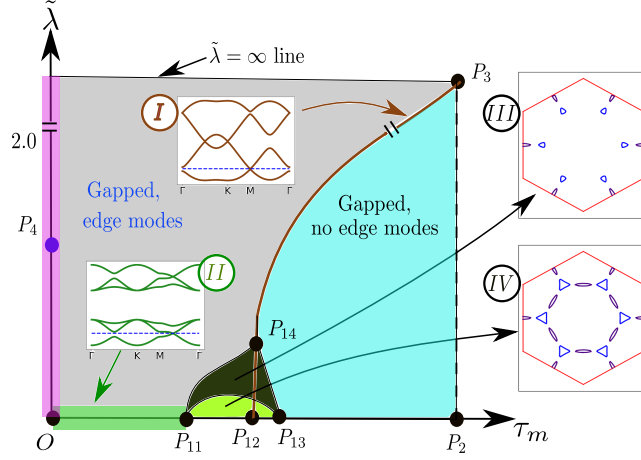


Figure 9.6: $\tau_m - \tilde{\lambda}$ phase diagram with $\rho = -1, r = 0, \tau'_m = 0$. The two gapped phases, shaded as gray and cyan, as well as pink coloured lines in the phase diagram are identical to those in Fig 9.1(a). The band structures on a typical point on the OP_{11} line is shown in inset II. The inset I shows the band structure on the transition line between the two gapped phases. Note that inset I shows only four bands since it is drawn for a large value of $\tilde{\lambda}$ where the four lower energy $J = 3/2$ orbitals are separated from the higher energy $J = 1/2$ orbitals by a large energy separation. As opposed to Fig 9.1(a), this phase diagram hosts two topological metallic phases, marked in lime-green and dark green shades. The Fermi surfaces for the two metallic regions are shown by insets III and IV.

to the $\tau_m - \tilde{\lambda}$ phase diagram, which determines the nature of the low energy single-particle starting point for these materials, without delving into the complexity of the sub-leading hopping like $t_{dd\tau}$ and t_{ddm} . The obtained results are shown in Fig. 9.6, which should be contrasted with Fig. 9.1(a).

First of all, we notice a similarity of the phase diagrams in Fig. 9.6 and Fig. 9.1(a), especially for large $\tilde{\lambda}$. This apparent similarity, however, hides an important contrast that can be best understood as follows. Starting from the SU(8) limit, P_3 in the present case is a *particle-hole* inverted version of Fig. 9.1(a) due to the change in sign of t_{ddm} . Thus, while the P_3 still gives a SU(8) DSM with four 4-component Dirac points at Γ and three M points, the associated spinors are not necessarily the same as in the previous case, but are related to it via a microscopic particle-hole transformation. In fact, this theory is therefore a particle-hole conjugate version of the SU(8) metal discussed in Ref. [156] and hence the same mass analysis can be applied to the present case. It is for this reason, we still have the same two gapped phases– the free fermion topological and trivial band insulators on deviating away from the SU(8) semi-metal– resulting from the two lattice singlet masses [156]. However, the difference in the eigen modes due to the

change in sign becomes apparent at the transition between the two insulators, which now is brought about by closing of the gap at the three M points on the line P_3P_{14} while that at the Γ point remains gapped— unlike in case for P_3P_1 line in Fig. 9.1(a). This leads to an enlarged SU(6) internal symmetry for the $N_F = 3$ free Dirac fermions on the P_3P_{14} line (see Appendix A.10).

Another consequence of the above change in the nature of the spinors is the appearance of additional compensated semi metals for lower values of $\tilde{\lambda}$ around $t_{dd\sigma} \sim t_{ddm}$. The corresponding Fermi surfaces are shown in insets *III* and *IV*. The lowest bands of these metals have non-zero Z_2 index on the closed region $P_{11}P_{12}P_{14}$, while the upper band is Z_2 -trivial. On the line $P_{12}P_{14}$, the lowest band touches the upper band at the M points and the Z_2 indices of these two bands switch. Thus, one of the bands of these metals always has non-zero Z_2 index and these are topological metals. On the $P_{13}P_{14}$ line, Fermi pockets of the metals shrink to zero and the system enters the trivial insulating phase. Hence, the change of sign of the indirect hopping makes the situation more favorable to the topological metallic phase, which may be stabilized even without inclusion of sub-leading hopping terms.

Chapter 10

Summary

This doctoral thesis conducts a comprehensive investigation into the low-energy physics of the d^1 honeycomb materials in the presence of spin-orbit coupling (SOC). The first part of the thesis focuses on the regime where the indirect hopping term t_{ddm} dominates and the SOC strength is strong. In this limit, the low-energy theory is described by a (2+1)-dimensional Dirac theory endowed with an enhanced SU(8) symmetry.

A key aspect of this theory is the non-trivial implementation of the microscopic symmetries on the low-energy spinor degrees of freedom arising because of strong SOC. In the presence of short-range interactions, we identify 64 distinct gap-opening instabilities of the Dirac theory. These instabilities are systematically classified according to their transformation properties under the microscopic symmetries, resulting in the identification of 24 distinct phases. The non-triviality of the symmetry implementation is reflected in the nature of the phases obtained in this process.

These 24 phases are organized into three broad categories based on how they break the SU(8) symmetry. Group-1 consists of two phases that break the chiral SU(2) symmetry while preserving the flavor SU(4) symmetry. Group-2 encompasses all the generalized quantum Hall phases which spontaneously break the flavor SU(4) symmetry while preserving the chiral SU(2) symmetry. Group-3 comprises phases that break both the flavor SU(4) and chiral SU(2) symmetries. The phases in this group include density waves, some of which exhibit non-trivial topological properties. Remarkably, the non-trivial symmetry implementation on the low-energy degrees of freedom gives rise to intriguing density wave semi-metallic phases group-3, where certain fermionic bands remain gapless while others acquire a gap, highlighting the profound consequences of the intricate symmetry

realizations in these systems.

The thesis further explores several intriguing phase transitions. One finding is the proposal that the condensation of skyrmions from the \mathcal{J}_{1g}^e octupolar quantum Hall phase can lead to the realization of an unconventional charge-4e superconductor. Additionally, the work unveils phases exhibiting unnecessary quantum critical points in the parameter space, a phenomenon arising from the incompatibility of the mass matrices, which eventually comes about because of the non-trivial symmetry implementation. Furthermore, the phase transition from the SU(8) symmetric Dirac semi-metal to the chiral stripy charge-density wave phase is investigated within the mean-field approximation, which shows a weakly first-order transition.

The second part of the thesis investigates the nearest-neighbor hopping model for d^1 honeycomb materials in a generalized regime, considering the effects of various hopping parameters and spin-orbit coupling (SOC) strengths. The analysis adopts a systematic approach, gradually incorporating the different hopping terms one by one into the Hamiltonian, enabling a comprehensive understanding of their individual and collective impacts. While certain hopping parameters drive the system towards the gapped phases identified in the first part of the study, the introduction of the additional hoppings and the finite strength of SOC unveils a multitude of distinct metallic phases which are distinguished based on the topology of their Fermi surfaces. Using the DFT estimates for some of the candidate materials, we also predict their position on the phase diagram.

Appendix A

Appendix

A.1 The microscopic details

A.1.1 The lattice

Similar to Kitaev materials [127], it is useful to consider the honeycomb lattice to lie in the plane perpendicular to the [111] direction of the global Cartesian coordinates (X, Y, Z) (see Fig. 2.1). Therefore the two orthogonal directions in the honeycomb plane are spanned by

$$\hat{x} = \frac{1}{\sqrt{2}}(-\hat{X} + \hat{Y}), \quad \hat{y} = \frac{1}{\sqrt{6}}(2\hat{Z} - \hat{X} - \hat{Y}) \quad (\text{A.1})$$

while

$$\hat{z} = \frac{1}{\sqrt{3}}(\hat{X} + \hat{Y} + \hat{Z}) \quad (\text{A.2})$$

is normal to the honeycomb plane. In this new coordinate system, the x , y , and z bonds in these new coordinates are shown in Fig. 2.2.

The lattice vectors (with reference to Fig. 2.2) are

$$\mathbf{b}_1 = \frac{3\ell}{2}\hat{x} + \frac{\sqrt{3}\ell}{2}\hat{y}, \quad \mathbf{b}_2 = \frac{3\ell}{2}\hat{x} - \frac{\sqrt{3}\ell}{2}\hat{y} \quad (\text{A.3})$$

A.1.2 Effective angular momentum of the t_{2g} orbitals

The SOC Hamiltonian for an electron in the d -orbitals is given by

$$H_{soc}^{(l=2)} = \lambda \mathbf{I}^{(2)} \cdot \mathbf{s}, \quad (\text{A.4})$$

where $\lambda(> 0)$ is the strength of the SOC, $\mathbf{I}^{(2)}$ are the $l = 2$ angular momentum matrices and \mathbf{s} are the spin angular momentum matrices. Projecting H_{soc} to the t_{2g} orbitals, we have the effective SOC Hamiltonian in the t_{2g} sector given by

$$H_{soc} = -\lambda \mathbf{l} \cdot \mathbf{s}, \quad (\text{A.5})$$

where the \mathbf{l} are the $l = 1$ angular momentum generator matrices. The extra $-ve$ sign appears as a result of the projection. Thus, the t_{2g} orbitals effectively behave as $l = 1$

states under rotations with

$$|l_Z = 0\rangle = |d_{XY}\rangle, \quad |l_Z = \pm 1\rangle = -\frac{1}{\sqrt{2}}(i|d_{XZ}\rangle \pm |d_{YZ}\rangle). \quad (\text{A.6})$$

Here, $|d_{XY}\rangle, |d_{YZ}\rangle, |d_{ZX}\rangle$ are the three t_{2g} orbitals.

A.1.3 The $j = 3/2$ orbitals

In the presence of SOC, these six degenerate (including spin degeneracy) states split into four with total angular momentum $j = 3/2$ and the other two with $j = 1/2$. The $j = 3/2$ states in terms of the t_{2g} states are given by

$$\begin{aligned} |3/2\rangle &= \frac{1}{\sqrt{2}}(-|d_{YZ}, \uparrow\rangle - i|d_{ZX}, \uparrow\rangle) \\ |1/2\rangle &= \frac{1}{\sqrt{6}}(-|d_{YZ}, \downarrow\rangle - i|d_{ZX}, \downarrow\rangle + 2|d_{XY}, \uparrow\rangle) \\ |-1/2\rangle &= \frac{1}{\sqrt{6}}(|d_{YZ}, \uparrow\rangle - i|d_{ZX}, \uparrow\rangle + 2|d_{XY}, \downarrow\rangle) \\ |-3/2\rangle &= \frac{1}{\sqrt{2}}(|d_{YZ}, \downarrow\rangle - i|d_{ZX}, \downarrow\rangle) \end{aligned} \quad (\text{A.7})$$

In terms of the second quantized operators, the inverse relations, when projected to the $j = 3/2$ orbitals are

$$\begin{aligned} \Psi_{\sigma,x}^\dagger(\mathbf{r}, \mathcal{J}) &= \frac{\sigma}{\sqrt{6}} \left(\psi_{\uparrow\bar{\sigma}}^\dagger(\mathbf{r}, \mathcal{J}) - \sqrt{3}\psi_{\downarrow\sigma}^\dagger(\mathbf{r}, \mathcal{J}) \right) \\ \Psi_{\sigma,y}^\dagger(\mathbf{r}, \mathcal{J}) &= \frac{i}{\sqrt{6}} \left(\psi_{\uparrow\bar{\sigma}}^\dagger(\mathbf{r}, \mathcal{J}) + \sqrt{3}\psi_{\downarrow\sigma}^\dagger(\mathbf{r}, \mathcal{J}) \right) \\ \Psi_{\sigma,z}^\dagger(\mathbf{r}, \mathcal{J}) &= \sqrt{\frac{2}{3}}\psi_{\uparrow\sigma}^\dagger(\mathbf{r}, \mathcal{J}), \end{aligned} \quad (\text{A.8a})$$

where on the LHS, $\Psi_{\sigma,x}^\dagger(\mathbf{r}, \mathcal{J}), \Psi_{\sigma,y}^\dagger(\mathbf{r}, \mathcal{J}), \Psi_{\sigma,z}^\dagger(\mathbf{r}, \mathcal{J})$ stand for the creation operators for the $|d_{YZ,\sigma}\rangle, |d_{ZX,\sigma}\rangle, |d_{XY,\sigma}\rangle$ orbitals respectively at the lattice sub-lattice site \mathcal{J} of the unit cell at \mathbf{r} and $\sigma = \uparrow, \downarrow$ are spin indices. The $\psi_{\uparrow\bar{\sigma}}^\dagger$ and $\psi_{\downarrow\sigma}^\dagger$ in the RHS refer to the creations operators in the $j = 3/2$ orbitals as [130]

$$(\psi_{\uparrow\uparrow}^\dagger, \psi_{\uparrow\downarrow}^\dagger, \psi_{\downarrow\uparrow}^\dagger, \psi_{\downarrow\downarrow}^\dagger) = (\psi_{1/2}^\dagger, \psi_{-1/2}^\dagger, \psi_{3/2}^\dagger, \psi_{-3/2}^\dagger). \quad (\text{A.9})$$

where $\bar{\sigma} = \downarrow$ (\uparrow) for $\sigma = \uparrow$ (\downarrow).

A.2 The Microscopic symmetries

The transformation of the t_{2g} orbitals under lattice translation and TR are straightforward and are given by

$$\begin{aligned}\mathbf{T}_{1(2)} : \Psi_{\sigma,\alpha}(\mathbf{r}, \mathcal{J}) &\rightarrow \Psi_{\sigma,\alpha}(\mathbf{r}', \mathcal{J}') \\ \mathbb{T} : \Psi_{\sigma,\alpha}(\mathbf{r}, \mathcal{J}) &\rightarrow (\iota\sigma_{\sigma\sigma'}^y) \Psi_{\sigma',\alpha}(\mathbf{r}, \mathcal{J})\end{aligned}\tag{A.10}$$

$\forall \alpha = x, y, z$ and $\sigma = \uparrow, \downarrow$, where $\mathbf{r}' = \mathbf{T}_{1(2)}[\mathbf{r}]$ as discussed in the main text.

For the point group symmetries listed in Table 2.1, the transformation of the t_{2g} orbitals have a generic form of

$$\mathbb{S} : \Psi_{\sigma,\alpha}^\dagger(\mathbf{r}, \mathcal{J}) \rightarrow \Psi_{\sigma,\alpha}^\dagger(\mathbf{r}, \mathcal{J}) = [\mathcal{R}_{\mathbb{S}}]_{\beta\alpha} \Psi_{\sigma,\beta}^\dagger(\mathbf{r}', \mathcal{J}').\tag{A.11}$$

where \mathbb{S} are the point group symmetry generators listed in Table 2.1 that takes $(\mathbf{r}', \mathcal{J}') \rightarrow (\mathbf{r}, \mathcal{J})$ on the honeycomb lattice. The form of the 3×3 matrices, $\mathcal{R}_{\mathbb{S}}$ for different symmetries are :

$$\mathcal{R}_{\mathbf{C}_3} = \begin{pmatrix} 0 & 0 & 1 \\ 1 & 0 & 0 \\ 0 & 1 & 0 \end{pmatrix}, \mathcal{R}_{\mathbf{S}_6} = \begin{pmatrix} 0 & 1 & 0 \\ 0 & 0 & 1 \\ 1 & 0 & 0 \end{pmatrix}, \mathcal{R}_{\mathbf{C}_2} = \begin{pmatrix} 0 & 1 & 0 \\ 1 & 0 & 0 \\ 0 & 0 & 1 \end{pmatrix},\tag{A.12}$$

while

$$\mathcal{R}_{\mathbf{I}} = \mathbb{I}_3, \quad \mathcal{R}_{\sigma_d} = \mathcal{R}_{\mathbf{C}_2'}.\tag{A.13}$$

The transformation of the $j = 3/2$ orbitals (Eq. 2.24) under the action of the microscopic symmetries can be obtained from the above relations. For TR, we have

$$\psi(\mathbf{r}, \mathcal{J}) \rightarrow i\Sigma_{13} K \psi(\mathbf{r}, \mathcal{J}).\tag{A.14}$$

For the lattice symmetries (Table 2.1), similar to Eq. A.11, the transformation of $\psi(\mathbf{r}, \mathcal{J})$ have the following generic form

$$\mathbb{S} : \psi_i^\dagger(\mathbf{r}, \mathcal{J}) \rightarrow \psi_i^\dagger(\mathbf{r}, \mathcal{J}) = [\mathcal{U}_{\mathbb{S}}]_{ji} \psi_j^\dagger(\mathbf{r}', \mathcal{J}').\tag{A.15}$$

The u_s are 4×4 unitary matrices which for different symmetries are

$$u_{\mathbf{T}_1} = u_{\mathbf{T}_2} = u_{\mathbf{I}} = \mathbb{I}_4, \quad (\text{A.16})$$

$$u_{\mathbf{C}_3} = \frac{1}{4} \begin{pmatrix} -1+i & -1-i & \frac{-1-i}{\sqrt{3}} & \frac{-1+i}{\sqrt{3}} \\ 1-i & -1-i & \frac{-1-i}{\sqrt{3}} & \frac{1-i}{\sqrt{3}} \\ \frac{-1+i}{\sqrt{3}} & \frac{1+i}{\sqrt{3}} & -1-i & 1-i \\ \frac{1-i}{\sqrt{3}} & \frac{1+i}{\sqrt{3}} & -1-i & -1+i \end{pmatrix}, \quad (\text{A.17})$$

$$u_{\mathbf{S}_6} = \frac{1}{4} \begin{pmatrix} 1+i & -1-i & \frac{1+i}{\sqrt{3}} & \frac{-1-i}{\sqrt{3}} \\ 1-i & 1-i & \frac{-1+i}{\sqrt{3}} & \frac{-1+i}{\sqrt{3}} \\ \frac{1-i}{\sqrt{3}} & \frac{1-i}{\sqrt{3}} & 1-i & 1-i \\ \frac{1+i}{\sqrt{3}} & \frac{-1-i}{\sqrt{3}} & -1-i & 1+i \end{pmatrix}, \quad (\text{A.18})$$

$$u_{\mathbf{C}'_2} = \frac{1}{\sqrt{2}} \begin{pmatrix} 0 & -1+i & 0 & 0 \\ 1+i & 0 & 0 & 0 \\ 0 & 0 & 0 & -1-i \\ 0 & 0 & 1-i & 0 \end{pmatrix}, \quad (\text{A.19})$$

$$u_{\sigma_d} = u_{\mathbf{C}'_2}. \quad (\text{A.20})$$

A.3 Relation between the $j = 3/2$ matrices and the Σ matrices generating $\text{SU}(4)$

Following reference [167], we define a basis for the set of 4-dimensional Hermitian matrices using the $\text{SU}(2)$ generators for spin-3/2. The three spin-3/2 matrices written in the J_z

eigenbasis are the following:

$$J_x = \begin{pmatrix} 0 & 1 & \frac{\sqrt{3}}{2} & 0 \\ 1 & 0 & 0 & \frac{\sqrt{3}}{2} \\ \frac{\sqrt{3}}{2} & 0 & 0 & 0 \\ 0 & \frac{\sqrt{3}}{2} & 0 & 0 \end{pmatrix}, \quad (\text{A.21})$$

$$J_y = \begin{pmatrix} 0 & -i & \frac{i\sqrt{3}}{2} & 0 \\ i & 0 & 0 & -\frac{i\sqrt{3}}{2} \\ -\frac{i\sqrt{3}}{2} & 0 & 0 & 0 \\ 0 & \frac{i\sqrt{3}}{2} & 0 & 0 \end{pmatrix}, \quad (\text{A.22})$$

$$J_z = \begin{pmatrix} \frac{1}{2} & 0 & 0 & 0 \\ 0 & -\frac{1}{2} & 0 & 0 \\ 0 & 0 & \frac{3}{2} & 0 \\ 0 & 0 & 0 & -\frac{3}{2} \end{pmatrix}. \quad (\text{A.23})$$

Note that, instead of the standard practice, we have used a different ordering of the J_z eigen-basis (see Eq. 2.24) to write these matrices which is evident from the form of the J_z matrix in Eq. A.23. In our choice of basis, the hopping matrices of the lattice Hamiltonian in Eq. 2.26 have a simpler form.

With the above matrices, one can define the following five Hermitian matrices:

$$\Sigma_1 = \frac{1}{\sqrt{3}}\{J_y, J_z\}, \quad (\text{A.24a})$$

$$\Sigma_2 = \frac{1}{\sqrt{3}}\{J_z, J_x\}, \quad (\text{A.24b})$$

$$\Sigma_3 = \frac{1}{\sqrt{3}}\{J_x, J_y\}, \quad (\text{A.24c})$$

$$\Sigma_4 = \frac{1}{\sqrt{3}}(J_x^2 - J_y^2), \quad (\text{A.24d})$$

$$\Sigma_5 = J_z^2 - \frac{5}{4}\mathbb{I}_4, \quad (\text{A.24e})$$

with $-\Sigma_1\Sigma_2\Sigma_3\Sigma_4\Sigma_5 = \mathbb{I}_4 \equiv \Sigma_0$. The above five matrices satisfy

$$\{\Sigma_\alpha, \Sigma_\beta\} = 2\delta_{\alpha\beta} \quad (\text{A.25})$$

	$\mathfrak{z} = \text{even}$				$\mathfrak{z} = \text{odd}$			
	$\mathcal{S} = B_2$	$\mathcal{S} = A_1$	$\mathcal{S} = B_1$	$\mathcal{S} = A_2$	$\mathcal{S} = B_2$	$\mathcal{S} = A_1$	$\mathcal{S} = B_1$	$\mathcal{S} = A_2$
$\rho_0(\mathfrak{z}_S)$	+1	+1	+1	+1	+1	+1	+1	+1
$\rho_1(\mathfrak{z}_S)$	+1	-1	+1	+1	-1	+1	-1	-1
$\rho_2(\mathfrak{z}_S)$	+1	+1	-1	+1	-1	-1	+1	-1
$\rho_3(\mathfrak{z}_S)$	+1	-1	-1	+1	+1	-1	-1	+1
$\rho_4(\mathfrak{z}_S)$	+1	-1	+1	-1	+1	-1	+1	-1
$\rho_5(\mathfrak{z}_S)$	+1	-1	+1	-1	+1	-1	1	-1
$\rho_{12}(\mathfrak{z}_S)$	+1	-1	-1	+1	+1	-1	-1	+1
$\rho_{13}(\mathfrak{z}_S)$	+1	+1	-1	+1	-1	-1	+1	-1
$\rho_{14}(\mathfrak{z}_S)$	+1	+1	+1	-1	-1	-1	-1	+1
$\rho_{15}(\mathfrak{z}_S)$	+1	+1	+1	-1	-1	-1	-1	+1
$\rho_{23}(\mathfrak{z}_S)$	+1	-1	+1	+1	-1	+1	-1	-1
$\rho_{24}(\mathfrak{z}_S)$	+1	-1	-1	-1	-1	+1	+1	+1
$\rho_{25}(\mathfrak{z}_S)$	+1	-1	-1	-1	-1	+1	+1	+1
$\rho_{34}(\mathfrak{z}_S)$	+1	+1	-1	-1	+1	+1	-1	-1
$\rho_{35}(\mathfrak{z}_S)$	+1	+1	-1	-1	+1	+1	-1	-1
$\rho_{45}(\mathfrak{z}_S)$	+1	+1	+1	+1	+1	+1	+1	+1

Table A.1: The values of $\rho_i(\mathfrak{z}_S) = \pm 1$ defined in Eq. A.33 are written in this table.

and therefore generate a (Euclidean) Clifford algebra [167]. The following 10 operators

$$\Sigma_{\alpha\beta} = \frac{1}{2i}[\Sigma_\alpha, \Sigma_\beta] \quad (\text{A.26})$$

then generate SO(5) rotations. Eq. A.24 and Eq. A.26 together define a basis for the 4-dimensional Hermitian matrices that generate SU(4).

The spin matrices can be written in terms of these Σ_i as

$$J_x = \frac{\sqrt{3}}{2}\Sigma_{15} - \frac{1}{2}(\Sigma_{23} - \Sigma_{14}); \quad (\text{A.27})$$

$$J_y = -\frac{\sqrt{3}}{2}\Sigma_{25} + \frac{1}{2}(\Sigma_{13} + \Sigma_{24}); \quad (\text{A.28})$$

$$J_z = -\Sigma_{34} - \frac{1}{2}\Sigma_{12} \quad (\text{A.29})$$

which generates an SU(2) subgroup of SU(4) with commutation relation

$$[J_i, J_j] = i\epsilon_{ijk}J_k. \quad (\text{A.30})$$

We now consider two kinds of lattice operators defined below

$$\mathcal{O}_i^{global}(\boldsymbol{z}_S) = \psi^\dagger(\boldsymbol{z}_S)\Sigma_i\psi(\boldsymbol{z}_S), \quad (\text{A.31})$$

and

$$\mathcal{O}_i^{local}(\boldsymbol{z}_S) = \phi^\dagger(\boldsymbol{z}_S)\Sigma_i\phi(\boldsymbol{z}_S), \quad (\text{A.32})$$

Using the relation between the ψ and the ϕ operators given in Eq. 2.34, we find that

$$\mathcal{O}_i^{local}(\boldsymbol{z}_S) = \rho_i(\boldsymbol{z}_S)\mathcal{O}_i^{global}(\boldsymbol{z}_S) \quad (\text{A.33})$$

where $\rho_i(\boldsymbol{z}_S) = \pm 1$. In table A.1, we write what $\rho_i(\boldsymbol{z}_S)$ are for different S and \boldsymbol{z} . In this table, we assume the form of \boldsymbol{z} as given in Eq. 2.32 which is

$$\boldsymbol{z} = n_x\mathbf{R}_1 + n_y\mathbf{R}_2. \quad (\text{A.34})$$

We say $\boldsymbol{z} = \text{even}$ (odd) if $(n_x + n_y)$ is even (odd).

A.4 The $\mathcal{G}(\boldsymbol{z}_S)$ matrices of transformation to manifestly SU(4) invariant local basis

The set of $\mathcal{G}(\boldsymbol{z}_S)$ matrices that lead to the form of $\eta(\boldsymbol{z}_S, \boldsymbol{z}'_{S'})$ is given in Eq. 2.37 is written below. Here we again take \boldsymbol{z} to be of the form as in Eq. A.34.

For $(n_x + n_y) = \text{even}$:

$$\begin{aligned} \mathcal{G}(\boldsymbol{z}_{B_2}) &= (-1)^{\frac{n_x - n_y}{2}} \\ \mathcal{G}(\boldsymbol{z}_{A_1}) &= (-1)^{\frac{n_x - n_y}{2}} U_y \\ \mathcal{G}(\boldsymbol{z}_{B_1}) &= (-1)^{\frac{n_x - n_y}{2}} U_z U_y \\ \mathcal{G}(\boldsymbol{z}_{A_2}) &= (-1)^{\frac{n_x - n_y}{2}} U_x U_z U_y \end{aligned} \quad (\text{A.35})$$

And for $(n_x + n_y) = \text{odd}$:

$$\begin{aligned}
\mathcal{G}(\boldsymbol{z}_{B_2}) &= (-1)^{\frac{n_x - n_y + 1}{2}} U_x U_y \\
\mathcal{G}(\boldsymbol{z}_{A_1}) &= (-1)^{\frac{n_x - n_y + 1}{2}} (-U_x) \\
\mathcal{G}(\boldsymbol{z}_{B_1}) &= (-1)^{\frac{n_x - n_y + 1}{2}} (-U_z U_x) \\
\mathcal{G}(\boldsymbol{z}_{A_2}) &= (-1)^{\frac{n_x - n_y + 1}{2}} U_z
\end{aligned} \tag{A.36}$$

Although we will be using this particular form, there are other choices for the $\mathcal{G}(\boldsymbol{z}_S)$ matrices which lead to same form for the $\eta(\boldsymbol{z}_S, \boldsymbol{z}'_{S'})$.

A.5 Low-energy Hamiltonian

A.5.1 Band structure

To diagonalize the Hamiltonian given by Eq. 2.35, we define Fourier space operators

$$\phi_f(\mathbf{k}, \mathcal{S}) = \frac{1}{\sqrt{N}} \sum_{\mathbf{z}} e^{i\mathbf{k}\cdot\mathbf{z}} \phi_f(\mathbf{z}_\mathcal{S}) \quad (\text{A.37})$$

where N is the total number of magnetic unit-cells, $f = 1, 2, 3, 4$ are the four SU(4) flavours and \mathbf{k} runs over the magnetic Brillouin zone (Fig. 3.1).

In terms of these Fourier space operators, the Hamiltonian in Eq. 2.35 can now be written as

$$H = -\frac{t}{\sqrt{3}} \sum_{f=1}^4 \sum_{\mathbf{k}} \sum_{\mathcal{S}, \mathcal{S}'} \phi_f(\mathbf{k}, \mathcal{S}) [h(\mathbf{k})]_{\mathcal{S}\mathcal{S}'} \phi_f(\mathbf{k}, \mathcal{S}') \quad (\text{A.38})$$

where

$$h(\mathbf{k}) = \begin{pmatrix} 0 & 1 + e^{-i\mathbf{k}\cdot\mathbf{R}_2} & 0 & e^{-i\mathbf{k}\cdot\mathbf{R}_1} \\ 1 + e^{i\mathbf{k}\cdot\mathbf{R}_2} & 0 & 1 & 0 \\ 0 & 1 & 0 & 1 - e^{i\mathbf{k}\cdot\mathbf{R}_2} \\ e^{i\mathbf{k}\cdot\mathbf{R}_1} & 0 & 1 - e^{-i\mathbf{k}\cdot\mathbf{R}_2} & 0 \end{pmatrix} \quad (\text{A.39})$$

Diagonalizing the $h(\mathbf{k})$ matrix, we get the band structure shown in Fig. 3.1.

A.5.2 The low energy Dirac Hamiltonian

At 1/4th filling, the valence band touches the conduction band at two Dirac points in the BZ given by Eq. 3.1. To get the low-energy Hamiltonian, we first write the $\phi(\mathbf{z}_\mathcal{S})$ operators in terms of the soft modes $\phi_{f\mathcal{S}\tau}$ as

$$\phi_f(\mathbf{z}_\mathcal{S}) = \sqrt{\mathcal{A}} \sum_{\tau=\pm 1} e^{i\tau\mathbf{Q}\cdot\mathbf{z}} \phi_{f\mathcal{S}\tau}(\mathbf{z}). \quad (\text{A.40})$$

Here, \mathbf{z} (defined in Eq. 2.32) denotes position of a particular magnetic unit cell and \mathcal{A} is the area of a single magnetic unit cell. The $\phi_{fS\tau}(\mathbf{z})$ operators are defined for each valley ($\tau = \pm 1$ labels the valleys) as

$$\phi_{fS\tau}(\mathbf{z}) = \frac{1}{\sqrt{\mathcal{A}}} \sum_{\mathbf{q}} e^{i\mathbf{q}\cdot\mathbf{z}} \phi_f(\tau\mathbf{Q} + \mathbf{q}, S). \quad (\text{A.41})$$

In the above summation, \mathbf{q} runs over half of the magnetic Brillouin zone for each τ such that the Dirac point $\tau\mathbf{Q}$ is contained in that half. These $\phi_{fS\tau}$ fields vary slowly over the magnetic unit cells.

Now to get the low-energy Hamiltonian, we use the form of $\phi(\mathbf{z}_S)$ as in Eq. A.40 to rewrite the Hamiltonian in Eq. 2.35 in terms of the $\phi_{fS\tau}(\mathbf{z})$ operators. We also use the following expansion for $\phi_{fS\tau}$:

$$\phi_{fS\tau}(\mathbf{z} + \vec{\delta}) = \phi_{fS\tau}(\mathbf{z}) + \vec{\delta} \cdot \nabla \phi_{fS\tau}(\mathbf{z}) + \mathcal{O}(\delta^2). \quad (\text{A.42})$$

Here, $\vec{\delta}$ can be some magnetic translation vector (\mathbf{R}_1 or \mathbf{R}_2). The soft-mode continuum Hamiltonian is then obtained by rewriting the Hamiltonian in Eq. 2.35 using the above expression and keeping terms that are linear in the derivative. The final form of the Hamiltonian is given below in Eq. A.43.

$$H = \sum_{f=1}^4 \sum_{\tau=\pm 1} \sum_{S,S'=A_1,A_2,B_1,B_2} \int d^2\mathbf{x} \phi_{fS\tau}^\dagger(\mathbf{x}) \left[h_0^{(\tau)} - i\tau h_x \partial_x - i\tau h_y \partial_y \right]_{SS'} \phi_{fS'\tau}(\mathbf{x}). \quad (\text{A.43})$$

where,

$$h_0^{(\tau)} = -\frac{t\ell}{\sqrt{3}} \begin{pmatrix} 0 & 1+i\tau & 0 & -i\tau \\ 1-i\tau & 0 & 1 & 0 \\ 0 & 1 & 0 & 1+i\tau \\ i\tau & 0 & 1-i\tau & 0 \end{pmatrix}, \quad h_x = \frac{t\ell}{\sqrt{3}} \begin{pmatrix} 0 & 0 & 0 & 3 \\ 0 & 0 & 0 & 0 \\ 0 & 0 & 0 & 0 \\ 3 & 0 & 0 & 0 \end{pmatrix},$$

$$h_y = \frac{t\ell}{\sqrt{3}} \begin{pmatrix} 0 & -\sqrt{3} & 0 & 0 \\ -\sqrt{3} & 0 & 0 & 0 \\ 0 & 0 & 0 & \sqrt{3} \\ 0 & 0 & \sqrt{3} & 0 \end{pmatrix}, \quad (\text{A.44a})$$

where ℓ is the length of each side of a hexagon of the honeycomb lattice.

As because the system is at 1/4th filling, we need to further project this Hamiltonian into the lowest two bands to get the low energy theory. For this, we take the eigenvectors corresponding to the lowest two eigenvalues of $h_0^{(\tau)}$ and project h_x, h_y into the subspace of these two eigenvectors. This way of projecting the Hamiltonian is correct up to linear order in derivatives, which is sufficient in this case since the Hamiltonian A.43 is also linear in derivatives.

With this, the final form of the low-energy Dirac Hamiltonian is the following

$$H_D = v_F \sum_{f=1}^4 \sum_{\tau=\pm 1} \int d^2\mathbf{x} \sum_{\alpha,\beta=1}^2 \chi_{f\alpha\tau}^\dagger(\mathbf{x}) [-i\tau\sigma_x\partial_x - i\sigma_y\partial_y]_{\alpha\beta} \chi_{f\beta\tau}(\mathbf{x}) \quad (\text{A.45})$$

Here, $v_F = \frac{t\ell}{\sqrt{2}}$ and $\sigma_x, \sigma_y, \sigma_z$ are the three Pauli matrices. Also the operators $\chi_{f\alpha\tau}(\mathbf{x})$ are defined as

$$\chi_{f\alpha\tau}(\mathbf{x}) = \sum_{s=A_1, A_2, B_1, B_2} \mathcal{W}_{s\alpha}^{(\tau)\dagger} \phi_{fs\tau}(\mathbf{x}). \quad (\text{A.46})$$

which is the inverse of Eq. 3.2 of the main text.

In the above equation,

$$\mathcal{W}_{s\alpha}^{(\tau)\dagger} = \sum_{\beta=1}^2 [W_\tau]_{\alpha\beta} [T_\tau]_{\beta s}. \quad (\text{A.47})$$

Here,

$$T_\tau = \begin{pmatrix} \frac{i\tau}{\sqrt{2}} & -\frac{1-i\tau}{\sqrt{6}} & 0 & \frac{1}{\sqrt{6}} \\ 0 & \frac{1}{\sqrt{6}} & \frac{1}{\sqrt{2}} & \frac{1+i\tau}{\sqrt{6}} \end{pmatrix} \quad (\text{A.48})$$

projects the annihilation operators to the lowest two bands. The matrices

$$W_\tau = \left[\exp\left(-i\tau\theta\frac{\sigma_x}{2}\right) \exp\left(-i\tau\frac{\pi}{4}\frac{\sigma_z}{2}\right) \right] \quad (\text{A.49})$$

with $\theta = \cos^{-1}\left(\frac{1}{\sqrt{3}}\right)$ are used to perform some extra unitary rotations on the spinors to bring the Dirac Hamiltonian in its canonical form.

A.6 Symmetry transformation of the soft modes

A.6.1 Action of lattice symmetry transformations on $\phi(\mathbf{z}_S)$ operators

The transformation properties of the soft modes $\chi(\mathbf{x})$ under the action of lattice symmetries can be determined from that of the original $j = 3/2$ operators $\psi(\mathbf{r}, s)$ as given in Eq. A.14-A.19. Using these, the transformations of the $\phi(\mathbf{z}_S)$ operators are obtained as follows

$$\mathbb{S} : \phi_f^\dagger(\mathbf{z}_S) \rightarrow \phi_f^\dagger(\mathbf{z}_S) = [\mathcal{G}(\mathbf{z}_S)^\dagger \mathcal{U}_\mathbb{S} \mathcal{G}(\mathbf{z}'_{S'})]_{f'f} \phi_{f'}^\dagger(\mathbf{z}'_{S'}). \quad (\text{A.50})$$

Here, the site at $\mathbf{z}'_{S'}$ goes to \mathbf{z}_S under the action of the lattice symmetry \mathbb{S} .

Using this, one can now derive the transformations of the soft modes $\chi(\mathbf{x})$ which are defined in terms of the Fourier transforms of the $\phi(\mathbf{z}_S)$ operators (Eq. A.46). Below we provide some details of the transformations of both the $\phi(\mathbf{z}_S)$ and the $\chi(\mathbf{x})$ operators under the action of various lattice symmetries. For $\phi(\mathbf{z}_S)$, we write down how the operators in a particular magnetic unit cell at \mathbf{z} transform where

$$\mathbf{z} = n_x \mathbf{R}_1 + n_y \mathbf{R}_2. \quad (\text{A.51})$$

with n_x, n_y being integers.

Transformation under translations \mathbf{T}_1 and \mathbf{T}_2 : Under the action of \mathbf{T}_1 ,

$$\begin{aligned} \phi(\mathbf{z}_{B_2}) &\rightarrow (-1)^{(n_x+n_y)} \left[\Omega_{\mathbf{T}_1}^f \right] \phi((\mathbf{z} - \mathbf{R}_1 - \mathbf{R}_2)_{B_1}), \\ \phi(\mathbf{z}_{A_1}) &\rightarrow (-1)^{(n_x+n_y+1)} \left[\Omega_{\mathbf{T}_1}^f \right] \phi((\mathbf{z} - \mathbf{R}_1)_{A_2}), \\ \phi(\mathbf{z}_{B_1}) &\rightarrow (-1)^{(n_x+n_y+1)} \left[\Omega_{\mathbf{T}_1}^f \right] \phi(\mathbf{z}_{B_2}), \\ \phi(\mathbf{z}_{A_2}) &\rightarrow (-1)^{(n_x+n_y+1)} \left[\Omega_{\mathbf{T}_1}^f \right] \phi((\mathbf{z} - \mathbf{R}_2)_{A_1}), \end{aligned} \quad (\text{A.52})$$

where,

$$\Omega_{\mathbf{T}_1}^f = -i\Sigma_{23}. \quad (\text{A.53})$$

Similarly, under the action of \mathbf{T}_2 ,

$$\begin{aligned} \phi(\boldsymbol{z}_{B_2}) &\rightarrow (-1)^{(n_x+n_y)} \left[\Omega_{\mathbf{T}_2}^f \right] \phi((\boldsymbol{z} - \mathbf{R}_1)_{B_1}) \\ \phi(\boldsymbol{z}_{A_1}) &\rightarrow (-1)^{(n_x+n_y+1)} \left[\Omega_{\mathbf{T}_2}^f \right] \phi((\boldsymbol{z} - \mathbf{R}_1 + \mathbf{R}_2)_{A_2}) \\ \phi(\boldsymbol{z}_{B_1}) &\rightarrow (-1)^{(n_x+n_y+1)} \left[\Omega_{\mathbf{T}_2}^f \right] \phi((\boldsymbol{z} + \mathbf{R}_2)_{B_2}) \\ \phi(\boldsymbol{z}_{A_2}) &\rightarrow (-1)^{(n_x+n_y+1)} \left[\Omega_{\mathbf{T}_2}^f \right] \phi(\boldsymbol{z}_{A_1}). \end{aligned} \quad (\text{A.54})$$

where

$$\Omega_{\mathbf{T}_2}^f = i\Sigma_{13}. \quad (\text{A.55})$$

Transformation under \mathbf{C}'_2 : Under a \mathbf{C}'_2 rotation,

$$\begin{aligned} \phi(\boldsymbol{z}_{B_2}) &\rightarrow (-1)^{n_x} \left[\Omega_{\mathbf{C}'_2}^f \right] \phi(\boldsymbol{z}'_{B_2}) \\ \phi(\boldsymbol{z}_{A_1}) &\rightarrow (-1)^{n_x} \left[\Omega_{\mathbf{C}'_2}^f \right] \phi((\boldsymbol{z}' - \mathbf{R}_2)_{A_1}) \\ \phi(\boldsymbol{z}_{B_1}) &\rightarrow (-1)^{n_x} \left[\Omega_{\mathbf{C}'_2}^f \right] \phi((\boldsymbol{z}' - \mathbf{R}_2)_{B_1}) \\ \phi(\boldsymbol{z}_{A_2}) &\rightarrow (-1)^{n_x+1} \left[\Omega_{\mathbf{C}'_2}^f \right] \phi(\boldsymbol{z}'_{A_2}) \end{aligned} \quad (\text{A.56})$$

Here,

$$\boldsymbol{z}' = n_x \mathbf{R}_1 - n_y \mathbf{R}_2, \quad (\text{A.57})$$

and

$$\Omega_{\mathbf{C}'_2}^f = \frac{i}{\sqrt{2}} (\Sigma_{14} - \Sigma_{24}). \quad (\text{A.58})$$

Transformation under \mathbf{C}_3 : Under the action of \mathbf{C}_3 rotation, transformation of the $\phi(\boldsymbol{z})$ operators are given below.

Sublattice	$(n_x + n_y) = \text{even}$	$(n_x + n_y) = \text{odd}$
$\phi(\mathbf{z}_{B_2}) \rightarrow$	$(-1)^{n_x} [\Omega_{\mathbf{C}_3}^f] \phi((\mathbf{C}_3[\mathbf{z}])_{B_1})$	$(-1)^{n_x} [\Omega_{\mathbf{C}_3}^f] \phi((\mathbf{C}_3[\mathbf{z}])_{B_2})$
$\phi(\mathbf{z}_{A_1}) \rightarrow$	$(-1)^{n_x} [\Omega_{\mathbf{C}_3}^f] \phi((\mathbf{C}_3[\mathbf{z}])_{A_2})$	$(-1)^{n_x} [\Omega_{\mathbf{C}_3}^f] \phi((\mathbf{C}_3[\mathbf{z}] - \mathbf{R}_2)_{A_1})$
$\phi(\mathbf{z}_{B_1}) \rightarrow$	$(-1)^{n_x+1} [\Omega_{\mathbf{C}_3}^f] \phi((\mathbf{C}_3[\mathbf{z}] - \mathbf{R}_2)_{B_1})$	$(-1)^{n_x} [\Omega_{\mathbf{C}_3}^f] \phi((\mathbf{C}_3[\mathbf{z}] - \mathbf{R}_2)_{B_2})$
$\phi(\mathbf{z}_{A_2}) \rightarrow$	$(-1)^{n_x+1} [\Omega_{\mathbf{C}_3}^f] \phi((\mathbf{C}_3[\mathbf{z}] - \mathbf{R}_2)_{A_1})$	$(-1)^{n_x} [\Omega_{\mathbf{C}_3}^f] \phi((\mathbf{C}_3[\mathbf{z}] - \mathbf{R}_1 - \mathbf{R}_2)_{A_2})$

Here

$$\mathbf{C}_3[\mathbf{z}] = \begin{cases} \frac{-n_x+n_y}{2}\mathbf{R}_1 - \frac{3n_x+n_y}{2}\mathbf{R}_2 & \text{if } n_x + n_y = \text{even} \\ \frac{-n_x+n_y+1}{2}\mathbf{R}_1 - \frac{3n_x+n_y-1}{2}\mathbf{R}_2 & \text{if } n_x + n_y = \text{odd} \end{cases} \quad (\text{A.59})$$

and

$$\Omega_{\mathbf{C}_3}^f = \frac{1}{4} \left(\Sigma_0 - \sqrt{3}\Sigma_1 - \sqrt{3}\Sigma_2 + \sqrt{3}\Sigma_3 - i\Sigma_{12} - i\Sigma_{13} + i\Sigma_{23} + i\sqrt{3}\Sigma_{45} \right). \quad (\text{A.60})$$

Transformation under \mathbf{S}_6 : Transformation of $\phi(\mathbf{z}_S)$ operators under the action of \mathbf{S}_6 are as follows

	$(n_x + n_y) = \text{even}$	$(n_x + n_y) = \text{odd}$
$\phi(\mathbf{z}_{B_2}) \rightarrow$	$(-1)^{\frac{n_x+n_y}{2}} [\Omega_{\mathbf{S}_6}^f] \phi((\mathbf{S}_6[\mathbf{z}])_{A_1})$	$(-1)^{\frac{n_x+n_y+1}{2}} [\Omega_{\mathbf{S}_6}^f] \phi((\mathbf{S}_6[\mathbf{z}])_{A_2})$
$\phi(\mathbf{z}_{A_1}) \rightarrow$	$(-1)^{\frac{n_x+n_y}{2}} [\Omega_{\mathbf{S}_6}^f] \phi((\mathbf{S}_6[\mathbf{z}])_{B_1})$	$(-1)^{\frac{n_x+n_y+1}{2}} [\Omega_{\mathbf{S}_6}^f] \phi((\mathbf{S}_6[\mathbf{z}] + \mathbf{R}_1)_{B_2})$
$\phi(\mathbf{z}_{B_1}) \rightarrow$	$(-1)^{\frac{n_x+n_y}{2}} [\Omega_{\mathbf{S}_6}^f] \phi((\mathbf{S}_6[\mathbf{z}])_{A_2})$	$(-1)^{\frac{n_x+n_y+1}{2}} [\Omega_{\mathbf{S}_6}^f] \phi((\mathbf{S}_6[\mathbf{z}] + \mathbf{R}_1 - \mathbf{R}_2)_{A_1})$
$\phi(\mathbf{z}_{A_2}) \rightarrow$	$(-1)^{\frac{n_x+n_y}{2}+1} [\Omega_{\mathbf{S}_6}^f] \phi((\mathbf{S}_6[\mathbf{z}] - \mathbf{R}_2)_{B_1})$	$(-1)^{\frac{n_x+n_y+1}{2}} [\Omega_{\mathbf{S}_6}^f] \phi((\mathbf{S}_6[\mathbf{z}] + \mathbf{R}_1 - \mathbf{R}_2)_{B_2})$

(A.61)

Here,

$$\mathbf{S}_6[\mathbf{z}] = \begin{cases} \frac{n_x+n_y}{2}\mathbf{R}_1 - \frac{3n_x-n_y}{2}\mathbf{R}_2 & \text{if } n_x + n_y = \text{even} \\ \frac{n_x+n_y-1}{2}\mathbf{R}_1 - \frac{3n_x-n_y-1}{2}\mathbf{R}_2 & \text{if } n_x + n_y = \text{odd} \end{cases} \quad (\text{A.62})$$

and

$$\Omega_{\mathbf{S}_6}^f = -\frac{1}{4} \left(\sqrt{3}\Sigma_0 + \Sigma_1 + \Sigma_2 - \Sigma_3 + i\sqrt{3}\Sigma_{12} \right. \\ \left. + i\sqrt{3}\Sigma_{13} - i\sqrt{3}\Sigma_{23} + i\Sigma_{45} \right) \quad (\text{A.63})$$

Transformation under \mathbf{I} : Under inversion,

$$\begin{aligned} \phi(\boldsymbol{\mathcal{Z}}_{B_2}) &\rightarrow (-1)^{n_x+n_y+1} \left[\Omega_{\mathbf{I}}^f \right] \phi \left((\mathbf{I}[\boldsymbol{\mathcal{Z}}])_{A_2} \right) \\ \phi(\boldsymbol{\mathcal{Z}}_{A_1}) &\rightarrow (-1)^{n_x+n_y} \left[\Omega_{\mathbf{I}}^f \right] \phi \left((\mathbf{I}[\boldsymbol{\mathcal{Z}}] - \mathbf{R}_2)_{B_1} \right) \\ \phi(\boldsymbol{\mathcal{Z}}_{B_1}) &\rightarrow (-1)^{n_x+n_y} \left[\Omega_{\mathbf{I}}^f \right] \phi \left((\mathbf{I}[\boldsymbol{\mathcal{Z}}] - \mathbf{R}_2)_{A_1} \right) \\ \phi(\boldsymbol{\mathcal{Z}}_{A_2}) &\rightarrow (-1)^{n_x+n_y} \left[\Omega_{\mathbf{I}}^f \right] \phi \left((\mathbf{I}[\boldsymbol{\mathcal{Z}}])_{B_2} \right) \end{aligned} \quad (\text{A.64})$$

where

$$\mathbf{I}[\boldsymbol{\mathcal{Z}}] = -n_x \mathbf{R}_1 - n_y \mathbf{R}_2, \quad (\text{A.65})$$

and

$$\Omega_{\mathbf{I}}^f = i\Sigma_{45}. \quad (\text{A.66})$$

Transformation under $\sigma_{\mathbf{d}}$: Under the action of reflection,

$$\begin{aligned} \phi(\boldsymbol{\mathcal{Z}}_{B_2}) &\rightarrow (-1)^{n_y} \left[\Omega_{\sigma_{\mathbf{d}}}^f \right] \phi \left((\sigma_{\mathbf{d}}[\boldsymbol{\mathcal{Z}}])_{A_2} \right) \\ \phi(\boldsymbol{\mathcal{Z}}_{A_1}) &\rightarrow (-1)^{n_y} \left[\Omega_{\sigma_{\mathbf{d}}}^f \right] \phi \left((\sigma_{\mathbf{d}}[\boldsymbol{\mathcal{Z}}])_{B_1} \right) \\ \phi(\boldsymbol{\mathcal{Z}}_{B_1}) &\rightarrow (-1)^{n_y} \left[\Omega_{\sigma_{\mathbf{d}}}^f \right] \phi \left((\sigma_{\mathbf{d}}[\boldsymbol{\mathcal{Z}}])_{A_1} \right) \\ \phi(\boldsymbol{\mathcal{Z}}_{A_2}) &\rightarrow (-1)^{n_y} \left[\Omega_{\sigma_{\mathbf{d}}}^f \right] \phi \left((\sigma_{\mathbf{d}}[\boldsymbol{\mathcal{Z}}])_{B_2} \right) \end{aligned} \quad (\text{A.67})$$

where

$$\sigma_{\mathbf{d}}[\boldsymbol{\mathcal{Z}}] = -n_x \mathbf{R}_1 + n_y \mathbf{R}_2, \quad (\text{A.68})$$

and

$$\Omega_{\sigma_a}^f = \frac{i}{\sqrt{2}} (\Sigma_{15} - \Sigma_{25}). \quad (\text{A.69})$$

A.6.2 Transformation of the $\chi(\mathbf{x})$ operators under lattice symmetries

Under the microscopic time-reversal, we have

$$\mathbb{T} : \chi(\mathbf{x}) \rightarrow \left(\Omega_{\mathbb{T}}^f \otimes \Omega_{\mathbb{T}}^c \right) K \chi(\mathbf{x}), \quad (\text{A.70})$$

where

$$\Omega_{\mathbb{T}}^f = i\Sigma_{13}, \quad (\text{A.71})$$

$$\Omega_{\mathbb{T}}^c = \gamma_1 \zeta_2. \quad (\text{A.72})$$

and K represents complex conjugation.

Under the action of $\mathbf{T}_{1(2)}$,

$$\mathbf{T}_{1(2)} : \chi(\mathbf{x}) \rightarrow \left(\Omega_{\mathbf{T}_{1(2)}}^f \otimes \Omega_{\mathbf{T}_{1(2)}}^c \right) \chi(\mathbf{x}). \quad (\text{A.73})$$

where,

$$\Omega_{\mathbf{T}_1}^f = -i\Sigma_{23}. \quad (\text{A.74})$$

$$\Omega_{\mathbf{T}_1}^c = -i\zeta_3. \quad (\text{A.75})$$

and

$$\Omega_{\mathbf{T}_2}^f = i\Sigma_{13}, \quad (\text{A.76})$$

$$\Omega_{\mathbf{T}_2}^c = -i\zeta_2 \quad (\text{A.77})$$

The superscripts f and c in $\Omega_{\mathbf{T}_1}^f, \Omega_{\mathbf{T}_1}^c$ stand for ‘‘flavor’’ and ‘‘chiral’’ respectively since these matrices act on the SU(4) flavor space and the chiral space.

Under the action of \mathbf{C}'_2 ,

$$\mathbf{C}'_2 : \chi(\mathbf{x}) \rightarrow \left(\Omega_{\mathbf{C}'_2}^f \otimes \Omega_{\mathbf{C}'_2}^c \right) \chi(\mathbf{C}'_2{}^{-1}\mathbf{x}). \quad (\text{A.78})$$

where,

$$\Omega_{\mathbf{C}'_2}^f = \frac{i}{\sqrt{2}} (\Sigma_{14} - \Sigma_{24}) \quad (\text{A.79})$$

$$\Omega_{\mathbf{C}'_2}^c = \frac{1}{\sqrt{2}} \gamma_2 (\zeta_3 - \zeta_2). \quad (\text{A.80})$$

Under the action of \mathbf{C}_3 , the soft modes transform in the following way:

$$\mathbf{C}_3 : \chi(\mathbf{x}) \rightarrow \left(\Omega_{\mathbf{C}_3}^f \otimes \Omega_{\mathbf{C}_3}^c \right) \chi(\mathbf{C}_3{}^{-1}\mathbf{x}). \quad (\text{A.81})$$

Here,

$$\Omega_{\mathbf{C}_3}^f = \frac{1}{4} \left(\Sigma_0 - \sqrt{3}\Sigma_1 - \sqrt{3}\Sigma_2 + \sqrt{3}\Sigma_3 - i\Sigma_{12} - i\Sigma_{13} + i\Sigma_{23} + i\sqrt{3}\Sigma_{45} \right), \quad (\text{A.82})$$

and

$$\Omega_{\mathbf{C}_3}^c = \frac{1}{4} \left(-\mathbb{I}_4 + i\sqrt{3}\gamma_0 \right) (\mathbb{I}_4 + i\zeta_1 + i\zeta_2 + i\zeta_3) \quad (\text{A.83})$$

Under \mathbf{S}_6 , the soft modes transform in the following way:

$$\mathbf{S}_6 : \chi(\mathbf{x}) \rightarrow \left(\Omega_{\mathbf{S}_6}^f \otimes \Omega_{\mathbf{S}_6}^c \right) \chi(\mathbf{S}_6{}^{-1}\mathbf{x}). \quad (\text{A.84})$$

Here,

$$\Omega_{\mathbf{S}_6}^f = -\frac{1}{4} \left(\sqrt{3}\Sigma_0 + \Sigma_1 + \Sigma_2 - \Sigma_3 + i\sqrt{3}\Sigma_{12} + i\sqrt{3}\Sigma_{13} - i\sqrt{3}\Sigma_{23} + i\Sigma_{45} \right) \quad (\text{A.85})$$

and

$$\Omega_{\mathbf{S}_6}^c = \frac{1}{4} \left(\sqrt{3} \mathbb{I}_4 - i\gamma_0 \right) (\mathbb{I}_4 - i\zeta_1 - i\zeta_2 - i\zeta_3) \quad (\text{A.86})$$

Under the action of inversion,

$$\mathbf{I} : \chi(\mathbf{x}) \rightarrow \left(\Omega_{\mathbf{I}}^f \otimes \Omega_{\mathbf{I}}^c \right) \chi(-\mathbf{x}). \quad (\text{A.87})$$

where,

$$\Omega_{\mathbf{I}}^f = i\Sigma_{45}, \quad (\text{A.88})$$

$$\Omega_{\mathbf{I}}^c = i\gamma_0 \quad (\text{A.89})$$

Under the action of $\sigma_{\mathbf{d}}$,

$$\sigma_{\mathbf{d}} : \chi(\mathbf{x}) \rightarrow \left(\Omega_{\sigma_{\mathbf{d}}}^f \otimes \Omega_{\sigma_{\mathbf{d}}}^c \right) \chi(\sigma_{\mathbf{d}}^{-1}\mathbf{x}). \quad (\text{A.90})$$

where,

$$\Omega_{\sigma_{\mathbf{d}}}^f = \frac{i}{\sqrt{2}} (\Sigma_{15} - \Sigma_{25}) \quad (\text{A.91})$$

$$\Omega_{\sigma_{\mathbf{d}}}^c = \frac{1}{\sqrt{2}} \gamma_1 (\zeta_2 - \zeta_3). \quad (\text{A.92})$$

A.7 Irreducible representations of the IR space group

As mentioned in the main text, the IR space group has total 96 elements and these can be divided into 20 conjugacy classes. So, there are 20 irreducible representations of the IR space group. Among these, 10 have *+*ve trace for 2π rotations. In the tables [A.2](#), [A.3](#), [A.4](#), we write down these irreducible representations by showing how fermions bilinears in Eq. [4.2](#) (which we symbolically denote as X_1, X_2, X_3 etc) transform.

Irrep	mass	\mathbf{T}_1	\mathbf{T}_2	\mathbf{I}	\mathbf{C}_3	\mathbf{S}_6	\mathbf{C}'_2	σ_d
\mathcal{A}_{1g}	$X \rightarrow$	X	X	X	X	X	X	X
\mathcal{A}_{2g}	$X \rightarrow$	X	X	X	X	X	$-X$	$-X$
\mathcal{A}_{1u}	$X \rightarrow$	X	X	$-X$	X	$-X$	X	$-X$
\mathcal{A}_{2u}	$X \rightarrow$	X	X	$-X$	X	$-X$	$-X$	X

Table A.2: List of 1-dimensional irreps of the IR space group

Irrep	mass	\mathbf{T}_1	\mathbf{T}_2	\mathbf{I}	\mathbf{C}_3	\mathbf{S}_6	\mathbf{C}'_2	σ_d
\mathcal{E}_g	$X_1 \rightarrow$	X_1	X_1	X_1	$-\frac{X_1}{2} + \frac{\sqrt{3}X_2}{2}$	$-\frac{X_1}{2} - \frac{\sqrt{3}X_2}{2}$	$-X_1$	$-X_1$
	$X_2 \rightarrow$	X_2	X_2	X_2	$-\frac{\sqrt{3}X_1}{2} - \frac{X_2}{2}$	$\frac{\sqrt{3}X_1}{2} - \frac{X_2}{2}$	X_2	X_2
\mathcal{E}_u	$X_1 \rightarrow$	X_1	X_1	$-X_1$	$-\frac{X_1}{2} + \frac{\sqrt{3}X_2}{2}$	$\frac{X_1}{2} + \frac{\sqrt{3}X_2}{2}$	$-X_1$	X_1
	$X_2 \rightarrow$	X_2	X_2	$-X_2$	$-\frac{\sqrt{3}X_1}{2} - \frac{X_2}{2}$	$-\frac{\sqrt{3}X_1}{2} + \frac{X_2}{2}$	X_2	$-X_2$

Table A.3: List of 2-dimensional irreps of the IR space group

Irrep	mass	\mathbf{T}_1	\mathbf{T}_2	\mathbf{I}	\mathbf{C}_3	\mathbf{S}_6	\mathbf{C}'_2	σ_d
\mathcal{T}_{1g}	$X_1 \rightarrow$	$-X_1$	$-X_1$	X_1	X_3	$-X_2$	X_1	X_1
	$X_2 \rightarrow$	X_2	$-X_2$	X_2	$-X_1$	$-X_3$	$-X_3$	$-X_3$
	$X_3 \rightarrow$	$-X_3$	X_3	X_3	$-X_2$	X_1	$-X_2$	$-X_2$
\mathcal{T}_{2g}	$X_1 \rightarrow$	$-X_1$	$-X_1$	X_1	X_3	$-X_2$	$-X_1$	$-X_1$
	$X_2 \rightarrow$	X_2	$-X_2$	X_2	$-X_1$	$-X_3$	X_3	X_3
	$X_3 \rightarrow$	$-X_3$	X_3	X_3	$-X_2$	X_1	X_2	X_2
\mathcal{T}_{1u}	$X_1 \rightarrow$	$-X_1$	$-X_1$	$-X_1$	X_3	X_2	X_1	$-X_1$
	$X_2 \rightarrow$	X_2	$-X_2$	$-X_2$	$-X_1$	X_3	$-X_3$	X_3
	$X_3 \rightarrow$	$-X_3$	X_3	$-X_3$	$-X_2$	$-X_1$	$-X_2$	X_2
\mathcal{T}_{2u}	$X_1 \rightarrow$	$-X_1$	$-X_1$	$-X_1$	X_3	X_2	$-X_1$	X_1
	$X_2 \rightarrow$	X_2	$-X_2$	$-X_2$	$-X_1$	X_3	X_3	$-X_3$
	$X_3 \rightarrow$	$-X_3$	X_3	$-X_3$	$-X_2$	$-X_1$	X_2	$-X_2$

Table A.4: List of 3-dimensional irreps of the IR space group

A.8 Determination of broken symmetry group

For the first \mathcal{T}_{1u}^o triplet given by Eq. 7.21 in the main text, at a generic point on the sphere in Fig. 6.2 such as C or D, the corresponding \mathcal{R} matrix (introduced in Eq. 7.26), when diagonalised, has the form

$$\mathcal{R} = \begin{pmatrix} a_1\sigma_3 & & & \\ & a_2\sigma_3 & & \\ & & a_3\sigma_3 & \\ & & & a_4\sigma_3 \end{pmatrix}. \quad (\text{A.93})$$

Here a_1, \dots, a_4 are four real numbers which are not equal to each other. There are seven linearly independent matrices that commute with \mathcal{R} in the above equation. These are

$$\begin{pmatrix} \sigma_0 & & & \\ & -\sigma_0 & & \\ & & \sigma_0 & \\ & & & -\sigma_0 \end{pmatrix}, \begin{pmatrix} \sigma_0 & & & \\ & -\sigma_0 & & \\ & & 0 & \\ & & & 0 \end{pmatrix}, \begin{pmatrix} 0 & & & \\ & 0 & & \\ & & \sigma_0 & \\ & & & -\sigma_0 \end{pmatrix},$$

$$\begin{pmatrix} 0 & & & \\ & \sigma_3 & & \\ & & 0 & \\ & & & 0 \end{pmatrix}, \begin{pmatrix} \sigma_3 & & & \\ & 0 & & \\ & & 0 & \\ & & & 0 \end{pmatrix}, \begin{pmatrix} 0 & & & \\ & 0 & & \\ & & \sigma_3 & \\ & & & 0 \end{pmatrix}, \begin{pmatrix} 0 & & & \\ & 0 & & \\ & & 0 & \\ & & & \sigma_3 \end{pmatrix}$$

All these matrices commute with each other and hence these generate a subgroup of $SU(8)$ which contains seven mutually commuting $U(1)$ groups. Thus, the $SU(8)$ at a general point on the sphere is broken down to $[U(1)]^7$.

For the points on the three great circles obtained by setting one of the Δ_i to zero, the corresponding \mathcal{R} matrix for the masses look like

$$\mathcal{R} = \begin{pmatrix} a_1\sigma_3 & & & \\ & a_1\sigma_3 & & \\ & & a_3\sigma_3 & \\ & & & a_3\sigma_3 \end{pmatrix}. \quad (\text{A.94})$$

There are 15 linearly independent matrices that commute with this \mathcal{R} which form a $U(1) \otimes [U(1) \otimes SO(4)]^2$ of the $SU(8)$.

Finally, at the special eight points where all the Δ_i s have equal magnitude such as point B on the sphere in Fig. 6.2, the \mathcal{R} matrix has the following form

$$\mathcal{R} = \begin{pmatrix} a_1\sigma_3 & & & \\ & a_1\sigma_3 & & \\ & & a_3\sigma_3 & \\ & & & 0 \end{pmatrix}. \quad (\text{A.95})$$

The SU(8) symmetry group at these points breaks down to $U(1) \otimes SO(4) \otimes U(1) \otimes U(1) \otimes U(2)$.

A.9 Basis transformation for the density wave semimetals

In Eq. 7.35, the 16×16 matrix U is given by Eq. A.96.

$$U = \frac{1}{\sqrt{2}} \begin{pmatrix} 0 & 0 & 0 & 0 & 0 & 0 & 0 & 0 & 0 & 0 & 0 & -i & i & 0 & 0 & 0 \\ 0 & 0 & 0 & 0 & 0 & 0 & 0 & 0 & 0 & 0 & i & 0 & 0 & i & 0 & 0 \\ -i & 0 & 0 & 0 & 0 & 0 & 0 & i & 0 & 0 & 0 & 0 & 0 & 0 & 0 & 0 \\ 0 & -i & 0 & 0 & 0 & 0 & -i & 0 & 0 & 0 & 0 & 0 & 0 & 0 & 0 & 0 \\ 0 & 0 & 0 & 0 & 0 & 0 & 0 & 0 & 0 & 0 & 0 & i & i & 0 & 0 & 0 \\ 0 & 0 & 0 & 0 & 0 & 0 & 0 & 0 & 0 & 0 & -i & 0 & 0 & i & 0 & 0 \\ i & 0 & 0 & 0 & 0 & 0 & 0 & i & 0 & 0 & 0 & 0 & 0 & 0 & 0 & 0 \\ 0 & i & 0 & 0 & 0 & 0 & -i & 0 & 0 & 0 & 0 & 0 & 0 & 0 & 0 & 0 \\ 0 & 0 & 0 & 0 & 0 & 0 & 0 & 0 & -i & 0 & 0 & 0 & 0 & 0 & 0 & i \\ 0 & 0 & 0 & 0 & 0 & 0 & 0 & 0 & 0 & -i & 0 & 0 & 0 & 0 & -i & 0 \\ 0 & 0 & 0 & -i & i & 0 & 0 & 0 & 0 & 0 & 0 & 0 & 0 & 0 & 0 & 0 \\ 0 & 0 & i & 0 & 0 & i & 0 & 0 & 0 & 0 & 0 & 0 & 0 & 0 & 0 & 0 \\ 0 & 0 & 0 & 0 & 0 & 0 & 0 & 0 & i & 0 & 0 & 0 & 0 & 0 & 0 & i \\ 0 & 0 & 0 & 0 & 0 & 0 & 0 & 0 & 0 & i & 0 & 0 & 0 & 0 & -i & 0 \\ 0 & 0 & 0 & i & i & 0 & 0 & 0 & 0 & 0 & 0 & 0 & 0 & 0 & 0 & 0 \\ 0 & 0 & -i & 0 & 0 & i & 0 & 0 & 0 & 0 & 0 & 0 & 0 & 0 & 0 & 0 \end{pmatrix}. \quad (\text{A.96})$$

A.9.1 The structure of the density wave semimetal masses

In terms of internal symmetry transformations, the 18 density wave semimetals can be divided up into two categories depending on whether the number of gapless fermionic modes changes depending on the particular linear combination of the mass term

$$\sum_i \Delta_i \bar{\chi} m_i \chi, \quad (\text{A.97})$$

where i sums over the appropriate number of components depending on the dimension of the irreducible representation. The first class where the number of gapless modes remains unchanged for all values of Δ_i consists of eight masses belonging to the two singlets (of Γ -DSM type) and two triplets (of M-DSM type). They respectively make up :

- \mathcal{A}_{1u}^0 and \mathcal{A}_{2u}^o (Eqs. 7.31 and 7.32) : Staggered spin-octupole density wave semimetal.
- \mathcal{J}_{1g}^o (Eq. 7.47) : Stripy spin-octupole density wave semimetal
- \mathcal{J}_{2g}^e (Eq. 7.55) : Stripy spin-quadrupole density wave semimetal.

The second class involves the rest of the 10 masses (of Γ -DSM type) whose number of gapless modes changes as one tunes Δ_i . These consist of two doublets and two triplets given by

- \mathcal{J}_{2g}^o (Eq. 7.50) : Stripy spin-octupolar density wave semimetal.
- \mathcal{J}_{1g}^e (Eq. 7.57) : Stripy spin-quadrupolar density wave semimetal.
- \mathcal{E}_g^e (Eq. 7.60) : Ferro spin-quadrupole density wave semimetal.
- \mathcal{E}_g^o (Eq. 7.64) : Ferro spin-octupole density wave semimetal.

For the first class, leaving out the two singlets the six masses in the \mathcal{J}_{1g}^o and \mathcal{J}_{2g}^e representations form a reducible representation of a $\text{SO}(4)$ subgroup of the low-energy $\text{SU}(8)$. This $\text{SO}(4)(\equiv \text{SU}(2) \otimes \text{SU}(2))$ subgroup is generated by the following six generators:

$$\mathbf{g}_1^+ = \frac{1}{2} \left(\mu_6 \tilde{\Sigma}_{15} - \mu_7 \tilde{\Sigma}_5 \right) \quad (\text{A.98a})$$

$$\mathbf{g}_2^+ = \frac{1}{2} \left(\mu_{14} \tilde{\Sigma}_{15} - \mu_{13} \tilde{\Sigma}_5 \right) \quad (\text{A.98b})$$

$$\mathbf{g}_3^+ = \frac{1}{2} \mu_{11} \left(\tilde{\Sigma}_1 - \tilde{\Sigma}_0 \right) \quad (\text{A.98c})$$

$$\mathbf{g}_1^- = \frac{1}{2} \left(-\mu_6 \tilde{\Sigma}_{15} - \mu_7 \tilde{\Sigma}_5 \right) \quad (\text{A.98d})$$

$$\mathbf{g}_2^- = \frac{1}{2} \left(-\mu_{14} \tilde{\Sigma}_{15} - \mu_{13} \tilde{\Sigma}_5 \right) \quad (\text{A.98e})$$

$$\mathbf{g}_3^- = \frac{1}{2} \mu_{11} \left(\tilde{\Sigma}_1 + \tilde{\Sigma}_0 \right) \quad (\text{A.98f})$$

The \mathbf{g}_i^+ and \mathbf{g}_i^- separately satisfy $\text{su}(2)$ algebra which we call as $\text{su}(2)_+$ and $\text{su}(2)_-$ respectively. Also, these two $\text{su}(2)$ s commute with each other, i.e., $[\mathbf{g}_i^+, \mathbf{g}_j^-] = 0 \quad \forall i, j$. Now we form the following linear combinations of the masses in the \mathcal{J}_{1g}^o and \mathcal{J}_{2g}^e triplets :

$$m_i^+ = (\mathcal{J}_{2g}^e)_i - (\mathcal{J}_{1g}^o)_i \quad (\text{A.99a})$$

$$m_i^- = (\mathcal{J}_{2g}^e)_i + (\mathcal{J}_{1g}^o)_i, \quad (\text{A.99b})$$

for $i = 1, 2, 3$. Here $(\mathcal{J}_{1g}^o)_i, (\mathcal{J}_{2g}^e)_i$ are the masses in the triplets \mathcal{J}_{1g}^o and \mathcal{J}_{2g}^e . The m_i^+ (m_i^-) masses transform in spin-1 (spin-0) representation under the action of $\text{su}(2)_+$ and in spin-0 (spin-1) representation under $\text{su}(2)_-$. Thus, the six masses in the two triplets transform in $(1, 1)$ representation under the action of the $\text{SO}(4)$.

It is interesting to note that the m_i^+ masses go to m_i^- under the action of the microscopic time-reversal (TR). Thus, TR symmetry enforces the two representations of $\text{SO}(4)$ to mix resulting in the two triplets resulting in the TR even and odd spin-quadrupole and spin-octupole phases respectively.

For the second group, the ten masses making up the two doublets $(\mathcal{E}_g^e, \mathcal{E}_g^o)$ and two triplets $(\mathcal{J}_{1g}^e, \mathcal{J}_{2g}^o)$ mix among themselves and actually form a $(2, 2)$ representation of the $\text{SO}(4)$ in Eq. A.98a. This is easy to see by writing the 10 masses in two sub-groups each consisting of five masses as

$$\tilde{m}_i^+ = (\mathcal{J}_{1g}^e)_i - (\mathcal{J}_{2g}^o)_i \quad \forall i = 1, 2, 3, \quad (\text{A.100a})$$

$$\tilde{m}_4^+ = (\mathcal{E}_g^e)_1 - (\mathcal{E}_g^o)_1 \quad (\text{A.100b})$$

$$\tilde{m}_5^+ = (\mathcal{E}_g^e)_2 - (\mathcal{E}_g^o)_2 \quad (\text{A.100c})$$

and

$$\tilde{m}_i^- = (\mathcal{J}_{1g}^e)_i + (\mathcal{J}_{2g}^o)_i \quad \forall i = 1, 2, 3, \quad (\text{A.101a})$$

$$\tilde{m}_4^- = (\mathcal{E}_g^e)_1 + (\mathcal{E}_g^o)_1 \quad (\text{A.101b})$$

$$\tilde{m}_5^- = (\mathcal{E}_g^e)_2 + (\mathcal{E}_g^o)_2 \quad (\text{A.101c})$$

The first (second) sub-group of masses, \tilde{m}_i^+ (\tilde{m}_i^-) transforms as a spin-2(0) representation under $\text{su}(2)_+$ and in spin-0 (spin-2) representation under $\text{su}(2)_-$.

A.10 Analysis in the global basis

As mentioned in the main text, Bloch diagonalizing the Hamiltonian in global basis (Eq. 2.26) obtains four bands arising from the four $j = 3/2$ orbitals (Eq. 2.24) and each two-fold degenerate due to inversion symmetry. The first set of bands touches the second set of bands at *four* distinct points with a Dirac cone structure, see Fig. A.1. With 1/4th

filling of the bands, the chemical potential is tuned to the Dirac points at the four \mathbf{Q}_g vectors, Γ, M_1, M_2, M_3 termed as valleys, in the original honeycomb lattice Brillouin zone.

Following an approach similar to that adopted in the main text, the IR physics can be obtained by expanding in terms of the four Dirac modes at quarter filling; one obtains four flavours of *two component* Dirac fermions $\chi_{g,\nu}(\mathbf{x})$ where $\nu(= \Gamma, M_1, M_2, M_3)$ refers to the four valleys (Fig. A.1). Combining them together, we get the 16-component Dirac spinor

$$\chi_g((x)) = (\chi_{g\Gamma}^T(\mathbf{x}), \chi_{gM_1}^T(\mathbf{x}), \chi_{gM_2}^T(\mathbf{x}), \chi_{gM_3}^T(\mathbf{x}))^T \quad (\text{A.102})$$

in the global basis. This should be contrasted with the 16-component spinor in the local basis obtained by stacking the four 4-component spinors in Eq. 3.4. The low-energy action in the global basis reads

$$\mathcal{L}_g = v_F \bar{\chi}_g (-i\cancel{D}) \chi_g \quad (\text{A.103})$$

repeated are summed over the spatial directions. The gamma matrices in the global basis are

$$\gamma_g^0 = M_{0003}, \gamma_g^1 = M_{0002}, \gamma_g^2 = -M_{0001} \quad (\text{A.104})$$

with

$$M_{\mu\nu\rho\tau} = \sigma_\mu \sigma_\nu \sigma_\rho \sigma_\tau, \quad \mu, \nu, \rho, \tau \in \{0, 1, 2, 3\} \quad (\text{A.105})$$

where σ_μ are the Pauli matrices $\sigma_0 = 1_{2 \times 2}, \sigma_1 = \sigma_x, \sigma_2 = \sigma_y$ and $\sigma_3 = \sigma_z$. The Dirac action obtained from Eq. (A.103) has an emergent global SU(8) symmetry, much like in the local basis. However, the crucial point is that the SU(4) symmetry of the transformed microscopic Hamiltonian in the local basis does not directly manifest in the Dirac lagrangian Eq. (A.103). This is the reason why we choose to represent the relevant matrices $M_{\mu\nu\sigma\tau}$ using the products of Pauli matrices as in Eq. (A.105), as there is no natural choice of flavor and chiral spaces in the global basis. Despite the burden of this additional notation, we will see that the global formulation provides key insights, particularly the semimetallic phases obtained in the main text.

The Dirac action obtained from Eq. (A.103) is invariant under the space group symmetry operations \mathbb{S} , the global basis spinors transform as $\chi_g(\mathbf{x}) \rightarrow \Omega_{\mathbb{S}} \chi_g(\mathbb{S}^{-1}\mathbf{x})$. The

matrices $\Omega_{\mathbb{S}}$ are obtained as (analogous to that discussed in appendix A.6.2)

$$\begin{aligned}
\Omega_{\mathbf{C}_3} &= \frac{1}{16} \left(-M_{0000} - i\sqrt{3}M_{0003} + i\sqrt{3}M_{0010} - 3M_{0013} + \sqrt{3}M_{0120} + 3iM_{0123} + M_{0130} + i\sqrt{3}M_{0133} \right. \\
&\quad + i\sqrt{3}M_{0220} - 3M_{0223} + iM_{0230} - \sqrt{3}M_{0233} - M_{0300} - i\sqrt{3}M_{0303} + i\sqrt{3}M_{0310} - 3M_{0313} \\
&\quad + \sqrt{3}M_{1020} + 3iM_{1023} - M_{1030} - i\sqrt{3}M_{1033} + M_{1100} + i\sqrt{3}M_{1103} + i\sqrt{3}M_{1110} - 3M_{1113} \\
&\quad - iM_{1200} + \sqrt{3}M_{1203} + \sqrt{3}M_{1210} + 3iM_{1213} - \sqrt{3}M_{1320} - 3iM_{1323} + M_{1330} + i\sqrt{3}M_{1333} \\
&\quad - i\sqrt{3}M_{2020} + 3M_{2023} + iM_{2030} - \sqrt{3}M_{2033} + iM_{2100} - \sqrt{3}M_{2103} - \sqrt{3}M_{2110} - 3iM_{2113} \\
&\quad + M_{2200} + i\sqrt{3}M_{2203} + i\sqrt{3}M_{2210} - 3M_{2213} + i\sqrt{3}M_{2320} - 3M_{2323} - iM_{2330} + \sqrt{3}M_{2333} \\
&\quad - M_{3000} - i\sqrt{3}M_{3003} + i\sqrt{3}M_{3010} - 3M_{3013} - \sqrt{3}M_{3120} - 3iM_{3123} - M_{3130} - i\sqrt{3}M_{3133} \\
&\quad \left. - i\sqrt{3}M_{3220} + 3M_{3223} - iM_{3230} + \sqrt{3}M_{3233} - M_{3300} - i\sqrt{3}M_{3303} + i\sqrt{3}M_{3310} - 3M_{3313} \right) \\
\Omega_{\boldsymbol{\sigma}_d} &= -\frac{1}{2}i(M_{0322} - M_{1122} - M_{2222} + M_{3022}), \quad \Omega_{\mathbf{C}'_2} = \frac{1}{2}i(M_{0331} + M_{1131} + M_{2231} + M_{3031}), \\
\Omega_{\mathbf{I}} &= -M_{3313}, \\
\Omega_{\mathbf{S}_6} &= \frac{1}{16} \left(3M_{0000} - i\sqrt{3}M_{0003} + i\sqrt{3}M_{0010} + M_{0013} + \sqrt{3}M_{0120} - iM_{0123} - 3M_{0130} + i\sqrt{3}M_{0133} \right. \\
&\quad + i\sqrt{3}M_{0220} + M_{0223} - 3iM_{0230} - \sqrt{3}M_{0233} + 3M_{0300} - i\sqrt{3}M_{0303} + i\sqrt{3}M_{0310} + M_{0313} \\
&\quad + \sqrt{3}M_{1020} - iM_{1023} + 3M_{1030} - i\sqrt{3}M_{1033} - 3M_{1100} + i\sqrt{3}M_{1103} + i\sqrt{3}M_{1110} + M_{1113} \\
&\quad + 3iM_{1200} + \sqrt{3}M_{1203} + \sqrt{3}M_{1210} - iM_{1213} - \sqrt{3}M_{1320} + iM_{1323} - 3M_{1330} + i\sqrt{3}M_{1333} \\
&\quad - i\sqrt{3}M_{2020} - M_{2023} - 3iM_{2030} - \sqrt{3}M_{2033} - 3iM_{2100} - \sqrt{3}M_{2103} - \sqrt{3}M_{2110} + iM_{2113} \\
&\quad - 3M_{2200} + i\sqrt{3}M_{2203} + i\sqrt{3}M_{2210} + M_{2213} + i\sqrt{3}M_{2320} + M_{2323} + 3iM_{2330} + \sqrt{3}M_{2333} \\
&\quad + 3M_{3000} - i\sqrt{3}M_{3003} + i\sqrt{3}M_{3010} + M_{3013} - \sqrt{3}M_{3120} + iM_{3123} + 3M_{3130} - i\sqrt{3}M_{3133} \\
&\quad \left. - i\sqrt{3}M_{3220} - M_{3223} + 3iM_{3230} + \sqrt{3}M_{3233} + 3M_{3300} - i\sqrt{3}M_{3303} + i\sqrt{3}M_{3310} + M_{3313} \right), \\
\Omega_{\mathbf{T}_1} &= M_{0300}, \quad \Omega_{\mathbf{T}_2} = M_{3000}, \quad \Omega_{\mathbf{T}} = iM_{0032}.
\end{aligned} \tag{A.106}$$

An important feature here is that χ_g transforms under the action of \mathbb{S} such that the space of spinors $\chi_{g\Gamma}$ is an invariant subspace, i. e., symmetry transformations do not mix $\chi_{g\Gamma}$ with any other $\chi_{g\nu}, \nu \in \{M_1, M_2, M_3\}$.

We now see that any fermion bilinear of the form

$$-i\bar{\chi}_g\gamma_g^0 M_{\mu\nu\rho 3}\chi_g \tag{A.107}$$

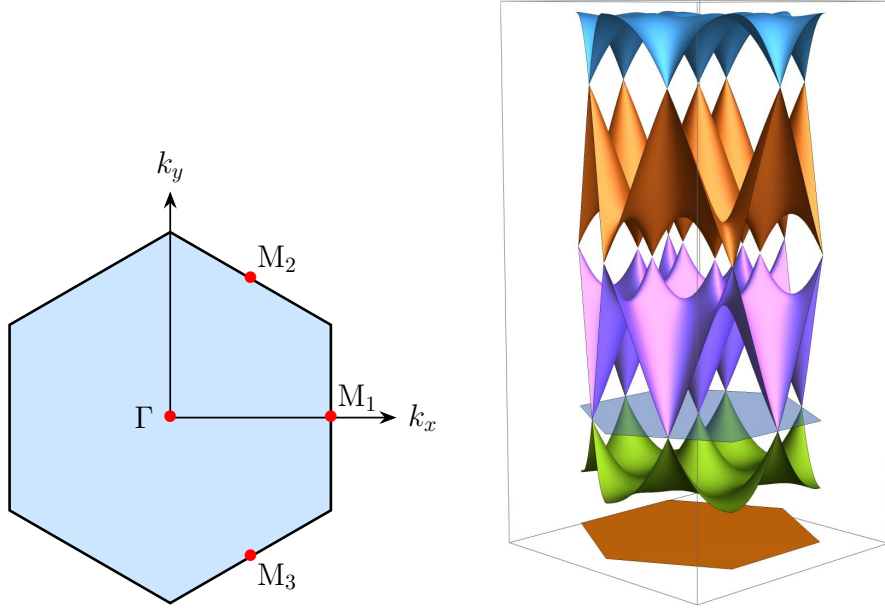


Figure A.1: Brillouin zone and band structure in the global basis. Each of the four bands indicated in a different color are twofold degenerate. At quarter filling, distinct Dirac cones appear at four points (valleys) Γ , M_1 , M_2 , M_3 . The light blue plane indicates the chemical potential at quarter-filling.

described by a mass matrix $M_{\mu\nu\rho 3}$, $\mu, \nu, \rho \in \{0, 1, 2, 3\}$ which anticommutes with γ_g^1 and γ_g^2 , gaps out the Dirac fermions. The 64 masses can be classified by the irreducible representations of the space group using the fact that the masses $M_{\mu\nu\rho 3}$ transform adjointly under the action of the operations Eq. (A.106). On carrying out the classification of mass terms according to the irreducible representations of the space group, the analysis based on the global basis produces identical results as those in tables. 4.3 to 4.6.

The global basis offers illuminating insights into understanding the phases, particularly the semimetallic ones. Central to this is the fact that symmetry operations \mathbb{S} do not mix $\chi_{g\Gamma}$ with any other $\chi_{g\nu}$, $\nu \in \{M_1, M_2, M_3\}$. Thus, a spinor can be decomposed into

$$\chi_g = \underbrace{P_\Gamma \chi_g}_{\chi_{g\Gamma}} + \underbrace{(1 - P_\Gamma) \chi_g}_{\chi_{gM}} \quad (\text{A.108})$$

where the operator P_Γ projects a general spinor to the valley Γ . The space of spinors $\chi_{g\Gamma}$ carries some irreps D^a (in the fundamental representation) of the space group labeled by index a . Similarly, the space of spinors χ_{gM} (spinors belonging to valleys M_1, M_1, M_1) may be decomposed into space group irreps D^b labelled by b . Also, the adjoint representation on the space of masses is decomposed into irreps D^c labeled by c . We can now study

the structure of the masses in one of the representations D^c , by exploring which product representations $D^{P*} \otimes D^c \otimes D^Q$ where $P, Q \in \{a, b\}$ contain a singlet representation. Several interesting possibilities arise, of which two are crucially important:

1. An irreducible mass matrix M^c (c labels the irrep D^c in the adjoint representation) is such that there is no identity representation in the decomposable tensor product representation $D^{a'*} \otimes D^c \otimes D^a$ for all a, a' representations carried by the $\chi_{g\Gamma}$ -space. Further, there is atleast one identity representation in $D^{b'*} \otimes D^c \otimes D^b$, where b, b' are irreps of the χ_{gM} -space. In such a scenario, the mass M^c acts like a “zero matrix” on spinors $\chi_{g\Gamma}$, and has the following structure,

$$M_{\Gamma\text{-DSM}}^c = \begin{matrix} & \Gamma & M_1 & M_2 & M_2 \\ \Gamma & \left(\begin{array}{cccc} 0_{4 \times 4} & 0_{4 \times 4} & 0_{4 \times 4} & 0_{4 \times 4} \\ 0_{4 \times 4} & \blacksquare & \blacksquare & \blacksquare \\ 0_{4 \times 4} & \blacksquare & \blacksquare & \blacksquare \\ 0_{4 \times 4} & \blacksquare & \blacksquare & \blacksquare \end{array} \right) & & & \\ M_1 & & & & \\ M_2 & & & & \\ M_3 & & & & \end{matrix}, \quad (\text{A.109})$$

where $\blacksquare \equiv$ non-zero entry. This guarantees that the Dirac cones at Γ are un-gapped, leading to a semimetallic phase, and we dub such a phase as “Gamma-Dirac semimetal (Γ -DSM)”. Examples of such semimetals are entries No. 17, 18, 20, 22, 23 and 24 in Table 4.6. As discussed in the main text, additional gapless modes may be possible if such masses arise in a doublet or triplet representation when the coefficients of the mass matrices satisfy special criteria (see, for example, 7.52).

2. The second interesting possibility for the mass M^c is such that while there is no identity representation in $D^{a'*} \otimes D^c \otimes D^a$ (a, a' are representations in $\chi_{g\Gamma}$ -space) or $D^{b'*} \otimes D^c \otimes D^b$ (b, b' are representations in χ_{gM} -space), but there is at least one identity representation in $D^{a'*} \otimes D^c \otimes D^b$. This implies that the mass M^c mixes $\chi_{g\Gamma}$ with χ_{gM} , but since mixing between spinors at Γ is forbidden as is the mixing between spinors between the M valleys, the remaining possibility is that of mixing

between spinors at Γ with those of M leading to the mass matrix structured as

$$M_{\text{M-DSM}}^c = \begin{matrix} & \Gamma & M_1 & M_2 & M_2 \\ \Gamma & \left(\begin{array}{cccc} 0_{4 \times 4} & \blacksquare & \blacksquare & \blacksquare \\ \blacksquare & 0_{4 \times 4} & 0_{4 \times 4} & 0_{4 \times 4} \\ \blacksquare & 0_{4 \times 4} & 0_{4 \times 4} & 0_{4 \times 4} \\ \blacksquare & 0_{4 \times 4} & 0_{4 \times 4} & 0_{4 \times 4} \end{array} \right) & & & \\ M_1 & & & & \\ M_2 & & & & \\ M_3 & & & & \end{matrix}, \quad (\text{A.110})$$

This type of mass matrix has an emergent sub-lattice symmetry where

$$U_{SL}^\dagger M_{\text{M-DSM}}^c U_{SL} = -M_{\text{M-DSM}}^c \quad (\text{A.111})$$

with

$$U_{SL} = \begin{matrix} & \Gamma & M_1 & M_2 & M_2 \\ \Gamma & \left(\begin{array}{cccc} 1_{4 \times 4} & 0_{4 \times 4} & 0_{4 \times 4} & 0_{4 \times 4} \\ 0_{4 \times 4} & -1_{4 \times 4} & 0_{4 \times 4} & 0_{4 \times 4} \\ 0_{4 \times 4} & 0_{4 \times 4} & -1_{4 \times 4} & 0_{4 \times 4} \\ 0_{4 \times 4} & 0_{4 \times 4} & 0_{4 \times 4} & -1_{4 \times 4} \end{array} \right) & & & \\ M_1 & & & & \\ M_2 & & & & \\ M_3 & & & & \end{matrix} \quad (\text{A.112})$$

which guarantees that there are at least 8 zero eigenvalues leading to (at least) 8 gapless modes for any such mass. Note that the gapless modes will be a linear combination of spinors from all the valleys and, in particular will depend on the non-zero entries denoted by \blacksquare . Such semimetals are dubbed "M-Dirac semimetals (M-DSM)". In Table 4.6, the entries 19 and 21 are of this type.

A.11 Spinless fermions on a honeycomb lattice with π -flux at 1/4-th filling

In this section, we revisit the physics of spinless fermions hopping on a honeycomb lattice with a π -flux through each of the honeycomb plaquettes. We adopt the unit cell shown in Fig. A.2, and choose a more convenient gauge for obtaining the π -flux (this enables an efficient implementation of lattice symmetries). We obtain four bands, each of which is two-fold degenerate. At quarter filling, we obtain two Dirac cones located at the Γ point of the hexagonal Brillouin zone as shown in Fig. A.1. The low energy physics is described

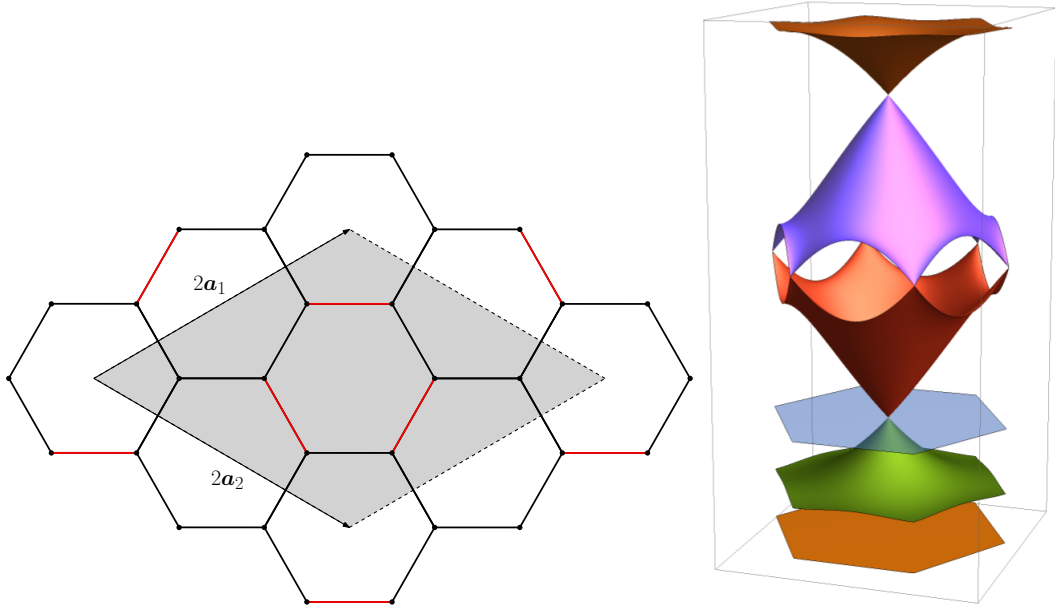


Figure A.2: Honeycomb lattice with π -flux. (Left) Unit cell consisting of 8 sites adopted for the analysis. Fermions hop to nearest neighbors where red links shown have a hopping amplitude with a negative sign. (Right) Band structure showing four bands, each of which is two-fold degenerate. The light blue plane shows the quarter-filled chemical potential.

by a four-component spinor χ_π with a Lagrangian density similar to Eq. (A.103) with,

$$\gamma_\pi^0 = M_{03}, \gamma_\pi^1 = -M_{02}, \gamma_\pi^2 = M_{01} \quad (\text{A.113})$$

where

$$M_{\mu\nu} = \sigma_\mu \sigma_\nu. \quad (\text{A.114})$$

where σ_μ are Pauli matrices defined just below Eq. (A.105). The system has an emergent global SU(2) symmetry generated by $M_{i0}, i \in \{1, 2, 3\}$ which is the analog of the chiral symmetry discussed near Eq. (3.9).

A fermion bilinear of the form

$$-i\bar{\chi}_\pi \gamma_\pi^0 M_{\mu 3} \chi_\pi \quad (\text{A.115})$$

described by a mass matrix $M_{\mu 3}, \mu \in \{0, 1, 2, 3\}$ which anticommutes with γ_π^1 and γ_π^2 , gaps out the Dirac fermions. The space of these mass matrices can be reduced in the irreps of the space group, resulting the phases described below.

A.11.1 Integer Chern insulator

This mass transforms as a one-dimensional irrep, breaking time reversal and reflection symmetries of the lattice while preserving all the proper rotational symmetries of the hexagonal lattice

\mathcal{A}_{2g}^o	
1	M_{03}

resulting in a mass term

$$\Delta_{\text{ICI}} = -i\langle\bar{\chi}_\pi\chi_\pi\rangle. \quad (\text{A.116})$$

It is clear that the SU(4) symmetric ICI found in Eq. (5.1) is a “larger dimensional” realization of such a phase with a larger value of the Chern-Simons level.

A.11.2 Stripy density waves

The remainder of the three masses organize as a triplet under the space group symmetries, preserving time reversal but breaking rotational and translational symmetries.

\mathcal{J}_{1g}^e	
1	$\frac{1}{\sqrt{2}}M_{13} + \frac{1}{\sqrt{6}}M_{23} - \frac{1}{\sqrt{3}}M_{33}$
2	$-\frac{1}{\sqrt{2}}M_{13} + \frac{1}{\sqrt{6}}M_{23} - \frac{1}{\sqrt{3}}M_{33}$
3	$\sqrt{\frac{2}{3}}M_{23} + \frac{1}{\sqrt{3}}M_{33}$

The three components of the masses correspond to the fermion bilinears

$$\begin{aligned} & -i\langle\bar{\chi}_\pi\left(\frac{1}{\sqrt{2}}M_{10} + \frac{1}{\sqrt{6}}M_{20} - \frac{1}{\sqrt{3}}M_{30}\right)\chi_\pi\rangle, \\ & -i\langle\bar{\chi}_\pi\left(-\frac{1}{\sqrt{2}}M_{10} + \frac{1}{\sqrt{6}}M_{20} - \frac{1}{\sqrt{3}}M_{30}\right)\chi_\pi\rangle, \\ & -i\langle\bar{\chi}_\pi\left(\sqrt{\frac{2}{3}}M_{20} + \frac{1}{\sqrt{3}}M_{30}\right)\chi_\pi\rangle \end{aligned} \quad (\text{A.117})$$

any one of which produces a stripy density wave similar to that shown in Fig. 5.2. The mass matrices that appear here are orthogonal linear combinations of the chiral symmetry generators discussed just below Eq. (A.113). Indeed, it is evident that the chiral masses shown in Eq. (5.5) correspond to this case.

A.12 A model with $j = 1/2$ spins

In this section, we construct a model on a honeycomb lattice where the spin-orbit coupling is realized in a $j = 1/2$ system, i. e., as a system with spin-1/2 degrees of freedom. Although this model is not directly motivated by a material system, it is nevertheless useful to study, in a simpler setting, the conceptual underpinnings of how spin-orbit coupling produces interesting new phenomena. The model is defined using Fig. 2.2 where each lattice site has two $j = 1/2$ orbitals. The hopping Hamiltonian is same as that in Eq. (2.26), with the key difference that $U_{\mathbf{r}\mathbf{r}'} = \{\tau_x, \tau_y, \tau_z\}$ (τ_i here are the Pauli matrices acting on the $j=1/2$ space) respectively when $\mathbf{r}\mathbf{r}'$ is the x, y, z type link shown in Fig. 2.2. This system has the following microscopic symmetries among those listed in table. 2.1 and time reversal,

1. Lattice translations as in \mathbf{T}_1 and \mathbf{T}_2
2. \mathbf{C}_3 rotations
3. σ_d dihedral reflection
4. Time reversal \mathbb{T} , with $\mathbb{T}^2 = -1$

The interesting aspect of this model is that by carrying out transformations similar to those discussed in appendix A.4, one can arrive at a system with a π -flux through each honeycomb plaquette, and a *global* SU(2) flavor symmetry. In other words, this model is the “SU(2) version” of the SU(4) model discussed in the main text.

We continue to discuss this model in the *global* basis. The band structure of this model is identical to that shown in Fig. A.1, the difference being that each band is non-degenerate. At quarter filling, the physics can be described by four Dirac cones, one each located at Γ, M_1, M_2, M_3 . We get a Dirac action similar to Eq. (A.103), with χ_g as in Eq. (A.102) where $\chi_{g\nu}$, $\nu \in \{\Gamma, M_1, M_2, M_3\}$ are 2-component spinors. The Dirac gamma matrices are

$$\gamma_g^0 = M_{003}, \gamma_g^1 = M_{002}, \gamma_g^2 = -M_{001} \quad (\text{A.118})$$

and

$$M_{\mu\nu\rho} = \sigma_\mu \sigma_\nu \sigma_\rho \quad (\text{A.119})$$

where Pauli matrices σ_μ are described just below Eq. (A.105)

The symmetry transformations are described by

$$\begin{aligned}
\Omega_{\mathbf{C}_3} &= \frac{1}{8} \left(M_{000} + i\sqrt{3}M_{003} - M_{010} - i\sqrt{3}M_{013} \right. \\
&\quad + iM_{020} - \sqrt{3}M_{023} + M_{030} + i\sqrt{3}M_{033} - M_{100} \\
&\quad - i\sqrt{3}M_{103} + M_{110} + i\sqrt{3}M_{113} + iM_{120} \\
&\quad - \sqrt{3}M_{123} + M_{130} + i\sqrt{3}M_{133} - iM_{200} \\
&\quad + \sqrt{3}M_{203} - iM_{210} + \sqrt{3}M_{213} + M_{220} \\
&\quad + i\sqrt{3}M_{223} + iM_{230} - \sqrt{3}M_{233} + M_{300} \\
&\quad + i\sqrt{3}M_{303} + M_{310} + i\sqrt{3}M_{313} - iM_{320} \\
&\quad \left. + \sqrt{3}M_{323} + M_{330} + i\sqrt{3}M_{333} \right) \\
\Omega_{\sigma_d} &= \frac{1}{2} (-M_{032} + M_{112} + M_{222} - M_{302}) \\
\Omega_{\mathbf{T}_1} &= M_{300} \\
\Omega_{\mathbf{T}_2} &= M_{030} \\
\Omega_{\mathbf{T}} &= iM_{002}
\end{aligned} \tag{A.120}$$

Again, we see that the spinors $\chi_{g\Gamma}$ (see Eq. (A.108)) form an invariant subspace under the action of the symmetries above. One, therefore, expects to obtain semimetallic phases when the mass matrices of the type $M_{\mu\nu 3}$, $\mu, \nu \in \{0, 1, 2, 3\}$ that gap out (see Eq. (A.107)) the Dirac Lagrangian Eq. (A.103) defined by Eq. (A.118) are resolved into irreducible components. Below we briefly describe seven irreducible masses and the resulting phases obtained by such an analysis.

A.12.1 Chiral masses

Integer Chern insulator

\mathbf{C}_3	σ_d	\mathbf{T}_1	\mathbf{T}_2	\mathbf{T}	\mathcal{A}^o	
✓	✗	✓	✓	✗	1	M_{003}

This mass is SU(2) symmetric and produces a fully gapped state. Viewed on the lattice, it produces spin-independent second neighbour hoppings akin to the Haldane honeycomb model as in Fig. 5.1 with an effective Chern-Simons action described by Eq. (5.2).

Stripy Density Wave Phase

\mathbf{C}_3	σ_d	\mathbf{T}_1	\mathbf{T}_2	\mathbb{T}
\times	\times	\times	\times	\checkmark

\mathcal{J}^e	
1	M_{123}
2	$-M_{203}$
3	$-M_{323}$

This is again an SU(2) invariant mass that results in a stripy density wave similar to the SU(4) invariant case found in Eq. (5.5).

The two cases described above exhaust the chiral masses.

A.12.2 SU(2) Flavor masses

Quantum dipolar Hall mass

\mathbf{C}_3	σ_d	\mathbf{T}_1	\mathbf{T}_2	\mathbb{T}
\times	\times	\times	\times	\checkmark

\mathcal{J}^e	
1	M_{213}
2	$-M_{233}$
3	$-M_{023}$

This mass produces spin-dependent second neighbour hopping that produces a uniform SU(2) flux in a second-neighbor triangle, gapping out the system. The phase with this mass is described by a mutual Chern-Simons theory like Eq. (6.5) resulting in dipole-filtered edge states and is analogous to the phase discussed in Sec. 6.1.2.

A.12.3 Mixed masses

Ferromagnetic insulator

\mathbf{C}_3	σ_d	\mathbf{T}_1	\mathbf{T}_2	\mathbb{T}
\checkmark	\times	\checkmark	\checkmark	\times

\mathcal{A}^o	
1	$\frac{M_{033}}{\sqrt{3}} + \frac{M_{303}}{\sqrt{3}} + \frac{M_{333}}{\sqrt{3}}$

This mass manifests as a uniform magnetic field in the direction perpendicular to the honeycomb and fully gap out the Dirac fermions. The analogous state corresponding to this in the SU(4) case is discussed in Sec. 7.1.2.

Ferromagnetic semimetal – Γ -Dirac Semimetal

\mathbf{C}_3	σ_d	\mathbf{T}_1	\mathbf{T}_2	\mathbb{T}
\times	\times	\checkmark	\checkmark	\times

\mathcal{G}^o	
1	$\frac{M_{033}}{\sqrt{2}} - \frac{M_{333}}{\sqrt{2}}$
2	$\frac{M_{033}}{\sqrt{6}} - \sqrt{\frac{2}{3}}M_{303} + \frac{M_{333}}{\sqrt{6}}$

The doublet mass produces a local magnetic field in the plane of the honeycomb lattice and the components rotate into each other under lattice symmetries; this phase is analogous to the ferro spin-octupolar semimetallic phase discussed in Sec. 7.2.5. For any generic linear combination of the masses, the Dirac cone at the Γ point remains ungapped, while for special linear combinations of the two masses, there is one additional gapless mode as discussed in Sec. 7.2.5. This is a semimetallic phase of Γ -DSM type.

Stripy spin density wave semimetal (M-Dirac Semimetal)

\mathbf{C}_3	σ_d	\mathbf{T}_1	\mathbf{T}_2	\mathbb{T}
\times	\times	\times	\times	\times

\mathcal{J}^o	
1	$\frac{M_{113}}{\sqrt{2}} - \frac{M_{223}}{\sqrt{2}}$
2	$-\frac{M_{103}}{\sqrt{2}} - \frac{M_{133}}{\sqrt{2}}$
3	$-\frac{M_{013}}{\sqrt{2}} - \frac{M_{313}}{\sqrt{2}}$

This mass produces a spin density wave of the stripy kind similar to that discussed in Eq. (7.47). Interestingly, this produces a semimetallic phase of the M-DSM kind, precisely as discussed for the $SU(4)$ case in Eq. (7.47).

Stripy spin density wave semimetal – (Γ -Dirac Semimetal)

\mathbf{C}_3	σ_d	\mathbf{T}_1	\mathbf{T}_2	\mathbb{T}
\times	\times	\times	\times	\times

T_u^o	
1	$\frac{M_{113}}{\sqrt{2}} + \frac{M_{223}}{\sqrt{2}}$
2	$\frac{M_{133}}{\sqrt{2}} - \frac{M_{103}}{\sqrt{2}}$
3	$\frac{M_{313}}{\sqrt{2}} - \frac{M_{013}}{\sqrt{2}}$

This is a triplet mass that produces a stripy magnetic field; the key difference between the one just discussed above, is that this possesses an isolated Dirac cone, where a single Dirac cone at Γ is always left ungapped. This is similar to the $SU(4)$ case discussed in

Eq. (7.50) that produces a stripy spin-octupolar density wave. For the SU(2) case one has a stripy density wave. Again, just as in the case discussed in Eq. (7.50), there are special linear combinations of the masses that obtain additional gapless modes.

A.13 Derivation of the effective action for the CDW order parameter

With the action for the CDW order parameter coupled to the fermions given by Eq. 8.11, the partition function is

$$\mathcal{Z} = \int \mathcal{D}\vec{\Delta} \mathcal{D}\bar{\chi} \mathcal{D}\chi \exp(-S[\vec{\Delta}, \bar{\chi}, \chi]) \quad (\text{A.121})$$

Now, integrating out the fermions, we get

$$\mathcal{Z} = \int \mathcal{D}\vec{\Delta} \exp(-S_{eff}[\vec{\Delta}]), \quad (\text{A.122})$$

where $S_{eff}[\vec{\Delta}]$ is the effective action for the CDW order parameter field and is given by

$$S_{eff}[\vec{\Delta}] = -N_f \text{tr} \ln \left(-i\cancel{\partial} - ig\vec{\Delta} \cdot \vec{\zeta} \right) + \int d^3x \mathcal{L}_b. \quad (\text{A.123})$$

Thus, S_{eff} is proportional to N_f and in the $N_f \rightarrow \infty$ limit, the partition function is dominated by the saddle point value of S_{eff} . In the following, We first evaluate S_{eff} with mean field approximation till order $1/N_f$.

To evaluate S_{eff} , we first calculate the fermionic determinant. For this, we first perform the following transformation on the spinors χ

$$\chi \rightarrow U \chi, \quad (\text{A.124})$$

such that

$$\vec{\Delta} \cdot \bar{\chi} \vec{\zeta} \chi = |\vec{\Delta}| \bar{\chi} \zeta_1 \chi \quad (\text{A.125})$$

Then, the determinant is

$$\begin{aligned}
&= -\text{tr} \ln [-i\cancel{\phi} - ig\Delta_1\zeta_1] \\
&= -\text{tr}(\log(-i\cancel{\phi})) - \text{tr} \ln \left(1 + \frac{1}{i\cancel{\phi}} ig|\vec{\Delta}| \zeta_1 \right) \\
&= -\sum_{n=1}^{\infty} \left(-\frac{V}{2n} \right) \text{tr} \int \frac{d^3k}{(2\pi)^3} \frac{(ig|\vec{\Delta}|\zeta_1)^{2n}}{(k^2)^n} + \mathcal{O}(1/N_f) \quad (V = \text{volume of space-time}) \\
&= \sum_{n=1}^{\infty} \left(\frac{V}{2n} \right) 4 \int \frac{d^3k}{(2\pi)^3} (-1)^n \frac{(g^2|\vec{\Delta}|^2)^n}{(k^2)^n} + \mathcal{O}(1/N_f) \\
&= (-1)4\frac{V}{2} \int \frac{d^3k}{(2\pi)^3} \log \left(1 + \frac{g^2|\vec{\Delta}|^2}{k^2} \right) + \mathcal{O}(1/N_f) \\
&= -2V \frac{4\pi}{(2\pi)^3} \frac{1}{3} \left[3g^2\Delta_1^2\Lambda - 2g^3|\vec{\Delta}|^3\frac{\pi}{2} \right] + \mathcal{O}(1/N_f) \\
&= V \left[-\frac{g^2}{\pi^2}|\Delta|^2\Lambda + \frac{g^3}{3\pi}|\Delta|^3 \right] + \mathcal{O}(1/N_f) \tag{A.126}
\end{aligned}$$

Here, Λ is the ultraviolet momentum cutoff. With this, the effective action for the CDW order parameter is

$$S_{eff}[\vec{\Delta}] = V \left[\mathcal{L}_b + -\frac{g^2}{\pi^2}|\Delta|^2\Lambda + \frac{g^3}{3\pi}|\Delta|^3 \right] \tag{A.127}$$

A.14 Evolution of the Band structures in τ_m - $\tilde{\lambda}$ Phase Diagram

The $\tilde{\lambda} = 0$ line

Fig. A.3 shows the band structures at different points on the $\tilde{\lambda} = 0$ line of the τ_m - $\tilde{\lambda}$ phase diagram in Fig. 6a of the main text. At $\tau_m = 0$ on this line, there are two flat bands, each of which are six-fold degenerate. As τ_m is increased, six 2-fold degenerate bands appear. Finally at $\tau_m = 1$, there are four bands with the lowest and the top bands being 2-fold and the rest being 4-fold degenerate.

The $\tau_m = 0$ line

The energy spectrum along the $\tau_m = 0$ line is shown in Fig. A.4. The band structure for $\tilde{\lambda} = 0$ is (cf. the $\tilde{\lambda} = 0, \tau_m = 0$ line in Fig. A.3) has two six-fold degenerate bands. As $\tilde{\lambda}$ is increased, six 2-fold degenerate bands appear, two of them being completely flat.

The $\tau_m = 1$ line

The evolution of energy spectrum along the $\tau_m = 1$ line is shown in Fig. A.5. The band structure for $\tilde{\lambda} = 0$ on this line is has four bands (cf. $\tilde{\lambda} = 0, \tau_m = 1$ in Fig. A.3). For large values of $\tilde{\lambda}$, the $J = 3/2$ and the $J = 1/2$ bands are separated. For $\tilde{\lambda} = 20, \tau_m = 1$, only the lowest $J = 3/2$ bands are shown.

A.15 Properties of gapped phases

SU(8) Dirac theory at the P_3 point

At P_3 point of the phase diagram in Fig. 9.1 and Fig. 9.6 of the main text, the low-energy effective theory is described by massless Dirac fermions with internal SU(8) symmetry. Below we sketch the derivation of the Dirac theory. The details can be found in Ref. [156].

At the P_3 point, the form of the Hamiltonian in Eq. 9.4 of the main text, when

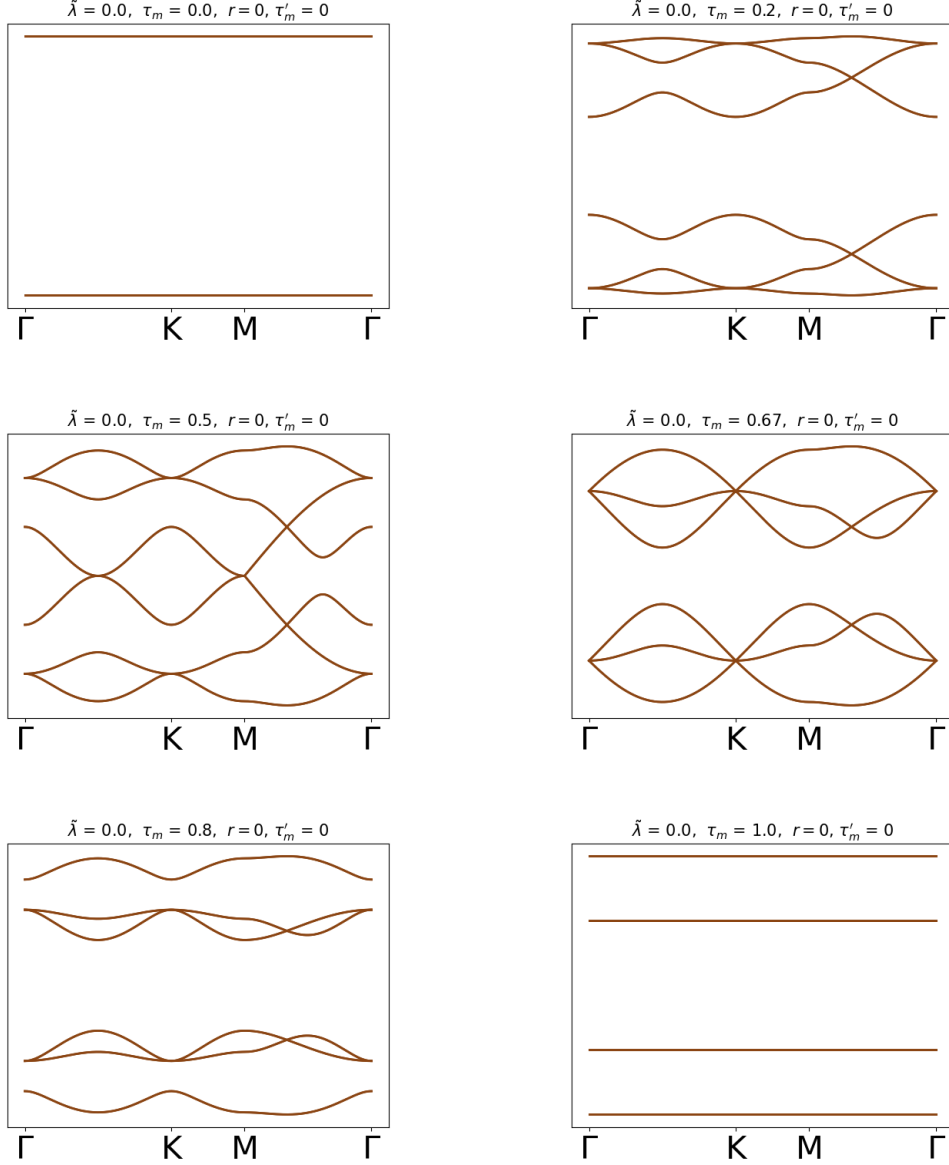


Figure A.3: Evolution of band structure along the $\tilde{\lambda} = 0$ line of the phase diagram in Fig. 6 of the main text.

projected to the low-energy $j = 3/2$ orbitals, is given by

$$\begin{aligned}
\mathcal{H}_{P_3} = & -\frac{\varepsilon}{\sqrt{3}} \left(\sum_{\langle \mathbf{r}, s; \mathbf{r}', s' \rangle \in X\text{-bonds}} \psi^\dagger(\mathbf{r}, s) U_X \psi(\mathbf{r}', s') + \sum_{\langle \mathbf{r}, s; \mathbf{r}', s' \rangle \in Y\text{-bonds}} \psi^\dagger(\mathbf{r}, s) U_Y \psi(\mathbf{r}', s') \right. \\
& \left. + \sum_{\langle \mathbf{r}, s; \mathbf{r}', s' \rangle \in Z\text{-bonds}} \psi^\dagger(\mathbf{r}, s) U_Z \psi(\mathbf{r}', s') \right) + h.c..
\end{aligned} \tag{A.128}$$

Here, ψ_i is a 4-component annihilation operator corresponding to the four $j = 3/2$

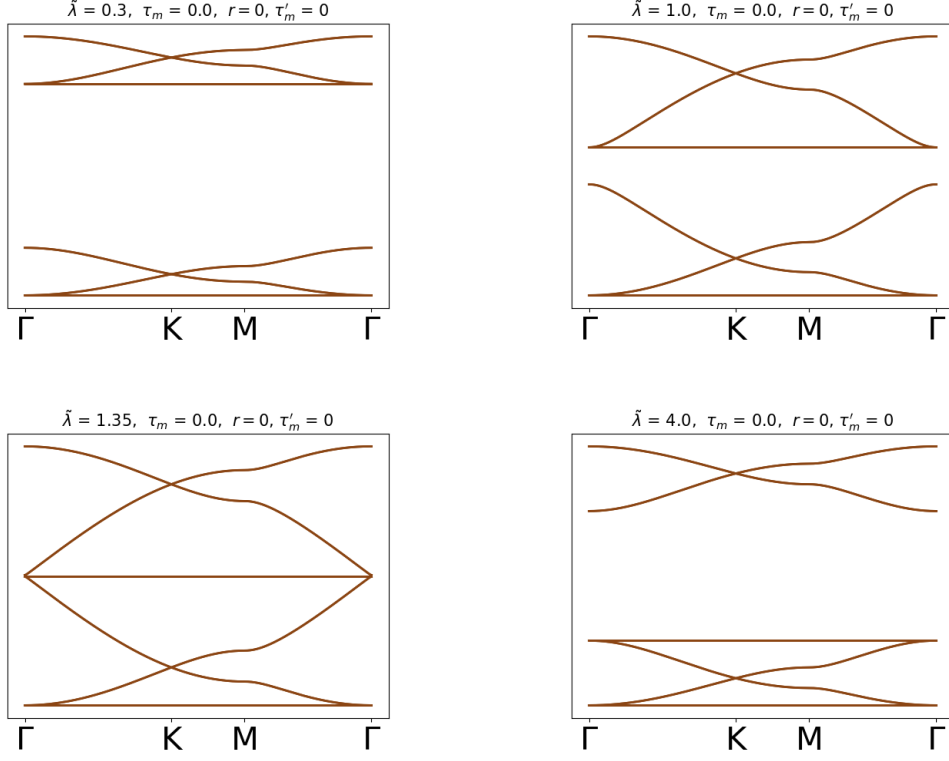


Figure A.4: Evolution of band structure along the $\tau_m = 0$ line of the phase diagram in Fig. 6 of the main text.

orbitals at the site i . The U_X, U_Y, U_Z are 4×4 Hermitian matrices, which are given by

$$U_X = -\rho \Sigma_1 \quad (\text{A.129})$$

$$U_Y = -\rho \Sigma_2 \quad (\text{A.130})$$

$$U_Z = -\rho \Sigma_3. \quad (\text{A.131})$$

Here, $\rho = +1$ for the phase diagram in Fig. 9.1(a) and $\rho = -1$ for Fig. 9.6.

Projecting this Hamiltonian in Eq A.128 to the two lowest two bands which touch linearly at the Fermi energy, we get the SU(8) symmetric Dirac Hamiltonian given by

$$\mathcal{H}_{Dirac} = \rho v_F \int d^2\mathbf{r} \chi^\dagger(\mathbf{r}) (-i\alpha_1 \partial_1 - i\alpha_2 \partial_2) \chi(\mathbf{r}), \quad (\text{A.132})$$

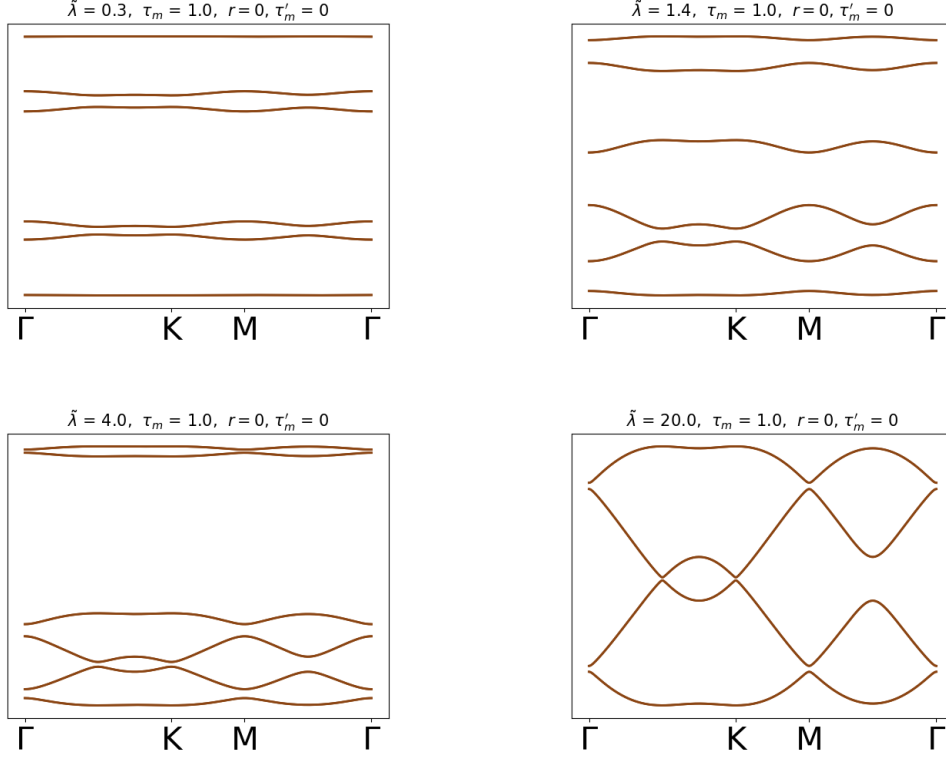


Figure A.5: Band structures along the $\tau_m = 1$ line of the phase diagram in Fig. 6 of the main text. All the bands are 2-fold degenerate. For $\tilde{\lambda} = 20$, only four bands are shown leaving out higher energy $J = 1/2$ orbitals.

with

$$\alpha_1 = \Sigma_0 \otimes \tau_3 \otimes \sigma_1 \quad (\text{A.133})$$

$$\alpha_2 = \Sigma_0 \otimes \tau_0 \otimes \sigma_2. \quad (\text{A.134})$$

Here, v_F is the Fermi velocity, which is related to the gradient of the linearly dispersing bands at the Dirac points. $\chi(\mathbf{r})$ is the 16-component Dirac spinor at the position \mathbf{r} . Both τ_i and σ_i (for $i = 1, 2, 3$) are the Pauli matrices with τ_0 and σ_0 being the 2×2 identity matrix. The generators of the $SU(8)$ symmetry are the set of 63 matrices given by

$$\{\Sigma_0, \Sigma_i\} \otimes \{\tau_3\sigma_0, \tau_1\sigma_2, \tau_2\sigma_2\}, \quad \Sigma_i \otimes \tau_0\sigma_0 \quad (\text{A.135})$$

for $i = 1, \dots, 15$.

The topological gapped phase

On moving left from the P_3 point along the $\tilde{\lambda} = \infty$ line by reducing the value of τ_m from 1, the effective hopping Hamiltonian in the $j = 3/2$ sector is given by

$$\mathcal{H}_{top} = -\frac{\varepsilon}{\sqrt{3}} \sum_{\langle \mathbf{r}, \mathcal{J}; \mathbf{r}', \mathcal{J}' \rangle} \psi^\dagger(\mathbf{r}, \mathcal{J}) \tilde{H}_{\mathbf{r}\mathbf{r}'}^{\mathcal{J}\mathcal{J}'} \psi(\mathbf{r}', \mathcal{J}'), \quad (\text{A.136})$$

with

$$\begin{aligned} \tilde{H}_X &= U_X + (1 - \tau_m) \left[\frac{1}{3} \Sigma_0 + \frac{1}{6} \left(-\sqrt{3} \Sigma_4 + \Sigma_5 \right) \right] \\ \tilde{H}_Y &= U_Y + (1 - \tau_m) \left[\frac{1}{3} \Sigma_0 + \frac{1}{6} \left(\sqrt{3} \Sigma_4 + \Sigma_5 \right) \right] \\ \tilde{H}_Z &= U_Z + (1 - \tau_m) \left[\frac{1}{3} \Sigma_0 - \frac{1}{3} \Sigma_5 \right]. \end{aligned} \quad (\text{A.137})$$

On projecting this Hamiltonian to the lowest two bands, we get the following effective low-energy Hamiltonian

$$\mathcal{H}_{top} = \mathcal{H}_{Dirac} + (1 - \tau_m) \mathcal{H}_m^{(1)} + (1 - \tau_m) \mathcal{H}'. \quad (\text{A.138})$$

Here, \mathcal{H}_{Dirac} is given by Eq. A.132. The $\mathcal{H}_m^{(1)}$ and \mathcal{H}' are given by

$$\mathcal{H}_m^{(1)} = \int d^2\mathbf{r} \chi^\dagger (\Sigma_1 \tau_1 \sigma_0 - \Sigma_2 \tau_2 \sigma_1 + \Sigma_3 \tau_0 \sigma_3) \chi, \quad (\text{A.139})$$

and

$$\mathcal{H}' = \chi^\dagger (-i\partial_x \delta\alpha_x - i\partial_y \delta\alpha_y) \chi, \quad (\text{A.140})$$

with

$$\delta\alpha_x = -\Sigma_3 \tau_3 \sigma_1 + \frac{1}{\sqrt{3}} \Sigma_{35} \tau_0 \sigma_0 + \frac{\sqrt{3}}{\sqrt{2}} \Sigma_{35} \tau_0 \sigma_3 \quad (\text{A.141})$$

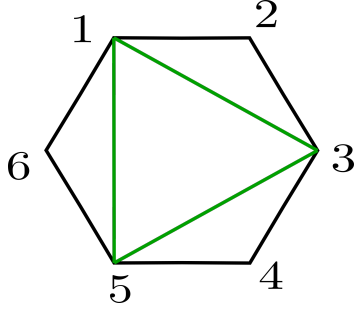


Figure A.6: A single hexagon of a honeycomb lattice showing the three kinds of next nearest neighbour bonds (green bonds). The six sites are labelled with integers from 1 to 6.

and

$$\begin{aligned} \delta\alpha_y = & \frac{1}{\sqrt{6}}(\Sigma_1\tau_1\sigma_2 - \Sigma_2\tau_2\sigma_2) + \frac{\sqrt{3}}{2\sqrt{2}}(\Sigma_{14}\tau_1\sigma_1 - \Sigma_{24}\tau_2\sigma_1) - \frac{1}{2}(\Sigma_{14}\tau_2\sigma_3 - \Sigma_{24}\tau_1\sigma_3) \\ & - \frac{1}{2\sqrt{2}}(\Sigma_{15}\tau_1\sigma_1 + \Sigma_{25}\tau_2\sigma_1) + \frac{1}{2\sqrt{3}}(\Sigma_{15}\tau_2\sigma_3 + \Sigma_{25}\tau_1\sigma_3) \end{aligned} \quad (\text{A.142})$$

The term $\mathcal{H}_m^{(1)}$ is the ferro-quadrupolar quantum Hall mass listed in Ref.[156] whose edge modes are protected by the time reversal (TR) symmetry. Thus, the phase obtained by moving left from the P_3 point in the phase diagram in Fig. 9.1(a) is a Z_2 topological insulator. The presence of \mathcal{H}' does not change the topological character of this phase since this term does not break the TR symmetry and can be tuned to zero without closing the fermionic energy gap.

The non-topological phase

On moving down vertically from the P_3 point along the $\tau_m = 1$ line, we encounter the non-topological gapped phase. This can be understood by doing a similar analysis as done for the previous gapped phase. For very large values of $\tilde{\lambda}$ and $\tau_m = 1$, the effective Hamiltonian is given by

$$\mathcal{H}_{non-top} = -\mathcal{E} \left(\sum_{\langle\mathbf{r},s;\mathbf{r}',s'\rangle} \psi^\dagger(\mathbf{r},s)U_{\mathbf{r}\mathbf{r}'}^{ss'}\psi(\mathbf{r}',s') + \frac{1}{\tilde{\lambda}} \sum_{\langle\langle\mathbf{r},s;\mathbf{r}',s'\rangle\rangle} \psi^\dagger(\mathbf{r},s)\tilde{H}_{\mathbf{r}\mathbf{r}'}^{ss'}\psi(\mathbf{r}',s') + h.c. \right) \quad (\text{A.143})$$

Where the $U_{\mathbf{r}\mathbf{r}'}^{ss'}$ are the matrices defined in Eq. A.129 and $\tilde{H}_{\mathbf{r}\mathbf{r}'}^{ss'}$ are the hopping matrices on the next-nearest(NNN) bonds of the lattice. On the three kinds of NNN bonds shown

in Fig A.6, the \tilde{H}_{ij} matrices are given by

$$\begin{aligned}\tilde{H}_{13} &= -\frac{1}{2\sqrt{3}}\Sigma_1 + \frac{i}{6}\left(-\Sigma_{14} - \sqrt{3}\Sigma_{15} - \Sigma_{23}\right) \\ \tilde{H}_{35} &= -\frac{1}{2\sqrt{3}}\Sigma_2 + \frac{i}{6}\left(\Sigma_{13} - \Sigma_{24} + \sqrt{3}\Sigma_{25}\right) \\ \tilde{H}_{51} &= -\frac{1}{2\sqrt{3}}\Sigma_3 + \frac{i}{6}\left(-\Sigma_{12} + 2\Sigma_{34}\right)\end{aligned}\tag{A.144}$$

On projecting this Hamiltonian to the lowest two bands near the Dirac points, we get the following low-energy theory

$$\mathcal{H}_{non-top} = \mathcal{H}_{Dirac} + \frac{1}{\lambda}\mathcal{H}_m^{(2)} + \frac{1}{\lambda}\mathcal{H}''.\tag{A.145}$$

Here, \mathcal{H}_{Dirac} is the SU(8) symmetric Dirac Hamiltonian. The $\mathcal{H}_m^{(2)}$ is given by

$$\mathcal{H}_m^{(2)} = \int d^2x \chi^\dagger \Sigma_{45} \tau_3 \sigma_3 \chi\tag{A.146}$$

The $\mathcal{H}_m^{(2)}$ is one of the topological masses proximate to the SU(8) Dirac semi-metal. The edge modes of this topological symmetry is protected by a U(1) symmetry which is generated by Σ_{45} . But the term \mathcal{H}'' breaks this U(1) symmetry and destroys the edge modes. This explains the existence of the non-topological phase in the phase diagram.

Phase transition lines in τ_m - $\tilde{\lambda}$ plane with $\rho = \pm 1$

On the phase transition line, the P_1P_3 line, between the two gapped phases shown in Fig. 6a of the main text, the lowest two bands touch each other linearly at the Γ point as shown in inset VI of the same figure. One can find the low-energy theory for this point of the phase diagram by projecting the Hamiltonian to the two lowest band that touch at the Γ point. The resultant theory is given by

$$\mathcal{H}_\Gamma = -iv_F \int d^2x \chi_\Gamma^\dagger (\tau_3 \sigma_1 \partial_1 + \tau_0 \sigma_2 \partial_2) \chi_\Gamma.\tag{A.147}$$

Here, χ_Γ is a 4-component spinor which comes from the two-fold degenerate Dirac cone at the Γ point. This Hamiltonian has an emergent SU(2) symmetry which is generated by $\{\tau_3 \sigma_0, \tau_1 \sigma_2, \tau_2 \sigma_2\}/2$.

Similarly, on the P_3P_{14} line of the phase of Fig. 11, the lower two bands touch each other linearly at the three M points. The low-energy theory at any point on this line is given by

$$\mathcal{H}_M = i \int d^2x \chi_M^\dagger (v_x \mathbb{I}_{3 \times 3} \otimes \tau_3 \sigma_1 \partial_1 + v_y \mathbb{I}_{3 \times 3} \otimes \tau_0 \sigma_2 \partial_2) \chi_M. \quad (\text{A.148})$$

Here, χ_M is a 12-component spinor that comes from the three two-fold degenerate Dirac cones at the three M points. v_x and v_y are the Fermi velocities along the two Cartesian directions. The values of these two numbers depend on the position on the phase transition line. $\mathbb{I}_{3 \times 3}$ is the three dimensional identity matrix that acts on the space of the three M valleys. This Hamiltonian has an internal SU(6) symmetry which are generated by the set of Hermitian matrices given by

$$\{\mathbb{I}_{3 \times 3}, \Lambda_i\} \otimes \{\tau_3 \sigma_0, \tau_1 \sigma_2, \tau_2 \sigma_2\}, \quad \Lambda_i \otimes \tau_0 \sigma_0 \quad (\text{A.149})$$

where the Λ_i are the eight 3×3 Gell-Mann matrices that generate an SU(3).

Bibliography

- [1] Jun Kondo. Resistance Minimum in Dilute Magnetic Alloys. *Progress of Theoretical Physics*, 32(1):37–49, 07 1964.
- [2] F. Steglich, J. Aarts, C. D. Bredl, W. Lieke, D. Meschede, W. Franz, and H. Schäfer. Superconductivity in the presence of strong pauli paramagnetism: CeCu_2Si_2 . *Phys. Rev. Lett.*, 43:1892–1896, Dec 1979.
- [3] H. R. Ott, H. Rudigier, T. M. Rice, K. Ueda, Z. Fisk, and J. L. Smith. p -wave superconductivity in UBe_{13} . *Phys. Rev. Lett.*, 52:1915–1918, May 1984.
- [4] Alexander Cyril Hewson. *The Kondo problem to heavy fermions*. Number 2. Cambridge university press, 1997.
- [5] M. C. Aronson, R. Osborn, R. A. Robinson, J. W. Lynn, R. Chau, C. L. Seaman, and M. B. Maple. Non-fermi-liquid scaling of the magnetic response in $\text{U}_{5-x}\text{Pd}_x$ ($x = 1, 1.5$). *Phys. Rev. Lett.*, 75:725–728, Jul 1995.
- [6] G. R. Stewart. Non-fermi-liquid behavior in d - and f -electron metals. *Rev. Mod. Phys.*, 73:797–855, Oct 2001.
- [7] B. Andraka and G. R. Stewart. Heavy-non-fermi-liquid behavior in $\text{U}(\text{Cu},\text{Pd})_5$. *Phys. Rev. B*, 47:3208–3212, Feb 1993.
- [8] Xiao-Gang Wen. Colloquium: Zoo of quantum-topological phases of matter. *Reviews of Modern Physics*, 89(4):041004, 2017.
- [9] William Witczak-Krempa, Gang Chen, Yong Baek Kim, and Leon Balents. Correlated quantum phenomena in the strong spin-orbit regime. *arXiv preprint arXiv:1305.2193*, 2013.

- [10] Jeffrey G. Rau, Eric Kin-Ho Lee, and Hae-Young Kee. Spin-orbit physics giving rise to novel phases in correlated systems: Iridates and related materials. *Annual Review of Condensed Matter Physics*, 7(Volume 7, 2016):195–221, 2016.
- [11] Robert Schaffer, Eric Kin-Ho Lee, Bohm-Jung Yang, and Yong Baek Kim. Recent progress on correlated electron systems with strong spin–orbit coupling. *Reports on Progress in Physics*, 79(9):094504, 2016.
- [12] Antoine Georges, Luca Medici, and Jernej Mravlje. Strong correlations from hund’s coupling. *Annual Review of Condensed Matter Physics*, 4:137–178, 2012.
- [13] T. Senthil. Symmetry-protected topological phases of quantum matter. *Annual Review of Condensed Matter Physics*, 6(1):299–324, 2015.
- [14] Titus Neupert, Claudio Chamon, Thomas Iadecola, Luiz H Santos, and Christopher Mudry. Fractional (chern and topological) insulators. *Physica Scripta*, 2015(T164):014005, aug 2015.
- [15] N. Regnault and B. Andrei Bernevig. Fractional chern insulator. *Phys. Rev. X*, 1:021014, Dec 2011.
- [16] Lucile Savary and Leon Balents. Quantum spin liquids: a review. *Reports on Progress in Physics*, 80(1):016502, nov 2016.
- [17] Yi Zhou, Kazushi Kanoda, and Tai-Kai Ng. Quantum spin liquid states. *Rev. Mod. Phys.*, 89:025003, Apr 2017.
- [18] Xiao-Gang Wen. Quantum orders and symmetric spin liquids. *Phys. Rev. B*, 65:165113, Apr 2002.
- [19] T. Senthil. Symmetry-protected topological phases of quantum matter. *Annual Review of Condensed Matter Physics*, 6(Volume 6, 2015):299–324, 2015.
- [20] M. Z. Hasan and C. L. Kane. Colloquium: Topological insulators. *Rev. Mod. Phys.*, 82:3045–3067, Nov 2010.
- [21] Shinsei Ryu, Christopher Mudry, Chang-Yu Hou, and Claudio Chamon. Masses in graphenelike two-dimensional electronic systems: Topological defects in order pa-

- rameters and their fractional exchange statistics. *Physical Review B*, 80(20):205319, 2009.
- [22] B. J. Kim, Hosub Jin, S. J. Moon, J.-Y. Kim, B.-G. Park, C. S. Leem, Jaejun Yu, T. W. Noh, C. Kim, S.-J. Oh, J.-H. Park, V. Durairaj, G. Cao, and E. Rotenberg. Novel $J_{\text{eff}} = 1/2$ mott state induced by relativistic spin-orbit coupling in Sr_2IrO_4 . *Phys. Rev. Lett.*, 101:076402, Aug 2008.
- [23] BJ Kim, H Ohsumi, T Komesu, S Sakai, T Morita, H Takagi, and T-h Arima. Phase-sensitive observation of a spin-orbital mott state in Sr_2IrO_4 . *Science*, 323(5919):1329–1332, 2009.
- [24] S. Fujiyama, H. Ohsumi, T. Komesu, J. Matsuno, B. J. Kim, M. Takata, T. Arima, and H. Takagi. Two-dimensional heisenberg behavior of $J_{\text{eff}}=1/2$ isospins in the paramagnetic state of the spin-orbital mott insulator sr_2iro_4 . *Phys. Rev. Lett.*, 108:247212, Jun 2012.
- [25] Jungho Kim, D Casa, MH Upton, T Gog, Young-June Kim, JF Mitchell, M Van Veenendaal, M Daghofer, J Van Den Brink, G Khaliullin, et al. Magnetic excitation spectra of Sr_2IrO_4 probed by resonant inelastic x-ray scattering: establishing links to cuprate superconductors. *Physical Review Letters*, 108(17):177003, 2012.
- [26] J. W. Kim, Y. Choi, Jungho Kim, J. F. Mitchell, G. Jackeli, M. Daghofer, J. van den Brink, G. Khaliullin, and B. J. Kim. Dimensionality driven spin-flop transition in layered iridates. *Phys. Rev. Lett.*, 109:037204, Jul 2012.
- [27] Jungho Kim, A. H. Said, D. Casa, M. H. Upton, T. Gog, M. Daghofer, G. Jackeli, J. van den Brink, G. Khaliullin, and B. J. Kim. Large spin-wave energy gap in the bilayer iridate $\text{sr}_3\text{ir}_2\text{o}_7$: Evidence for enhanced dipolar interactions near the mott metal-insulator transition. *Phys. Rev. Lett.*, 109:157402, Oct 2012.
- [28] S. Fujiyama, K. Ohashi, H. Ohsumi, K. Sugimoto, T. Takayama, T. Komesu, M. Takata, T. Arima, and H. Takagi. Weak antiferromagnetism of $J_{\text{eff}} = \frac{1}{2}$ band in bilayer iridate $\text{sr}_3\text{ir}_2\text{o}_7$. *Phys. Rev. B*, 86:174414, Nov 2012.

- [29] P. D. C. King, T. Takayama, A. Tamai, E. Rozbicki, S. McKeown Walker, M. Shi, L. Patthey, R. G. Moore, D. Lu, K. M. Shen, H. Takagi, and F. Baumberger. Spectroscopic indications of polaronic behavior of the strong spin-orbit insulator $\text{Sr}_3\text{Ir}_2\text{O}_7$. *Phys. Rev. B*, 87:241106, Jun 2013.
- [30] Yogesh Singh and P. Gegenwart. Antiferromagnetic mott insulating state in single crystals of the honeycomb lattice material Na_2IrO_3 . *Phys. Rev. B*, 82:064412, Aug 2010.
- [31] Yogesh Singh, S. Manni, J. Reuther, T. Berlijn, R. Thomale, W. Ku, S. Trebst, and P. Gegenwart. Relevance of the heisenberg-kitaev model for the honeycomb lattice iridates A_2IrO_3 . *Phys. Rev. Lett.*, 108:127203, Mar 2012.
- [32] H. Gretarsson, J. P. Clancy, X. Liu, J. P. Hill, Emil Bozin, Yogesh Singh, S. Manni, P. Gegenwart, Jungho Kim, A. H. Said, D. Casa, T. Gog, M. H. Upton, Heung-Sik Kim, J. Yu, Vamshi M. Katukuri, L. Hozoi, Jeroen van den Brink, and Young-June Kim. Crystal-field splitting and correlation effect on the electronic structure of A_2IrO_3 . *Phys. Rev. Lett.*, 110:076402, Feb 2013.
- [33] X. Liu, T. Berlijn, W.-G. Yin, W. Ku, A. Tsvelik, Young-June Kim, H. Gretarsson, Yogesh Singh, P. Gegenwart, and J. P. Hill. Long-range magnetic ordering in Na_2IrO_3 . *Phys. Rev. B*, 83:220403, Jun 2011.
- [34] J. P. Clancy, N. Chen, C. Y. Kim, W. F. Chen, K. W. Plumb, B. C. Jeon, T. W. Noh, and Young-June Kim. Spin-orbit coupling in iridium-based $5d$ compounds probed by x-ray absorption spectroscopy. *Phys. Rev. B*, 86:195131, Nov 2012.
- [35] SK Choi, R Coldea, AN Kolmogorov, T Lancaster, II Mazin, SJ Blundell, PG Radaelli, Yogesh Singh, Philipp Gegenwart, KR Choi, et al. Spin waves and revised crystal structure of honeycomb iridate Na_2IrO_3 . *Physical review letters*, 108(12):127204, 2012.
- [36] Daiki Yanagishima and Yoshiteru Maeno. Metal-nonmetal changeover in pyrochlore iridates. *Journal of the Physical Society of Japan*, 70(10):2880–2883, 2001.
- [37] Kazuyuki Matsuhira, Makoto Wakeshima, Ryo Nakanishi, Takaaki Yamada, Akira Nakamura, Wataru Kawano, Seishi Takagi, and Yukio Hinatsu. Metal–insulator

- transition in pyrochlore iridates $\text{In}_2\text{Ir}_2\text{O}_7$ ($\text{In} = \text{Nd, Sm, and Eu}$). *Journal of the Physical Society of Japan*, 76(4):043706, 2007.
- [38] T F Qi, O B Korneta, Xiangang Wan, L E DeLong, P Schlottmann, and G Cao. Strong magnetic instability in correlated metallic $\text{Bi}_2\text{Ir}_2\text{O}_7$. *Journal of Physics: Condensed Matter*, 24(34):345601, jul 2012.
- [39] Masatoshi Imada, Atsushi Fujimori, and Yoshinori Tokura. Metal-insulator transitions. *Rev. Mod. Phys.*, 70:1039–1263, Oct 1998.
- [40] Th Pruschke and Ralf Bulla. Hund’s coupling and the metal-insulator transition in the two-band hubbard model. *The European Physical Journal B-Condensed Matter and Complex Systems*, 44:217–224, 2005.
- [41] Andriy H. Nevidomskyy and P. Coleman. Kondo resonance narrowing in d - and f -electron systems. *Phys. Rev. Lett.*, 103:147205, Oct 2009.
- [42] J. E. Han, M. Jarrell, and D. L. Cox. Multiorbital hubbard model in infinite dimensions: Quantum monte carlo calculation. *Phys. Rev. B*, 58:R4199–R4202, Aug 1998.
- [43] Akihisa Koga, Yoshiki Imai, and Norio Kawakami. Stability of a metallic state in the two-orbital hubbard model. *Phys. Rev. B*, 66:165107, Oct 2002.
- [44] Philipp Werner and Andrew J. Millis. High-spin to low-spin and orbital polarization transitions in multiorbital mott systems. *Phys. Rev. Lett.*, 99:126405, Sep 2007.
- [45] Philipp Werner, Emanuel Gull, and Andrew J. Millis. Metal-insulator phase diagram and orbital selectivity in three-orbital models with rotationally invariant hund coupling. *Phys. Rev. B*, 79:115119, Mar 2009.
- [46] Luca de’ Medici. Hund’s coupling and its key role in tuning multiorbital correlations. *Phys. Rev. B*, 83:205112, May 2011.
- [47] Nicola Manini, Giuseppe E. Santoro, Andrea Dal Corso, and Erio Tosatti. Sensitivity of the mott transition to noncubic splitting of the orbital degeneracy: Application to $\text{NH}_3\text{K}_3\text{C}_{60}$. *Phys. Rev. B*, 66:115107, Sep 2002.

- [48] Alexander I. Poteryaev, Michel Ferrero, Antoine Georges, and Olivier Parcollet. Effect of crystal-field splitting and interband hybridization on the metal-insulator transitions of strongly correlated systems. *Phys. Rev. B*, 78:045115, Jul 2008.
- [49] Xiao-Liang Qi and Shou-Cheng Zhang. Topological insulators and superconductors. *Rev. Mod. Phys.*, 83:1057–1110, Oct 2011.
- [50] M. Zahid Hasan and Joel E. Moore. Three-dimensional topological insulators. *Annual Review of Condensed Matter Physics*, 2(Volume 2, 2011):55–78, 2011.
- [51] Xiangang Wan, Ari M Turner, Ashvin Vishwanath, and Sergey Y Savrasov. Topological semimetal and fermi-arc surface states in the electronic structure of pyrochlore iridates. *Physical Review B*, 83(20):205101, 2011.
- [52] William Witczak-Krempa and Yong Baek Kim. Topological and magnetic phases of interacting electrons in the pyrochlore iridates. *Phys. Rev. B*, 85:045124, Jan 2012.
- [53] A. A. Burkov and Leon Balents. Weyl semimetal in a topological insulator multilayer. *Phys. Rev. Lett.*, 107:127205, Sep 2011.
- [54] Xiang Hu, Zhicheng Zhong, and Gregory A Fiete. First principles prediction of topological phases in thin films of pyrochlore iridates. *Scientific Reports*, 5(1):11072, 2015.
- [55] Qi Chen, Hsiang-Hsuan Hung, Xiang Hu, and Gregory A. Fiete. Correlation effects in pyrochlore iridate thin films grown along the [111] direction. *Phys. Rev. B*, 92:085145, Aug 2015.
- [56] Xiangang Wan, Ashvin Vishwanath, and Sergey Y. Savrasov. Computational design of axion insulators based on 5d spinel compounds. *Phys. Rev. Lett.*, 108:146601, Apr 2012.
- [57] Ara Go, William Witczak-Krempa, Gun Sang Jeon, Kwon Park, and Yong Baek Kim. Correlation effects on 3d topological phases: From bulk to boundary. *Phys. Rev. Lett.*, 109:066401, Aug 2012.

- [58] Ari M. Turner, Yi Zhang, Roger S. K. Mong, and Ashvin Vishwanath. Quantized response and topology of magnetic insulators with inversion symmetry. *Phys. Rev. B*, 85:165120, Apr 2012.
- [59] Taylor L. Hughes, Emil Prodan, and B. Andrei Bernevig. Inversion-symmetric topological insulators. *Phys. Rev. B*, 83:245132, Jun 2011.
- [60] Gang Chen and Leon Balents. Spin-orbit coupling in d^2 ordered double perovskites. *Phys. Rev. B*, 84:094420, Sep 2011.
- [61] Masahiko G. Yamada, Masaki Oshikawa, and George Jackeli. SU(4)-symmetric quantum spin-orbital liquids on various lattices. *Phys. Rev. B*, 104:224436, Dec 2021.
- [62] Ryosuke Shiina, Osamu Sakai, Hiroyuki Shiba, and Peter Thalmeier. Interplay of field-induced multipoles in CeB_6 . *Journal of the Physical Society of Japan*, 67(3):941–949, 1998.
- [63] Yoshio Kuramoto, Hiroaki Kusunose, and Annamaria Kiss. Multipole orders and fluctuations in strongly correlated electron systems. *Journal of the Physical Society of Japan*, 78(7):072001, 2009.
- [64] Hiroaki Kusunose. Description of multipole in f-electron systems. *Journal of the Physical Society of Japan*, 77(6):064710, 2008.
- [65] Paolo Santini, Stefano Carretta, Giuseppe Amoretti, Roberto Caciuffo, Nicola Magnani, and Gerard H Lander. Multipolar interactions in f-electron systems: The paradigm of actinide dioxides. *Reviews of Modern Physics*, 81(2):807, 2009.
- [66] Adarsh S. Patri, Akito Sakai, SungBin Lee, Arun Paramakanti, Satoru Nakatsuji, and Yong Baek Kim. Unveiling hidden multipolar orders with magnetostriction. *Nature Communications*, 10(1):4092, Sep 2019.
- [67] A. Paramakanti, D. D. Maharaj, and B. D. Gaulin. Octupolar order in d -orbital mott insulators. *Phys. Rev. B*, 101:054439, Feb 2020.

- [68] Oskar Vafek and Ashvin Vishwanath. Dirac fermions in solids: From high- T_c cuprates and graphene to topological insulators and weyl semimetals. *Annual Review of Condensed Matter Physics*, 5(1):83–112, 2014.
- [69] Mark Goerbig and Gilles Montambaux. *Dirac Fermions in Condensed Matter and Beyond*, pages 25–53. Springer International Publishing, Cham, 2017.
- [70] P. R. Wallace. The band theory of graphite. *Phys. Rev.*, 71:622–634, May 1947.
- [71] Kostya S Novoselov, Andre K Geim, Sergei Vladimirovich Morozov, Dingde Jiang, Michail I Katsnelson, IVa Grigorieva, SVb Dubonos, and andAA Firsov. Two-dimensional gas of massless dirac fermions in graphene. *Nature*, 438(7065):197–200, 2005.
- [72] Yuanbo Zhang, Yan-Wen Tan, Horst L Stormer, and Philip Kim. Experimental observation of the quantum hall effect and berry’s phase in graphene. *Nature*, 438(7065):201–204, 2005.
- [73] A. K. Geim. Graphene: Status and prospects. *Science*, 324(5934):1530–1534, 2009.
- [74] A. H. Castro Neto, F. Guinea, N. M. R. Peres, K. S. Novoselov, and A. K. Geim. The electronic properties of graphene. *Rev. Mod. Phys.*, 81:109–162, Jan 2009.
- [75] M. O. Goerbig. Electronic properties of graphene in a strong magnetic field. *Rev. Mod. Phys.*, 83:1193–1243, Nov 2011.
- [76] S. Das Sarma, Shaffique Adam, E. H. Hwang, and Enrico Rossi. Electronic transport in two-dimensional graphene. *Rev. Mod. Phys.*, 83:407–470, May 2011.
- [77] K. S. Novoselov. Nobel lecture: Graphene: Materials in the flatland. *Rev. Mod. Phys.*, 83:837–849, Aug 2011.
- [78] Andre K. Geim. Nobel lecture: Random walk to graphene. *Rev. Mod. Phys.*, 83:851–862, Aug 2011.
- [79] T.O. Wehling, A.M. Black-Schaffer, and A.V. Balatsky. Dirac materials. *Advances in Physics*, 63(1):1–76, 2014.

- [80] Steve M. Young and Charles L. Kane. Dirac semimetals in two dimensions. *Phys. Rev. Lett.*, 115:126803, Sep 2015.
- [81] Michihiro Hirata, Akito Kobayashi, Claude Berthier, and Kazushi Kanoda. Interacting chiral electrons at the 2D Dirac points: a review. *Reports on Progress in Physics*, 84(3):036502, mar 2021.
- [82] Akito Kobayashi, Shinya Katayama, Yoshikazu Suzumura, and Hidetoshi Fukuyama. Massless fermions in organic conductor. *Journal of the Physical Society of Japan*, 76(3):034711, 2007.
- [83] M. O. Goerbig, J.-N. Fuchs, G. Montambaux, and F. Piéchon. Tilted anisotropic dirac cones in quinoid-type graphene and α -(BEDT-TTF)₂I₃. *Phys. Rev. B*, 78:045415, Jul 2008.
- [84] D. A. Wollman, D. J. Van Harlingen, J. Giapintzakis, and D. M. Ginsberg. Evidence for $d_{x^2-y^2}$ pairing from the magnetic field modulation of yba₂cu₃o₇-pb josephson junctions. *Phys. Rev. Lett.*, 74:797–800, Jan 1995.
- [85] JR Kirtley, CC Tsuei, JZ Sun, CC Chi, Lock See Yu-Jahnes, A Gupta, M Rupp, and MB Ketchen. Symmetry of the order parameter in the high-T_c superconductor YBa₂Cu₃O_{7- δ} . *Nature*, 373(6511):225–228, 1995.
- [86] GE Volovik. Superconductivity with lines of gap nodes: density of states in the vortex. *Jetp Letters*, 58(6):469–473, 1993.
- [87] Yong Wang and A. H. MacDonald. Mixed-state quasiparticle spectrum for d-wave superconductors. *Phys. Rev. B*, 52:R3876–R3879, Aug 1995.
- [88] Leon Balents, Matthew PA Fisher, and Chetan Nayak. Nodal liquid theory of the pseudo-gap phase of high-T_c superconductors. *International Journal of Modern Physics B*, 12(10):1033–1068, 1998.
- [89] S. M. Young, S. Zaheer, J. C. Y. Teo, C. L. Kane, E. J. Mele, and A. M. Rappe. Dirac semimetal in three dimensions. *Phys. Rev. Lett.*, 108:140405, Apr 2012.
- [90] J. E. Moore and L. Balents. Topological invariants of time-reversal-invariant band structures. *Phys. Rev. B*, 75:121306, Mar 2007.

- [91] Rahul Roy. Topological phases and the quantum spin hall effect in three dimensions. *Phys. Rev. B*, 79:195322, May 2009.
- [92] Liang Fu, C. L. Kane, and E. J. Mele. Topological insulators in three dimensions. *Phys. Rev. Lett.*, 98:106803, Mar 2007.
- [93] YL Chen, James G Analytis, J-H Chu, ZK Liu, S-K Mo, Xiao-Liang Qi, HJ Zhang, DH Lu, Xi Dai, Zhong Fang, et al. Experimental realization of a three-dimensional topological insulator, Bi_2Te_3 . *Science*, 325(5937):178–181, 2009.
- [94] D Pacile, JC Meyer, Ç Ö Girit, and AJAPL Zettl. The two-dimensional phase of boron nitride: Few-atomic-layer sheets and suspended membranes. *Applied Physics Letters*, 92(13):133107, 2008.
- [95] Guohong Li, Adina Luican, and Eva Y Andrei. Scanning tunneling spectroscopy of graphene on graphite. *Physical review letters*, 102(17):176804, 2009.
- [96] Rahul Raveendran Nair, Peter Blake, Alexander N Grigorenko, Konstantin S Novoselov, Tim J Booth, Tobias Stauber, Nuno MR Peres, and Andre K Geim. Fine structure constant defines visual transparency of graphene. *Science*, 320(5881):1308–1308, 2008.
- [97] ZhiQuan Li, Eric A Henriksen, Zhifang Jiang, Zhao Hao, Michael C Martin, Phaly Kim, Horst Ludwig Stormer, and Dimitri N Basov. Dirac charge dynamics in graphene by infrared spectroscopy. *Nature physics*, 4(7):532–535, 2008.
- [98] N Levy, SA Burke, KL Meaker, M Panlasigui, A Zettl, F Guinea, AH Castro Neto, and Michael F Crommie. Strain-induced pseudo-magnetic fields greater than 300 tesla in graphene nanobubbles. *Science*, 329(5991):544–547, 2010.
- [99] Joseph G. Checkelsky, Lu Li, and N. P. Ong. Divergent resistance at the dirac point in graphene: Evidence for a transition in a high magnetic field. *Phys. Rev. B*, 79:115434, Mar 2009.
- [100] Jens H Bardarson and Joel E Moore. Quantum interference and Aharonov–Bohm oscillations in topological insulators. *Reports on Progress in Physics*, 76(5):056501, 2013.

- [101] Michael Hermele, T. Senthil, and Matthew P. A. Fisher. Algebraic spin liquid as the mother of many competing orders. *Phys. Rev. B*, 72:104404, Sep 2005.
- [102] Ian Affleck and J Brad Marston. Large-n limit of the heisenberg-hubbard model: Implications for high- T_c superconductors. *Physical Review B*, 37(7):3774, 1988.
- [103] J Brad Marston and Ian Affleck. Large-n limit of the hubbard-heisenberg model. *Physical Review B*, 39(16):11538, 1989.
- [104] Walter Rantner and Xiao-Gang Wen. Electron spectral function and algebraic spin liquid for the normal state of underdoped high T_c superconductors. *Phys. Rev. Lett.*, 86(17):3871, 2001.
- [105] Xiao-Gang Wen. Quantum orders and symmetric spin liquids. *Physical Review B*, 65(16):165113, 2002.
- [106] Michael Hermele, T Senthil, Matthew PA Fisher, Patrick A Lee, Naoto Nagaosa, and Xiao-Gang Wen. Stability of U(1) spin liquids in two dimensions. *Physical Review B*, 70(21):214437, 2004.
- [107] M. Franz and Z. Tešanović. Algebraic fermi liquid from phase fluctuations: “topological” fermions, vortex “berryons,” and QED₃ theory of cuprate superconductors. *Phys. Rev. Lett.*, 87:257003, Dec 2001.
- [108] Walter Rantner and Xiao-Gang Wen. Spin correlations in the algebraic spin liquid: Implications for high- T_c superconductors. *Phys. Rev. B*, 66:144501, Oct 2002.
- [109] Dam Thanh Son. Is the composite fermion a dirac particle? *Phys. Rev. X*, 5:031027, Sep 2015.
- [110] Rufus Boyack, Hennadii Yerzhakov, and Joseph Maciejko. Quantum phase transitions in dirac fermion systems. *The European Physical Journal Special Topics*, 230(4):979–992, 2021.
- [111] S Yi Zhou, G-H Gweon, AV Fedorov, de First, PN, WA De Heer, D-H Lee, F Guinea, AH Castro Neto, and A Lanzara. Substrate-induced bandgap opening in epitaxial graphene. *Nature materials*, 6(10):770–775, 2007.

- [112] Igor F. Herbut, Vladimir Juričić, and Bitan Roy. Theory of interacting electrons on the honeycomb lattice. *Phys. Rev. B*, 79:085116, Feb 2009.
- [113] Akihiro Tanaka and Xiao Hu. Many-body spin berry phases emerging from the π -flux state: Competition between antiferromagnetism and the valence-bond-solid state. *Phys. Rev. Lett.*, 95:036402, Jul 2005.
- [114] David J. Gross and André Neveu. Dynamical symmetry breaking in asymptotically free field theories. *Phys. Rev. D*, 10:3235–3253, Nov 1974.
- [115] Jean Zinn-Justin. Four-fermion interaction near four dimensions. *Nuclear Physics B*, 367(1):105–122, 1991.
- [116] Subir Sachdev. Quantum phase transitions. *Physics world*, 12(4):33, 1999.
- [117] Igor F. Herbut. Interactions and phase transitions on graphene’s honeycomb lattice. *Phys. Rev. Lett.*, 97:146401, Oct 2006.
- [118] Todadri Senthil, Ashvin Vishwanath, Leon Balents, Subir Sachdev, and Matthew PA Fisher. Deconfined quantum critical points. *Science*, 303(5663):1490–1494, 2004.
- [119] T. Senthil and Matthew P. A. Fisher. Competing orders, nonlinear sigma models, and topological terms in quantum magnets. *Phys. Rev. B*, 74:064405, Aug 2006.
- [120] Pavan Hosur, Shinsei Ryu, and Ashvin Vishwanath. Chiral topological insulators, superconductors, and other competing orders in three dimensions. *Phys. Rev. B*, 81:045120, Jan 2010.
- [121] Michael Hermele, Ying Ran, Patrick A. Lee, and Xiao-Gang Wen. Properties of an algebraic spin liquid on the kagome lattice. *Phys. Rev. B*, 77:224413, Jun 2008.
- [122] A Banerjee, CA Bridges, J-Q Yan, AA Aczel, L Li, MB Stone, GE Granroth, MD Lumsden, Y Yiu, Johannes Knolle, et al. Proximate kitaev quantum spin liquid behaviour in a honeycomb magnet. *Nature materials*, 15(7):733–740, 2016.
- [123] Luke J Sandilands, Yao Tian, Kemp W Plumb, Young-June Kim, and Kenneth S Burch. Scattering continuum and possible fractionalized excitations in α -RuCl₃. *Physical review letters*, 114(14):147201, 2015.

- [124] KW Plumb, JP Clancy, LJ Sandilands, V Vijay Shankar, YF Hu, KS Burch, Hae-Young Kee, and Young-June Kim. α - RuCl₃ : A spin-orbit assisted mott insulator on a honeycomb lattice. *Physical Review B*, 90(4):041112, 2014.
- [125] Brian Harold Bransden and Charles Jean Joachain. *Physics of atoms and molecules*. Pearson Education India, 2003.
- [126] Alexei Kitaev. Anyons in an exactly solved model and beyond. *Annals of Physics*, 321(1):2–111, 2006.
- [127] Animesh Nanda, Kusum Dhochak, and Subhro Bhattacharjee. Phases and quantum phase transitions in an anisotropic ferromagnetic kitaev-heisenberg- Γ magnet. *Phys. Rev. B*, 102:235124, Dec 2020.
- [128] Manoj Gupta, Basudeb Mondal, Subhro Bhattacharjee, and Tanusri Saha Dasgupta. Ab initio insights on the fermiology of d^1 transition metals on the honeycomb lattice: Hierarchy of hopping pathways and spin-orbit coupling. *Phys. Rev. Res.*, 5:043219, Dec 2023.
- [129] Judit Romhányi, Leon Balents, and George Jackeli. Spin-orbit dimers and non-collinear phases in d^1 cubic double perovskites. *Phys. Rev. Lett.*, 118:217202, May 2017.
- [130] Masahiko G Yamada, Masaki Oshikawa, and George Jackeli. Emergent SU(4) symmetry in α - ZrCl₃ and crystalline spin-orbital liquids. *Physical Review Letters*, 121(9):097201, 2018.
- [131] Martin Bercx, Martin Hohenadler, and Fakher F. Assaad. Kane-mele-hubbard model on the π -flux honeycomb lattice. *Phys. Rev. B*, 90:075140, Aug 2014.
- [132] David B Kaplan. Chiral symmetry and lattice fermions. *Modern Perspectives in Lattice QCD: Quantum Field Theory and High Performance Computing. Proceedings, International School, 93rd Session*, pages 223–272, 2009.
- [133] Ankush Chaubey, Basudeb Mandal, Subhro Bhattacharjee, and V. B. Shenoy. Superconductivity in spin-orbit coupled su(8) dirac fermions on honeycomb lattice. unpublished.

- [134] C. L. Kane and E. J. Mele. Quantum spin hall effect in graphene. *Phys. Rev. Lett.*, 95:226801, Nov 2005.
- [135] Chang-Yu Hou, Claudio Chamon, and Christopher Mudry. Electron fractionalization in two-dimensional graphenelike structures. *Phys. Rev. Lett.*, 98:186809, May 2007.
- [136] F. D. M. Haldane. Model for a quantum hall effect without landau levels: Condensed-matter realization of the "parity anomaly". *Phys. Rev. Lett.*, 61:2015–2018, Oct 1988.
- [137] Xiao-Liang Qi, Yong-Shi Wu, and Shou-Cheng Zhang. Topological quantization of the spin hall effect in two-dimensional paramagnetic semiconductors. *Phys. Rev. B*, 74:085308, Aug 2006.
- [138] D. J. Thouless, M. Kohmoto, M. P. Nightingale, and M. den Nijs. Quantized hall conductance in a two-dimensional periodic potential. *Phys. Rev. Lett.*, 49:405–408, Aug 1982.
- [139] S. Raghu, Xiao-Liang Qi, C. Honerkamp, and Shou-Cheng Zhang. Topological mott insulators. *Phys. Rev. Lett.*, 100:156401, Apr 2008.
- [140] Curtis G Callan Jr and Jeffrey A Harvey. Anomalies and fermion zero modes on strings and domain walls. *Nuclear Physics B*, 250(1-4):427–436, 1985.
- [141] Tarun Grover and T. Senthil. Topological spin hall states, charged skyrmions, and superconductivity in two dimensions. *Phys. Rev. Lett.*, 100:156804, Apr 2008.
- [142] Claudio Chamon, Chang-Yu Hou, Roman Jackiw, Christopher Mudry, So-Young Pi, and Andreas P. Schnyder. Irrational versus rational charge and statistics in two-dimensional quantum systems. *Phys. Rev. Lett.*, 100:110405, Mar 2008.
- [143] Ying Ran, Ashvin Vishwanath, and Dung-Hai Lee. A direct transition between a Neel ordered mott insulator and a $d_{x^2-y^2}$ superconductor on the square lattice. *arXiv preprint arXiv:0806.2321*, 2008.
- [144] S. O. Valenzuela and M. Tinkham. Direct electronic measurement of the spin hall effect. *Nature*, 442(7099):176–179, Jul 2006.

- [145] Luqiao Liu, Takahiro Moriyama, D. C. Ralph, and R. A. Buhrman. Spin-torque ferromagnetic resonance induced by the spin hall effect. *Phys. Rev. Lett.*, 106:036601, Jan 2011.
- [146] Mahmoud AA Sbaih, Moeen KH Srour, MS Hamada, and HM Fayad. Lie algebra and representation of $SU(4)$. *Electronic Journal of Theoretical Physics*, 28, 2013.
- [147] Monica Bapna and Subhro Bhattacharjee. Elastic signatures of a spin-nematic, 2023.
- [148] Dian Jing, Alexander Conkey Tyner, and Pallab Goswami. Mechanism of skyrmion condensation and pairing for twisted bilayer graphene. *Phys. Rev. B*, 105:184505, May 2022.
- [149] AG Abanov and Paul B Wiegmann. Theta-terms in nonlinear sigma-models. *Nuclear Physics B*, 570(3):685–698, 2000.
- [150] Alexander G. Abanov. Hopf term induced by fermions. *Physics Letters B*, 492(3):321–323, 2000.
- [151] Erez Berg, Eduardo Fradkin, and Steven A Kivelson. Charge-4e superconductivity from pair-density-wave order in certain high-temperature superconductors. *Nature Physics*, 5(11):830–833, 2009.
- [152] T Senthil and Matthew PA Fisher. Z_2 gauge theory of electron fractionalization in strongly correlated systems. *Physical Review B*, 62(12):7850, 2000.
- [153] Zhen Bi and T. Senthil. Adventure in topological phase transitions in $3 + 1$ -d: Non-abelian deconfined quantum criticalities and a possible duality. *Phys. Rev. X*, 9:021034, May 2019.
- [154] Chao-Ming Jian and Cenke Xu. Generic “unnecessary” quantum critical points with minimal degrees of freedom. *Phys. Rev. B*, 101:035118, Jan 2020.
- [155] Yunchao Zhang, Xue-Yang Song, and T Senthil. Dirac spin liquid as an” unnecessary” quantum critical point on square lattice antiferromagnets. *arXiv preprint arXiv:2404.11654*, 2024.

- [156] Basudeb Mondal, Vijay B Shenoy, and Subhro Bhattacharjee. Emergent SU(8) dirac semimetal and novel proximate phases of spin-orbit coupled fermions on a honeycomb lattice. *arXiv preprint arXiv:2304.07223*, 2023.
- [157] Masahiko G. Yamada, Masaki Oshikawa, and George Jackeli. Emergent SU(4) symmetry in α -ZrCl₃ and crystalline spin-orbital liquids. *Phys. Rev. Lett.*, 121:097201, Aug 2018.
- [158] Pavel A. Maksimov, Alexey V. Ushakov, Zlata V. Pchelkina, Ying Li, Stephen M. Winter, and Sergey V. Streltsov. Ab initio guided minimal model for the “Kitaev” material BaCo₂(AsO₄)₂: Importance of direct hopping, third-neighbor exchange, and quantum fluctuations. *Phys. Rev. B*, 106:165131, Oct 2022.
- [159] Daniel Guterding, Harald O Jeschke, and Roser Valentí. Prospect of quantum anomalous hall and quantum spin hall effect in doped kagome lattice mott insulators. *Scientific reports*, 6(1):1–8, 2016.
- [160] N. Goldman, D. F. Urban, and D. Bercioux. Topological phases for fermionic cold atoms on the Lieb lattice. *Phys. Rev. A*, 83:063601, Jun 2011.
- [161] IM Lifshitz et al. Anomalies of electron characteristics of a metal in the high pressure region. *Sov. Phys. JETP*, 11(5):1130–1135, 1960.
- [162] GE Volovik. Topological Lifshitz transitions. *Low Temperature Physics*, 43(1):47–55, 2017.
- [163] Liang Fu and C. L. Kane. Topological insulators with inversion symmetry. *Phys. Rev. B*, 76:045302, Jul 2007.
- [164] Youhei Yamaji, Takahiro Misawa, and Masatoshi Imada. Quantum and topological criticalities of Lifshitz transition in two-dimensional correlated electron systems. *Journal of the Physical Society of Japan*, 75(9):094719–094719, 2006.
- [165] Marlon Rodney, H. Francis Song, Sung-Sik Lee, Karyn Le Hur, and Erik S. Sørensen. Scaling of entanglement entropy across Lifshitz transitions. *Phys. Rev. B*, 87:115132, Mar 2013.

- [166] Veronika Sunko, Edgar Abarca Morales, Igor Marković, Mark E Barber, Dijana Milosavljević, Federico Mazzola, Dmitry A Sokolov, Naoki Kikugawa, Cephise Cacho, Pavel Dudin, et al. Direct observation of a uniaxial stress-driven Lifshitz transition in Sr_2RuO_4 . *npj Quantum Materials*, 4(1):46, 2019.
- [167] Shuichi Murakami, Naoto Nagosa, and Shou-Cheng Zhang. $\text{SU}(2)$ non-abelian holonomy and dissipationless spin current in semiconductors. *Phys. Rev. B*, 69:235206, Jun 2004.

Publications

Publications relevant to the thesis

1. Basudeb Mondal, Vijay B. Shenoy and Subhro Bhattacharjee, “*Emergent $SU(8)$ Dirac semimetal and novel proximate phases of spin-orbit coupled fermions on a honeycomb lattice*”, [PRB 108, 245106](#).
2. Manoj Gupta, Basudeb Mondal, Subhro Bhattacharjee and Tanusri Saha Dasgupta, “*Ab-initio Insights on the Fermiology of d^1 Transition metals in Honeycomb lattice : Hierarchy of hopping pathways and spin-orbit coupling* ”, [PRR 5, 043219](#) .

Other Publications

1. Ankush Chaubey, Basudeb Mondal, Vijay B. Shenoy, and Subhro Bhattacharjee, “*Superconductivity in Spin-Orbit coupled $SU(8)$ Dirac Fermions on Honeycomb lattice*”, Manuscript under preparation.